MODELING AND SIMULATIONS OF EVAPORATING SPRAY, TURBULENT FLOW, AND COMBUSTION IN INTERNAL COMBUSTION ENGINES

By

Shalabh Srivastava

A DISSERTATION

Submitted to
Michigan State University
in partial fulfillment of the requirements
for the degree of

Mechanical Engineering - Doctor of Philosophy

2015

ABSTRACT

MODELING AND SIMULATIONS OF EVAPORATING SPRAY, TURBULENT FLOW, AND COMBUSTION IN INTERNAL COMBUSTION ENGINES

By

Shalabh Srivastava

A multicomponent droplet evaporation model, which discretizes the one-dimensional mass and temperature profiles inside a droplet with a finite volume method and treats the liquid phase as thermodynamically real, has been developed and implemented into a large-eddy simulation (LES) code for evaporating and reacting spray simulations. Single drop evaporation results obtained by the variable property multicomponent model are shown to match with the constant property model in the limiting conditions. The LES code with the multicomponent model is used along with the Kelvin-Helmholtz - Rayleigh-Taylor (KH-RT) droplet breakup model to simulate realistic fuel sprays in a closed vessel and is found to reasonably well predict the experimentally observed non-linear behavior of spray penetration lengths with changing ambient conditions for n-hexadecane and 4 different multicomponent surrogate diesel fuels with 2-8 components. The effects of various modeling assumptions and gas and liquid parameters on the drop and spray evolution and evaporation are investigated in details. A previously studied single piston Rapid Compression Machine (RCM), extended to a twin-piston RCM, is simulated by LES for different stroke ratios of the two pistons, as a precursor to the study of opposed piston two-stroke engines. Opposed piston engines, which have recently generated interest due to their high power density and fuel economy, are mechanically simpler compared to conventional four-stroke engines but involve highly unsteady, turbulent and cycle-variant flows. LES of turbulent spray combustion in a generic single cylinder, opposed-piston, two-stroke engine configuration has been conducted with the

two-phase filtered mass density function (FMDF) model, which is an Eulerian-Lagrangian-Lagrangian subgrid-scale probability density function (PDF) model for LES of two-phase turbulent reacting flows. The effects of various geometric parameters, operating conditions and spray parameters on the flow evolution, turbulence, spray and combustion in the engine are studied. The cycle-to-cycle variations in the flow variables like swirl and tumble are found to be significant while those in thermodynamic variables like temperature are negligible. The hybrid LES/FMDF methodology has been applied to simulate non-reacting turbulent spray for single-component and multi-component fuels and the consistency of the method has been established. The effects of spray parameters like nozzle hole diameter, injection pressure and injected fuel temperature on the spray penetration length are found to qualitatively follow experimental trends. Combustion simulations of n-dodecane fuel sprays are carried out for the opposed piston engine with a global kinetics mechanism and the consistency of the LES and FMDF components is demonstrated.

To my parents
Dr. and Mrs. Srivastava

ACKNOWLEDGMENTS

I would like to gratefully acknowledge the invaluable guidance and support of my advisor Dr. Farhad Jaberi during my years as a graduate student at Michigan State University. This work would not have been possible without his patience, scholarly inputs, and consistent encouragement. It has been an enlightening experience working with him.

My sincere thanks go to my committee members Dr. Giles Brereton, Dr. Dennis Miller, and Dr. Harold Schock for their helpful suggestions and comments at all stages of this work. Dr. Brereton's insights on heat and mass transfer concepts were interesting and helpful. I would also like to thank Dr. David L.S. Hung for his advice regarding the practical aspects of fuel spray systems.

Financial support for the majority of this work was provided by the U.S. Department of Energy under agreement DE-FC26-07NT43278 and the Defense Logistics Agency under agreement DFARS-252235-7010. Additional support was provided by the MSU Graduate School via the Dissertation Completion Fellowship and by the Department of Mechanical Engineering Fellowship. Computational resources were provided by the High Performance Computing Center at Michigan State University.

I am indebted to Dr. Araz Banaeizadeh for his invaluable help at various stages of my research career. A special thanks to Dr. Abolfazl Irannejad for numerous, deep discussions regarding CFD, sprays, and everything else. I would also like to thank all my colleagues and friends, especially Dr. Avinash Jammalamadaka, Dr. Pramod Thupaki, Dr. Jameel Al-Haddad, and future Drs. Rajib Mandal, Husam Abdulrahman, and AbdoulAhad Validi, for their involvement in various academic and extracurricular activities with me during the last few years.

Last but not the least, I would like to acknowledge my indebtedness to my parents and sister. Their unconditional love, support, and sacrifice have been the driving force behind everything I have achieved in life, including this dissertation.

TABLE OF CONTENTS

LIST OF TABLES

LIST OF FIGURES

KEY TO SYMBOLS

Roman Symbols

A_{orif}	Injector orifice exit area, m^2
B_d	Spalding mass transfer number
B_M	Mass transfer number for single species
B_T	Spalding heat transfer number
C_p	Specific heat at constant pressure, J/kgK
C_v	Specific heat at constant volume, J/kgK
$C_{a,inj}$	Injector orifice area-contraction coefficient
C_d	Smagorinsky model constant
$C_{d,inj}$	Injector discharge coefficient
C_F	Friction drag coefficient
B_1	KH breakup model constant
C_{RT}	RT breakup model constant
$C_{v,inj}$	Injection velocity coefficient
D	Diffusion constant, m^2/s
D_{blob}	Diameter of injected spray droplet, m
D_{orif}	Injector orifice diameter
f_1	Drag factor
F_i	ith component of drag force on the droplet, N
G	Filter Function, $1/m^3$
h	Enthalpy, J
J	Jacobian of transformation
J	Jacobian of transformation
K_{RT}	Wave number of RT wave

L_b	Breakup-length, m
L_v	Latent heat of evaporation, J/kg
$\dot{M}$	Momentum flow rate, N
m_d	Mass of the droplet, kg
Nu	Nusselt number
p	Pressure, N/m^2
P_{inj}	Spray injection pressure, Pa
P_L	Filtered Mass Density Function (FMDF)
Pr	Prandtl number
Pr_t	Turbulent Prandtl Number
Sc_t	Turbulent Schmidt Number
r	Radius, m
$r_{c,KH}$	Radius of child droplet after KH breakup, m
$r_{c,RT}$	Radius of child droplet after RT breakup, m
Re_{sl}	Droplet Reynolds number based on the slip velocity
$\|\overline{S}\|$	Rate-of-strain magnitude, 1/s
$\tilde{S}_\alpha^{cmp}$	Source term due to compressibility effect
S_α^{rea}	Source term for species α due to reaction
S_α^{spy}	Production of species α due to evaporation
Sc	Schmidt number
Sh	Sherwood number
S	Rate of strain tensor
T	Temperature, K
t	Time, s
T_d	Temperature of the droplet, K
U	Solution vector
u_i	ith component of gas velocity at droplet location, m/s

U_s	Maximum liquid surface velocity, m/s
v_i	ith component of droplet velocity, m/s
We_g	Gas Weber number
W_i	Wiener process
X	Mole fraction
x_i	ith component of droplet position vector, m
Y	Mass fraction
Z	Ohnesorge number

Abbreviations

$1D$	One-dimensional
$2-EHB$	2-ehtylhexyl butyrate
$2-EHN$	2-ethylhexyl nonanoate
$2D$	Two-dimensional
$3D$	Three-dimensional
BDC	Bottom Dead Center
BN	Butyl nonanoate
CA	Crank Angle
CAD	Crank Angle Degree
CAT	Caterpillar
CCV	Cycle-to-Cycle Variation
CFA	8 species diesel surrogate
CFM	Coherent Flame Model
CHT	Conjugate Heat Transfer
CMC	Conditional Moment Closure
CTC	Characteristic Time Scale
$D2N$	2 species diesel surrogate
$D6N$	6 species diesel surrogate

DBS	Dibutyl Succinate
$DISI$	Direct Injection Spark Ignition
DNS	Direct Numerical Simulation
$ECFM$	Extended Coherent Flame Model
$ECFM-3z$	Extended Coherent Flame Model-3 zone
EGR	Exhaust Gas Recirculation
FD	Finite Difference
$FD9A$	Fuels for Advanced Combustion Engines Diesel#9 Batch A, 8 species diesel surrogate
FSD	Flame Surface Density
GDI	Gasoline Direct Injection
iBN	isobutyl nonanoate
IC	Internal Combustion
IEM	Interaction by exchange with the mean
KH	Kelvin-Helmholtz
LES	Large Eddy Simulation
LHS	Left Hand Side
$LMSE$	Linear mean-square estimation
MC	Monte Carlo
MO	Methyl Oleate
MPI	Message Passing Interface
$MUSCL$	Monotone Upstream-centered Schemes for Conservation Laws
NOx	Nitrous Oxides
$OP2S$	Opposed-Piston, Two-Stroke
$OpenFOAM$	Open source Field Operation And Manipulation
$OPOC$	Opposed-Piston Opposed-Cylinder
PDF	Probability Density Function

PIV	Particle Image Velocimetry
$RANS$	Reynolds-Averaged Navier Stokes
RCM	Rapid Compression Machine
RHS	Right Hand Side
RIF	Representative Interactive Flamelet
RNG	Re-normalization Group
RPM	Revolutions per minute
RT	Rayleigh-Taylor
SDE	Stochastic Differential Equation
SGS	Subgrid Scale
SOI	Start of Injection
SR	Swirl Ratio
TDC	Top Dead Center
TR	Tumble Ratio
$UNIFAC$	UNIversal Functional Activity Coefficient
VOF	Volume-of-Fluid
$WALE$	Wall-adopting local eddy-viscosity
Greek Symbols	
Δ	Characteristic size of the filter function, m
δ	Dirac Delta function
γ_k	Activity Coefficient of species k
γ_k^C	Combinatoric part of activity coefficient
γ_k^R	Rest part of activity coefficient
Γ	Thermal Diffusivity, Pa.S
Γ_t	Turbulent Diffusivity, Pa.S
λ	Thermal Conductivity, W/mK

Λ_{KH}	Wavelength of the KH wave with the maximum growth rate, m
ν_t	Turbulent Viscosity, m^2/s
Ω_{KH}	Frequency of the fastest growing KH wave, /s
Ω_m	SGS Mixing Frequency, 1/s
Ψ	Scalar vector in sample space
ρ	Density, kg/m^3
ρ_f	Fuel density at injection temperature, kg/m^3
σ	Fine-grained density
τ_d	Droplet characteristic time, s
τ_{KH}	Breakup time for KH breakup, s
τ_{RT}	Breakup time for RT breakup, s
Subscripts	
α	Gas phase species 'α' value
g	Gas phase value
i, j	Variable number
k	Liquid phase species 'k' value
l	Liquid phase value
s	Liquid-vapor interface value
Conventions	
$\bar{f}$	Filtered value
$\widetilde{f}$	Favre filtered value

Chapter 1

Large Eddy Simulations of Turbulent Sprays with a Multicomponent Evaporation Model

1.1 Introduction

Vaporization of liquid fuels and its prediction is of fundamental importance in many engineering applications, particularly in internal combustion engines. The type of model used for predicting the evaporation of liquid droplets can have a significant effect on the spatial and temporal distribution of the fuel in the vapor phase and consequently the combustion. In most spray calculations conducted with direct numerical simulation (DNS) or large eddy simulation (LES) methods [1]-[8], the modeling approach to heat transfer and evaporation has been that of assuming the fuel to be composed of a single component with lumped properties. This assumption has been convenient numerically and has been widely utilized. However, for multicomponent fuels like gasoline, diesel or biodiesels, more complex multicomponent evaporation models are usually needed. The presence of components with a wide range of volatility and the consequent non-monotonicity of the mass fraction and temperature profiles inside the fuel droplet makes it imperative to resolve the physico-chemical

features of multicomponent evaporation.

Various single component and multicomponent models have been proposed over the years for the droplet evaporation [9], [10]. These models can be divided into two different types: discrete-component and continuous thermodynamics models. Continuous thermodynamic models, originally developed by Tamim and Hallett [11], use a continuous distribution function to model the complex fuel composition. This distribution function is based on properties like molecular weight or boiling point and is used for the evaluation of the multicomponent fuel properties. The continuous models have much less computational overhead but are relatively difficult to be used for combustion simulations. Nevertheless, they have been used in several studies in the past in both original and modified forms [12]-[15]. For example, Zhang et al.[15] have developed a hybrid model using continuous thermodynamics to describe the petroleum fuel and the discrete components approach to represent the biofuels in a petroleum-biofuel blend. Discrete component models characterize the complex fuel as a mixture of several representative species and track the individual components during the evaporation process. This allows coupling of the evaporation process with the combustion and comprehensive reaction mechanisms. References [16] - [24] present some of the discrete component models used for multicomponent evaporation. Landis and Mills [16] studied the spherically symmetric evaporation of a heptane-octane droplet in air and concluded that the evaporation becomes quasi-steady after the early transition, with both components evaporating at a rate nearly proportional to their initial mass fractions. Lara-Urbaneja and Sirignano [18] developed a model for studying the transient evaporation of liquid droplets. The gas and liquid phase boundary layers in this model were analyzed by an integral method and the mass and heat transfer in the droplet core were described by a vortex model. They found that the internal circulation and higher mixture volatility reduce the nonuniformity inside

the droplet. Aggarwal [19] analyzed the effects of different liquid and gas phase models for a dilute spray in a laminar, hot gas stream and found the results to be sensitive to the model used. The model with infinitely fast diffusion overpredicted and underpredicted the vapor mass fractions of the most volatile and the least volatile components, respectively. The model with limited diffusion gave better predictions due to its ability to resolve the internal liquid temperature and mass fraction profiles. Chen et al. [20] studied the evaporation of multicomponent fuels in laminar flows and concluded that for relatively low ambient temperatures, both the models with finite and infinite diffusion yield good results, provided that variable properties are used in both the liquid phase and the gas film surrounding the droplet. Renksizbulut and Bussmann [21] studied the droplet evaporation with an axisymmetric model and concluded that the liquid phase mass transfer is highly transient with preferential vaporization of more volatile species and that a constant Lewis number approximation is not valid. They also found that the commonly used correlations for the drag coefficient and Nusselt and Sherwood numbers are reasonably accurate for multicomponent droplet evaporation predictions at intermediate Reynolds numbers ($\sim$100). Zeng and Lee [22, 23] developed a multicomponent droplet model which solves the difference equations between surface and average temperatures and mass fractions and uses polynomial functions for the inner droplet temperature and mass fractions. In the work by Ra and Reitz [24], an approximate solution of the quasi-steady energy equation is used to calculate the heat flux from the gas to the droplet. The model considers finite heat transfer rates but assumes the liquid phase to be well mixed in both normal or flash-boiling conditions. The high rate of fossil fuel consumption has been a major contributor to greenhouse emissions and environmental pollution. Not only the environmental impacts, but also the limited availability of fossil fuels and the concerns over energy security in the future have led to considerable re-

search into more efficient vehicles and fuels with lower environmental impacts, and which are renewable and locally available. Among other alternatives, considerable research efforts have been put into plant-derived biofuels. Some of the alternatives being studied are liquid and gaseous fuels derived from biomass including biodiesel, bioethanol, biomethanol , etc. ([52], [53], [54]). Soy- and Canola-derived biodisels have been the subject of many studies aimed at the evaluation of the fuel's preformance in engines and modeling of the fuel's combustion ([55]-[60]). The main objective of this paper is to develop and test practical multicomponent droplet heat and mass transfer models for LES of realistic evaporating sprays. For this we use Lagrangian spray models with one-dimensional, finite rate, variable-property models for the heat transfer and evaporation inside all simulated droplets. The model is used for predictions of liquid and gas quantities of high speed evaporating sprays in high temperature and pressure conditions.

1.2 Mathematical Formulation and Computational Models

The multicomponent evaporation model we use in our LES calculations is based on that developed by Torres et al. [25, 26, 27]. The model discretizes the radial and symmetric profiles of the time-dependent temperature and mass fractions inside each droplet and solves them with a finite volume numerical method. The model has been modified to treat the liquid phase as real by using activity coefficients using the UNIversal Functional Activity Coefficient (UNIFAC) method. In the following, the multicomponent model is described in detail after describing the simpler single-component model and before describing the gas phase LES equations with spray-coupling terms.

1.2.1 Single Component droplet model

The following Lagrangian equations [2] describe the transient position (x_i) and velocity (v_i) of a droplet:

$$\frac{dx_i}{dt} = v_i, \tag{1.1}$$

$$\frac{dv_i}{dt} = \frac{F_i}{m_d} = \frac{f_1}{\tau_d}(u_i - v_i), \tag{1.2}$$

The Lagrangian equations for the temperature and mass of the droplet in the constant property, single-component lumped model [2] are:

$$\frac{dT_d}{dt} = \frac{Q + \dot{m}_d L_v}{m_d C_{p,l}} = \frac{Nu_g}{3Pr_g}\left(\frac{C_{p,g}}{C_{p,l}}\right)\left(\frac{f_2}{\tau_d}\right)(T_g - T_d) + \left(\frac{\dot{m}_d}{m_d}\right)\frac{L_v}{C_{p,l}}, \tag{1.3}$$

$$\frac{dm_d}{dt} = \dot{m}_d = -\frac{Sh_g}{3Sc_g}\left(\frac{m_d}{\tau_d}\right) ln[1 + B_M], \tag{1.4}$$

In these equations, m_d is the mass of the droplet, T_d is the temperature of the droplet, T_g is the gas phase temperature at the droplet location, L_v is the latent heat of vaporization of the liquid fuel, C_{p_l} is the heat capacity of the liquid, and C_{pg} is the heat capacity of the gas phase which is calculated as,

$$C_{p,g} = (1 - Y_v)C_{p,c} + Y_v C_{p,v} \tag{1.5}$$

Here, Y_v is the mass fraction of the evaporated vapor, $C_{p,c}$ is the heat capacity of the carrier gas and $C_{p,v}$ is the heat capacity of the evaporated vapor.

The mass transfer number B_M, the droplet characterisitc time τ_d, and the gas phase

Prandtl, Schimdt, Nusselt and Sherwood numbers, are obtained from the following equations:

$$B_M = \frac{Y_{v,s} - Y_v}{1 - Y_{v,s}}, \tag{1.6}$$

$$\tau_d = \frac{\rho_l d^2}{18\mu_g} \tag{1.7}$$

$$Pr_g = \mu_g C_{p,g}/\lambda_g, Sc_g = \mu_g/(\rho_g D_v) \tag{1.8}$$

$$Nu_g = 2 + 0.552 Re_{sl}^{1/2} Pr_g^{1/3}, Sh_g = 2 + 0.552 Re_{sl}^{1/2} Sc_g^{1/2} \tag{1.9}$$

where $Y_{v,s}$ is the vapor mass fraction at the droplet surface, ρ_l is the liquid fuel density, μ_g is the gas viscosity and Re_{sl} is the Reynolds number based on the droplet slip velocity.

1.2.2 Multicomponent droplet model

The multicomponent model used in this work tracks the evolution of temperature and all species mass fractions inside a spherically symmetric droplet. The heat and mass diffusions are assumed to be based on Fourier and Fickian assumptions. Internal circulation caused by the relative motion between the gas and the liquid is accounted for by using effective mass and thermal liquid diffusivities. The fuel densities are temperature dependent and the advective terms related to the expansion velocities due to fuel density changes are included. The enthalpy diffusion terms in the liquid internal energy equations are also retained. The gas phase temperature and mass fraction gradients are modeled using Nusselt and Sherwood numbers. Other assumptions include insolubility of the gas phase in the liquid and the use of Raoult's law for vapor-liquid phase equilibrium, which has been modified here, as explained later. Soret and Dufour effects and thermal radiation are ignored.

With the above assumpstions, the conservation equations for the droplet density, species

mass fractions and energy in the liquid phase may be written as,

$$\frac{\partial \rho_l}{\partial t} + \frac{1}{r_l^2}\frac{\partial}{\partial r_l}(r_l^2 \rho_l v_l) = 0, \tag{1.10}$$

$$\frac{\partial (\rho_l Y_{l,k})}{\partial t} + \frac{1}{r_l^2}\frac{\partial}{\partial r_l}(r_l^2 \rho_l v_l Y_{l,k}) = \frac{1}{r_l^2}\frac{\partial}{\partial r_l}\left(r_l^2 \rho_l D_l \frac{\partial Y_{l,k}}{\partial r_l}\right), \tag{1.11}$$

$$\begin{aligned}\frac{\partial (\rho_l T_l)}{\partial t} + \frac{1}{r_l^2}\frac{\partial}{\partial r_l}(r_l^2 T_l \rho_l v_l) =& \frac{1}{C_{p,l} r_l^2}\frac{\partial}{\partial r_l}\left(r_l^2 \lambda_l \frac{\partial T_l}{\partial r_l}\right) \\ &+ \frac{\rho_l D_l}{C_{p,l} r_l^2}\sum_k \left[\frac{\partial}{\partial r_l}\left(r_l^2 h_{l,k}\frac{\partial Y_{l,k}}{\partial r_l}\right)\right. \\ &\left. - h_{l,k}\frac{\partial}{\partial r_l}\left(r_l^2 \frac{\partial Y_{l,k}}{\partial r_l}\right)\right]\end{aligned} \tag{1.12}$$

Here, ρ_l, T_l, v_l, and $Y_{l,k}$ are the density, temperature, velocity and mass fraction of species k in the liquid phase, respectively. D_l, λ_l, and $h_{l,k}$ are the diffusion constant, thermal conductivity, and enthalpy in the liquid phase, respectively. The specific heat of the liquid mixture at constant pressure, $C_{p,l}$, is defined as:

$$C_{p,l} = \sum_k Y_{l,k}\frac{\partial h_{l,k}}{\partial T_l}\bigg|_p = \sum_k Y_{l,k}\left(C_{v,l,k} - \frac{p_l}{(\rho_{l,k}^o)^2}\frac{d\rho_{l,k}^o}{dT_l}\right) \tag{1.13}$$

where $C_{v,l,k}$ is the specific heat at constant volume for pure species k. Here it is assumed that liquid internal energy and pure fuel species density are functions of temperature alone.

The interface condition for the mass fraction of fuel species k is represented by the following equation:

$$\begin{aligned}\rho_{l,s}(v_{l,s} - \dot{r}_s)(Y_{v,s,k} - Y_{l,s,k}) + \rho_{l,s} D_l \frac{\partial Y_k}{\partial r}\bigg|_{l,s} \\ - \rho_{g,s} D_{g,k} Sh_{g,k}\left(\frac{Y_{v,\infty,k} - Y_{v,s,k}}{2r_s}\right) = 0\end{aligned} \tag{1.14}$$

Here, $Y_{v,\infty,k}$ is the fuel vapor mass fraction at infinity and $D_{g,k}$ is the diffusion constant of species k in the gas phase. The subscript s denotes the values of the quantities at the liquid-vapor interface.

The surface regression rate can be obtained by summing equation (1.14) over all fuel species as,

$$\dot{r}_s - v_{l,s} = \frac{\rho_{g,s} \sum_k D_{g,k} Sh_{g,k} \left(Y_{v,\infty,k} - Y_{v,s,k}\right)}{2\rho_{l,s} r_s \left(1 - Y_{l,s,f}\right)} \tag{1.15}$$

The interface condition for the temperature is imposed through the following equation,

$$\begin{aligned} \sum_{k_{fuel}} L_{v,k,s}\rho_{l,s}\left[(\dot{r}_{l,s} - v_{l,s})Y_{l,s,k} + D_l \frac{\partial Y_k}{\partial r}\bigg|_{l,s}\right] - \lambda_l \frac{\partial T}{\partial r}\bigg|_{l,s} \\ + \lambda_{g,s} Nu_g \frac{T_{g,\infty} - T_s}{2r_s} = 0, \end{aligned} \tag{1.16}$$

The effect of internal circulation in the droplet is modeled by using effective thermal conductivity coefficient λ_l^e and mass diffusivity coefficient D_l^e. The expressions for λ_l^e and D_l^e are derived based on the following 2D assymetric model [28] which assigns the Hill spherical vortex solution to the velocities.

$$\frac{\lambda_l^e}{\lambda_l} = \frac{D_l^e}{D_l} = 1.86 + 0.86 tanh\left\{2.245 log_{10}\left(\frac{Re_l Pr_l}{30}\right)\right\} \tag{1.17}$$

where $Re_l = 2U_s r_s \rho_l / \mu_l$, and U_s is the maximum liquid surface velocity given by

$$U_s = \frac{1}{32}|u + u' - v|(\mu_g/\mu_l) Re_g C_F, \tag{1.18}$$

and $C_F = 12.69 Re_g^{-2/3}/(1 + B_d)$ is the friction drag coefficient.

The gas phase Nusselt number Nu_g [1] is obtained from the well-known Ranz-Marshall

correlation,

$$Nu_g = (2.0 + 0.6Re_g^{1/2}Pr_g^{1/3})\frac{ln(1+B_T)}{B_T}, \tag{1.19}$$

The analogous form of Sherwood number $Sh_{g,k}$ [21],

$$Sh_{g,k} = (2.0 + 0.6Re_g^{1/2}Sc_{g,k}^{1/3})\frac{ln(1+B_d)}{B_d}, \tag{1.20}$$

is used for mass transfer. In equation (1.20), B_T is the Spalding heat transfer number and B_d is the Spalding mass transfer number,

$$B_T = \frac{C_v(\hat{T} - T_s)}{L_{v,s} - (|\dot{q_d}|/\dot{m_d})} \tag{1.21}$$

$$B_d = \frac{Y_{v,s,F} - \sum_k Y_{v,\infty,k}}{1 - Y_{v,s,F}}, \tag{1.22}$$

Here, C_v is the specific heat at constant volume for the fuel vapor mixture, $L_{v,s}$ is the latent heat of evaporation at the droplet surface temperature and $\dot{q_d}$ and $\dot{m_d}$ are the heat and mass transfer rates, respectively. The gas phase properties are calculated at the temperature $\hat{T} = (T_{g_\infty} + T_s)/3$ using the "1/3" rule.

In many multicomponent mixtures, the phase equilibrium solution deviates from the ideal case solution provided by Raoult's law. Here, the Raoult's law for relatively low pressures has been modified by using activity coefficients to make it more suitable for real liquids. For this, we use the following equation,

$$p_{v,k} = \gamma_k X_{l,s,k} p^0_{vap,k} \tag{1.23}$$

where $p_{v,k}$ is the partial pressure of species k in the gas phase at the droplet surface, γ_k is

the activity coefficient of component k, $X_{l,s,k}$ is the mole fraction of species k in the liquid phase at the droplet surface, and $p^0_{vap,k}$ is the equilibrium vapor pressure for a pure species k at the surface temperature T_s.

The parameter γ_k is calculated using the UNIFAC method [29, 30], described in Appendix 3.6.

The surface mole fraction at the liquid phase and the surface mass fraction in the gas phase can be obtained from the following equations,

$$X_{l,s,k} = \frac{Y_{l,s,k}/W_k}{\sum_j Y_{l,s,j}/W_j}, \tag{1.24}$$

$$Y_{v,s,k} = \frac{X_{v,s,k}W_k}{\sum_j X_{v,s,j}W_j} = \frac{p_{v,k}W_k}{\sum_j p_{g,s,j}W_j} \tag{1.25}$$

The internal linear equations (1.10) - (1.12) and the non-linear interface equations (1.14) - (1.16) are solved simultaneously by decoupling them using matrix manipulation. An implicit finite volume scheme is used to discretize the conservation equations and the non-linear interfacial constraints are implemented through Broyden's method. Broyden's method is an extension of the secant method developed for solving systems of non-linear equations. In this method, an approximate Jacobian is used to update the multidimensional solution as described in detail by Dennis et al. [31]. The particle location and velocity are obtained by solving equations (1.1) and (1.2), respectively. The thermo-physical properties, including surface tension, are a function of temperature and are calculated using suitable correlations and methods given in Poling et al. [32]

1.2.3 Gas Phase Equations

As mentioned before, a hybrid Eulerian-Lagrangian mathematical computational method is used in this work for the solution of liquid-gas system. For the gas phase LES solution, the filtered form compressible Navier-Stokes, energy and scalar equations are solved along with the equation of state [33, 34]. These equations are as follows:

$$\frac{\partial \bar{\rho}}{\partial t} + \frac{\partial \bar{\rho}\widetilde{u}_i}{\partial x_i} = \bar{S}_\rho \tag{1.26}$$

$$\frac{\partial \bar{\rho}\widetilde{u}_i}{\partial t} + \frac{\partial \bar{\rho}\widetilde{u}_i\widetilde{u}_j}{\partial x_j} = -\frac{\partial \bar{p}}{\partial x_i} + \frac{\partial \bar{\tau}_{ij}}{\partial x_j} - \frac{\partial \tau_{ij}^{sgs}}{\partial x_j} + \bar{S}_{ui} \tag{1.27}$$

$$\frac{\partial \bar{\rho}\widetilde{E}}{\partial t} + \frac{\partial \bar{\rho}\widetilde{u}_i\widetilde{E}}{\partial x_i} + \frac{\partial \widetilde{u}_i\bar{p}}{\partial x_i} = -\frac{\partial \bar{q}_i}{\partial x_i} + \frac{\partial \widetilde{u}_j\bar{\tau}_{ij}}{\partial x_i} - \frac{\partial H_i^{sgs}}{\partial x_i} + \bar{S}_e \tag{1.28}$$

$$\frac{\partial \bar{\rho}\widetilde{Y}_\alpha}{\partial t} + \frac{\partial \bar{\rho}\widetilde{u}_i\widetilde{Y}_\alpha}{\partial x_i} = \frac{\partial \bar{\rho}\widetilde{Y}_\alpha\widetilde{V}_{i,\alpha}}{\partial x_i} - \frac{\partial Y_{i,\alpha}^{sgs}}{\partial x_i} + \bar{S}_\rho^\alpha \tag{1.29}$$

$\alpha = 1, 2, ...N_s$

$$\bar{p} = \bar{\rho}R_u\widetilde{T}\sum_1^{N_s}\frac{\widetilde{Y}_\alpha}{W_\alpha} \tag{1.30}$$

Here, $\bar{f}$ and $\widetilde{f} = \overline{\rho f}/\bar{\rho}$ are the filtered and the Favre-filtered values of the transport variable $f(x,t)$, respectively. Also, ρ is the gas phase density, u_i is the gas velocity, E is the gas energy, T is the gas temperature, p is the thermodynamic pressure, Y_α is the mass fraction of the gas phase species α, $V_{i,\alpha}$ is the diffusion velocity of species α, W_α is the molecular weight and R_u is the universal gas constant. The diffusion velocities in the scalar

equations are approximated using Fickian diffusion. The subgrid stress terms are closed by gradient-type closures, with the effective viscosity defined to be $\mu_e = \mu + \rho\nu_t$. The SGS turbulent kinematic viscosity, ν_t, is calculated by the Smagorinsky type model [35, 36]as:

$$\nu_t = (C_d\Delta)^2|\overline{S}| \tag{1.31}$$

Here, the model coefficient C_d is either fixed or obtained dynamically ([37]-[39]). In Equation (1.31), $\Delta = (volume)^{1/3}$ is the characteristic size of the filter function, and $|\overline{S}|$ denotes the magnitude of the rate of strain tensor. The SGS velocity correlations in the energy and scalar equations are modeled with the following closures [40], [41]:

$$H_i^{sgs} = \bar{\rho}(\widetilde{u_i E} - \widetilde{u}_i\widetilde{E}) + (\overline{\rho u_i} - \bar{\rho}\widetilde{u}_i) = -\bar{\rho}\frac{\nu_t}{Pr_t}\frac{\partial\widetilde{H}}{\partial x_i} \tag{1.32}$$

$$Y_{i,\alpha}^{sgs} = \bar{\rho}(\widetilde{u_i Y_\alpha} - \widetilde{u}_i\widetilde{Y_\alpha}) = -\bar{\rho}\frac{\nu_t}{Sc_t}\frac{\partial\widetilde{Y_\alpha}}{\partial x_i}, \tag{1.33}$$

where $\widetilde{H} = \widetilde{E} + \bar{p}/\bar{\rho}$ is the total filtered enthalpy and Pr_t and Sc_t are the turbulent Prandtl and Schmidt numbers, respectively.

The phase coupling terms in the gas-phase equations, S_ρ, S_ρ^α, S_{ui} and S_e are the total fuel vapor mass, individual fuel species mass, momentum and energy source/sink terms, respectively, and are defined as:

$$S_\rho^\alpha = -\sum_\beta \left\{ \frac{w_\beta}{\Delta V_\beta}[\dot{m}_{d,k}]_\beta \right\}, \tag{1.34}$$

$$[\dot{m}_d]_\beta = \sum_k [\dot{m}_{d,k}]_\beta \tag{1.35}$$

$$S_\rho = -\sum_\beta \left\{ \frac{w_\beta}{\Delta V_\beta} [\dot{m}_d]_\beta \right\}, \tag{1.36}$$

$$S_{ui} = -\sum_\beta \left\{ \frac{w_\beta}{\Delta V_\beta} [F_i + \dot{m}_d v_i]_\beta \right\}, \tag{1.37}$$

$$S_e = -\sum_\beta \left\{ \frac{w_\beta}{\Delta V_\beta} [v_i F_i + Q + \dot{m}_d \left\{ \frac{v_i v_i}{2} + h_{V,s} \right\}]_\beta \right\}, \tag{1.38}$$

Here, $\dot{m}_{d,k}$ is the evaporation rate of liquid fuel component k, $\dot{m}_d$ is the overall evaporation rate of the droplet, F_i is the drag force on the droplet, and Q is the heat transfer rate. These quantities are obtained by the single component and multicomponent models as described in sections 1.2.1 and 1.2.2, respectively. The terms S_ρ, S_ρ^α, S_{ui} and S_e are obtained by summing over all the droplets β in a discretization volume ΔV_β, using a weighting factor w_β. The weighting factor is determined geometrically on the basis of the location of the droplet in the discretization volume.

1.3 Results and Discussion

The multicomponent evaporation model has been incorporated into the spray and LES models and has been used for the simulations of single-component and multicomponent evaporating fuel sprays in Sandia's experimental closed vessel configuration [42]. Before discussing the LES-spray results, we assess the multicomponent droplet model and its finite rate heat and mass transfer solver below by comparing its results with the much simpler single-component droplet heat and mass transfer model, referred to as the "lumped" model in this paper.

1.3.1 Single Droplet Calculations

The single droplet calculations have been carried out for both single component and multicomponent liquids. The single component simulations demonstrate the differences between the lumped and multicomponent models and allow us to islolate and to study various subcomponents of the multicomponent model.

1.3.1.1 Single Component Liquid

Simulations have been carried out for a single-component n-hexadecane fuel with both the multicomponent evaporation model and the single component "lumped" evaporation model, under the same operating conditions at gas temperature and pressure of 700 K and 1 atm, respectively. In both simulations, the n-hexadecane droplets are released with temperature of 293 K into a gas chamber. The multicomponent model is capable of utilizing fully variable physical properties for the fuel. However, in order to compare the results of the multicomponent model with the simpler lumped model, constant physical properties, evaluated at the average temperature of the droplet, have been used. Also, the liquid velocity inside the droplet is not considered and the liquid thermal conductivity is increased artificially to very high values to simulate infinite thermal conductivity and mass diffusivity conditions in the lumped model. With these additional features of the multicomponent model turned off, the results obtained from these two models should be similar.

Figure 1.1(a) shows the time variation of the bulk droplet temperature for the multicomponent and lumped models. Both models predict similar behavior for the droplet temperature during the heating period due to high thermal conductivity used in the multicomponent model, and the similarity of liquid properties. As the droplet temperature increases and

evaporation starts at the droplet surface, the average droplet temperature remains nearly constant. Nevertheless, the results obtained by the multicomponent model remain very close to those predicted by the lumped model for the simulated limiting conditions.

Figure 1.1(b) shows the time variation of the droplet area (or D^2), normalized by the initial area, for a droplet with initial diameter of $20\mu m$. Again, both models predict a similar rate of evaporation and as expected for single-component droplets, both models predict a "D-square" law behavior, i.e. the square of droplet diameter decreases linearly in time after the initial heating period. This confirms that the multicomponent model's predictions match with the lumped model's predictions in the limiting conditions, even though the mathematical and computational methods used in them are quite different.

In order to study the effect of various liquid fuel properties on the droplet evaporation, the fuel properties were systematically changed with respect to the base line model shown in Figure 1.1. Figures 1.2 and 1.3 show the effect of liquid thermal conductivity, heat capacity coefficient, and latent heat of vaporization on the droplet lifetime and bulk temperature. When finite thermal conductivity is considered, there is a slight increase in the droplet lifetime (Figure 1.2(a)). This increase in lifetime can be attributed to the slower rate of heating and lower temperatures during the heating phase of the droplet, as seen in Figure 1.2(b). As shown in Figure 1.3(a), variable liquid specific heat causes a much faster evaporation rate due to the lower specific heat at lower drop temperatures. Consequently a higher drop temperature is achieved in the heating phase of the liquid droplet as seen in Figure 1.3(b).

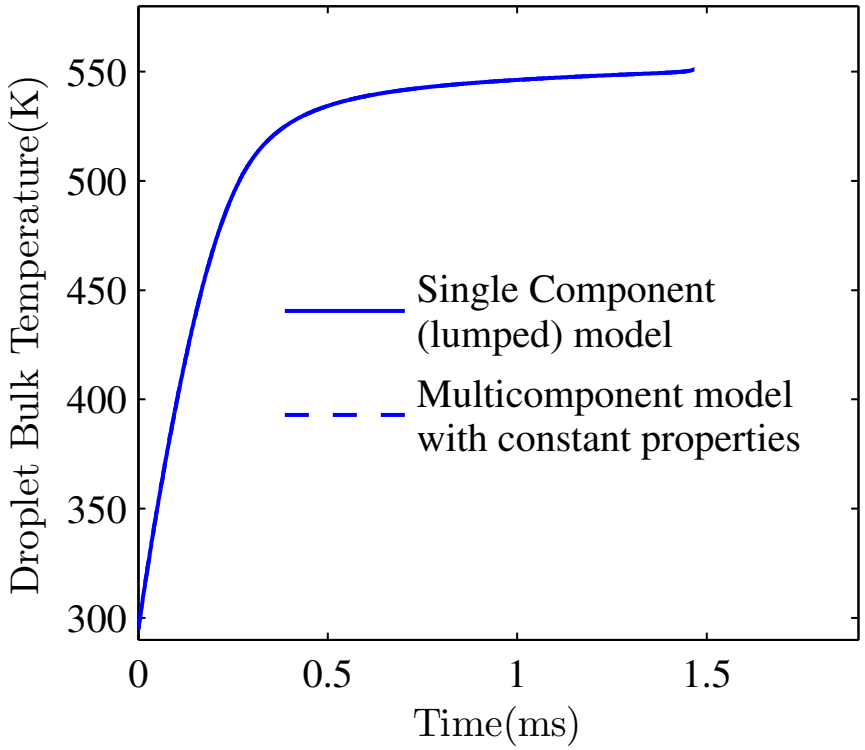

(a)

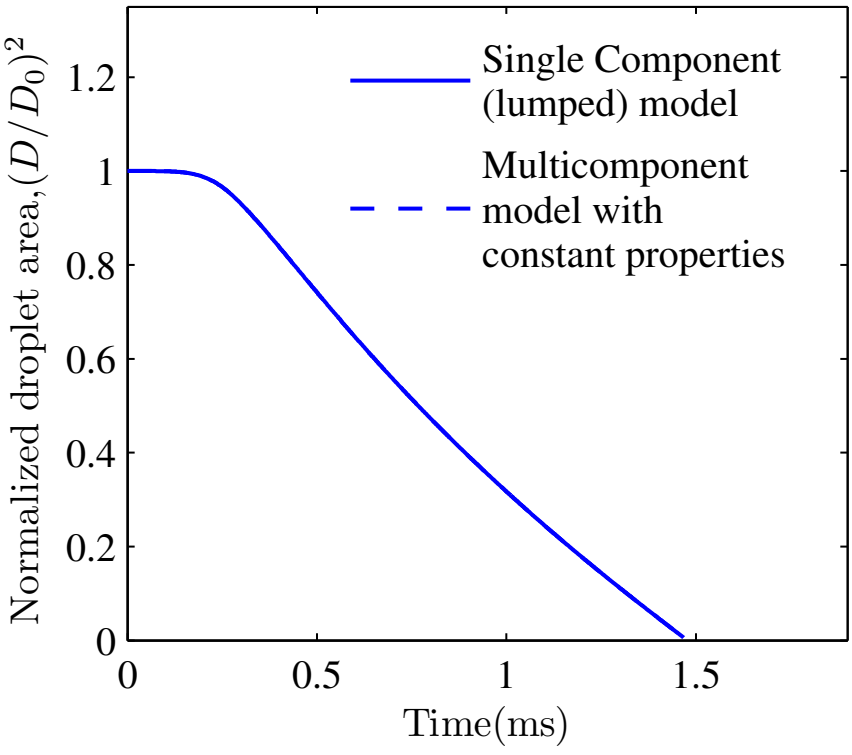

(b)

Figure 1.1: Variation of Droplet (a) temperature, and (b) area, with time. Initial Droplet Diameter = 20 μm, Initial Droplet Temperature = 293 K, Initial Gas Temperature = 700 K, Gas Pressure = 1 atm, Boiling Point of n-hexadecane at 1 atm. = 560 K. .

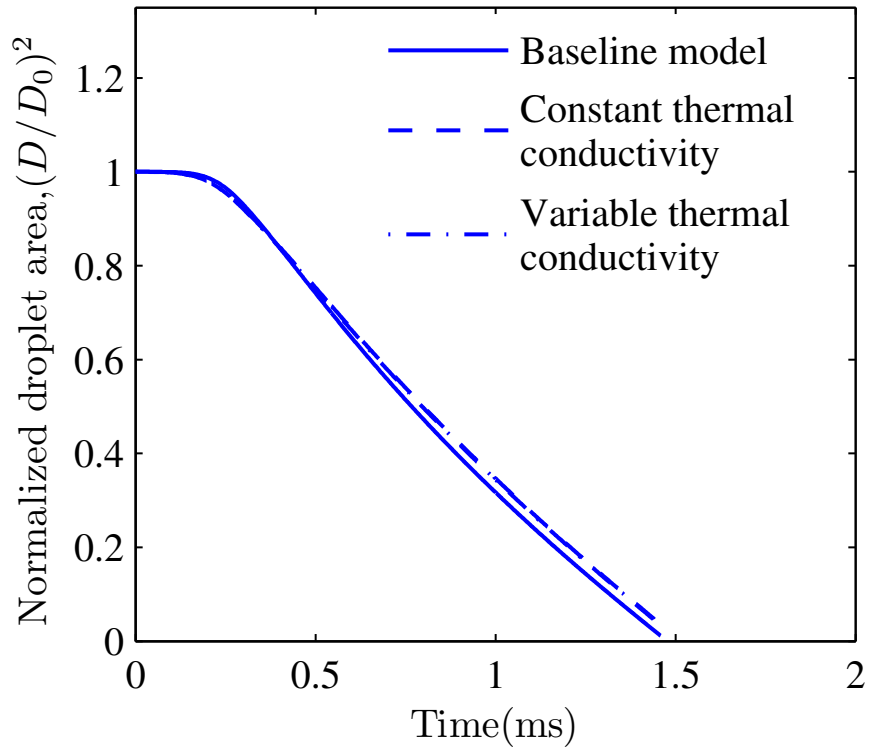

(a)

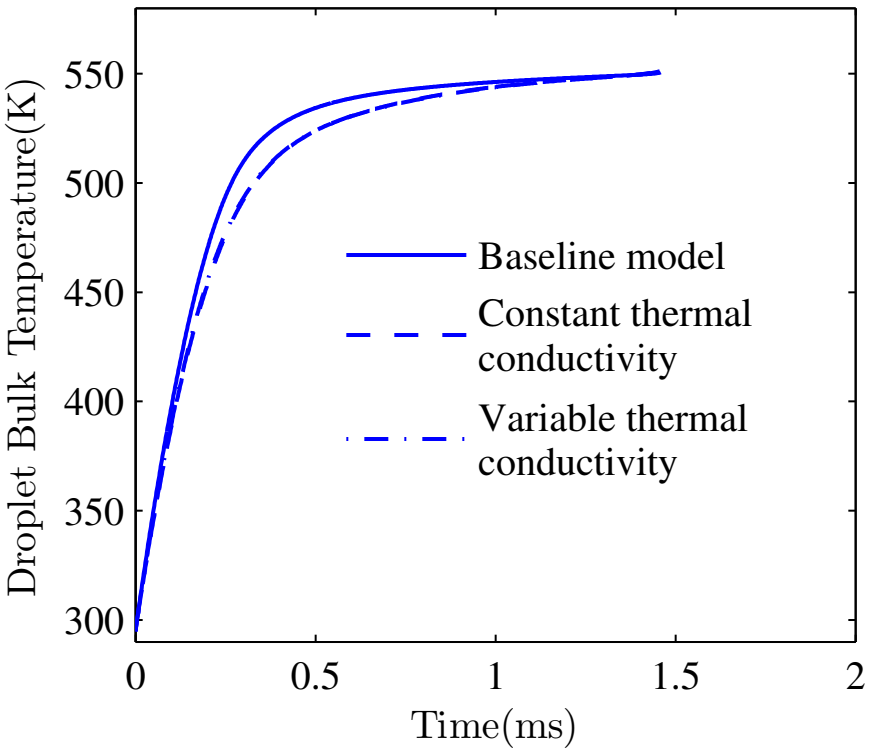

(b)

Figure 1.2: Effect of finite thermal conductivity on droplet (a) area, and (b) temperature.

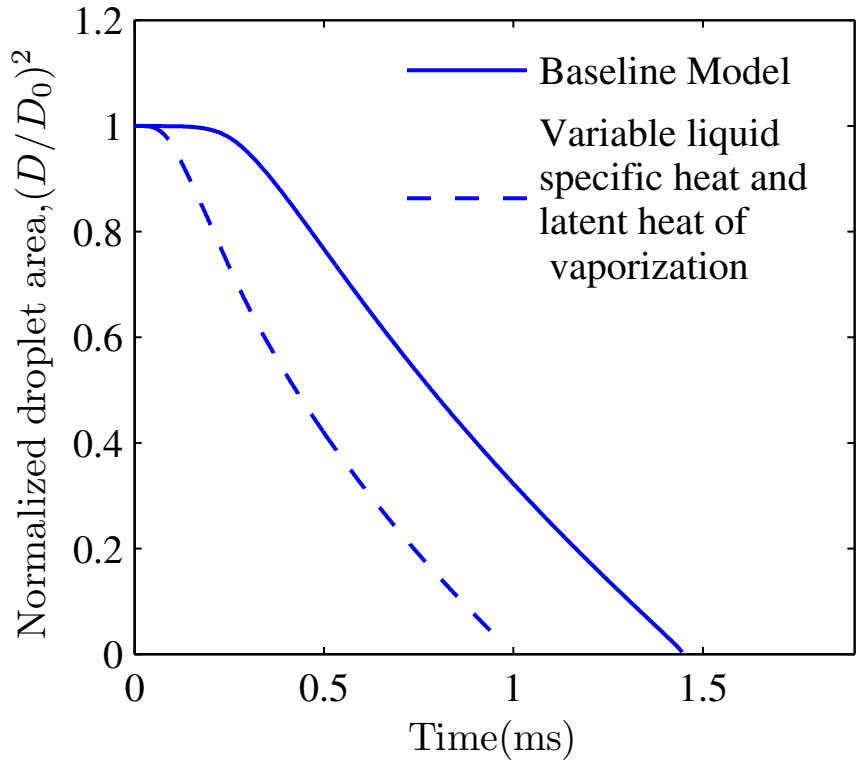

(a)

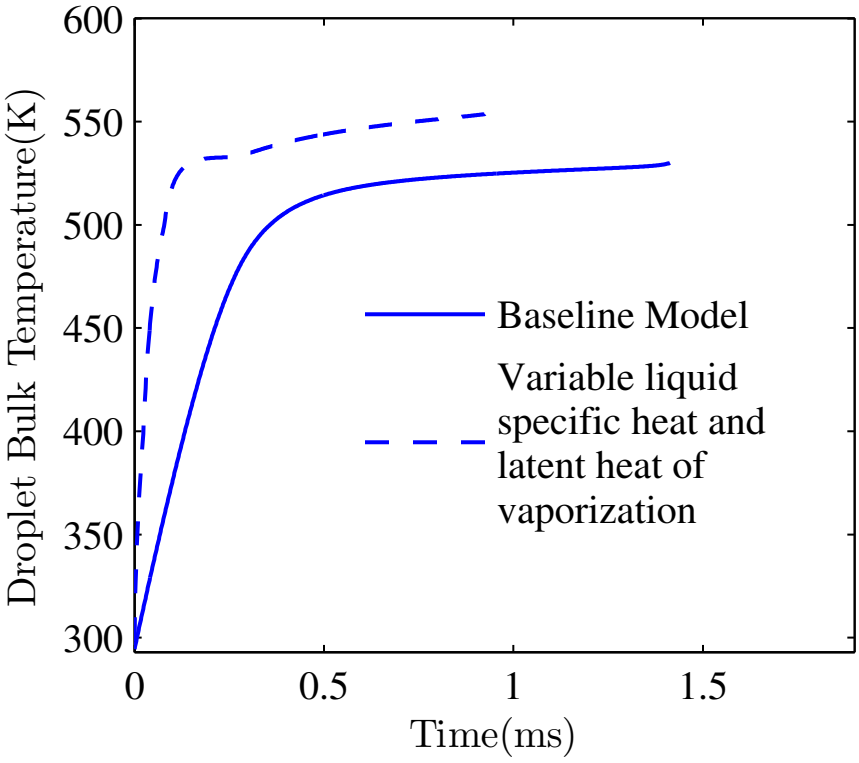

(b)

Figure 1.3: Effect of variable liquid specific heat and latent heat of vaporization on droplet (a) area, (b) temperature.

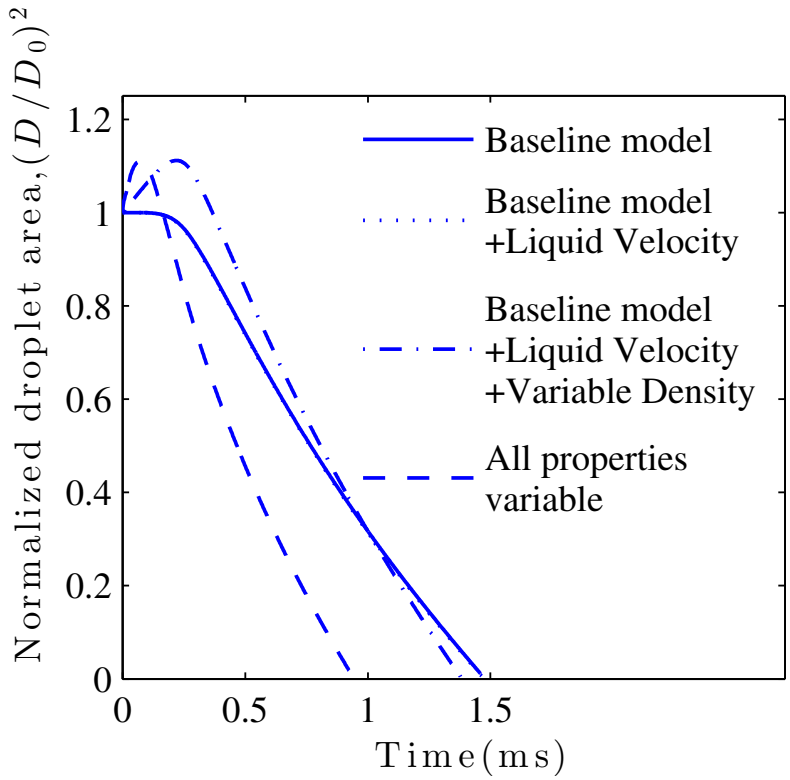

(a)

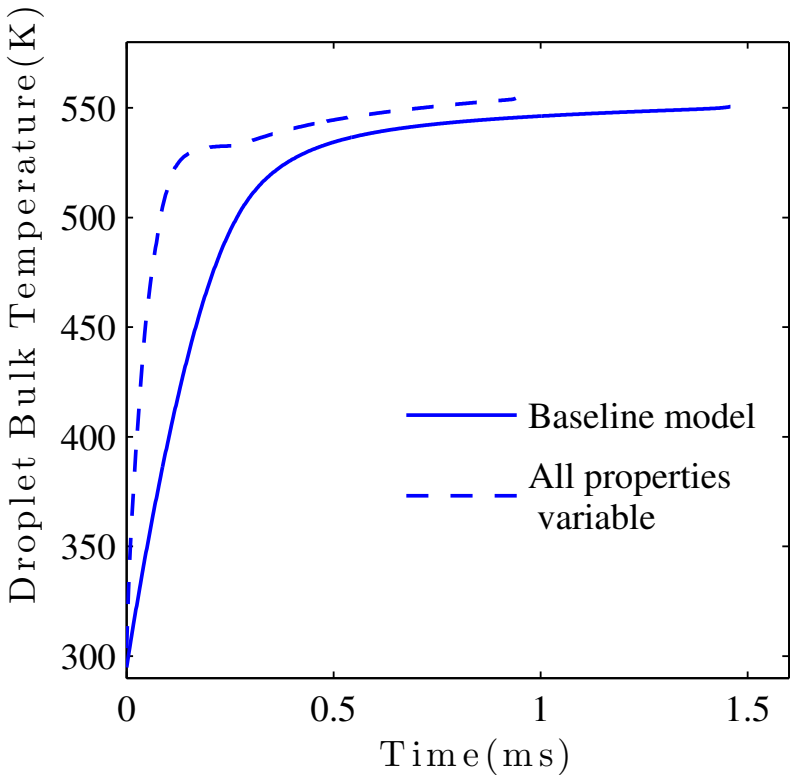

(b)

Figure 1.4: (a) Effect of liquid velocity, variable liquid density and all properties variable on droplet area, (b) Effect of variable properties on droplet temperature.

The effect of variable liquid density on the droplet heating and evaporation is shown in Figure 1.4(a). The thermal expansion of the fuel droplet caused by the decrease in liquid density of the fuel during the droplet heating phase is well captured by the model, even though there is no significant change in droplet lifetime. The constant density model fails to capture the thermal expansion of the droplet. The difference between constant and variable property results is also evident in Figures 1.4(a) and 1.4(b), where the time variations of the normalized droplet area and temperature, respectively, are shown for droplets with constant properties and fully variable properties. It is clear that the droplet evaporates at a faster rate and has a higher temperature than the baseline, constant property droplet. The effect of all the properties being variable is significant and illustrates the importance of using variable properties in droplet evaporation models. The variable property droplet also has a slightly higher final temperature.

Using the variable property multicomponent evaporation model, a systematic study is carried out to examine the effect of changing various fuel properties from their "reference" (actual) values. Keeping all the other properties at their reference values and the gas properties constant, one of the considered properties is varied from its baseline values to simulate fuels with concomitant properties. For instance, Figures 1.5 - 1.7 show the effects of the liquid density, latent heat of vaporization and thermal conductivity on the droplet heating, evaporation, lifetime and bulk temperature. It is shown in Figure 1.5(a) that by decreasing the liquid density (while keeping the initial droplet size the same), the droplet lifetime decreases simply because the droplet mass is changing. During the heating phase, the droplet bulk temperature increases with decreasing liquid density (Figure 1.5(b)). This is due to the lower energy required to heat lesser amount of fuel. Figures 1.6(a) and 1.6(b) show that decreasing the latent heat of vaporization decreases the droplet lifetime, while the maximum

droplet bulk temperature increases. This is due to the corresponding decrease in the energy required for the evaporation. Increasing the liquid thermal conductivity has no significant effect on the droplet lifetime and bulk temperature as illustrated in Figures 1.7(a) and 1.7(b).

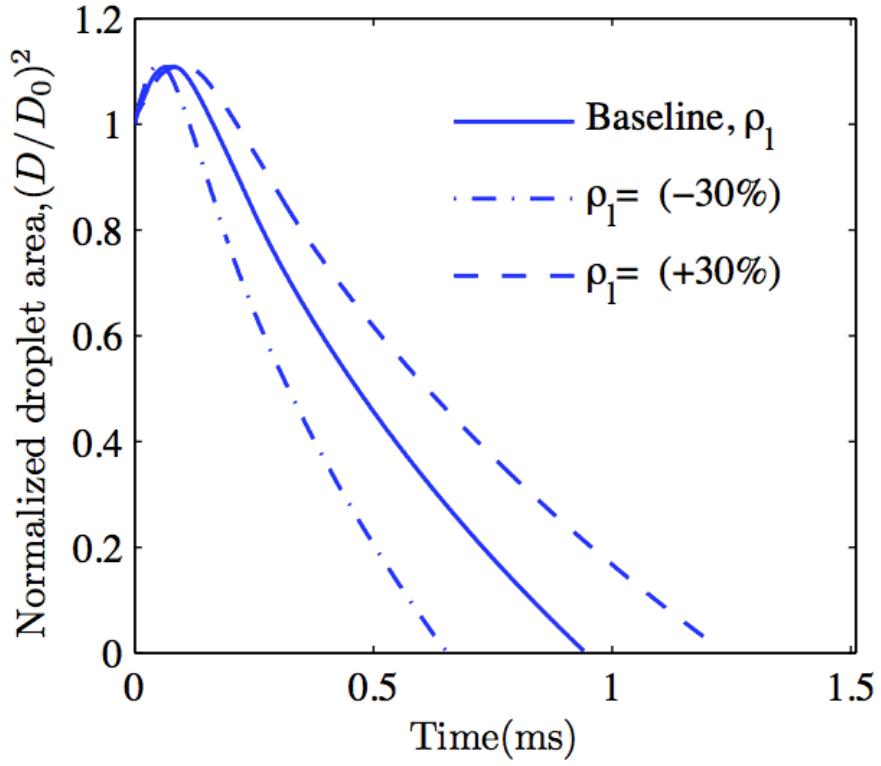

(a)

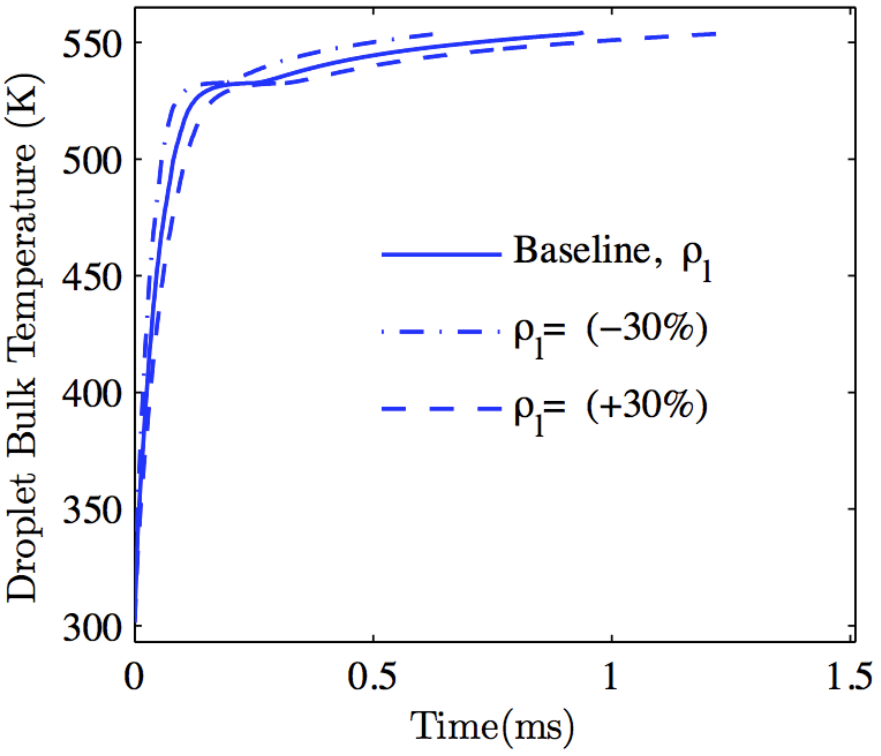

(b)

Figure 1.5: Time variation of (a) droplet area, and (b) droplet bulk temperature for different values of the liquid density, ρ_l.

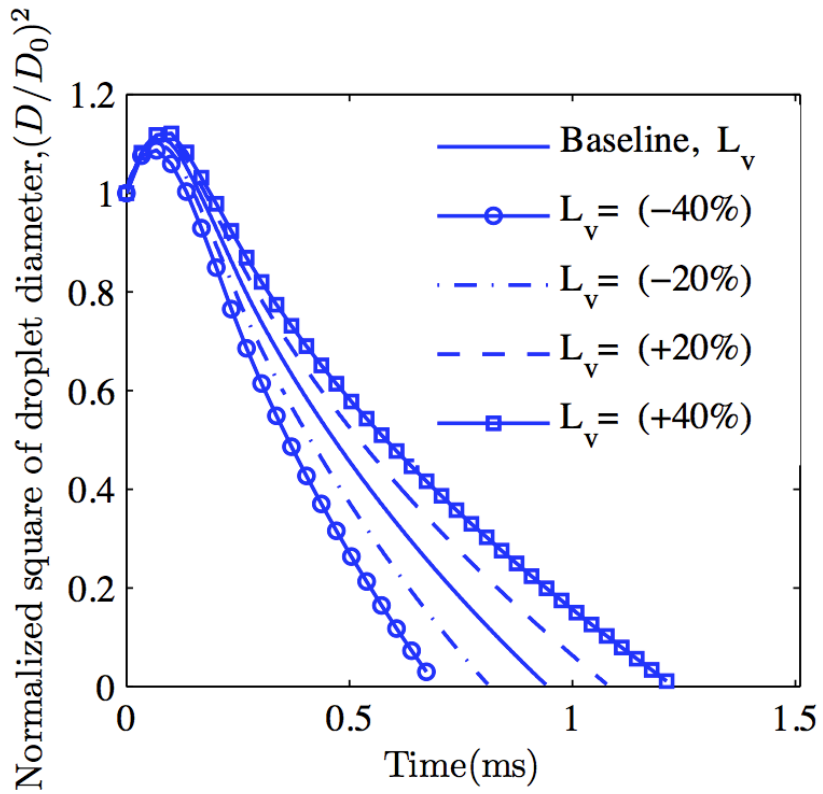

(a)

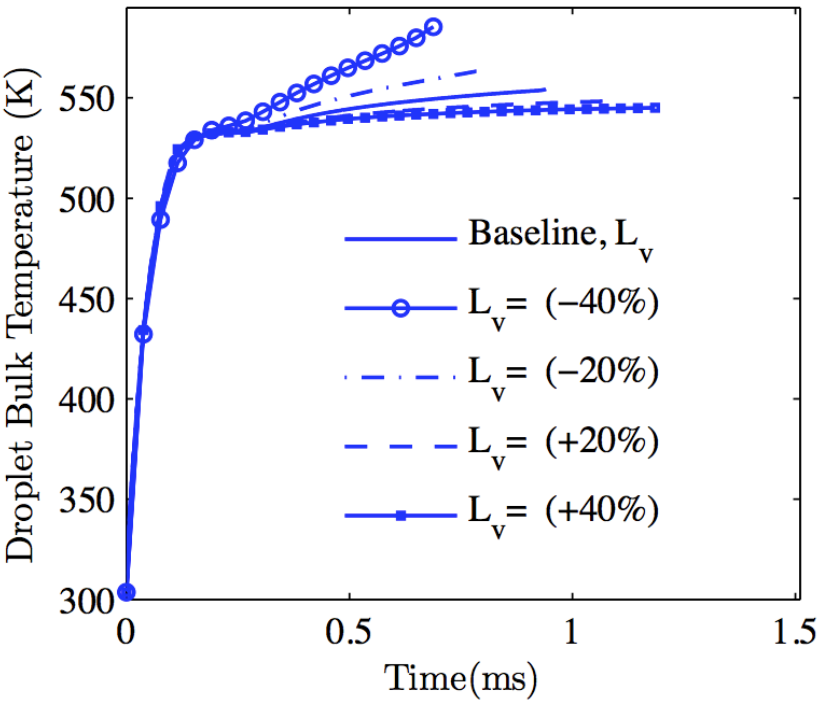

(b)

Figure 1.6: Time variation of (a) droplet area, and (b) droplet bulk temperature for different values of the latent heat of vaporization, L_v.

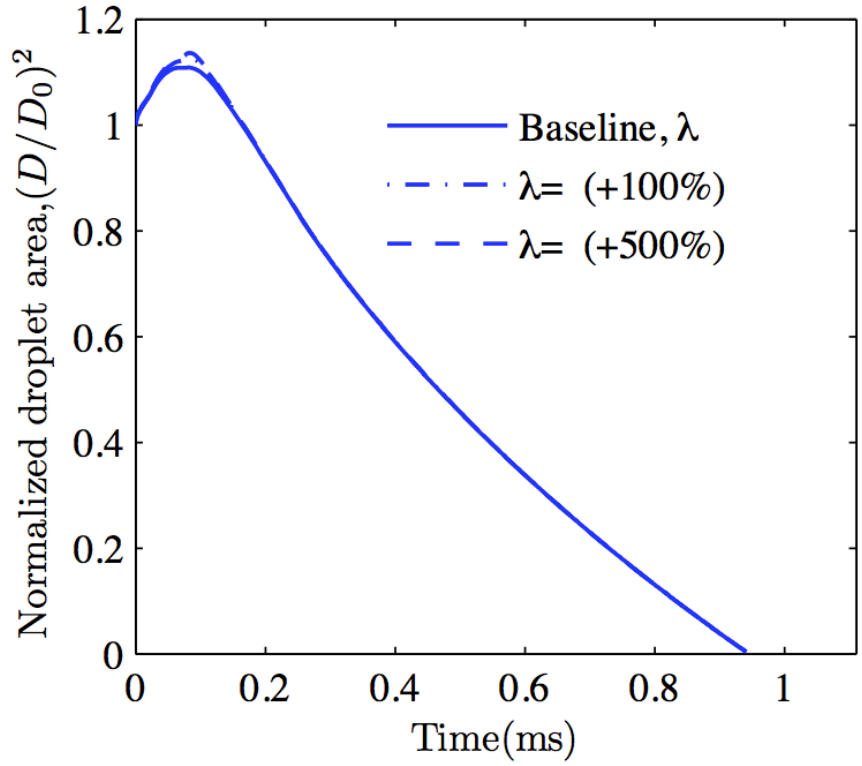

(a)

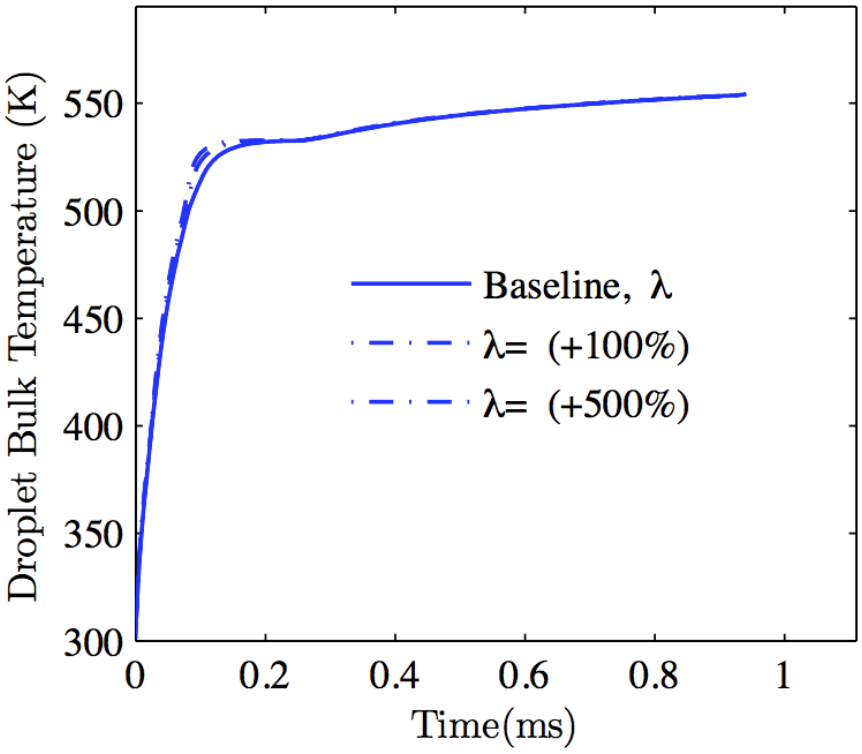

(b)

Figure 1.7: Time variation of (a) droplet area, and (b) droplet bulk temperature for different values of the liquid thermal conductivity, λ.

Diesel Fuel Surrogates	
2 species	70% n-heptane + 30% toluene
	D2N: 70% n-decane ($C_{10}H_{22}$) + 30% α - methylnaphthalene ($C_{11}H_{10}$) by volume [43]
	80% n-decane + 20% n-propylbenzene [45]
3 species	39% n-propylcyclohexane + 28% n-butylbenzene + 33% 2,2,4,4,6,8,8-heptamethylnonane by mass [44]
4 species	n-decane + iso-octane + methylcyclohexane + toluene [45]
	n-hexadecane + heptamethylnonane + n-decylbenzene + 1-methylnaphthalene [45]
6 species	D6N: 16% toluene (C_7H_8) + 14 % n-decane ($C_{10}H_{22}$) + 22% n-dodecane ($C_{12}H_{26}$) + 24 % n-tetradecane ($C_{14}H_{30}$) + 13 % n-hexadecane ($C_{16}H_{34}$) + 11% n-octadecane ($C_{18}H_{38}$) by mole fraction [24]
8 species	CFA 20.2% n-octadecane ($C_{18}H_{38}$) + 2.7% n-hexadecane ($C_{16}H_{34}$) + 29.2% 2,2,4,4,6,8,8-heptamethylnonane ($C_{16}H_{34}$) + 5.1% n-butylcyclohexane ($C_{10}H_{20}$) + 5.5% trans-decalin ($C_{10}H_{18}$) + 7.5% 1,2,4-trimethylbenzene (C_9H_{12}) + 15.4% tetralin ($C_{10}H_{12}$) + 14.4% 1-methylnaphthalene ($C_{11}H_{10}$) by mole fraction [46]
	FD9A 7.8% n-eicosane ($C_{20}H_{42}$) +13.1% n-octadecane ($C_{18}H_{38}$) + 28.2% 2,2,4,4,6,8,8-heptamethylnonane ($C_{16}H_{34}$) + 5.0% n-butylcyclohexane ($C_{10}H_{20}$) + 10.0% trans-decalin ($C_{10}H_{18}$) + 18.8% 1,2,4-trimethylbenzene (C_9H_{12}) + 11.3% tetralin ($C_{10}H_{12}$) + 5.8% 1-methylnaphthalene ($C_{11}H_{10}$) by mole fraction [46]

Table 1.1: Multicomponent surrogate fuels used for simulation of Diesel

1.3.1.2 Multicomponent Liquid

To assess the true performance of the multicomponent model for real fuels, an attempt is made in this section to simulate the evaporation of Diesel2 fuel. Diesel2 is a chemically complex multicomponent mixture with a wide distillation character. In order to reduce the chemical and physical complexity of the diesel fuel, surrogate fuels have often been used in studies focusing on deeper understanding of processes involved in diesel fuel vaporization,

mixing and combustion. Some of the diesel surrogate fuels which have been used in previous studies are presented in Table 1.1. Four of these mixtures have been used as surrogates for the simulation of the physical behavior of diesel in this paper, namely the bi-component mixture of n-decane($C_{10}H_{22}$) and α - methylnaphthalene($C_{11}H_{10}$), the 6-species mixture of 5 n-alkanes and 1 aromatic compound [24], and the 8 species surrogates CFA and FD9A developed by Mueller et al.[46]. Here, CFA is the acronym for a 2007 #2 ULSD certification fuel from Chevron-Phillips Chemical Co., while FD9A stands for Fuels for Advanced Combustion Engines (FACE) Diesel#9 Batch A. The 8 species surrogates were created by optimising the compositions using a multiproperty regression algorithm to match the known carbon bond types and ignition qualities and volatilities of the target fuels and comprise of all the major hydrocarbon classes found in the target fuels, viz. n-alkanes, *iso*-alkanes, mono- and dicycloalkanes; mono- and diaromatics; and naphtho-aromatics.

In order to evaluate the effect of non-idealities of the liquid phase on the evaporation process, the computational results for the evaporation of a droplet of 70% n-decane and 30% α - methylnaphthalene (by volume) for ideal and non-ideal models are compared. In the ideal case, the activity coefficient in equation (1.23) is set to $\gamma_k = 1$. Figure 1.8 shows the variations of the droplet area and bulk temperature. Changes in the droplet lifetime and maximum temperature are insignificant but there is a slight decrease in the evaporation rate when the non-ideal model is used. There is also a slight increase in the droplet temperature at intermediate times (which accounts for the increase in the evaporation rate at later stages), resulting in a negligible net change in the droplet lifetime. However, there are significant differences in the liquid fuel species composition as seen in the mass fraction profiles in Figure 1.9. The rate of evaporation of the more volatile component n-decane is adversely affected due to the presence of a less volatile α - methylnaphthalene when their mutual interaction

viz. non-ideal effects are considered. This effect is important for the fuel-vapor distribution in the gas phase and exemplifies the significance of considering the real liquid effects on the fuel evaporation.

The evaporation of a single drop of the 6-species diesel surrogate is simulated to gain an understanding of the behavior of more complex multicomponent fuels. Figure 1.10 shows the evolution of the average species mass fractions for the whole droplet in time and the mass fraction profiles inside the droplet at a particular time. The most volatile component, toluene (C_7H_8), evaporates first as expected and as can be seen in Figure 1.10(a). As the drop temperature increases, the heavier species evaporate too. At the end of its lifetime, the droplet is mostly composed of the heaviest and least volatile species, n-octadecane ($C_{18}H_{38}$). Figure 1.10(b) shows the mass fraction profiles in the droplet interior at the initial stages of the evaporation process. The evaporation starts at the surface, with the most volatile fuel evaporating first, resulting in the creation of nonuniform inner droplet distribution, which is captured well by the multicomponent model.

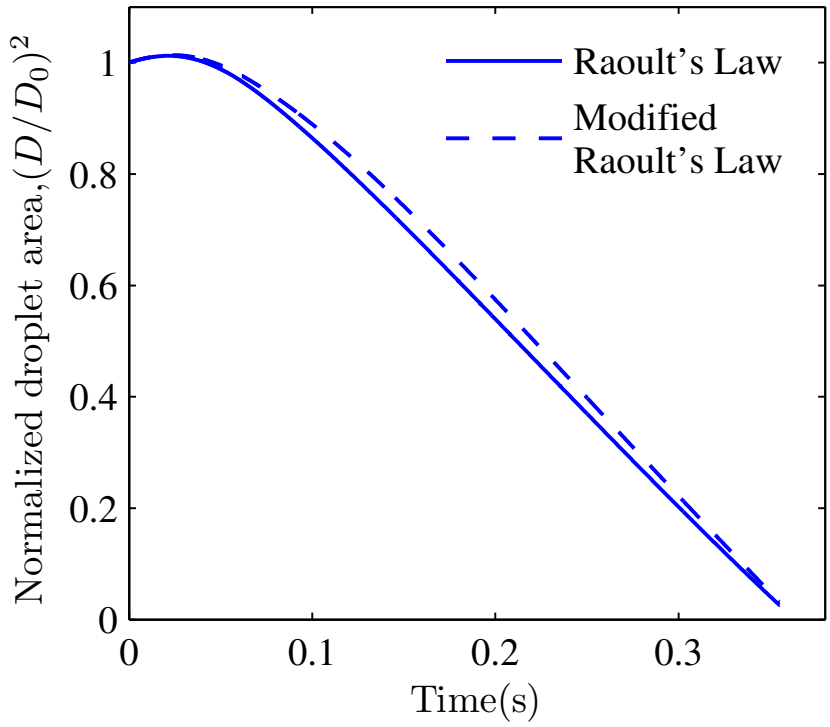

(a)

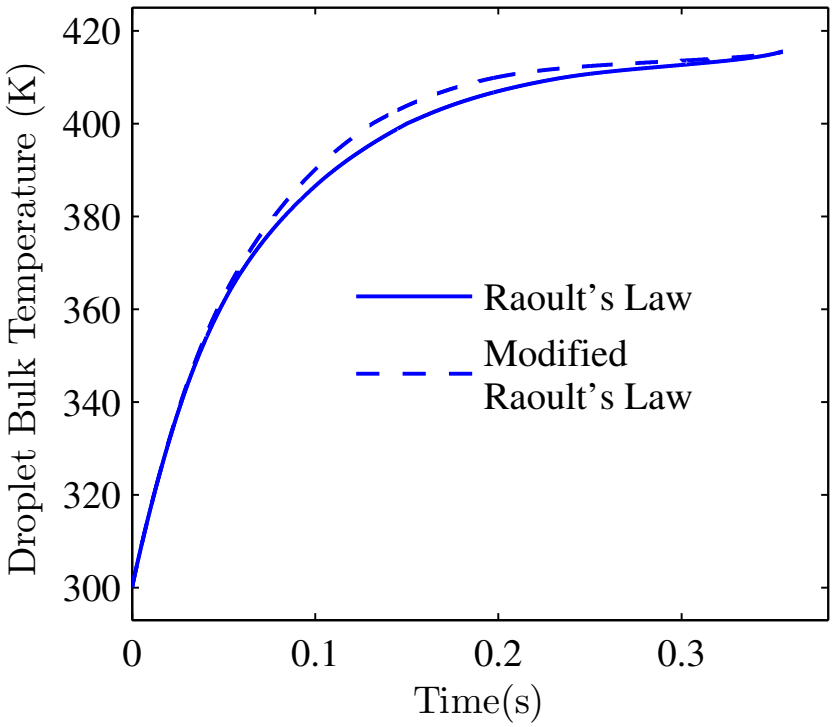

(b)

Figure 1.8: Variation of (a) droplet area, (b) droplet temperature, with time for a fuel with composition 61% decane + 39%α-methylnaphthalene (by mass) and initial droplet diameter = 200μm , gas temperature = 550 K, gas pressure = 1.01325e+05 N/m^2.

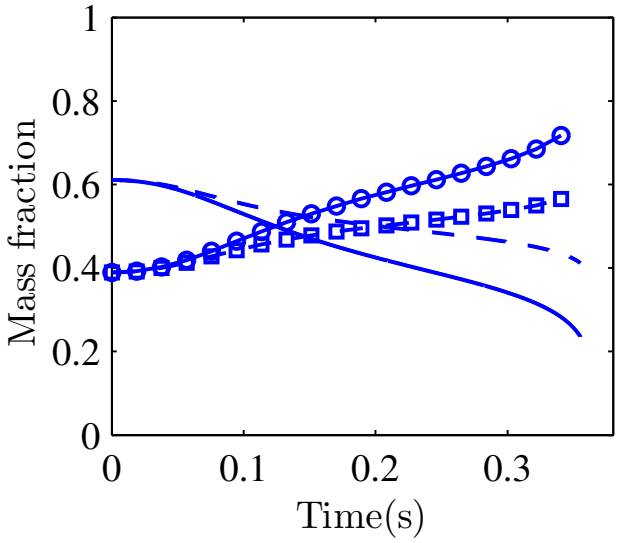

(a)

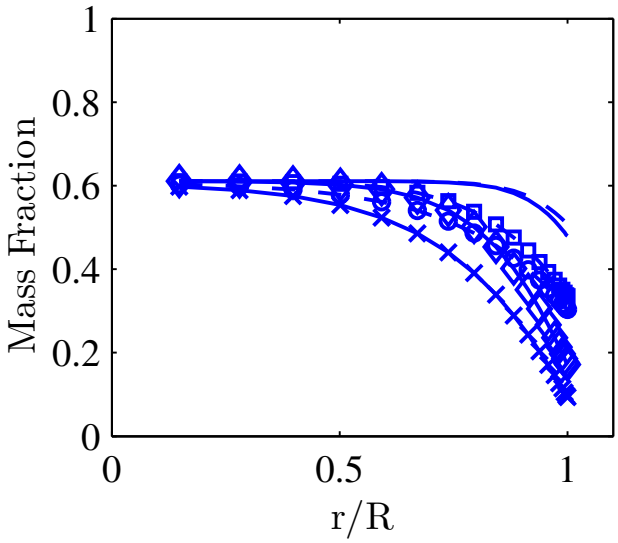

(b)

Figure 1.9: (a) Variation of total species mass fraction inside the droplet with time, $C_{10}H_{22}$: [−] ideal, [−−] real; $C_{11}H_{10}$: [− ∘ −] ideal, [−□−] real, (b) Mass fraction profiles of n-decane inside the droplet at different times, [−] t=0.05s(ideal liquid); [−−] t=0.05s(real liquid); [−◇−] t=0.15s(ideal liquid); [− − □ − −] t=0.15s(real liquid); [− × −] t=0.25s(ideal liquid); [− − ∘ − −] t=0.25s(real liquid).

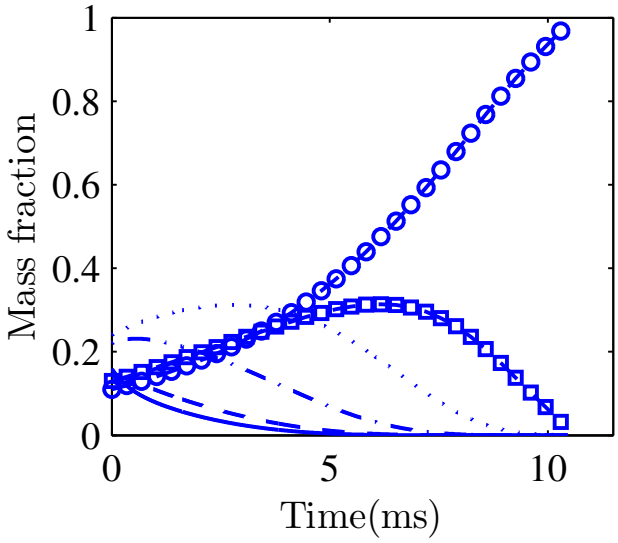

(a)

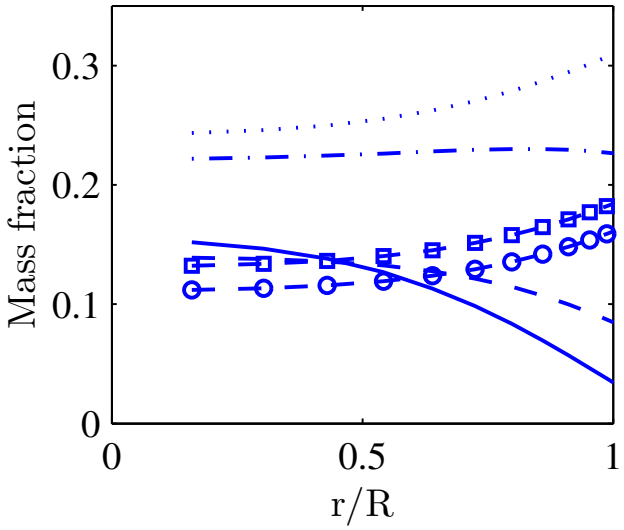

(b)

Figure 1.10: (a) Variation of average species mass fraction inside droplet with time for a six-component diesel surrogate, (b) Mass fraction profiles of fuel components inside the droplet during the evaporation process. [−] C_7H_8; [−−] $C_{10}H_{22}$; [−.] $C_{12}H_{26}$; [....] $C_{14}H_{30}$; [−□−] $C_{16}H_{34}$; [− ∘ −] $C_{18}H_{38}$.

1.3.2 Biofuel

The multi-component evaporation model developed in this study can be applied to study the behavior of different fuels including biofuels. Single drop studies have been carried out here to characterize the behavior of blends of Methyl Oleate (Canola Biodiesel, $C_{19}H_{36}O_2$), Dibutyl Succinate (DBS, $C_{12}H_{22}O_4$), 2-ethylhexyl nonanoate (2-EHN,$C_{17}H_{34}O_2$), Butyl nonanoate (BN, $C_{13}H_{26}O_2$), isobutyl nonanoate (iBN, $C_{13}H_{26}O_2$), 2-ethylhexyl butyrate (2-EHB, $C_{12}H_{24}O_2$) and a Diesel surrogate (n-hexadecane, $C_{16}H_{34}$). The physical properties of these components have been calculated using suitable correlations and methods given in Poling et al. [32]. Appendix 3.6 gives a list of the methods and relations used to calculate the properties. Figures 1.11(a) - 1.11(e) show the variation of some of the physical properties, considered to be important for evaporation, with the temperature. Methyl Oleate has the highest liquid specific heat (Figure 1.11(a)) and latent heat of vaporization (Figure 1.11(b)) and the lowest vapor pressure (Figure 1.11(c)) and thermal conductivity at lower temperatures, (Figure 1.11(d)). This implies that a higher concentration of Methyl Oleate would require higher heat input for droplet heating and evaporation. On the contrary, 2-EHB lies at the other end of the spectrum with the lowest liquid specific heat and latent heat of vaporization and the highest vapor pressure and is the most volatile of the components considered here. BN and iBN have properties similar to 2-EHB and similar results can be expected for fuels containing these species. The specific heat and vapor pressure of 2-EHN are closer to Methyl Oleate as compared to other components and its volatility should be similar too. DBS has intermediate properties but its density (Figure 1.11(e)) is also the highest. Consequently, droplets with DBS would take longer to evaporate due to the higher mass.

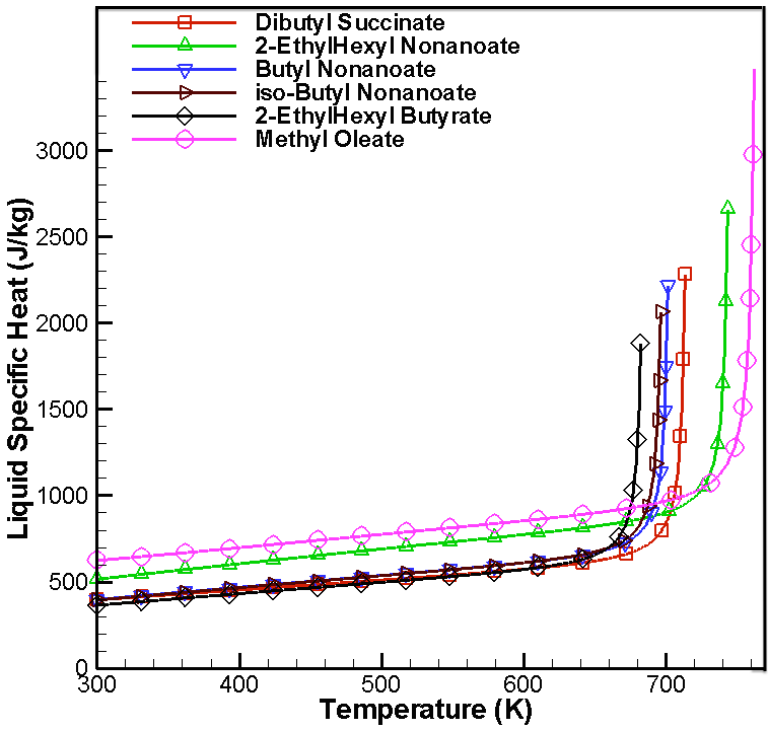

(a)

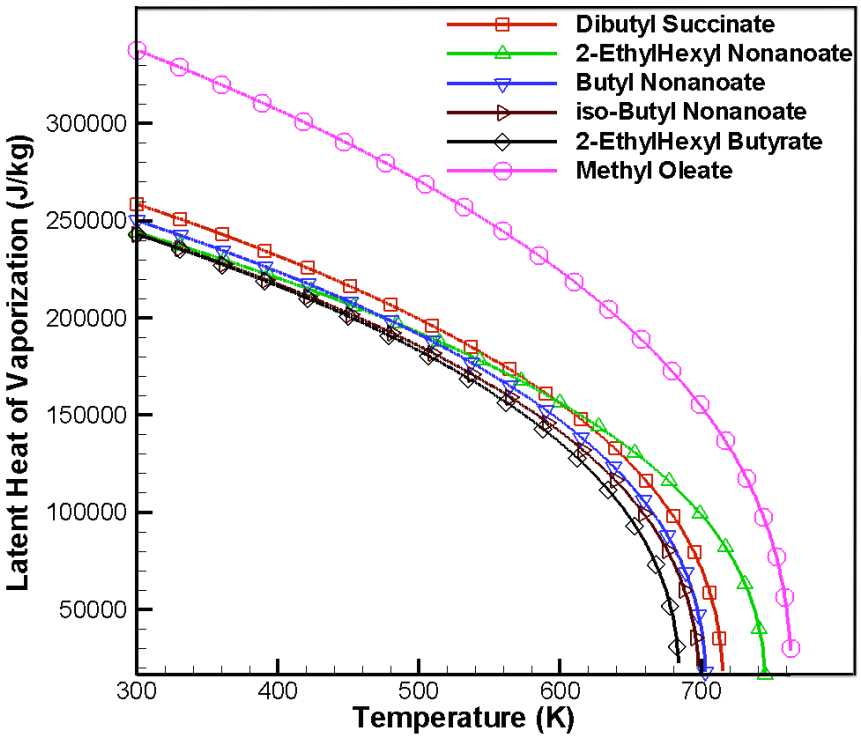

(b)

Figure 1.11: Physical properties of biofuel components. (a) Liquid Specific heat, (b) Latent Heat of Vaporization, (c) Vapor Pressure, (d) Thermal Conductivity, (e) Density.

Figure 1.11: (cont'd)

(c)

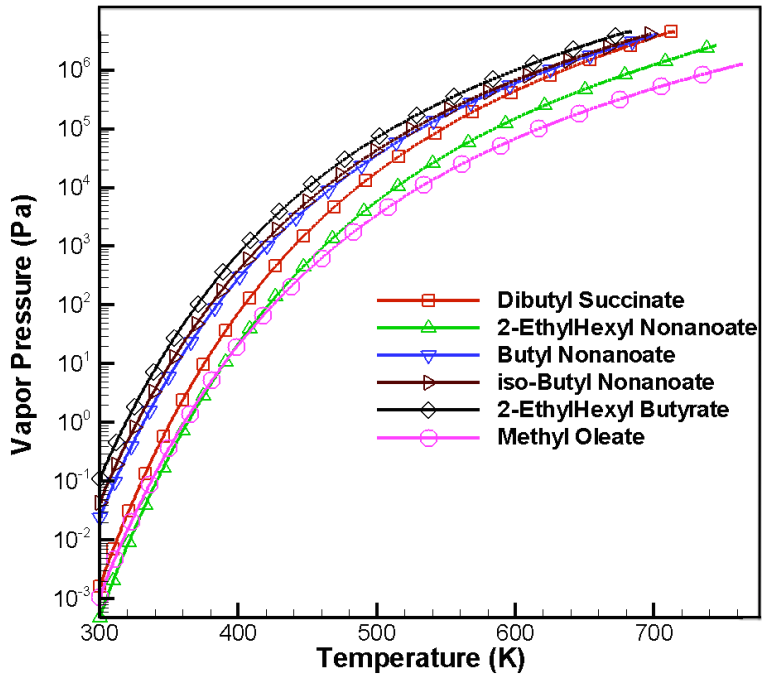

(d)

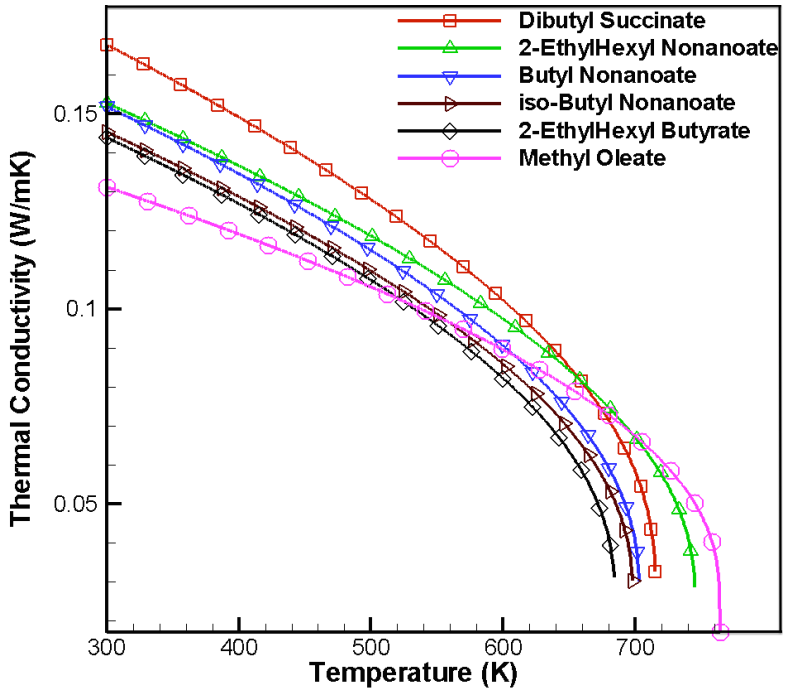

Figure 1.11: (cont'd).

(e)

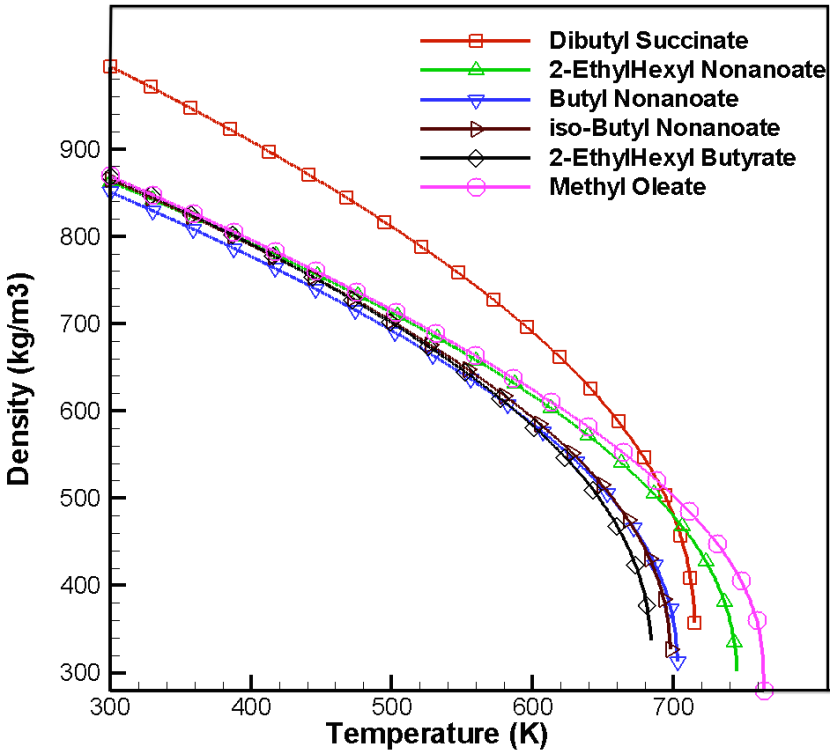

In order to understand the heat and mass transfer characteristics of the bio-fuel components, a set of simulations consisting of stationary droplets, suspended in a stagnant environment is considered. The droplets are composed of two components, with Methyl Oleate as the base fuel and a second component. The initial droplet size and temperature are 50 μm and 400 K, respectively. The gas pressure and temperature are 1 atm and 700 K, respectively. Figure 1.12 shows the droplet lifetimes for stationary droplets of bi-component

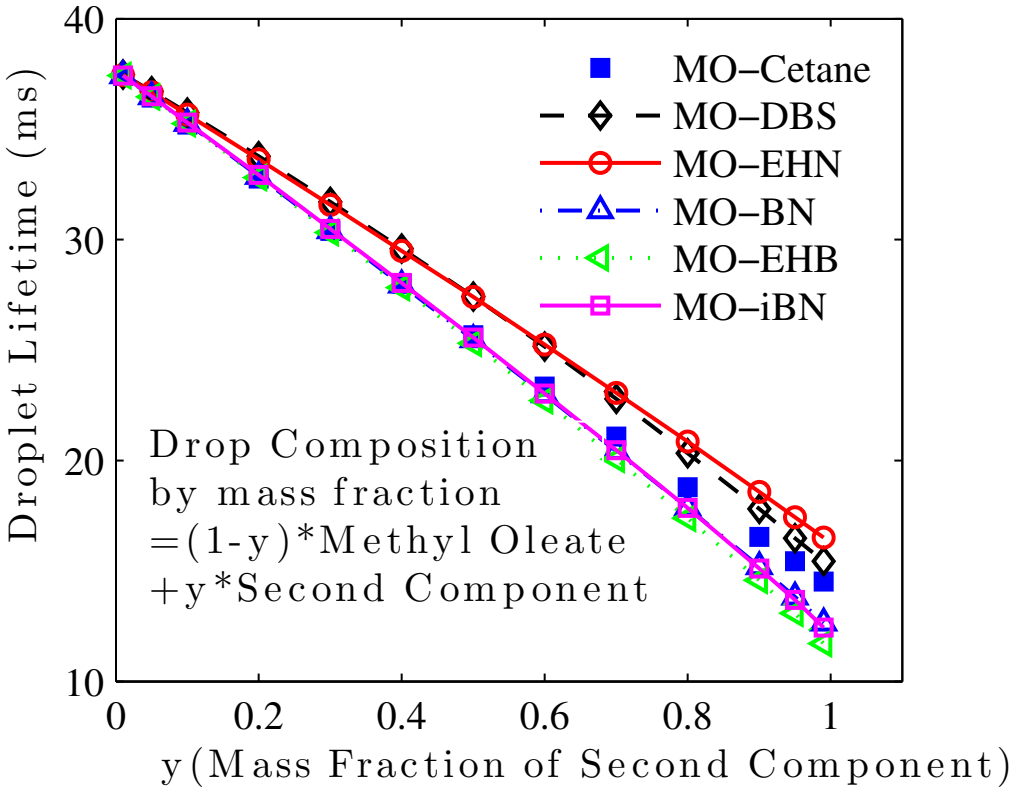

Figure 1.12: Lifetimes for Biofuel and Biodiesel Blend droplets suspended in stagnant air at atmospheric pressure and 700 K. Initial Droplet Temperature = 400 K. Initial Droplet Diameter = 50 μm.

biofuel blends. As expected, the shortest droplet lifetimes are for bi-component droplets with 2-EHB due to its higher volatility. Since Methyl Oleate is the least volatile of all the

species considered, the droplet lifetimes decrease as the mass fraction of the second, more volatile component, is increased. The longest droplet lifetimes are for Methyl Oleate + 2-EHN droplets, especially when the mass fraction of 2-EHN is higher. This is due to the low vapor pressure and higher latent heat of vaporization of these droplets. The droplet lifetimes for BN and iBN are similar and relatively higher than 2-EHB. Although n-Hexadecane is the lightest of the species considered here, it is less volatile than 2-EHB, BN and iBN and consequently its lifetimes are higher.

1.3.3 Spray Simulations

The variable property multicomponent model has been used together with our hybrid Eulerian-Lagrangian LES/spray model to simulate spray experiments performed at Sandia National Laboratory [42]. The experimental setup consisted of an optically accessible constant-volume cubical combustion vessel with a characteristic dimension of 108 mm. The fuel is injected through a high-pressure injection system and is visualized using the Mie-scattering technique. The spray "length" or the maximum axial penetration distance of the liquid fuel is obtained from the time averaged Mie scattered images by determining the maximum axial distance of the droplets with a light intensity above a selected threshold [42]. The experiments were repeated for various sets of ambient gas conditions and spray/injector parameters, summarized in Table 1.2.

Some of the most important processes affecting the evaporation and mixing of liquid fuels are the primary and secondary breakup of the liquid jet and droplets, and the droplet transport, collision, coalescence, and evaporation. Models affecting the prediction of spray length include those used for the droplet drag, heat and mass transfer and breakup process. Here, the spray has been numerically simulated using the "blob" model in which monodisperse particles are injected into the computational domain with particle size equal to the effective diameter of the nozzle orifice, given by $D_{blob} = C_{a,inj} D_{orif}$, where $C_{a,inj}$ is the orifice area-contraction coefficient and D_{orif} is the orifice diameter. $C_{a,inj}$ represents the reduction in the blob size due to the cavitating flow during the main injection phase.

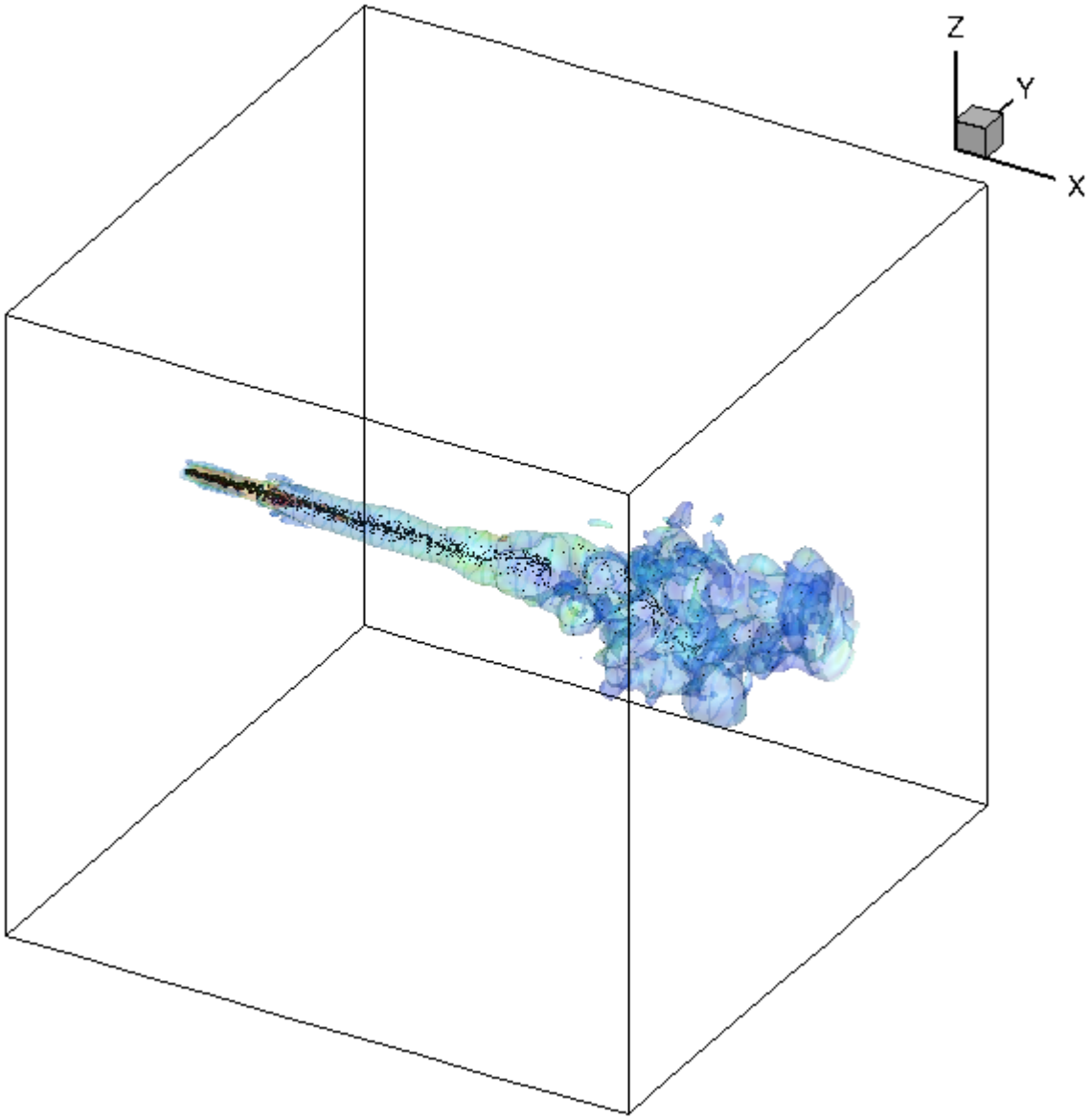

Figure 1.13: LES simulation domain with spray and iso-surfaces of gas temperature.

Fuel	n-hexadecane, Diesel2, etc.
Gas Temperature	700-1300 K
Gas Pressure	3.6-58.5 kg/m^3
Injection Pressure	41-172 MPa
Nozzle Diameter	0.1-0.498 mm

Table 1.2: Parameters of Sandia's Spray Experiments

For the Sandia sprays, $C_{a,inj}$ is obtained using the relation $C_{a,inj} = 2A_{orif}C_{d,inj}^2 P_{inj}/\dot{M}_f$, where A_{orif} is the orifice exit area, $C_{d,inj}$ is the discharge coefficient, $P_{inj} = P_f - P_a$ is the injection pressure, P_f is the fuel pressure, P_a is the air pressure and $\dot{M}_f$ is the momentum flow rate, measured using a piezoelectric pressure transducer. The spray velocity is given by $U_{spray} = C_{v,inj}U_b$, where $U_b = \sqrt{2P_{inj}/\rho_f}$ is the maximum potential fluid velocity at the orifice exit, ρ_f is the fuel density and $C_{v,inj} = C_{d,inj}/C_{a,inj}$ is the velocity coefficient. $C_{a,inj}$ and $C_{v,inj}$ together constitute the effect of cavitation on the initial droplet size and velocity but are unable to capture the increase of turbulence and break-up energy due to cavitation, which are potentially important features affecting the evolution of the spray.

The injected blobs undergo secondary breakup subject to the combined KH-RT model [48], [49], which is a competitive implementation of the Kelvin-Helmholtz (KH) and Rayleigh-Taylor (RT) models. Unstable waves grow on the droplet surface due to aerodynamic forces caused by the relative velocity between the liquid and gas phases. In the KH model, new child droplets, with sizes proportional to the wavelength of the fastest growing and most unstable waves on the droplet surface, are stripped off the parent droplet. The diameter of the child droplet is given by $r_{c,KH} = 0.61\Lambda_{KH}$, where

$$\Lambda_{KH} = \frac{9.02r(1 + 0.45\sqrt{z})(1 + 0.4T^{0.7})}{(1 + 0.865We_g^{1.67})^{0.6}} \tag{1.39}$$

is the wavelength of the KH wave having the maximum growth rate and $We_g = \rho_g U_r^2 r/\sigma$, and $Z = \sqrt{We_l}/Re_l$ are the gas Weber number and Ohnesorge number, respectively. The breakup time for calculating the rate of change of the radius of the droplet is given by $\tau_{KH} = 3.726 B_1 r/\Omega_{KH}\Lambda_{KH}$, where Ω_{KH} is the frequency of the fastest growing KH wave. In the RT model, the droplet breaks up completely into child droplets with sizes corresponding to the wavelength of the fastest growing wave with frequency of,

$$\Omega = \sqrt{\frac{2}{3\sqrt{3\sigma}} \frac{[-g_t(\rho_f - \rho_a)]^{3/2}}{\rho_f + \rho_a}}, \tag{1.40}$$

wave number of $K_{RT} = \sqrt{g_t(\rho_f - \rho_a)/3\sigma}$ and wavelength of $2\pi C_{RT}/K_{RT}$. Droplets with diameter greater than the wavelength of the fastest growing wave have RT waves growing on their surface which ultimately leads to the complete breakup of the droplet when the droplet breakup time $\tau_{RT} = C_\tau/\Omega_{RT}$ ($C_\tau = 1$) is exceeded. The diameter of the child droplet in this case is given by $r_{c,RT} = \pi C_{RT}/K_{RT}$. The RT model is applied beyond the breakup-length,

$$L_b = 0.5 B_1 d_0 \sqrt{\rho_f/\rho_a}, \tag{1.41}$$

of the dense fragmented core to prevent severe reduction of droplet sizes, only KH breakup is allowed to occur near the nozzle. The implementation of the KH-RT models requires two adjustable parameters B_1 and C_{RT} based on the nozzle geometry and initial conditions of the spray. The parameter B_1 determines the length L_b of the dense fragmented core, while the parameter C_{RT} controls the size of the daughter droplets after the RT breakup.

In the near nozzle dense region, the droplets are tightly packed and it can be expected that a large number of them are in the wake region of other droplets preceding them. This

implies that they do not"see" the effect of the surrounding air completely. In the absence of a comprehensive model to predict the droplet wake and the effect of nearby droplets on the droplet heat and mass transfer, semi-empirical correlations for the Nusselt and Sherwood numbers are used in this study with some corrections for high speed droplets. Also, the multicomponent evaporation model is currently unable to fully consider high pressure, transcritical and supercritical conditions and deviations from experimental results can be expected under some extreme conditions.

1.3.3.1 Single Component Liquid Sprays

One of the important global spray parameters, characterizing the effectiveness of spray breakup and evaporation is the liquid penetration length or spray length. The numerical spray length is defined as the axial location before which most of the mass of the liquid jet is located. Since the experimental definition of the spray length is based on a threshold of light intensity and cannot be directly converted into an exact percentage of liquid penetration, this length has been defined differently in literature. Beale et al. [49] defined the penetration length as the location of the 3% liquid volume contour at the edge of the spray, while Ricart et al. [50] used both 90% of the liquid mass and the location of the farthest droplet from the nozzle, as the definition of penetration length. Som [51] used the axial location of 97% of the injected mass as the penetration length. Figure 1.14 compares the liquid lengths obtained for 95%, 97% and 99% penetration of the liquid mass for a gas temperature of 700 K by our LES/spray model. The penetration length predicted by the 97% criteria yields the best overall match with the experimental results for this particular temperature. The parametric nature of the breakup model necessitates the study of the effect of different breakup parameters on the spray quantities like liquid penetration length.

Figure 1.15 shows the effect of the KH model constant B_1, which controls the breakup length or the dense core of the liquid jet, with the RT breakup constant C_{RT} fixed at 0.1. The gas temperature is 700 K. The predicted liquid length increases as B_1 is increased due to the onset of Rayleigh-Taylor breakup at a later axial location. The numerical results match well for $B_1 = 40$ for all cases except at the gas density of 58.5 kg/m^3. For B_1 values lower than 20, the liquid jet never reaches a steady state condition and keeps on penetrating axially. Figure 1.16 shows the effect of the RT breakup constant C_{RT}, on the penetration length for a gas temperature of 700 K and constant B_1 value of 40. C_{RT} determines the droplet size after RT breakup; hence a larger value of C_{RT} yields bigger daughter droplets, which take longer to evaporate, leading to a longer penetration length. This trend can be clearly observed in Figure 1.16. For $C_{RT} = 0.06$, the liquid jet does not reach steady state condition at lower gas densities. Apparently, the numerical results match well with the experimental results for a C_{RT} value of 0.10. Based on the results in Figure 1.15 and 1.16, the breakup constants $B_1 = 40$ and $C_{RT} = 0.10$ are expected to give the best match between experimental and numerical results for n-hexadecane.

Figure 1.17 shows the comparison between experimental and numerical results for gas temperatures of 700-1150 K and gas densities of 3.6-58.5 kg/m^3. The experimental trends of decreasing penetration length with increasing temperature and pressure seem to be captured well by the LES/spray model. The numerical results compare well with the experimental results at gas densities of 3.6 kg/m^3 and 7.3 kg/m^3 at all gas temperatures. The results at gas density of 14.8 kg/m^3 also match well at lower temperatures with a slight over-prediction at temperature 1150 K. As the gas temperature and density are increased, there are slight deviations from the experimental results. The liquid length at gas density of 30.0 kg/m^3 is predicted reasonably well for lower gas temperatures of 700 and 850 K, however at higher

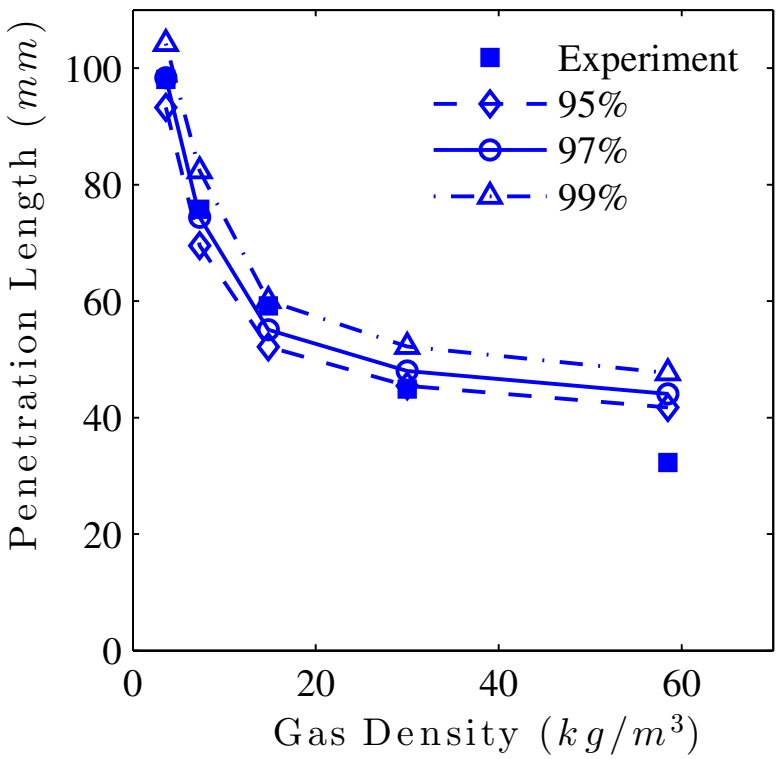

Figure 1.14: Liquid penetration length for gas temperature of 700 K based on penetration of 95%, 97% and 99% of the liquid mass.

temperatures there is an over-prediction of the spray penetration length. The penetration length at gas density of 58.5 kg/m^3 is also over-predicted at all temperatures. There can be several possible reasons for the over-prediction of numerical results at high gas temperatures and pressures. For gas temperatures of 1000 K and 1150 K, the breakup length of the dense fragment core as predicted by Equation 1.41 when the ambient gas density is 30.0 kg/m^3 and 58.5 kg/m^3, is nearly equal to or greater than the experimental penetration length. This implies that the RT breakup, and consequently the evaporation of the smaller droplets, starts only after the liquid droplets are near or have crossed the axial location of the experimental penetration length, leading to over-prediction of the penetration length for these cases. The over-prediction at higher gas densities (e.g. 30.0 kg/m^3 and 58.5 kg/m^3) can also be explained by the gas conditions being supercritical for n-hexadecane and the possibility

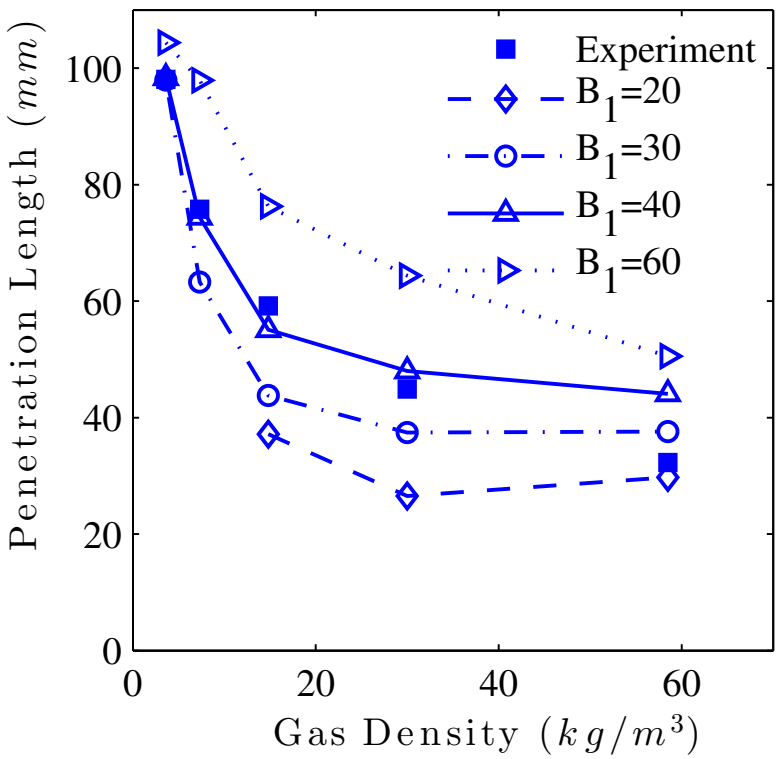

Figure 1.15: Liquid penetration length for different values of the KH breakup constant, B_1, $C_{RT} = 0.10$. Fuel: n-hexadecane.

of the droplet surface reaching supercritical condition, which the current evaporation model is not designed to handle. Note that for the gas pressure and temperature of 58.5 kg/m^3 and 1150 K, the reduced pressure and temperature are 15.13 and 1.60, respectively, which imply supercritical conditions. Although the conditions are also supercritical for lower gas densities of 14.8 kg/m^3 and 7.3 kg/m^3, the effect on the penetration length does not seem to be significant for these conditions. It is probable that while the liquid length over-prediction is not significant, the effect of supercritical evaporation on the fuel vapor distribution is appreciable. The computational and experimental results indicate that the penetration length decreases on increasing gas temperature and density. However, the effects of gas temperature and density on the spray length are more significant at lower values of these variables. The gas density effect is strongly non-linear. The effect of gas temperature is also non-linear, but

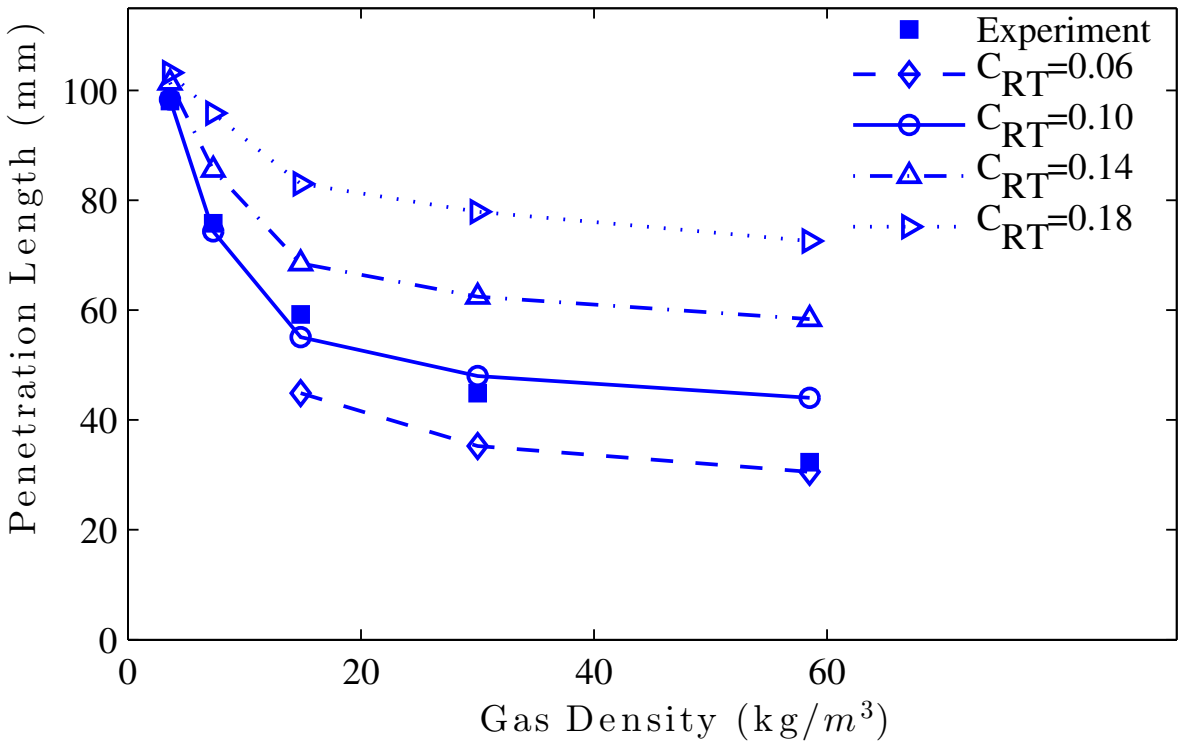

Figure 1.16: Liquid penetration length for gas temperature of 700 K for different values of the RT breakup constant, C_{RT}, $B_1 = 40$.

to a lesser extent. This can be explained by higher energy content of the entrained gas at higher temperatures and consequently faster evaporation rates. At higher gas densities, the total mass of entrained air increases and more energy is available for the fuel evaporation. All of these indicate that the penetration length is significantly dependent on the amount and energy of the entrained air in the spray zone.

Figure 1.18 compares the experimental results with the numerical results obtained with the lumped droplet model for the same spray conditions, for two different RT breakup constants, $C_{RT} = 0.10$ and 0.18. It is clear that the lumped model is unable to predict the liquid penetration lengths for the wide range of conditions studied in this paper. While $C_{RT} = 0.10$ gives a good match for a gas temperature of 1000 K and a decent comparison for 850 K, the penetration lengths at higher temperatures are overpredicted and those at T=700

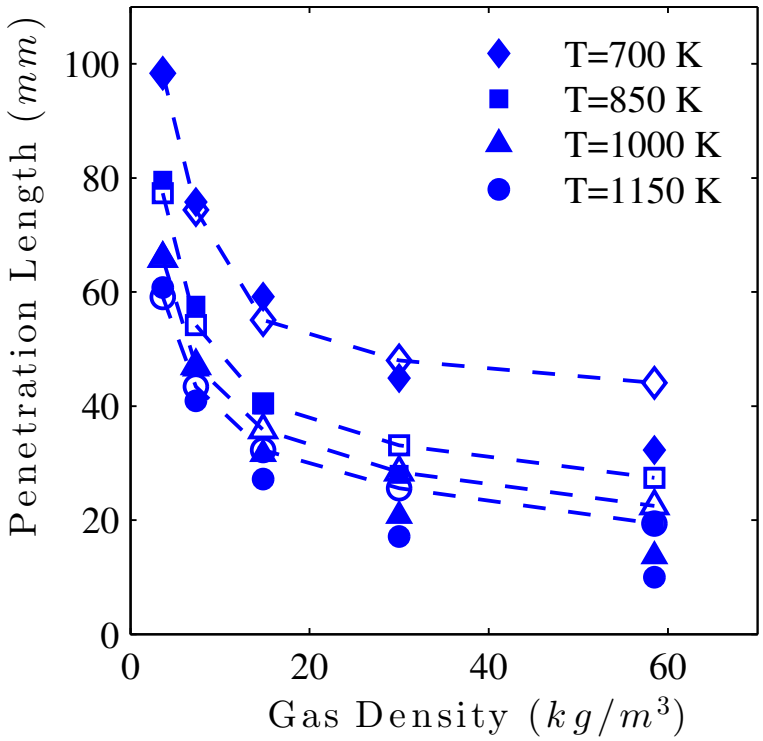

Figure 1.17: Liquid penetration length for different gas temperatures and densities, $B_1 = 40$, $C_{RT} = 0.10$. The solid and hollow symbols represent the experimental and numerical results, respectively. Fuel: n-hexadecane.

K are significantly underpredicted by the model. By increasing C_{RT} to 0.18, the predictions for T=700 K improve but there is overprediction of experimental results for most other cases. Overall, the LES results indicate that the lumped model is less sensitive to changes in the gas temperature, while the trend of penetration length decreasing with the gas density seems to be followed. The lumped model is not able to fully capture the effect of temperature on the penetration length mostly because of constant physical properties and the assumption of uniform droplet temperature and concentrations. As compared to the lumped model, the variable property multicomponent model provides a better match with the experimental data at various temperatures.

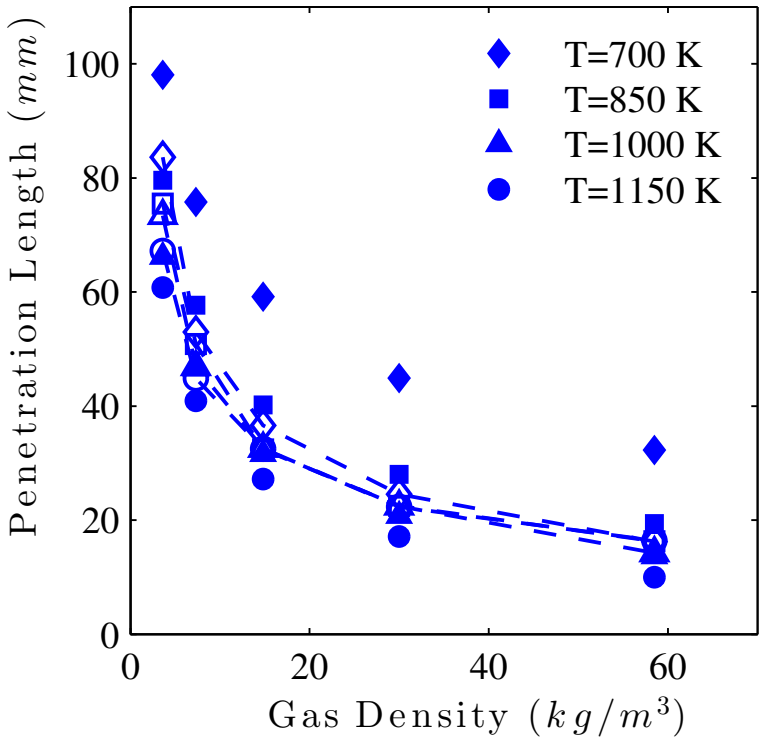

(a)

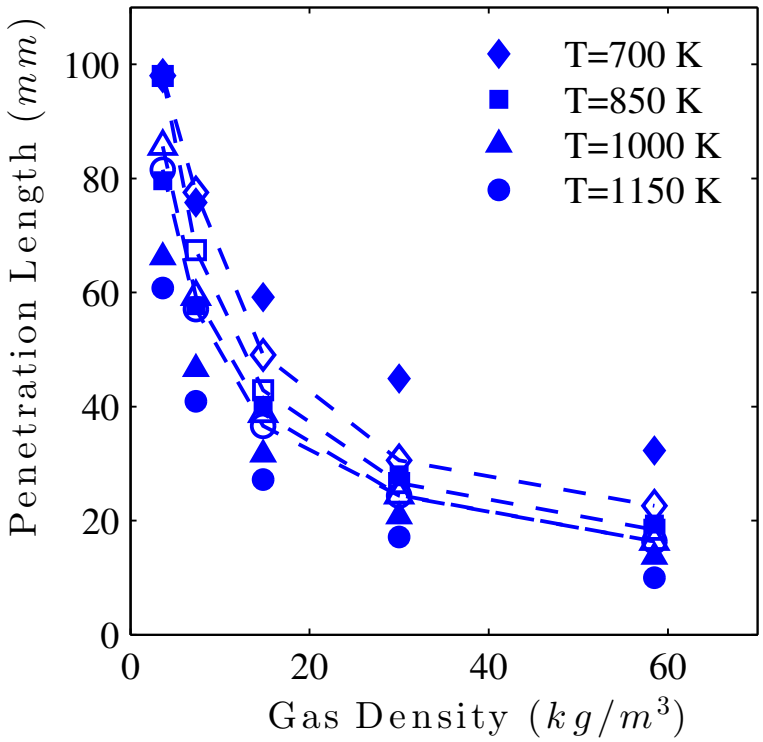

(b)

Figure 1.18: Liquid penetration length for different gas temperatures and densities as predicted by LES/spray model with lumped evaporation model, (a) $B_1 = 40$, $C_{RT} = 0.10$, (b) $B_1 = 40$, $C_{RT} = 0.18$. Fuel: n-hexadecane.

1.3.3.2 Multicomponent Liquid Sprays

In this section, spray simulations are conducted with LES and more complex heat and mass transfer models for multicomponent liquids. Four different fuel mixtures from Table 1.1 are considered as surrogates for commercial grade Diesel2: D2N, D6N, CFA and FD9A. Figure 1.19 shows the numerically simulated 97% spray length of the diesel surrogates for various gas temperatures. For the case with the ambient gas temperature of 700 K (Figure 1.19(a)), the trend of nonlinear decrease of liquid length with gas density is well followed but the experimental values are considerably under-predicted by LES with all surogate fuel models. As the gas temperature is increased to 850 K- 1150 K (Figures 1.19(b) - 1.19(d)), there is an improvement in the numerical results, but the experimental values are still underpredicted. D2N has the smallest liquid length at low temperatures and densities and the highest at high temperatures and densities. The liquid lengths of the 8 species surrogates CFA and FD9A are nearly the same at all temperatures and are maximum at lower temperatures and pressures as compared to other surrogates, while the liquid lengths of D6N are generally in between the 2 and 8 species surrogates. Figure 1.20 shows the 99 % liquid length obtained by LES with different surrogates. Evidently, there is a considerable improvement in the numerical results for all surrogates and at all temperatures. The liquid lengths predicted by LES with all the surrogates are in good agreement with experiment at higher temperatures of 1000 K and 1150 K. The liquid lengths at 850 K are slightly underpredicted. However, at gas temperature of 700 K, the liquid lengths are still underpredicted, although the 8 species surrogates predict them better than other surrogates, specially at lower temperatures and densities. The difference between 97% and 99% liquid lengths can be explained through the preferential evaporation of lighter fuel species over heavier components. The heavier species

(C18-C20) persist longer and tend to become the major components of smaller droplets at the tip of the spray. This explains the better prediction of the liquid lengths by the 8 species surrogates at lower temperatures and densities, especially when 99% liquid mass criterion is used since these surrogates have higher amounts of the heavier species. CFA, DCFA and D6N have 27.3 %, 29.8 %, and 15.79 % of C18-C20 species by mass, while D2N does not have any of these species. Figure 1.21 demonstrates the effect of the presence of heavier species by comparing the 99 % liquid length of the heaviest species in the mixtures with the experimental results. n-octadecane ($C_{18}H_{38}$) is the heaviest component in D6N and CFA, while n-eicosane ($C_{20}H_{42}$) and 1-methylnaphthalene ($C_{11}H_{10}$) are the heaviest components in FD9A and D2N, respectively. The comparisons in 1.21 indicate that the liquid length of the heaviest species matches the experimental results reasonably well at all temperatures for the mixtures containing C18-C20. The liquid length of 1-methylnaphthalene in D2N falls considerably short of the experimental results at gas temperature of 700 K, whereas the lengths of n-octadecane in D6N and CFA and n-eicosane in FD9A are in good agreement. This also indicates that it might be reasonable to compare the numerical liquid lengths of the heaviest species of the fuel mixture with the experimental results. It is not clear whether the presence of heavier components near the tip of the spray has any effect on the experimental results obtained based on light intensity.

The slower evaporation rates of the heavier species and their persistence in liquid form near the tip of the spray also has a significant effect on the distribution of the species in the vapor phase. Figure 1.22 compares the mass fraction contours of the various components of D6N in the vapor phase during the evaporation process. The spray parcels are sized proportional to the mass fraction of the fuel component in the contour plot. For example, in Figure 1.22(a), each spray parcel is scaled proportional to the mass fraction of Toulene

in the parcel. Thus, the reduction in the size of the parcels indicates the reduction in the mass fraction of Toluene in the liquid phase as the jet penetrates into the chamber. This is because Toluene is the lightest and the most volatile species and evaporates first, forming a higher concentration in the part of the vapor plume closest to the injector. As the weight of the species increases and their volatility decreases, their concentration in the central and downstream regions of the vapor plume increases (Figures 1.22(b) - 1.22(e)). The highest weight and least volatile component, n-octadecane, has relatively higher concentrations in the central region and regions near the tip of the vapor plume (Figure 1.22(f)). This preferential evaporation and concentration of the fuel species in the vapor phase can have a significant effect on the combustion characteristics of the fuel and deserves further investigation.

In Figures 1.8 and 1.9 it was shown that the use of activity coefficients for modifying the Raoult's Law does not have a significant effect on the droplet diameter and temperature but the mass fraction profiles of species inside the droplet are affected. Figures 1.23-1.25 compare the vapor mass fraction contours for D6N and its components with and without the use of activity coefficients. Figures 1.23(a) and 1.23(b) show the overall mass fraction contours of D6N with and without activity coefficients. The mass fraction distributions are nearly the same in the initial portion of the vapor plume, but there are noticeable differences, both in shape and mass fraction values, near the tip of the vapor plume. The penetration of the vapor plume is the same, but it is slightly wider in the simulations conducted with activity coefficients. Similar patterns can be seen in the components of D6N, n-dodecane (Figures 1.24(a) and 1.24(b)) and n-octadecane (Figures 1.25(a) and 1.25(b)). As in the case of single droplets, the inclusion of real liquid effects does not have a significant influence on the mean spray quantities; the liquid penetration does not change but the distribution of components in the vapor phase changes, and this may affect the overall combustion behavior. This implies

that real liquid effects should be considered while studying the behavior of multicomponent fuel surrogates, but the overall effect on the combustion performance requires further detailed study.

A set of biofuel spray simulations, with the droplets having the same composition as the stationary biofuel droplets in Section 1.3.2 were conducted in order to understand the spray characteristics of biofuel blends. In these simulations, the gas temperature and density are 700 K and 7.3 kg/m^3, the injection pressure is 55 MPa, the nozzle diameter is 0.100 mm and the injected liquid temperature is 436 K. Figure 1.26 presents the spray penetration length results for some of the bi-component mixtures considered. Most of the trends observed in the single drop studies are followed but there are also some significant differences. The mixtures containing iBN show the lowest penetration lengths due to it being more volatile than BN, DBS and EHN. The penetration lengths of 2-EHB are similar to iBN. The mixtures of MO-BN penetrate more into the domain as compared to iBN and 2-EHB, specially when the percentage of MO is low. This is due to the slightly higher latent heat and lower pressure of BN, the effects of which were not readily apparent in the case of a single droplet. The liquid lengths of 2-EHN and DBS mixtures are higher than other species and MO-DBS mixtures have the highest liquid lengths. In the single drop simulations, lifetimes for MO-EHN mixtures were higher. Since the total mass of the fuel injected is higher in the case of MO-DBS mixtures due to the higher density of DBS as compared to 2-EHN, the energy required to evaporate the fuel droplets is more. The air entrained by the liquid jet is nearly the same for both cases, thus the MO-DBS mixtures take longer to evaporate and penetrate further. In all the fuel mixtures studied here, the trend of liquid penetration lengths is nearly linear, with the penetration lengths increasing with increase in proportions of MO. There is a change in the slope of the lines when the mass fraction of the second species decreases

from 0.7 to 0.6; the lines become closer to each other and the difference in liquid lengths decreases significantly as the mass fraction of MO increases. This shows that the difference in the properties of the components decreases in significance as the percentage of the least volatile component MO increases.

The results for the different biofuel mixtures obtained above give an estimate of the effect of different components on the spray process and is made possible by the use of the multicomponent evaporation model. Understanding the effect of various biofuel mixtures on the overall combustion process requires reliable chemical kinetics mechanisms for these mixtures and more detailed studies.

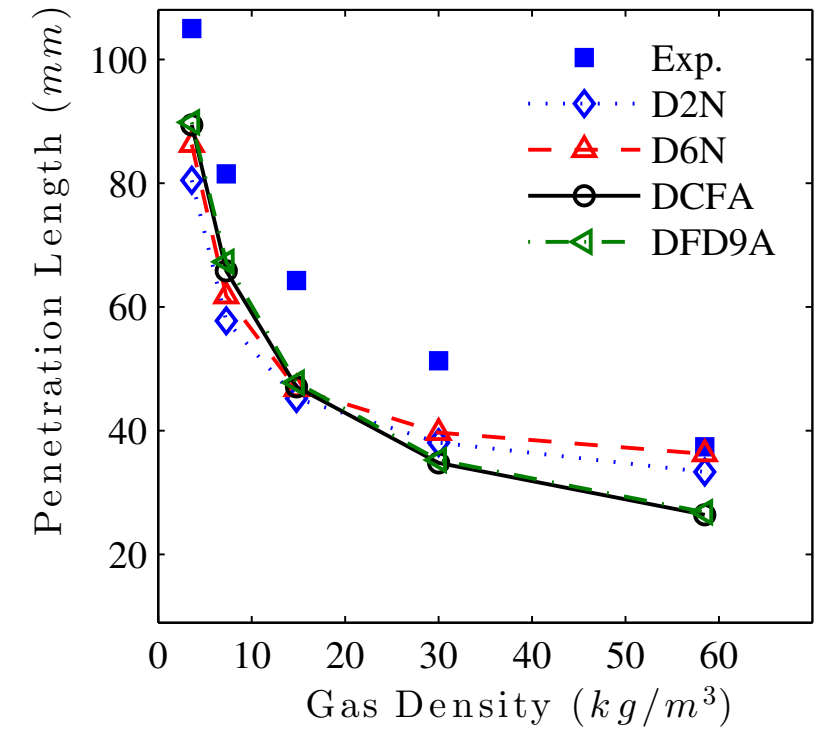

(a)

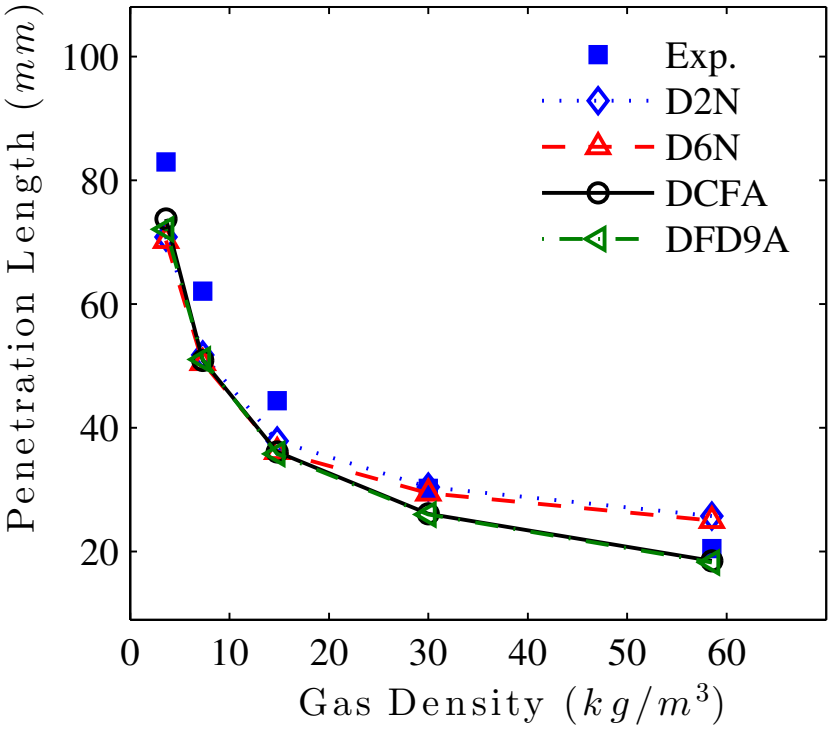

(b)

Figure 1.19: Variation of 97% penetration length of surrogate diesel fuels with gas density for different gas temperatures as predicted by LES. (a) $T_g = 700$ K, (b) $T_g = 850$ K, (c) $T_g = 1000$ K, and (d) $T_g = 1150$ K.

Figure 1.19: (cont'd)

(c)

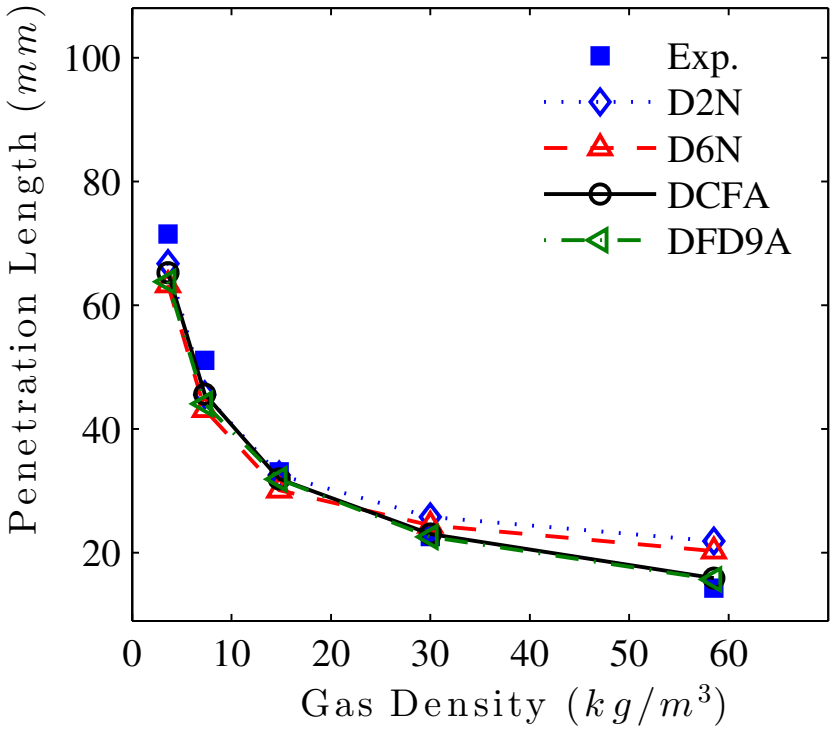

(d)

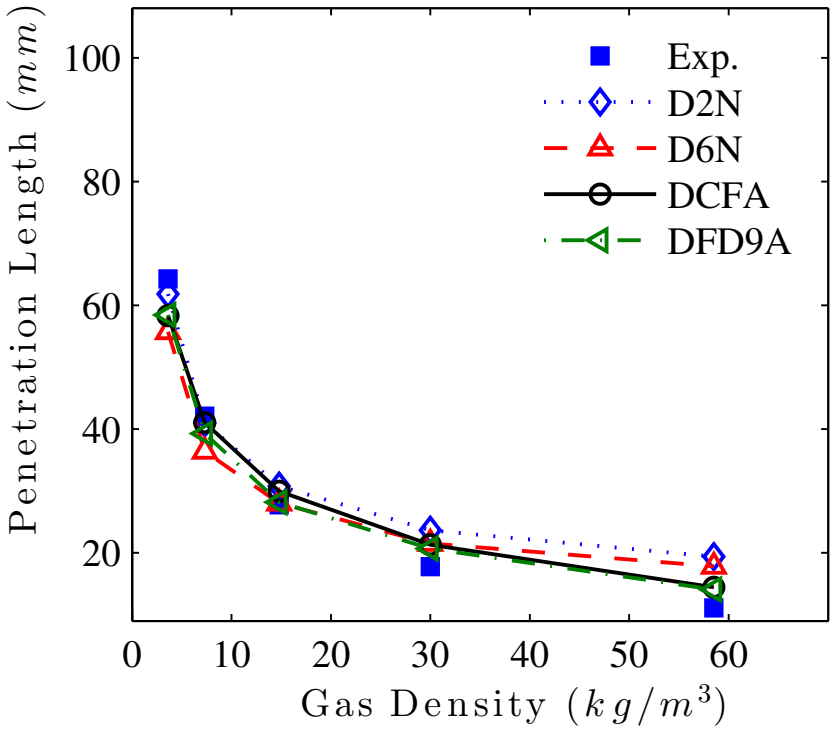

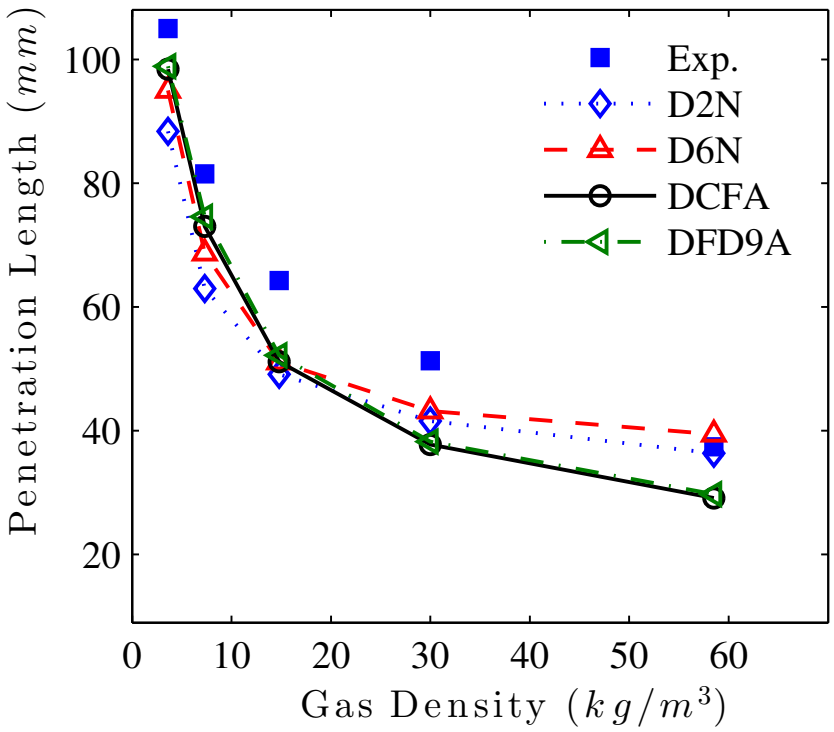

(a)

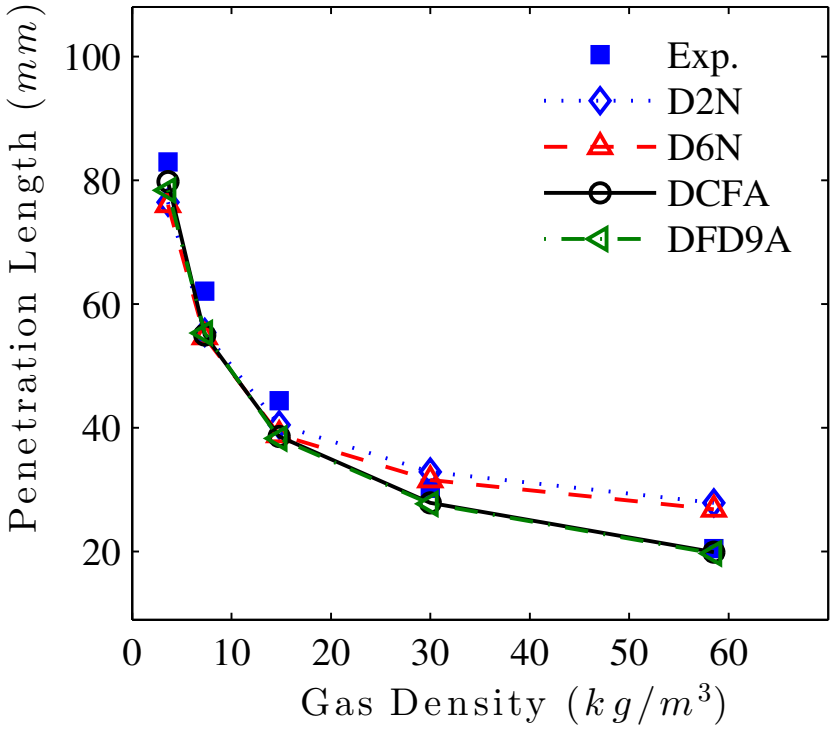

(b)

Figure 1.20: Variation of 99% penetration length of surrogate diesel fuel with gas density for different gas temperatures as predicted by LES. (a) $T_g = 700$ K, (b) $T_g = 850$ K, (c) $T_g = 1000$ K, and (d) $T_g = 1150$ K.

Figure 1.20: (cont'd)

(c)

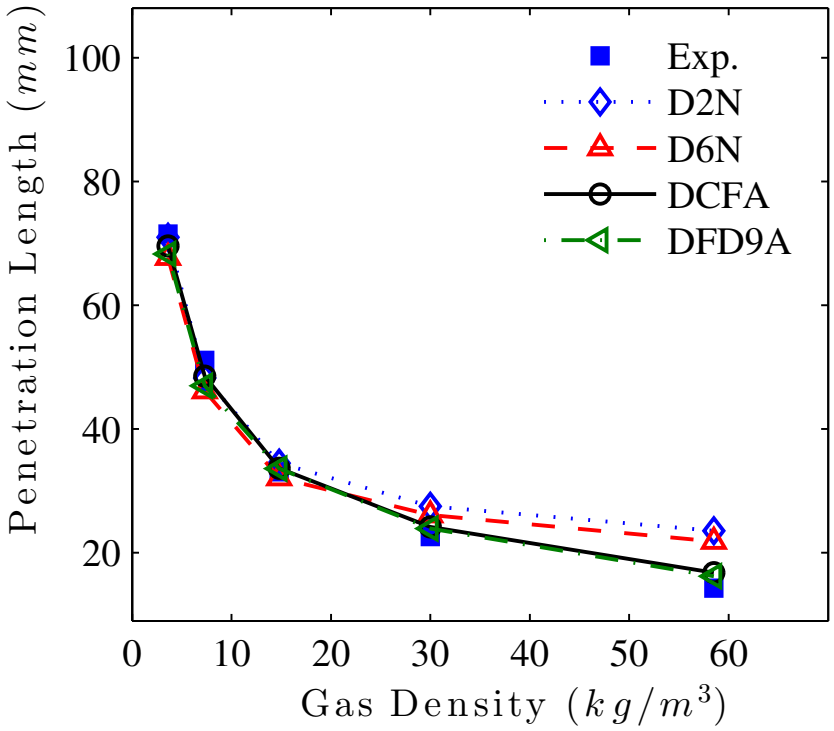

(d)

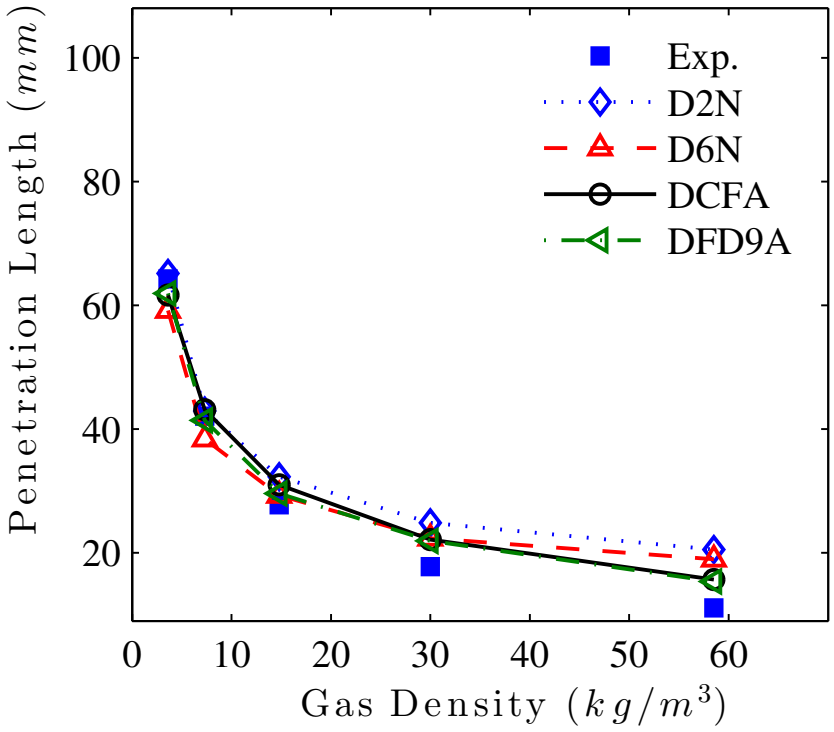

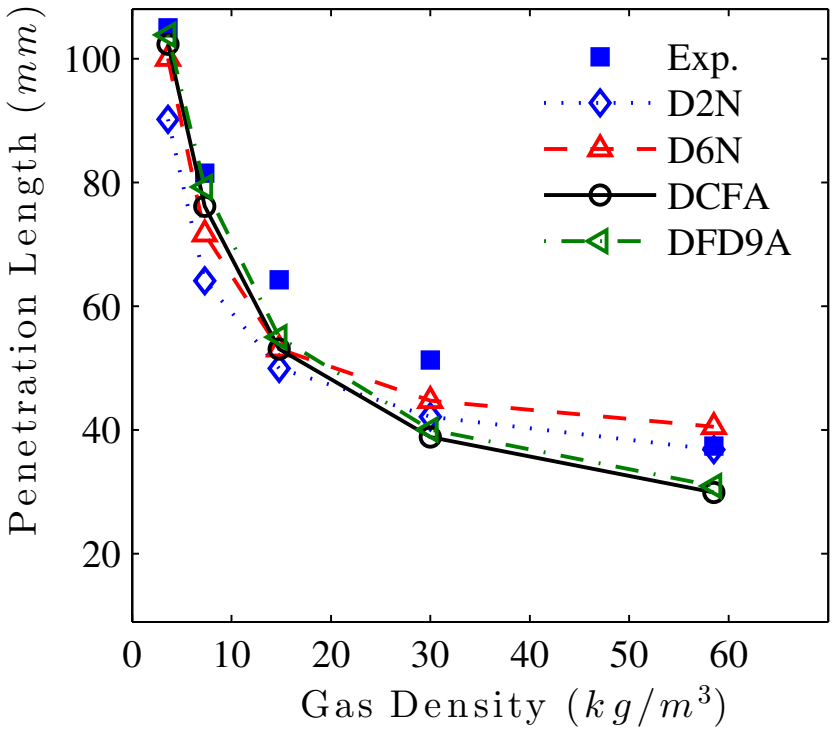

(a)

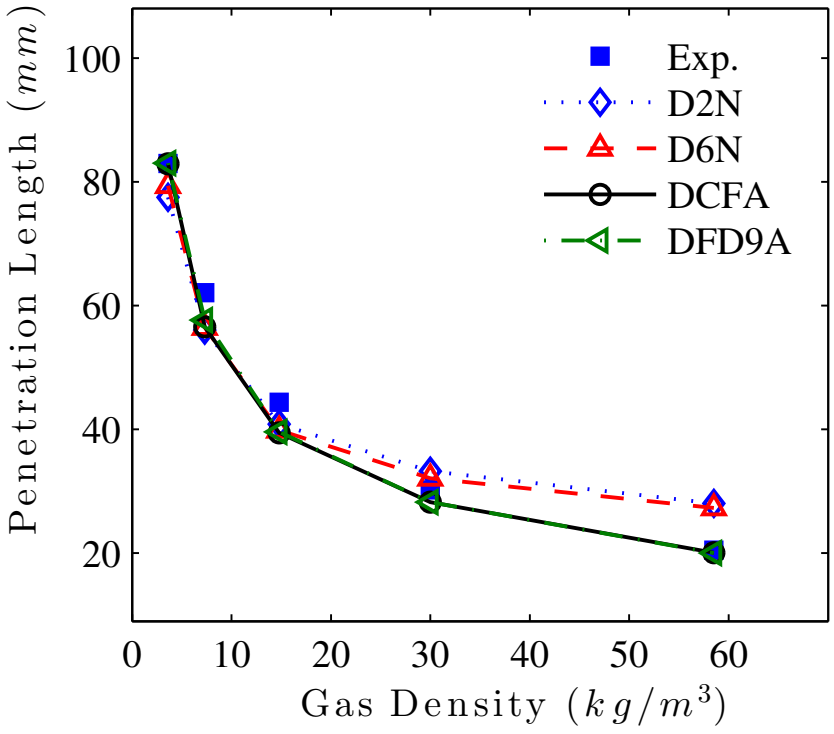

(b)

Figure 1.21: Variation of 99% penetration length of the heaviest species of the surrogate diesel fuel with gas density for different gas temperatures as predicted by LES. The heaviest species are: 1-methylnaphthalene for D2N, n-octadecane for D6N and CFA, and n-eicosane for FD9A. (a) $T_g = 700$ K, (b) $T_g = 850$ K, (c) $T_g = 1000$ K, and (d) $T_g = 1150$ K.

Figure 1.21: (cont'd)

(c)

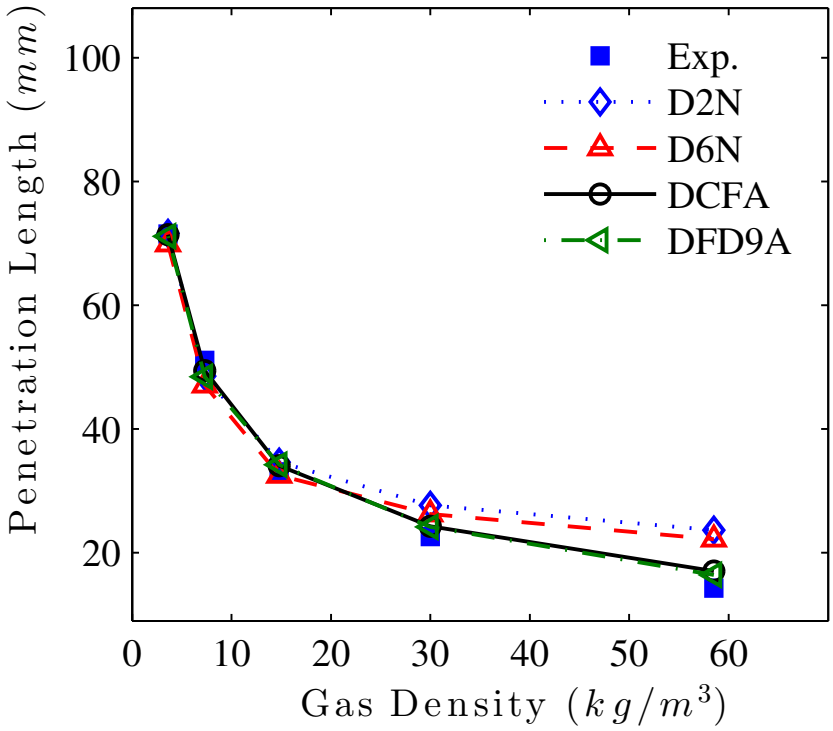

(d)

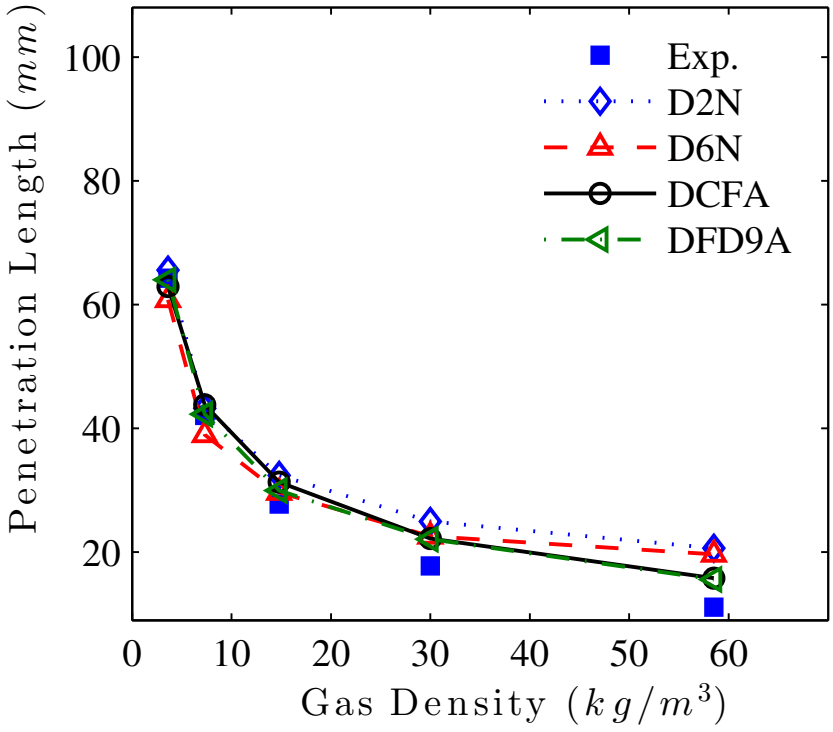

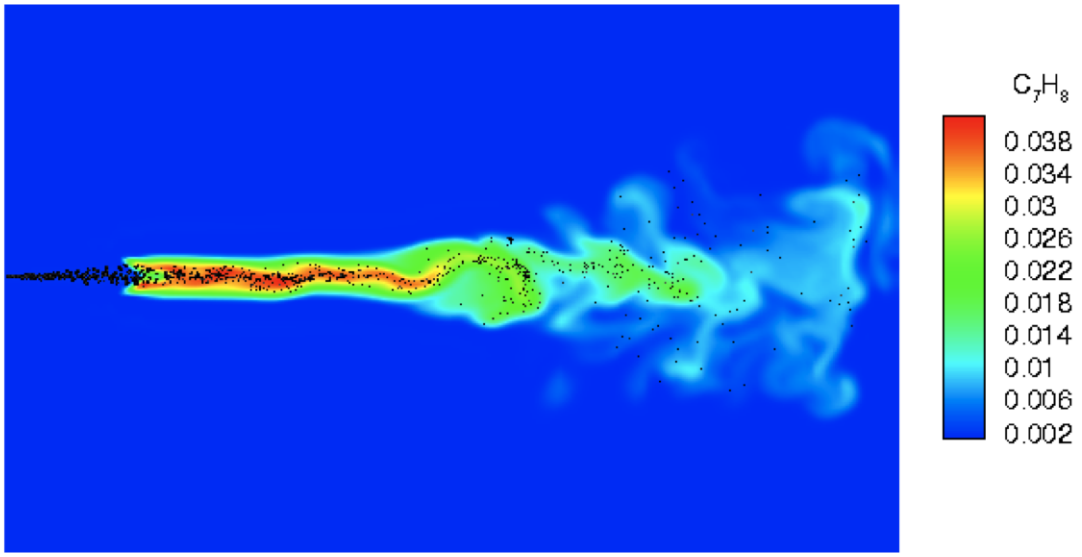

(a)

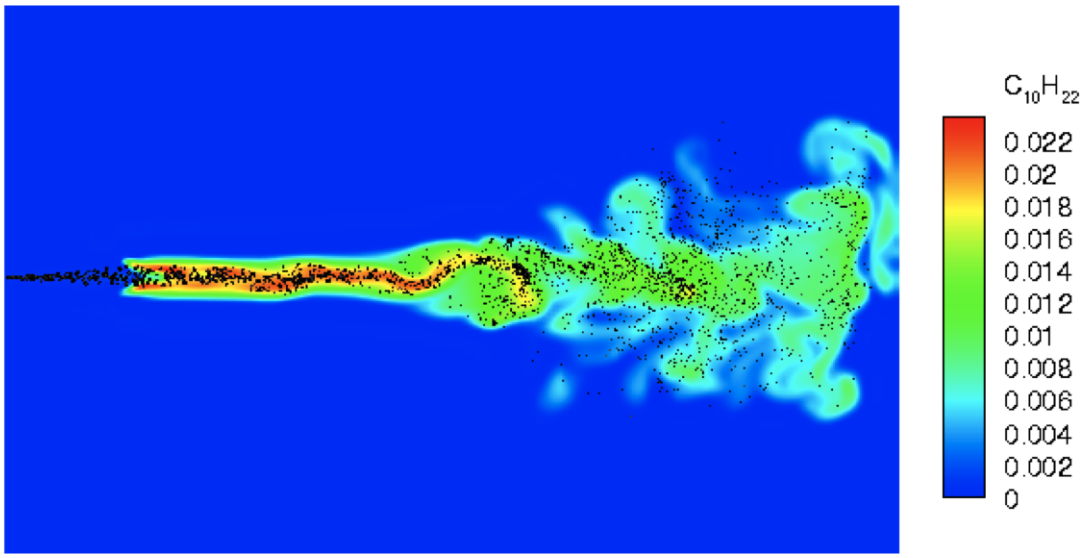

(b)

Figure 1.22: Vapor mass fraction contours for various components of D6N as predicted by LES, (a) toluene, (b) n-decane, (c) n-dodecane, (d) n-tetradecane, (e) n-hexadecane, and (f) n-octadecane.

Figure 1.22: (cont'd)

(c)

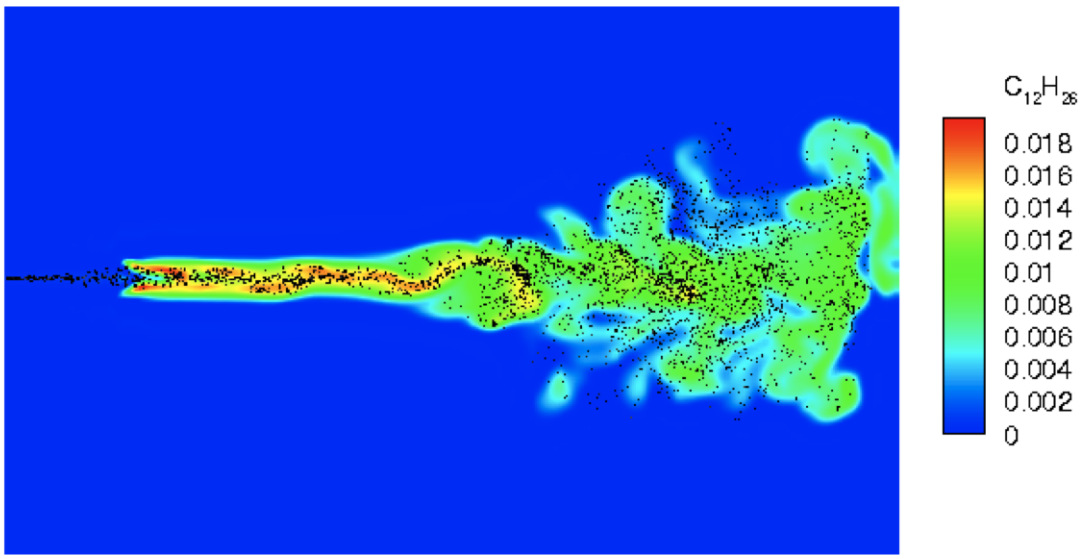

(d)

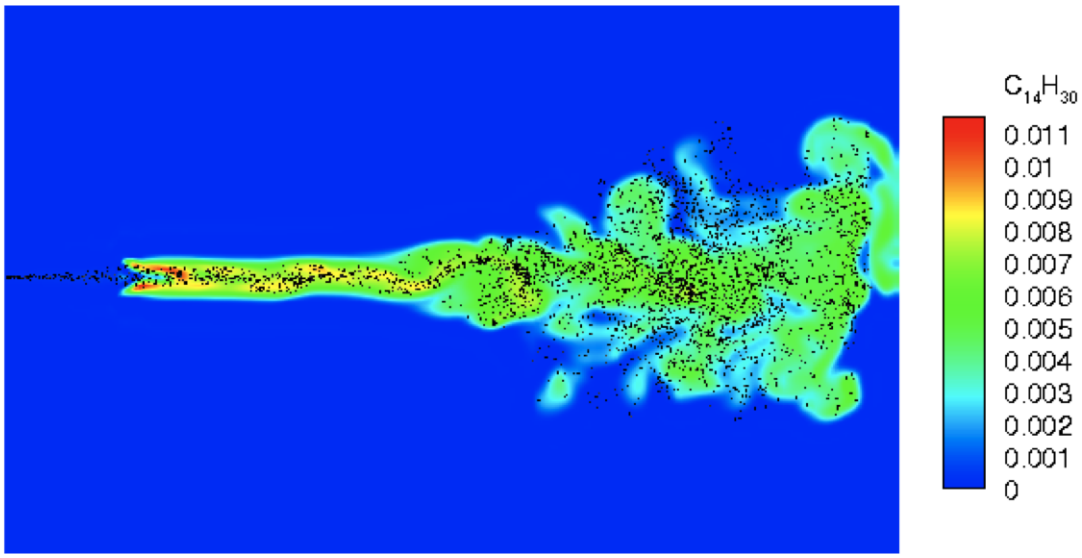

Figure 1.22: (cont'd)

(e)

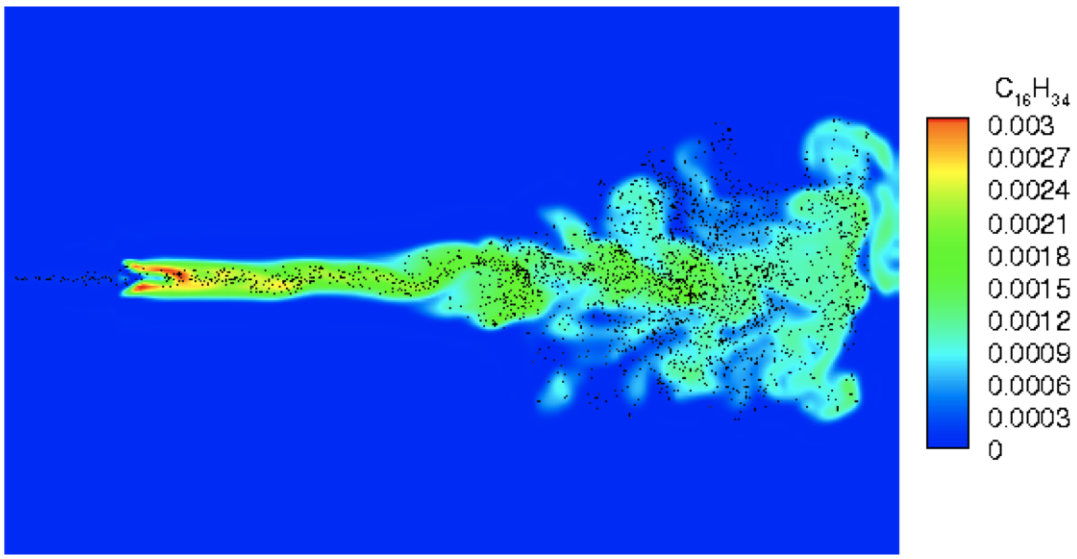

(f)

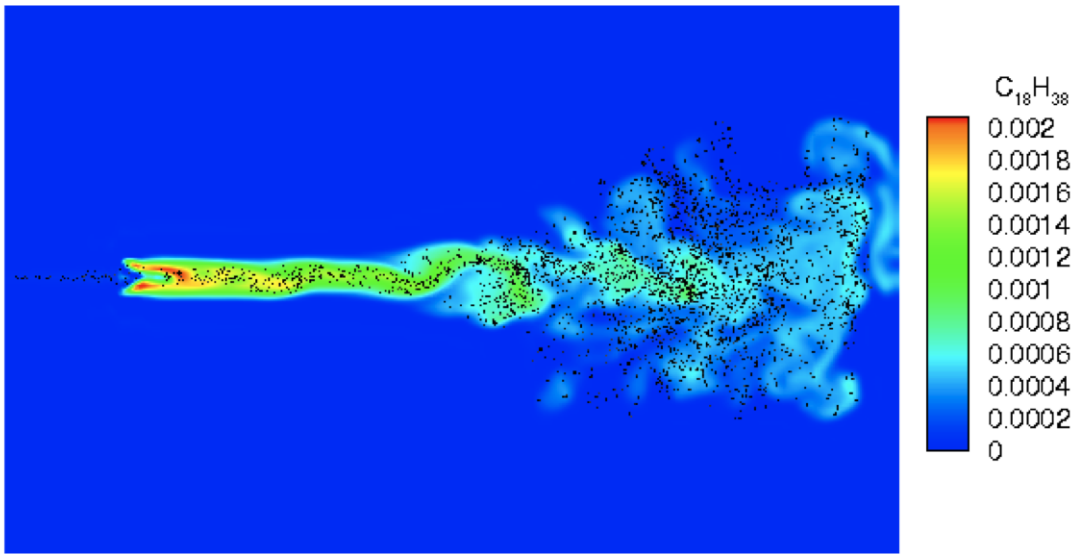

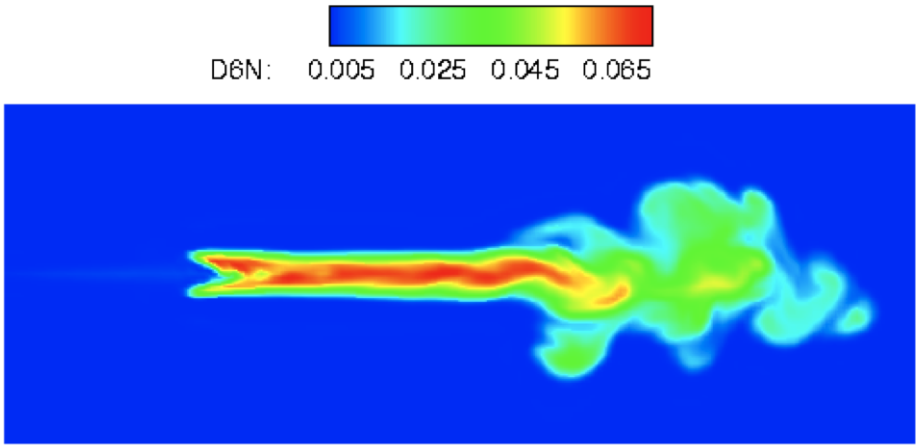

(a)

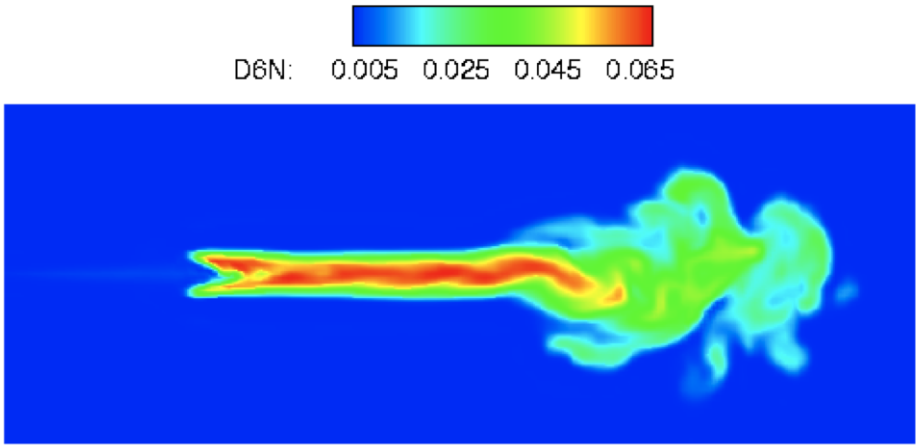

(b)

Figure 1.23: Effect of activity coefficients on the overall vapor mass fraction contours for D6N as predicted by LES, (a) with activity coefficients, (b) without activity coefficients.

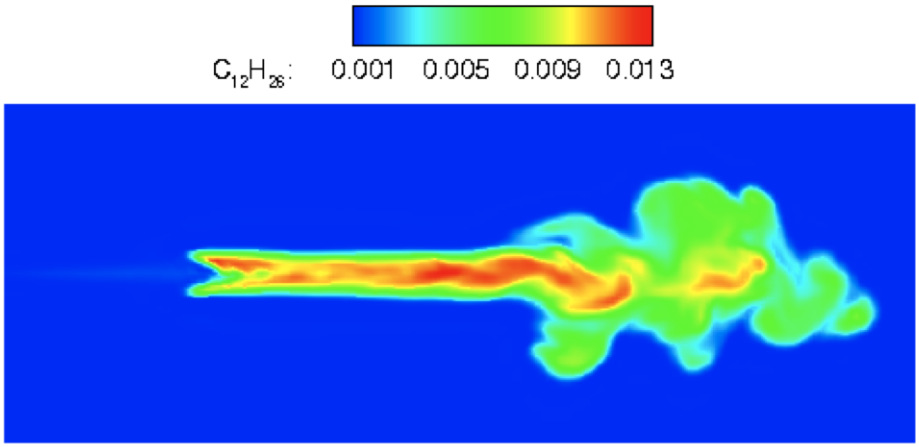

(a)

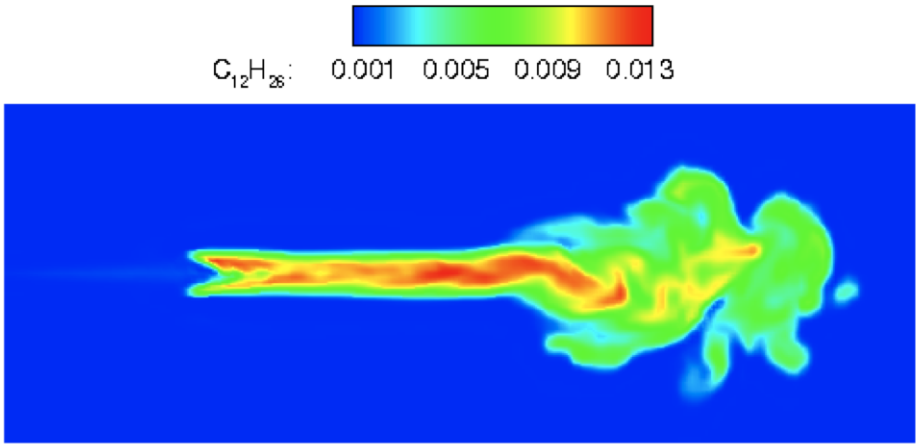

(b)

Figure 1.24: Effect of activity coefficients on the vapor mass fraction contours of n-dodecane in the surrogate D6N, as predicted by LES, (a) with activity coefficients, (b) without activity coefficients.

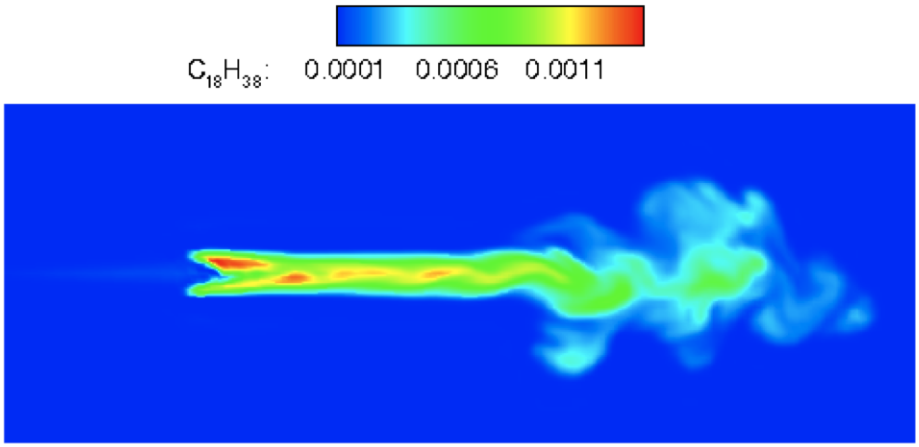

(a)

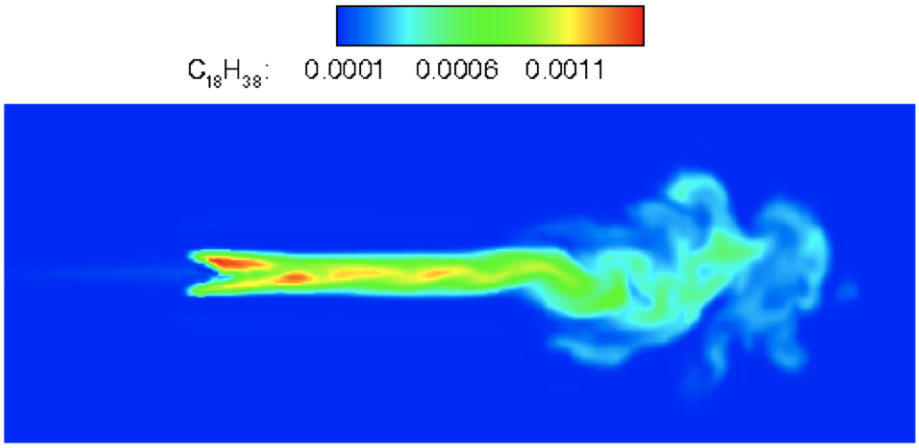

(b)

Figure 1.25: Effect of activity coefficients on the vapor mass fraction contours of n-octadecane in the surrogate D6N, as predicted by LES, (a) with activity coefficients, (b) without activity coefficients.

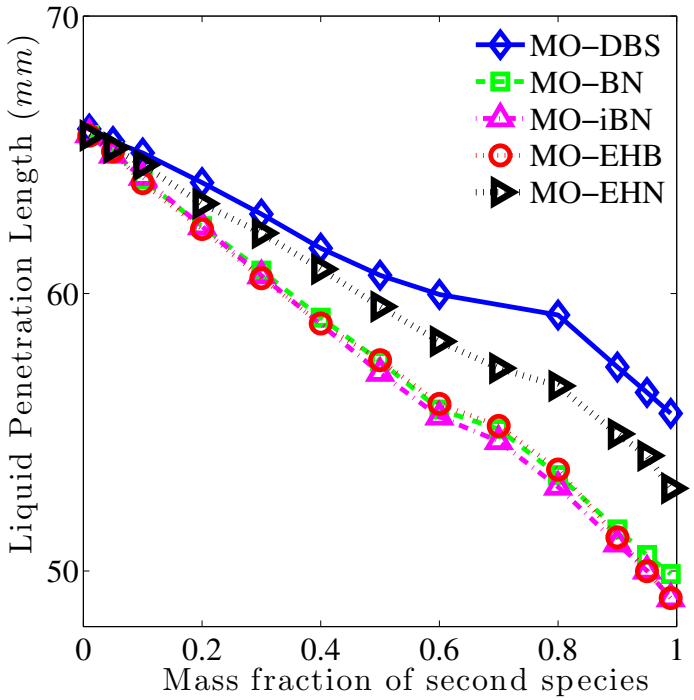

Figure 1.26: Liquid penetration lengths for biofuel spray at gas temperature and density 700 K and 7.3 kg/m^3, respectively, injection pressure 55 MPa, nozzle diameter 0.100 mm, and injected liquid temperature 436 K.

1.4 Summary and Conclusions

A multicomponent fuel heat transfer and evaporation model has been implemented and used for large eddy simulations (LES) of evaporating fuel droplets and sprays. The model solves the one-dimensional mass and energy equations for the mass fraction and temperature profiles inside each of the droplets with a finite volume method and includes real liquid effects on the evaporation process through activity factors. For a single droplet, the variable property multicomponent results were shown to compare well with the constant property lumped model in the limiting conditions. The LES model along with variable property multicomponent droplet heat and mass transfer models and the Kelvin-Helmholtz - Rayleigh-Taylor (KH-RT) droplet breakup model, is used for numerical simulations of spray experiments conducted at the Sandia National Laboratory [42] for single component n-hexadecane and multicomponent diesel fuels. The numerically predicted liquid penetration lengths for n-hexadecane were found to be in better agreement with the experimental results when the multicomponent heat and mass transfer models are used instead of much simpler lumped model. The LES results for liquid lengths of four different multicomponent diesel surrogates with 2-8 components indicate that the mixtures with larger number of species, with a wider range of properties, and with heavier species in the range C18-C20, give a better prediction of the spray penetration lengths as compared to experiments. The effect of real liquid properties on the evaporation process was also evaluated and it was observed that while the single droplet lifetime and liquid spray penetration are relatively unaffected, the liquid mass fractions inside the droplet and the mass fractions of different components in the evaporated vapor plume as well as the shape of the vapor plume are influenced by the real liquid effects. The multicomponent evaporation model was also used for studying the behavior of single

droplets and sprays of different biofuel blends. The numerical results show that for biofuel mixtures with Methyl Oleate (MO), the droplet lifetimes and penetration lengths increase with increase in proportions of the low volatility MO.

Based on the above results, it can be safely stated that variable property models are important and should be used for predicting the evaporation of both single component and multicomponent fuels in droplet and spray calculations. With fully variable properties, the droplet lifetime and consequently the spray length, are predicted to be shorter. Changes in the liquid density and latent heat of vaporization have a direct effect on the droplet lifetime, while changes in the liquid thermal conductivity have little effect. Real liquid effects on the vapor-liquid equilibrium should be included in the evaporation modeling of multicomponent fluids since they affect the droplet surface vapor mass fractions and consequently the mass fraction profiles in both the liquid and gas phase.

Spray length decreases non-linearly with increasing pressure and to a lesser extent with temperature, with decreasing sensitivity to changes in ambient gas conditions at higher temperatures and pressures. These trends are captured by the LES with variable property multicomponent and KH-RT breakup models. Use of multicomponent evaporation model improves the prediction of spray length and fuel vapor distribution for single component fuels and enables the calculation of complex fuels like diesel using surrogate mixtures. The model is not, however, fully accurate. Over-prediction of spray length at higher gas temperatures may be due to the gas conditions being supercritical for the liquid fuel components, especially at higher gas pressures. The prediction of the spray quantities like spray length is also dependent on the composition of the mixture and requires an accurate knowledge of fuel composition. For non-reacting sprays, radiation effects are expected to be negligible since the gas temperatures are not high. In order to rule out the effect of radiation, a model for

absorption of thermal radiation in a semi-transparent spherical droplet [61] was implemented and was found to have no effect on the droplet evaporation rates in the range of temperatures concerned. It is important to note that the spray penetration length is sensitive to the spray breakup process and incorporating a more comprehensive breakup model might be a necessary step in improving the comparison with the experimental results. A stochastic breakup model [64] has recently been implemented by Irannejad et al. [62, 63], along with the multicomponent evaporation model and a droplet wake model. In the stochastic breakup model, the size distribution of daughter droplets after breakup is based on the solution of a Fokker-Planck equation and the probability of the parent droplet breaking into a certain number of droplets is assumed to be independent of the size of the parent droplet. The droplet wake model considers the wake effect of leading droplets on the felt relative velocity of the trailing droplets and is based on concepts developed in Silverman and Sirignano [65]. The studies presented an improved prediction of the liquid spray length, and discussed in detail the relative importance of grid resolution, droplet wake model, and subgrid turbulence and particle models on the spray dynamics. The overall conclusion was that all these parameters are important and should be considered along with the stochastic breakup model for better prediction of sprays.

The multicomponent evaporation model allows the study of the effect of fuel composition on the fuel spray and evaporation characteristics and can be a utilized as a tool in the design of fuels to meet specific requirements. The discrete component nature of the evaporation model allows the coupling of evaporation and combustion but requires a better knowledge of the composition of the fuel and the availabilty of detailed chemical reaction mechanisms for the individual species and their mixtures.

Chapter 2

Large Eddy Simulation of Two-phase Turbulent Reacting Flows with Filtered Mass Density Function

2.1 Introduction

The in-cylinder flow in internal combustion (IC) engines is highly unsteady and turbulent featuring substantial cycle-to-cycle variations (CCV), with the presence of liquid spray and combustion further increasing the complexity. Traditionally, in-cylinder flows have been simulated with the Reynolds-averaged Navier-Stokes (RANS) models, which provide information on the mean flow features, but the transient features and the large-scale flow features are lost in modeling due to averaging. The ability of Large-Eddy Simulation (LES) models to capture these features has been recognized and various studies of in-cylinder flow with LES have been reported in the literature ([34], [66], [67], [71], [73]-[76], [79]-[100], [102]-[103]). A brief review of some of these studies is given in Banaeizadeh et al. [34]. Some of the earliest studies involving LES for IC engines were carried out by Naitoh et al.[66], in which they were able to compute the large in-cylinder coherent structures, using a third order upwind space-differencing scheme on a coarse grid, but over-predicted the subgrid scale (SGS) tur-

bulent kinetic energy. Haworth et al. [67] and Verzicco et al. [69] used LES and the body force method of Mohd-Yusof [70] and obtained a good comparison with the experimental results of Morse et al. [68] for a simple engine-like axisymmetric geometry with a slowly moving piston, a nonmoving central valso been used to perform LES of IC engines. The widely used open-source code for IC engine simulations, KIVA 3V [1], was used by Sone et al. [73] and Lee et al. ([74]-[75]), along with the linear-eddy model, for simulating the in-cylinder flow, fuel mixing and combustion. LES was able to predict CCV in a CAT 3351 engine, in a study conducted by Jhavar et al. [76] using KIVA, a one-equation SGS stress model [77], and a CHEMKIN-based combustion model. The commercial code Star-CD [78] was also used by Dugue et al. [79] for both RANS and LES of in-cylinder flows. Enaux et al. [80] studied CCV using LES in a spark-ignition engine and attributed them to large-scale velocity fluctuations around the spark plug. These fluctuations were shown to affect the location and growth of the early flame kernel and the overall combustion duration. Bodin et al. [81] studied the exhaust manifold flow in a heavy duty Diesel engine using LES and found significant unsteadiness and flow separation, with secondary flows generated due to geometric features. Global features like total pressure loss were found to be better predicted by LES than RANS. LES predictions for cycle-to-cycle variations and mean and root mean square(rms) velocities using the commercial code CONVERGE compared well with Particle Image Velocimetry (PIV) results in a study conducted by Kuo et al. [81]. Misdariis et al. [83] conducted LES of two spark-ignition engines, a naturally aspirated four-valve F7P engine and a highly supercharged engine called Ecosural, and for different high order numerical schemes and SGS models. Different SGS models and numerical schemes were found to not generate significantly different mean results during the non-reacting gas-exchange phase. Sakowitz et al. [86] studied EGR mixing in the intake manifold and found that

LES provides better insight into the EGR mixing in the presence of flow pulsations. CCV for a highly downsized turbocharged direct injection spark-ignition engine were found to be also better predicted by LES than RANS by Fontanesi et al. [88]. Richard et al. [89] used a flame surface density (FSD) approach along with an Eulerian spark model for LES of a real engine and found LES results to be weakly dependent on the filter size. Zhuo et al. [91] conducted LES with KIVA code, modified to include the MUSCL (Monotone Upstream-centered Schemes for Conservation Laws) differencing scheme and obtained good comparisons with the experiment. Zhou et al. [92] conducted LES with KIVA-3V for a high-speed direct-injection Ford diesel engine with the Smagorinsky , wall-adopting local eddy viscosity (WALE) and a one-equation SGS turbulent kinetic energy model. They found the liquid and vapor penetration lengths to compare well with the experimental results. Single-phase LES of a model Gasoline Direct Injection (GDI) engine was conducted by Devesa et al. [93] with a two-step Taylor Galerkin scheme and a wall adapting local eddy viscosity model. The momentum of the injected spray in a real engine was modeled by injecting a gaseous jet with similar properties and its effect on the tumbling motion was studied. The LES results were compared with PIV measurements and the CCV were demonstrated to be important. Befrui et al. [94] studied the influence of nozzle design and geometric features on near nozzle flow and primary breakup using the hybrid Volume-of-Fluid - Large Eddy Simulation (VOF-LES) method. The nozzle shape was found to have significant influence on the nozzle flow, hydraulic efficiency and the jet breakup characteristics. The open source CFD software, OpenFOAM was used by Keskinen et al. [95] to conduct LES of Sisu Diesel 84 engine with the piston removed, exhaust valves closed and the intake valves kept open with a constant valve lift. The swirl flow and mixing were studied in details and the fill port was found to have a larger impact on swirl generation than the swirl port. Ranasinghe et

al. [96] conducted LES of a spark-ignition engine using the flame surface density approach, with ignition and flame kernel models. The model was able to predict the combustion rate and pressure rise with good comparison with experimental results and significant variations in flame propagation were observed. Keskinen et al. [97] studied the in-cylinder flow structures and turbulence-enhanced mixing generated by the intake jets in a simplified geometry with a fixed lift valve, using an incompressible flow solver. They were able to qualitatively reproduce the major features seen in experiments. Piscaglia et al. [98] first evaluated the dynamic Smagorinsky and the compressible WALE SGS models for LES of a backward facing step and then used the WALE model for LES of a fixed valve configuration. They found a good correlation between the computed and experimental mean velocities. They describe a parallel methodology for OpenFOAM calculations with a topologically changing mesh with potential applications in LES of two-stroke engines, but cited the work in progress and did not present any results. Mobasheri and Peng [100] studied the combustion and pollutant emissions in a DI Diesel engine with LES, using a modified version of the Extended Coherent Flame Model (ECFM-3Z) with the extended Zeldovich mechanism for NOx formation and the Kennedy, Hiroyasu and Magnusson mechanism [101] for soot formation. The models were able to capture the experimental trends for in-cylinder pressure, heat release rate and pollutant formation.

2.2 Combustion Modeling in LES

The various studies described above used different combustion models for calculating the chemical reaction terms in the energy and species conservation equations. There are several approaches to combustion modeling that can be used along with LES. A good classification

of the different approaches that have been applied to combustion modeling with LES is given in Rutland [103]. The various approaches can briefly be classified as:

1. **Direct Integration** – The chemical source terms are obtained by direct integration of the chemical reaction mechanism using the filtered values of temperature and species mass fractions. The approach can be computationally expensive if detailed mechanisms are used and is mostly applicable to homogeneous flows.

2. **Representative Interactive Flamelet (RIF) Model** – In the RIF model developed in Peters et al. ([104]-[107]), the combustion process is modeled by tracking individual flamelets using a Lagrangian approach. This model can be used for diesel combustion and is computationally more efficient than the direct integration approach.

3. **Time-scale models** – The time-scale approach, as developed in Abraham et al. [108] and Kong et al. [109], for spark-ignition and diesel engines, respectively, assumes that the species concentrations approach their local thermodynamic equilibrium values with a characteristic conversion time. This time scale is a combination of a turbulent mixing time and a chemical conversion time. The model is known as the characteristic time scale (CTC) model.

4. **Transport-equation models** – In this class of models, the approach is to solve the transport equations of various functions representing the flame front, progress variable, etc.

   (a) **Progress variable** – The progress variable C-equation approach is a flame-sheet approach in which the transport equation of the progress variable C, which can be the normalized temperature, is solved. An example of the method's application

is given in Thobois et al. [110].

(b) **Level set – G-equation** – In this level set method, a specific line of the continuous variable G represents the flame front. The solution of the transport equation for G requires the laminar flame speed and models for the subgrid scalar flux. An example of this approach for premixed combustion using LES is given in Im et al. [111].

(c) **Flame surface area density** – In this approach, also called the Coherent Flame Model (CFM), the transport equation of the flame surface density is solved to obtain the total reaction rate in the cell. Various models have been developed based on this approach, including the ECFM, ECFM-3Z ([112]-[114]), and ECFM-LES ([89],[115]) models.

(d) **Mixture fraction** – In this approach (Hu et al. [116],[117]), the transport equation of the assumed PDF of the mixture fraction is solved using laminar flamelet solutions.

(e) **Conditional moment closure (CMC)** – The CMC approach ([118]-[120]) is an expansion of the mixture fraction approach in which some of the terms in the transport equation are evaluated conditionally at the flame front. It is computationally more expensive than the mixture fraction approach and generally gives better results.

5. **PDF transport** – In this approach, the transport equation for the joint probability density function (PDF) of the scalar variables is solved for as opposed to the presumed PDF of the mixture fraction and CMC approaches. The approach has been applied to both RANS and LES of internal combustion engines, and has the significant advantage

that the reaction term is in a closed form and no additional modeling is required. A description of this approach to LES as applied to turbulent spray combustion in internal combustion engines would be the focus of this chapter.

2.3 LES/FMDF of turbulent spray combustion

A potent method for the LES of turbulent spray combustion is the two-phase filtered mass density function (FMDF), which is an extension of the single-phase subgrid-scale (SGS) FMDF model, developed by Jaberi et al. [121], to two-phase flows. FMDF represents the joint PDF of the SGS variables, and is obtained by the solution of its transport equation with a Lagrangian Monte-Carlo method. An important feature of the FMDF formulation is that the reaction term appears in a closed form, irrespective of the type of reaction. The method is thus suitable for various types of reacting flows, including premixed, non-premixed, etc. and is an attractive proposition for turbulent combustion simulations. The FMDF model has been successfully applied to LES of a wide variety of turbulent combustion simulations [[121]-[137]]. The FMDF model has also been extended to compressible flows [138] and multiphase flows ([139]-[143]).

The two-phase LES/FMDF model, as described in detail in Ref. [34], is implemented via an efficient, hybrid numerical method. In this method, the filtered compressible Navier-Stokes equations in curvilinear coordinate systems are solved with a generalized, high-order, multi-block, compact differencing scheme, while the spray and the FMDF are implemented with Lagrangian methods.

Banaeizadeh et al. [34] recently applied the two-phase FMDF model to LES of turbulent spray combustion in IC engines. The LES/FMDF model was used for the simulation of in-

cylinder turbulent flow and spray mixing and combustion in three different configurations. The first two configurations, viz., a poppet valve in a sudden expansion, and a piston-cylinder assembly with a stationary valve, were relatively simple. The mean and rms of the axial velocity in the sudden expansion flow matched well with the experimental data when the dynamic Smagorinsky model was used. The harmonic movement of the piston in the second configuration generates unsteady and turbulent flow over the valve and in the cylinder, and this flow was also well predicted by LES in comparison to experiment. The third configuration was MSU's 3-valve, optically accessible, single cylinder Direct Injection Spark Ignition (DISI) engine [152] which had two tilted intake valves and one exhaust valve, with 90 mm bore, 106 mm stroke, and a compression ratio of 11:1. LES results for this engine indicate considerable CCV for the vorticity and SGS turbulent viscosity, but insignificant CCV for the mean temperature, as also seen in the experimental results. Spray and reacting flow simulations were also carried out with the two-phase LES/FMDF model. The secondary break-up was modeled using the Rayleigh-Taylor breakup model, however due to the small droplet size, secondary breakup was insignificant. Flame propagation was also found to be in agreement with the experimental observation. Comparison between the LES-FD and FMDF-MC components at different crank angles and locations indicate these components to be consistent, thus establishing the numerical accuracy of the hybrid two-phase compressible LES/FMDF methodology.

2.3.1 Mathematical Formulation

The two-phase compressible LES/FMDF model has three main components: (1) the filtered gas dynamics equations, (2) the FMDF and its equivalent stochastic equations, and (3) the Lagrangian spray equations.

2.3.2 Filtered Gas Dynamics Equations

The compact form of the compressible Favre-filtered continuity, momentum, energy and scalar equations in curvilinear coordinates is written as:

$$\frac{\partial(JU)}{\partial\tau} + \frac{(\partial\hat{F} - \hat{F}_v)}{\partial\xi} + \frac{(\partial\hat{G} - \hat{G}_v)}{\partial\eta} + \frac{(\partial\hat{H} - \hat{H}_v)}{\partial\zeta} = JS_0\,, \tag{2.1}$$

where $J = \frac{\partial(x,y,z,t)}{\partial(\xi,\eta,\zeta,\tau)}$ is the Jacobian of transformation, $U = (\bar{\rho}, \bar{\rho}\tilde{u}, \bar{\rho}\tilde{v}, \bar{\rho}\tilde{w}, \bar{\rho}\tilde{E}, \bar{\rho}\tilde{\phi})$ is the solution vector, $\bar{\rho}$ is the filtered density, $\tilde{u}, \tilde{v}, \tilde{w}$ are the Favre filtered velocities, $\tilde{E} = \tilde{e} + \frac{1}{2}\tilde{u_i}\tilde{u_i}$ is the Favre filtered total energy, $\tilde{\phi}$ is the Favre filtered scalar mass fraction, S_0 is the source term and $\tilde{F}, \tilde{G}, \tilde{H}$ are the inviscid fluxes given by:

$$\tilde{F} = \begin{bmatrix} \bar{\rho}\hat{U} \\ \bar{\rho}\tilde{u}\hat{U} + \bar{\rho}\hat{\xi_x} \\ \bar{\rho}\tilde{v}\hat{U} + \bar{\rho}\hat{\xi_y} \\ \bar{\rho}\tilde{w}\hat{U} + \bar{\rho}\hat{\xi_z} \\ (\bar{\rho}\tilde{E} + \bar{p})\hat{U} - \hat{\xi_t} \\ \bar{\rho}\tilde{\phi}\hat{U} \end{bmatrix}, \tilde{G} = \begin{bmatrix} \bar{\rho}\hat{V} \\ \bar{\rho}\tilde{u}\hat{V} + \bar{\rho}\hat{\eta_x} \\ \bar{\rho}\tilde{v}\hat{V} + \bar{\rho}\hat{\eta_y} \\ \bar{\rho}\tilde{w}\hat{V} + \bar{\rho}\hat{\eta_z} \\ (\bar{\rho}\tilde{E} + \bar{p})\hat{V} - \hat{\eta_t} \\ \bar{\rho}\tilde{\phi}\hat{V} \end{bmatrix}, \tilde{H} = \begin{bmatrix} \bar{\rho}\hat{W} \\ \bar{\rho}\tilde{u}\hat{W} + \bar{\rho}\hat{\zeta_x} \\ \bar{\rho}\tilde{v}\hat{W} + \bar{\rho}\hat{\zeta_y} \\ \bar{\rho}\tilde{w}\hat{W} + \bar{\rho}\hat{\zeta_z} \\ (\bar{\rho}\tilde{E} + \bar{p})\hat{W} - \hat{\zeta_t} \\ \bar{\rho}\tilde{\phi}\hat{W} \end{bmatrix} \tag{2.2}$$

$$\hat{U} = \hat{\xi_t} + \hat{\xi_x}\tilde{u} + \hat{\xi_y}\tilde{v} + \hat{\xi_z}\tilde{w}, \tag{2.3}$$

$$\hat{V} = \hat{\eta_t} + \hat{\eta_x}\tilde{u} + \hat{\eta_y}\tilde{v} + \hat{\eta_z}\tilde{w}, \tag{2.4}$$

$$\hat{W} = \hat{\zeta_t} + \hat{\zeta_x}\tilde{u} + \hat{\zeta_y}\tilde{v} + \hat{\zeta_z}\tilde{w} \tag{2.5}$$

Here, $\tilde{\xi}_x = J\delta\xi/\delta x, ...$,etc. are the metric coefficients and $\bar{p}$ is the filtered pressure. The temporal term on the left hand side of Equation 2.1 is decomposed as:

$$\frac{\partial(JU)}{\partial\tau} = J\frac{\partial U}{\partial\tau} + U\frac{\partial J}{\partial\tau} \tag{2.6}$$

where the time derivative of the Jacobian is calculated as

$$\frac{\partial J}{\partial\tau} = -[(\hat{\xi_t})_\xi + (\hat{\eta_t})_\eta + (\hat{\zeta_t})_\zeta] \tag{2.7}$$

with

$$\begin{aligned}
\hat{\xi_t} &= -[x_x(\hat{\xi_x}) + y_x(\hat{\xi_y}) + z_x(\hat{\xi_z})], \\
\hat{\eta_t} &= -[x_x(\hat{\eta_x}) + y_x(\hat{\eta_y}) + z_x(\hat{\eta_z})], \\
\hat{\zeta_t} &= -[x_x(\hat{\zeta_x}) + y_x(\hat{\zeta_y}) + z_x(\hat{\zeta_z})].
\end{aligned} \tag{2.8}$$

and (x_x, y_y, z_z) is the grid speed vector.

The subgrid stress terms are closed via gradient type closures [1] and the Smagorinsky [35, 36] models for the turbulent viscosity. The turbulent viscosity in the Smagorinsky model is:

$$\nu_t = (C_d\Delta)^2|\tilde{S}| \tag{2.9}$$

Here, $|\tilde{S}|$ is the magnitude of the rate-of-strain tensor, and $\Delta = (volume)^{1/3}$ is the characteristic size of the filter function. The coefficient C_d is either fixed and has to be adjusted for different configurations and operating conditions or can be obtained dynamically

by the procedure suggested in References [[37]-[39]]. The SGS velocity correlations in the energy and scalar equations are modeled with the following closures [[40], [41]]:

$$\bar{\rho}(\widetilde{u_i E} - \tilde{u_i}\tilde{E}) + (\widetilde{\rho u_i} - \tilde{\rho}\tilde{u_i}) = -\bar{\rho}\frac{\nu_t}{Pr_t}\frac{\partial \tilde{H}}{\partial x_i} \tag{2.10}$$

$$\bar{\rho}(\widetilde{u_i \phi} - \tilde{u_i}\tilde{\phi}) = -\bar{\rho}\frac{\nu_t}{Sc_t}\frac{\partial \tilde{\phi}}{\partial x_i} \tag{2.11}$$

where $\tilde{H} = \tilde{E} + \frac{\bar{p}}{\bar{\rho}}$ is the total filtered enthalpy and Pr_t and Sc_t are the turbulent Prandtl and Schmidt numbers, respectively.

2.3.3 Compressible two-phase FMDF equations

The scalar FMDF represents the joint SGS PDF of the scalar vector and is defined as

$$P_L(\Psi; x, t) = \int_{-\infty}^{+\infty} \rho(x', t)\sigma[\Psi, \Phi(x', t)]G(x' - x)dx' \tag{2.12}$$

$$\sigma[\Psi, \Phi(x', t)] = \prod_{\alpha=1}^{N_s+1} \delta(\Psi_\alpha - \phi_\alpha(x, t)) \tag{2.13}$$

,

tepaper:obrien-pdf, defined based on a set of delta functions, δ, and the scalar vector $\Phi \equiv \phi_\alpha, (\alpha = 1, ..., N_s + 1)$, includes the species mass fractions for $\alpha = 1, ..., N_s$, and the specific enthalpy for $\alpha \equiv N_s + 1$.

The time derivative of FMDF is given by:

$$\frac{\partial P_L(\Psi; x, t)}{\partial t} = -\frac{\partial}{\partial \psi_\alpha}\left[\left\langle \frac{\partial \phi_\alpha}{\partial t} \mid \Psi \right\rangle_l P_L(\Psi; x, t)\right] \tag{2.14}$$

The unfiltered equation for the scalar is given as:

$$\rho\frac{\partial\phi_\alpha}{\partial t}+\rho u_i\frac{\partial\phi_\alpha}{\partial x_i}=\frac{\partial}{\partial x_i}\left(\Gamma\frac{\partial\phi_\alpha}{\partial x_i}\right)+S_\alpha^{rea}+S_\alpha^{cmp}+S_\alpha^{spy}-\phi_\alpha S_m \tag{2.15}$$

The transport equation for FMDF is obtained by inserting Equation (2.15) into Equation (2.14):

$$\frac{\partial P_L}{\partial t}+\frac{\partial[\langle u_i|\Psi\rangle_l P_L]}{\partial x_i}-\left\langle\left(\frac{1}{\rho}\left[\frac{\partial\rho}{\partial t}+\frac{\partial(\rho u_i)}{\partial x_i}\right]\right)\middle|\Psi\right\rangle_l P_L$$

$$=\frac{\partial}{\partial\psi_\alpha}\left[\left\langle-\left(\frac{1}{\rho}\frac{\partial}{\partial x_i}\left(\Gamma\frac{\partial\phi_\alpha}{\partial x_i}\right)\right)\middle|\Psi\right\rangle_l P_L\right]$$

$$-\frac{\partial}{\partial\psi_\alpha}\left[\left\langle\frac{S_\alpha^{rea}}{\rho}\middle|\Psi\right\rangle_l P_L\right]-\frac{\partial}{\partial\psi_\alpha}\left[\left\langle\frac{S_\alpha^{cmp}}{\rho}\middle|\Psi\right\rangle_l P_L\right]$$

$$-\frac{\partial}{\partial\psi_\alpha}\left[\left\langle\frac{S_\alpha^{spy}}{\rho}\middle|\Psi\right\rangle_l P_L-\left\langle\frac{\psi_\alpha S_m}{\rho}\middle|\Psi\right\rangle_l P_L\right] \tag{2.16}$$

In this equation, the source/sink terms for species and energy are defined as:

$$S_\alpha^{rea}=\rho\dot{\omega}_\alpha,\ S_\alpha^{cmp}=0,\ S_\alpha^{spy}=S_m,\ \alpha\equiv 1,.....,N_s$$

$$S_\alpha^{rea}=\rho\dot{Q},\ S_\alpha^{cmp}=\left(\frac{\partial p}{\partial t}+u_i\frac{\partial p}{\partial x_i}+\tau_{ij}\frac{\partial u_i}{\partial x_j}\right),\ S_\alpha^{spy}=S_h,\ \alpha\equiv N_{s+1} \tag{2.17}$$

Equation (2.16) is an exact transport equation for the FMDF. In this equation molecular Prandtl and Schmidt numbers are the same, so the mass/thermal diffusion coefficients are $\Gamma=\mu/Sc$. The second term on the right-hand side (RHS) of equation (2.16) is the chemical

reaction term and is closed when the effect of SGS pressure fluctuations are ignored and $\langle S_\alpha^{rea}|\Psi\rangle_l = S_\alpha^{rea}(\psi)$. This term is not closed in the filtered scalan be solved. The first one is the second term on the left hand side (LHS) of equation (2.16). This (convection) term can be decomposed into large-scale convection by the filtered velocity and the SGS convection as:

$$\langle u_i|\Psi\rangle_l P_L = \langle u_i\rangle_L P_L + (\langle u_i|\Psi\rangle_l P_L - \langle u_i\rangle_L P_L). \tag{2.18}$$

The SGS convection is modeled here with a gradient type closure:

$$\langle u_i|\Psi\rangle_l P_L - \langle u_i\rangle_L P_L = -\Gamma_t \frac{\partial(P_L/\langle\rho\rangle_l)}{\partial x_i}\,, \tag{2.19}$$

where $\Gamma_t = \langle\rho\rangle_l \nu_t/Pr_t$ is the turbulent diffusivity. Here $\langle\rangle_L$ and $\langle\rangle_l$ denote the Favre filtered and filtered values, respectively.

The first term on the RHS of Equation (2.16) is also unclosed and is decomposed into two parts, the molecular transport and the SGS dissipation. The SGS dissipation is modeled with the linear mean-square estimation (LMSE) model [[145],[146]] or the interaction by exchange with the mean (IEM) model [147]:

$$\frac{\partial}{\partial\psi_\alpha}\left[\left\langle -\left(\frac{1}{\rho}\frac{\partial}{\partial x_i}\left(\Gamma\frac{\partial\phi_\alpha}{\partial x_i}\right)\right)\right|\Psi\Big\rangle_l P_L\right]$$

$$= \frac{\partial}{\partial x_i}\left[\Gamma\frac{\partial\left(\frac{P_L}{\langle\rho\rangle_l}\right)}{\partial x_i}\right] + \frac{\partial}{\partial\psi_\alpha}[\Omega_m(\psi_\alpha - \langle\phi_\alpha\rangle_L)P_L]\,, \tag{2.20}$$

where the SGS mixing frequency, $\Omega_m = C_\omega(\Gamma+\Gamma_t)/(\Delta_G^2\langle\rho\rangle_l$ is obtained from the molecular and SGS turbulent diffusivities and the filter length. Delarue and Pope [148] considered

pressure as one of the random variables in the PDF formulation while extending the RANS PDF method to compressible flows and solved a set of modeled stochastic equations for the joint velocity-frequency-energy-pressure PDF. In the scalar FMDF model here, the pressure is not directly included in the FMDF formulation, and only the effect of filtered pressure on the scalar FMDF is considered [73]. The last term on the RHS of equation (2.16) represents the effect of pressure and viscosity on the scalar. The part due to the temporal derivative of pressure is approximated as:

$$\left\langle \left(\frac{1}{\rho}\frac{\partial p}{\partial t}\right) \middle| \Psi \right\rangle_l P_L = \frac{1}{\langle\rho\rangle_l}\left(\frac{\partial\langle\rho\rangle_l}{\partial t}\right) P_L, \alpha \equiv N_{s+1} \tag{2.21}$$

The spatial derivative of the pressure term and the viscous dissipation term are decomposed into the resolved and SGS parts as:

$$\left\langle \left(\frac{1}{\rho}u_i\frac{\partial p}{\partial x_i}\right) \middle| \Psi \right\rangle_l P_L = \frac{1}{\langle\rho\rangle_l}\langle u_i\rangle_L \left(\frac{\partial\langle p\rangle_l}{\partial t}\right) P_L$$

$$+ \left(\left\langle \frac{1}{\rho}u_i\frac{\partial p}{\partial x_i} \middle| \Psi \right\rangle_l P_L - \frac{1}{\langle\rho\rangle_l}\langle u_i\rangle_L \frac{\partial\langle p\rangle_l}{\partial x_i} P_L \right), \alpha \equiv N_{s+1} \tag{2.22}$$

$$\left\langle \left(\frac{1}{\rho}\tau_{ij}\frac{\partial u_i}{\partial x_j}\right) \middle| \Psi \right\rangle_l P_L = \frac{1}{\langle\rho\rangle_l}\langle \tau_{ij}\rangle_L \left(\frac{\partial\langle u_i\rangle_L}{\partial x_j}\right) P_L$$

$$+ \left(\left\langle \frac{1}{\rho}\tau_{ij}\frac{\partial u_i}{\partial x_j} \middle| \Psi \right\rangle_l P_l - \frac{1}{\langle\rho\rangle_l}\langle \tau_{ij}\rangle_L \frac{\partial\langle u_i\rangle_l}{\partial x_j} P_L \right), \alpha \equiv N_{s+1} \tag{2.23}$$

There are three terms in the FMDF equation due to spray/droplets; the third term on the LHS of this equation is due to the mass addition of the evaporated gas and the last two

terms on the RHS are due to other droplet-gas interactions. These terms are approximated here as:

$$-\frac{\partial}{\partial\psi_\alpha}\left[\left\langle\frac{S_\alpha^{spy}}{\rho}\middle|\Psi\right\rangle_l P_L-\left\langle\frac{\psi_\alpha S_m}{\rho}\middle|\Psi\right\rangle_l P_L\right]+\frac{\langle S_m|\psi\rangle_l P_L}{\langle\rho\rangle_l}$$

$$=-\frac{\partial}{\partial\psi_\alpha}\left[\frac{\langle S_\alpha^{spy}\rangle_l P_L}{\langle\rho\rangle_l}-\frac{\psi_\alpha\langle S_m\rangle_l P_L}{\langle\rho\rangle_l}\right]+\frac{\langle S_m\rangle_l P_L}{\langle\rho\rangle_l} \tag{2.24}$$

The final form of the FMDF transport equation is obtained by inserting equations (2.18)-(2.24) into equation (2.16). The final form of the FMDF equation is:

$$\frac{\partial P_L}{\partial t}+\frac{\partial\left[\langle u_i\rangle_L P_L\right]}{\partial x_i}=\frac{\partial}{\partial x_i}\left[(\Gamma+\Gamma_t)\frac{\partial(P_L/\langle\rho\rangle_l)}{\partial x_i}\right]$$

$$+\frac{\partial}{\partial\psi_\alpha}\left[\Omega_m(\Psi_\alpha-\langle\psi_\alpha\rangle_L)P_L\right]$$

$$-\frac{\partial}{\partial\psi_\alpha}\left[\frac{S_\alpha^{rea}P_L}{\langle\rho\rangle_l}\right]-\frac{\partial}{\partial\psi_\alpha}\left[\frac{\tilde{S}_\alpha^{cmp}P_L}{\langle\rho\rangle_l}\right]$$

$$-\frac{\partial}{\partial\psi_\alpha}\left[\frac{\langle S_\alpha^{spy}\rangle_l P_L}{\langle\rho\rangle_l}-\frac{\Psi_\alpha\langle S_m\rangle_l P_L}{\langle\rho\rangle_l}\right]+\frac{\langle S_m\rangle_l P_L}{\langle\rho\rangle_l} \tag{2.25}$$

where

$$S_\alpha^{rea}=\langle\rho\rangle_l\dot{\omega}_\alpha,\ \tilde{S}_\alpha^{cmp}=0,\ \langle S_\alpha^{spy}\rangle_l=\langle S_m\rangle_l$$

for $\alpha\equiv 1,...,N_s$

and

$$S_\alpha^{rea} = \langle\rho\rangle_l \dot{Q},\ \tilde{S}_\alpha^{cmp} = \frac{\partial\langle p\rangle_l}{\partial t} + \langle u_i\rangle_L \frac{\partial\langle p\rangle_l}{\partial x_i} + \langle\tau_{ij}\rangle_L \frac{\partial\langle u_i\rangle_L}{\partial x_j},$$

$$\langle S_\alpha^{spy}\rangle_l = \langle S_h\rangle_l\,,$$

for $\alpha \equiv N_s + 1$.

$S_\alpha^{rea} = \langle\rho\rangle_l \dot{\omega}_\alpha$ is the source term for species α due to reaction, $S_\alpha^{spy} = S_m$ is the production of species α due to droplet evaporation. For $\alpha \equiv N_s + 1$, $S_\alpha^{rea} = \langle\rho\rangle_l \dot{Q}$ is the heat of combustion, $\tilde{S}_\alpha^{cmp}$ is the source term due to compressibility effect, $S_\alpha^{spy} = S_h$ is the source term due to phase change or evaporation.

2.3.4 Lagrangian fuel droplets

The following Lagrangian equations describe the transient position (X_i) and velocity (V_i) of the droplets:

$$\frac{dX_i}{dt} = V_i \tag{2.26}$$

$$\frac{dV_i}{dt} = \frac{F_i}{m_d} = \frac{f_1}{\tau_d}(\tilde{u}_i - v_i) \tag{2.27}$$

The change in mass and temperature of the droplet is calculated via a finite-rate multicomponent evaporation model, the details of which can be found in Ref. [160] and in Chapter 1 of this dissertation. The spray source terms for the two-way coupling between the liquid and gas phases are presented in Ref [34]. Various spray sub-models used for these simulations have been implemented in our previous works [[34],[163]] and validated against experimental data. These models include the "blob" model for primary atomization, the Kelvin-Helmholtz - Rayleigh-Taylor (KH-RT) model for secondary breakup, the dynamic

drag model, and the finite-rate multicomponent heat and mass transfer models.

2.3.5 Numerical Solution Procedure

The three components of the LES/FMDF model interact with each other in a consistent manner. The carrier gas velocity and pressure fields and the spray source terms, which are not known in the FMDF transport equation (Eq. 2.16), are obtained by solving Eq. (2.1) using Finite Difference (FD) methods, and the spray droplet equations with a Lagrangian method, respectively. Once these terms are known, the FMDF is obtained by solving Eq. (2.16) with its corresponding Fokker-Planck equation using a Lagrangian Monte Carlo (MC) procedure [149]. In this procedure, each MC particle undergoes motion on physical space due to filtered velocity and molecular and subgrid diffusivities. The particle motion effectively represents the spatial transport of the FMDF and is modeled by the following stochastic differential equation (SDE) [150]:

$$dX_i^+ = \left[\langle u_i\rangle_L + \frac{1}{\langle\rho\rangle_l}\frac{\partial(\Gamma+\Gamma_t)}{\partial x_i}\right]dt + \left[\sqrt{\frac{2(\Gamma+\Gamma_t)}{\langle\rho\rangle_l}}\right]dW_i(t) \tag{2.28}$$

where W_i denotes the Wiener process. The compositional value of each particle is changed due to mixing, reaction, droplet evaporation, viscous dissipation and pressure variations in time and space. The change in composition is described by the following SDEs:

$$d\phi_\alpha^+ = -\Omega_m(\phi_\alpha^+ - \langle\phi_\alpha\rangle_L)dt + \frac{1}{\langle\rho\rangle_l}\left[S_\alpha^{rea} + \tilde{S}_\alpha^{cmp} + \langle S_\alpha^{spy}\rangle_l - \phi_\alpha^+\langle S_m\rangle_l\right]dt, \alpha \equiv 1, ..., N_s+1 \tag{2.29}$$

The combined processes described by Equations (2.28) and (2.29) have a corresponding

Fokker-Planck equation identical to the FMDF transport equation. The spray terms in the FMDF equation are weight-averaged from the FD grid points to the MC particle locations. Compressibility effects are included in the FMDF formulation by interpolating the $\tilde{S}_{\alpha}^{cmp}$ terms calculated from Eulerian grid points and by adding them to the corresponding MC particles. In order to manage the number of MC particles and to reduce the computational cost, nonuniform weights are used. This allows a smaller number of particles in regions with a low degree of variations and larger number of particles in high-variation regions. This also maintains the particle number density above a set threshold, regardless of the density variations. The Favre-filtered values of any variable at a given point are calculated by weight-averaging the MC particles over a box of size Δ_E centered at the point of interest [121]. The sum of weights within the ensemble averaging domain, Δ_E, is related to the filtered fluid density as ([121], [149]):

$$\langle \rho \rangle_l \approx \frac{\Delta m}{V_E} \sum_{n \in \Delta_E} w^{(n)}, \tag{2.30}$$

where V_E is the volume of the domain and Δ_m is the mass of a MC particle with a unit weight. The particle weights are also modified in the case of spray simulations to allow for the mass added to the carrier gas by the evaporating droplets. The particle weights are adjusted as:

$$dw^{(n)} = \frac{V_E}{\Delta m} \langle S_m \rangle_l dt \tag{2.31}$$

The Favre-filtered value of any scalar function $Q(\phi)$ is obtained as:

$$\langle Q \rangle_L \approx \frac{\sum_{n \in \Delta_E} w^{(n)} Q(\phi)}{\sum_{n \in \Delta_E} w^{(n)}} \tag{2.32}$$

The filtered Eulerian carrier gas equations are solved using the fourth order compact FD scheme [151] and the low storage Runge-Kutta method. For moving boundaries, the grids are moved to their new locations based on the piston/valve-lift profiles at each time step, and the grid speed vector, Jacoboians and metrics are then calculated based on the new grid locations. The computational grid is multi-block and structured and a highly efficient, parallel code using the MPI library is used for the calculations. Other details of the solution procedure are presented in Ref [34]. An important feature of the hybrid LES/FMDF methodology is that the filtered values of various variables like temperature and species mass fractions are obtained from both the LES-FD and FMDF-MC components and their consistency can be used as the basis for the numerical accuracy of both the solvers. To achieve this for reacting flows, the chemical source terms, needed in FD equations, which are closed in the FMDF formulation, are calculated from the MC particles.

2.4 Results and Discussions

The two-phase LES/FMDF model has recently been applied to a Rapid Compression Machine (RCM) with both creviced and non-creviced pistons [153]. RCMs are piston cylinder assemblies used for fundamental studies of chemical kinetics and combustion of fuels at different temperatures and pressures and ideally should be homogeneous, thus allowing zero-dimensional study of combustion. However, fluid dynamics and heat transfer effects generally make the flow conditions inhomogeneous, thus necessitating the use of CFD simulations to understand the causes and effects of the non-homogeneities. While most previous CFD studies of RCMs ([154]-[159]) had used traditional RANS models, Banaeizadeh [153] utilized the hybrid LES/FMDF method to conduct numerical simulations of non-reacting and reacting

turbulent flows for the Michigan State University (MSU) RCM [160]. The simulations were carried out for both flat and creviced pistons, with compression ratios of 21 and 17.147, respectively. The wall conditions were considered to be isothermal, with the wall temperature fixed to the initial temperature of the working fluid, which is pure Nitrogen. In a previous study by Banaeizadeh et al. [138], RCM simulations were carried out with adiabatic wall conditions. The grid for the RCM consisted of a rectangular H-H block with grid density 250 x 13 x 13 in the center to avoid singularity at the centerline, surrounded by an O-H grid with grid density 250 x 45 x 42, with additional blocks for the creviced piston. Significant differences exist between the flow fields generated by the two piston shapes; the flat piston generates a large 3D vortical structure in front of the piston, this flow structure is absent in the creviced piston case. The temperature distribution is also different, with the creviced piston having a more uniform temperature as compared to the non-uniform distribution in the flat piston case with a warmer region in-between the cold cylinder core and cold region near the cylinder wall. The LES/FMDF results for both piston shapes were compared with experimental results provided in Mittal et al. [157]. The in-cylinder temperature obtained by LES/FMDF along a radial line matched well with the experimental results for the creviced piston. The temperatures in the cold flow regions for the flat piston were under-predicted which was explained to be due to the use of isothermal wall boundary conditions. Single-phase reactive flow was also simulated using the LES/FMDF methodology, with an initial mixture of evaporated ethanol having an equivalence ratio of 0.5. The volume averaged pressure trace matched well with the experimental results during compression and before ignition, but the ignition delay was not captured well due to the use of the simplified 1-step global reaction for this study. The LES-FD and FMDF-MC components matched well before and after the auto-ignition, establishing the validity and numerical accuracy of the hybrid

LES/FMDF methodology.

In the present study, the two-phase LES/FMDF model is applied to two new configurations. In the first configuration, the single piston RCM case has been extended to a twin-piston RCM and simulations have been carried out to study the effect of different stroke ratios for the two pistons on the flow evolution. The LES/FMDF methodology has also been applied to an opposed-piston engine configuration which is described in Chapter 3. The double piston RCM has been studied as a precursor to the study of the opposed piston two-stroke engine. The flow and temperature fields in the double piston RCM are relatively simpler than those in the opposed piston engine, but as shown below they are still physically interesting and complex.

2.4.1 Double-Piston Rapid Compression Machine

Two different types of double piston RCM have been studied: one is symmetric and has equal strokes for both the pistons and the other is asymmetric, with different stoke lengths for the two pistons. Double piston RCMs have been considered in previous studies ([161], [162]). Wurmel et al. [156] studied the evolution of the flow and temperature fields in the Shell Thornton RCM [161] by two-dimensional CFD method and concluded that the creation of corner vortices in front of the flat piston results in a non-uniform temperature field, but can be suppressed by using creviced pistons.

The symmetric double piston RCM studied here is based on the dimensions of the MSU's RCM, with the same overall compression ratio and bore, but with two pistons: one having the same motion profile as the original RCM, the other having the same piston motion profile as the first piston, but in the opposite direction. Thus, the stationary wall for the single piston RCM becomes the fluid centerline of the double piston RCM. A representation of the

Dimension/Operating Parameter	Value
Bore	50 mm
Left Piston Stroke	254 mm
Right Piston Stroke	254 mm
Compression Ratio	21:1
Wall Boundary Condition	Isothermal, 297 K

Table 2.1: Dimensions and operating parameters of the symmetric double piston RCM

single piston RCM and the double piston symmetric RCM is given in Figure 2.1. The grid size and structure are similar to the simulations for the single piston RCM in Ref [153].

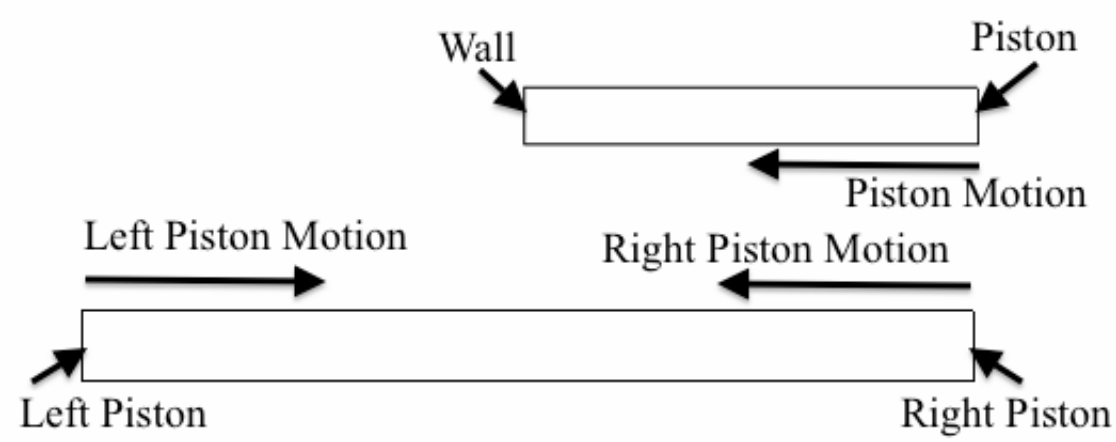

Figure 2.1: Schematic of the single piston and the double piston symmetric RCM

The dimensions and operating parameters of the symmetric double piston are given in Table 2.1.

Figures 2.2(a) and 2.2(b) show the iso-contours of temperature for the RCM at t=25 ms and t=26 ms, respectively, and and the the 3D colder recirculating zones can be clearly seen. Figure 2.3 shows various stages in the evolution of temperature and velocity fields of the symmetric double piston RCM. The simulation starts at the Bottom Dead Center (BDC) at time t=0 and the Top Dead Centre (TDC) is reached at t = 27 ms. Figure 2.3(a) shows the velocity vectors and temperature contours at t=15 ms. As the pistons accelerate towards the TDC, boundary layers start developing near the walls. The gas in the boundary

layer is cool as the cylinder and piston walls are maintained isothermally at 297 K, but mixes with the warmer central regions of the cylinder by the radial velocity component of the fluid velocity developed close to the wall. This creates a circulation in the temperature field and the generation of vortical structures near the corners, in front of the pistons. These vortical structures, which are nearly symmetrical with respect to the axis of the cylinder, are clearly shown in Figure 2.3(a). As the pistons move closer, the circulation zones grow bigger in size and the zones from opposite corners of the same piston start merging Figure 2.3(b). The temperature gradient between the circulation zones and the central regions also increases. The flows generated by the two pistons reach the central region of the cylinder, with a stagnation region between them. Further motion of the pistons pushes the circulation zones from the opposite corners of the same piston to completely merge as seen in Figure 2.3(c). By time t=26 ms, as observed in Figure 2.3(d), large portions of the central region of the RCM is filled by the colder fluids transported from the recirculation zones but there is still a small central core with warmer stagnant fluid. The stagnation region in the center of the cylinder, seen clearly in enlarged views of the velocity vectors in Figure 2.4, prevents the colder recirculation zones from the opposite pistons to merge completely. Figures 2.4(a), 2.4(b) and 2.4(c) are enlarged views of velocity vectors corresponding to Figures 2.3(b), 2.3(c), and 2.3(d), respectively.

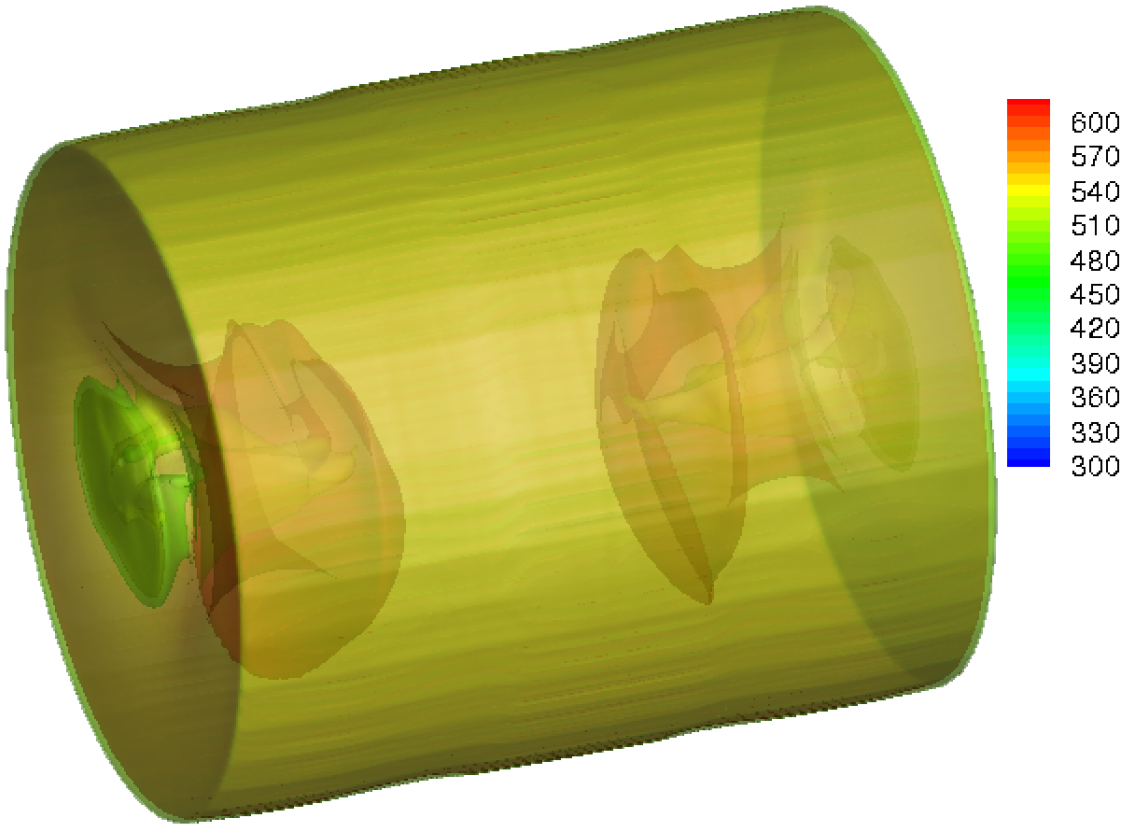

(a)

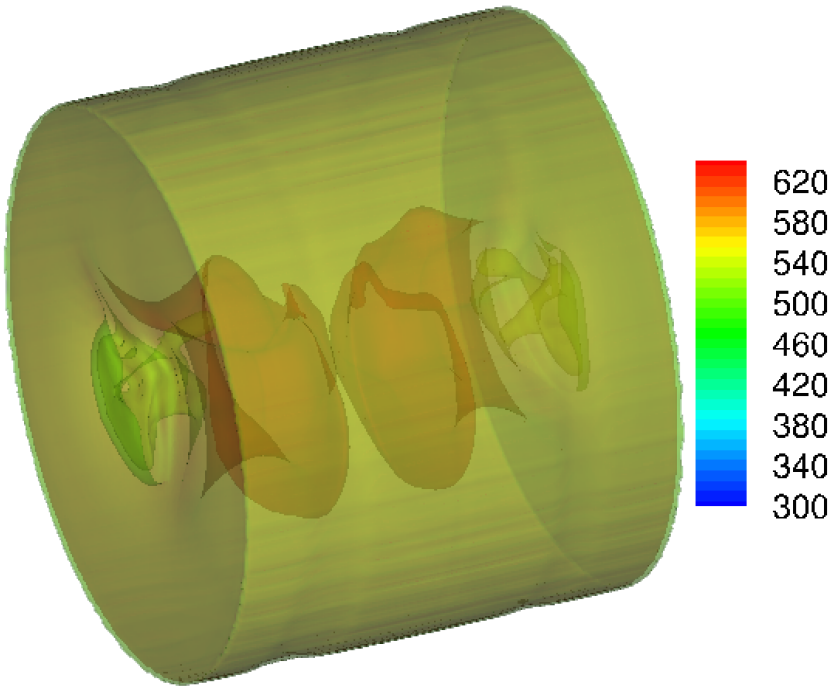

(b)

Figure 2.2: Iso-contours of temperature for the symmetric double piston RCM, (a) t=25 ms, (b) t=26 ms.

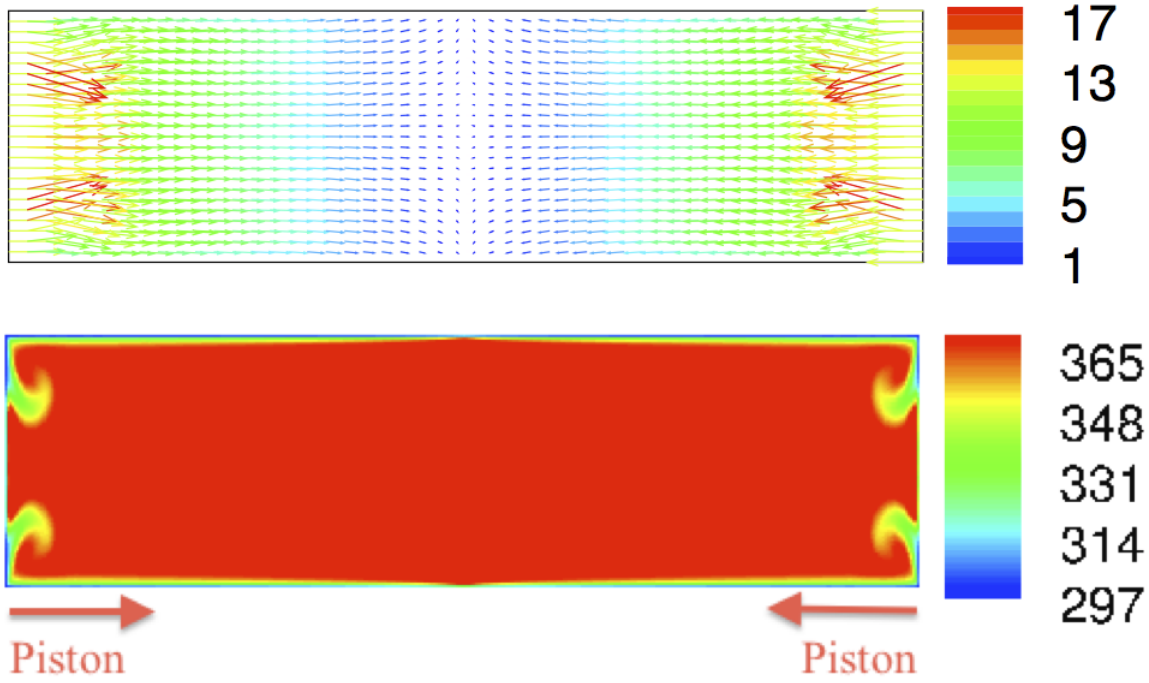

(a)

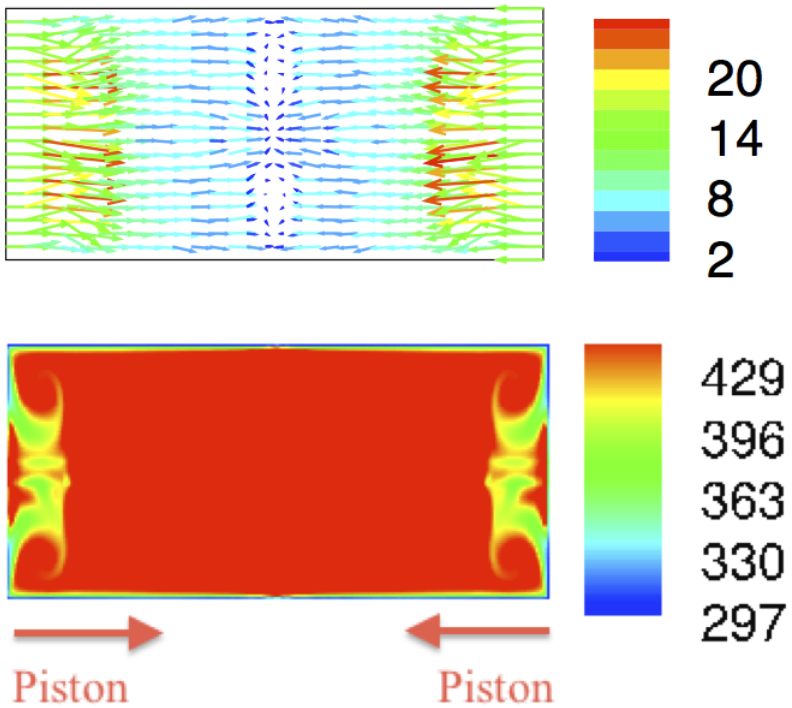

(b)

Figure 2.3: Velocity vectors and temperature contours at the center plane Z=0 for the symmetric double piston RCM at (a) time = 15 ms, (a) time = 20 ms, (c) time = 25 ms, and (d) time = 26 ms.

Figure 2.3: (cont'd)

(c)

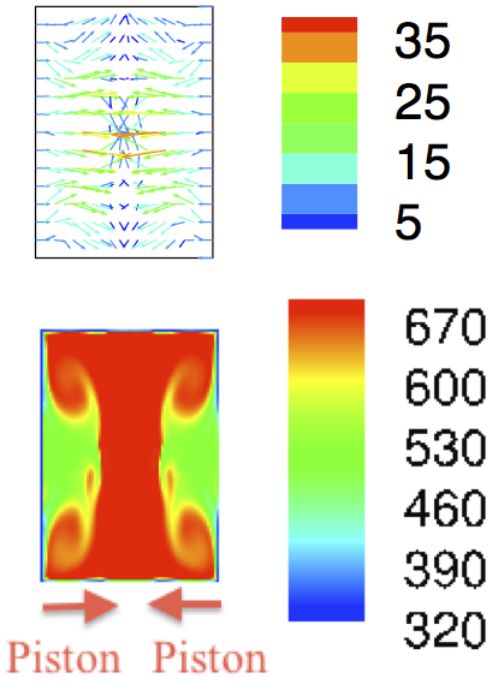

(d)

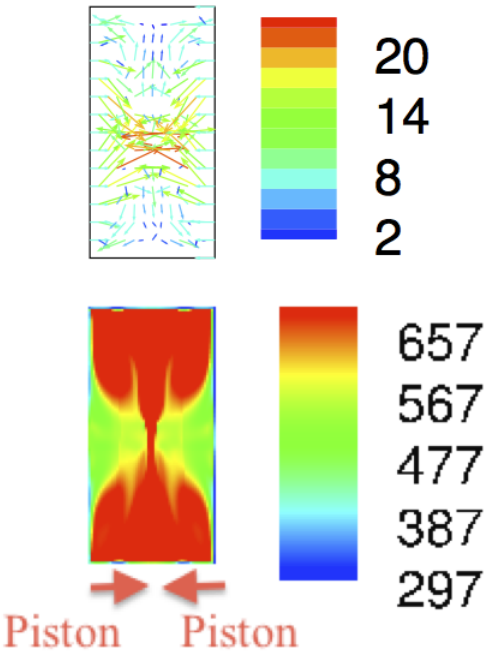

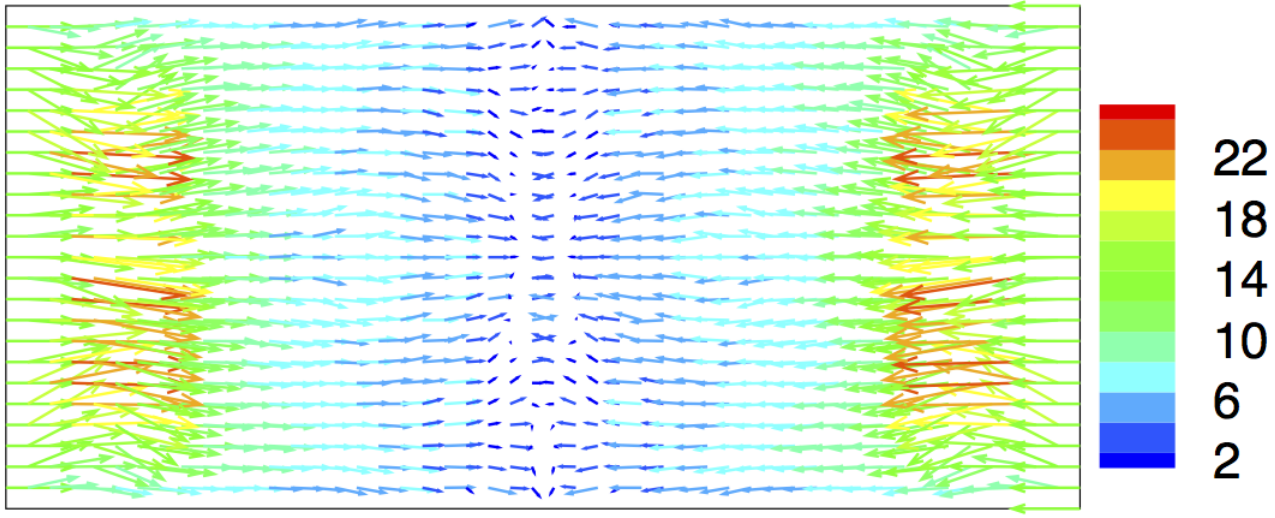

(a)

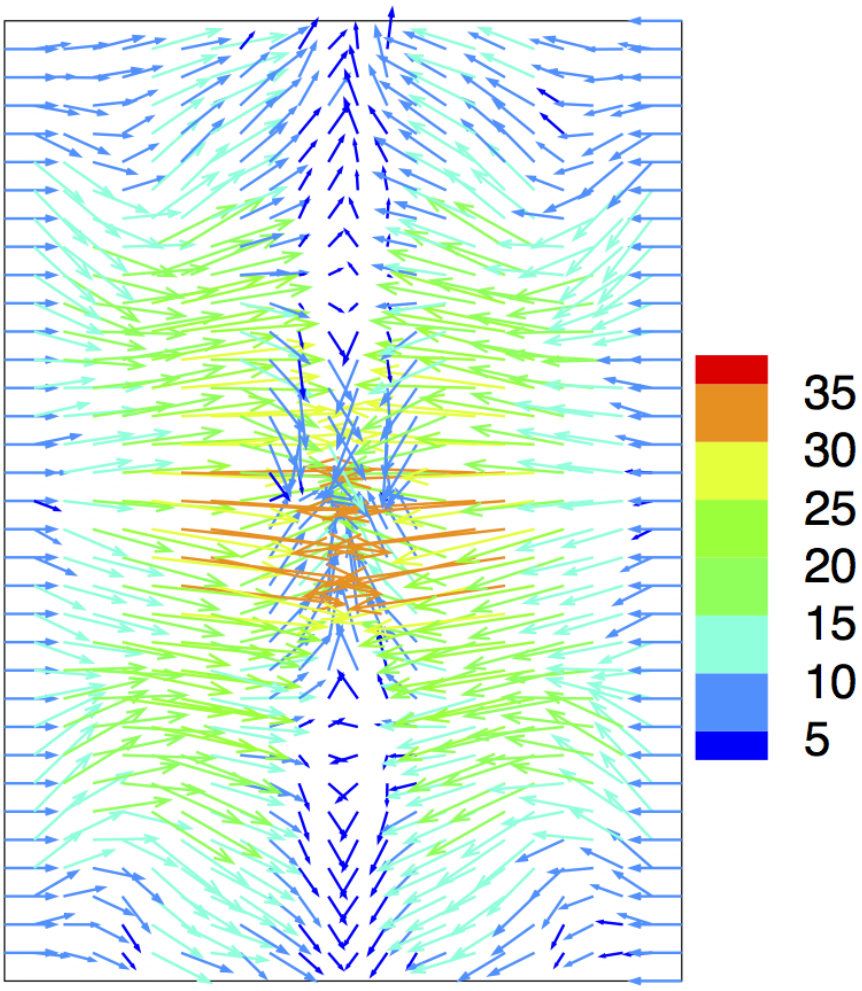

(b)

Figure 2.4: Enlarged views of the velocity vectors at the center plane Z=0 for the symmetric double piston RCM (a) time = 20 ms, (b) time = 25 ms, and (c) time = 26 ms.

Figure 2.4: (cont'd)

(c)

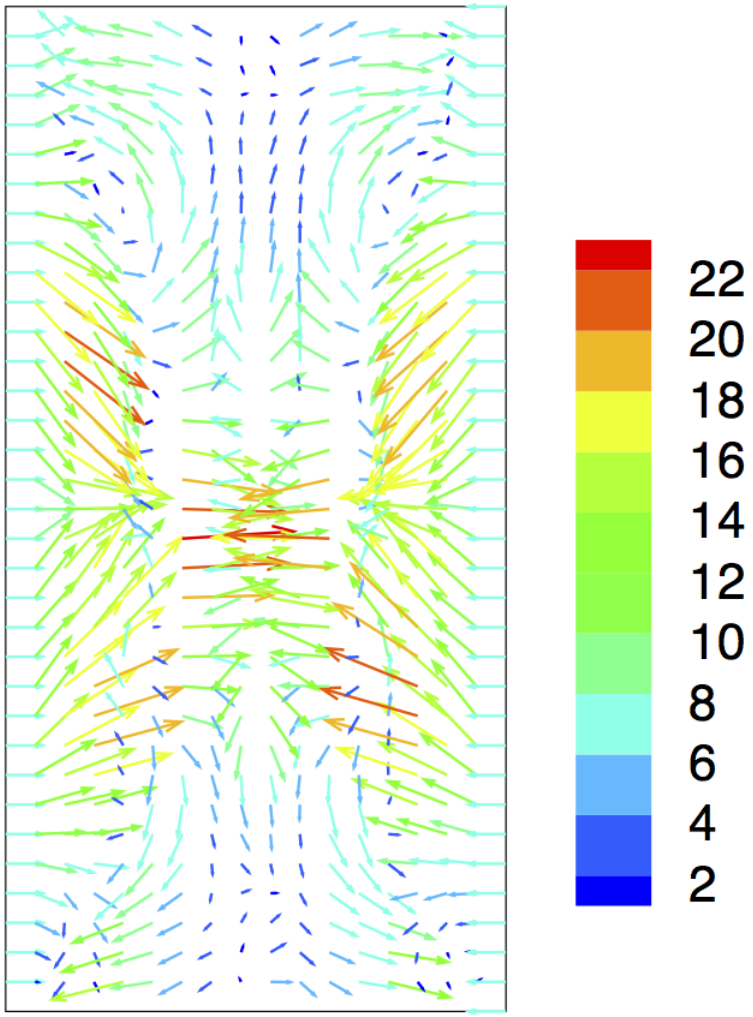

Dimension/Operating Parameter	Value
Bore	50 mm
Left Piston Stroke	35 mm
Right Piston Stroke	45 mm
Compression Ratio	17:1
RPM	2100, 3500
Wall Boundary Condition	Isothermal, 297 K

Table 2.2: Dimensions and operating parameters of the asymmetric double piston RCM

2.4.2 Double piston RCM with unequal strokes

Simulations have also been conducted for a double piston RCM with unequal strokes. The purpose of these simulations is not only to understand the effect unequal strokes can have on the performance of the double piston RCM, but also as a preliminary step in simulating an opposed-piston two-stroke engine (Chapter 3). The opposed piston engine has unequal strokes for the intake and exhaust sides, with the exhaust side having a smaller stroke and the intake side with a larger stroke. The two pistons are also out of phase, with the exhaust piston slightly advanced than the intake side. The asymmetric double piston RCM studied here has the same bore to stroke ratios and compression ratio as the opposed piston engine, but the bore itself is smaller (nearly half of the opposed piston engine bore). The details of the operating parameters of the RCM are given in Table 2.2.

The strokes of the asymmetric double piston RCM are much smaller than the symmetric one and the RPM is also high. The piston can thus complete one complete cycle (from BDC to TDC and back to BDC) in 28.57 ms for RPM 2100 and 17.14 ms for RPM 3500. The bore-to-stroke ratios of the asymmetric RCM (1.43 for the left piston and 1.11 for the right piston) are much larger than those for the symmetric RCM (0.197 for both the pistons). This difference can have a significant impact on the evolution of the flow in the RCM. Figures 2.5

and 2.6 show the temperature contours at different crank angles for the asymmetric double piston RCM for rpms of 2100 and 3500, respectively. Figures 2.5(a) and 2.6(a) show the temperature contours at a crank angle of 120 degrees. The recirculation zones present in the symmetric double piston RCM are much smaller in size in the simulated asymmetric RCM at this crank angle. As the left piston reaches its TDC at CA 169.8 (Figures 2.5(b) and 2.6(b)), the temperature distribution in the core of the cylinder is still uniform. The minimum clearance between the pistons is reached at CA 183.6 (Figures 2.5(b) and 2.6(b)) and the right piston reaches its TDC at CA 191.2 (Figures 2.5(c) and 2.6(c)). The colder zones from opposite corners of same piston merge, but a uniform temperature distribution is maintained at the core of the cylinder. The distance traversed by the pistons and the time taken is much lower in the simulated asymmetric RCM compared to the symmetric RCM, and although the radial velocity components are higher due to higher rpm, the recirculation zones do not have enough time to grow and merge. Thus, overall the asymmetric pistons generate a uniform core temperature. As both pistons start receding back, the uniform temperature zone in the cylinder core enlarges, however the overall temperature distribution does not reach a uniform state, as seen in Figures 2.5(c), 2.5(d), 2.6(c) and 2.6(d). The thickness and size of the colder recirculating zones is relatively higher in the RCM with 2100 rpm as compared to that with rpm 3500. This is due to the relatively higher time available for the recirculating zones to develop in the 2100 rpm case.

The study of the flow evolution for the symmetric and asymmetric double piston RCM provides the groundwork for the development of a better understanding of the flow in the opposed piston two-stroke engine, which is the focus of the next Chapter.

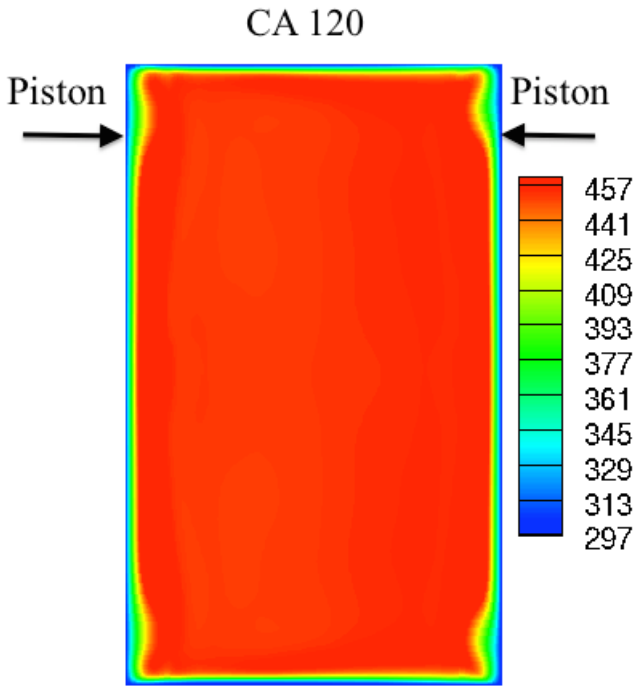

(a)

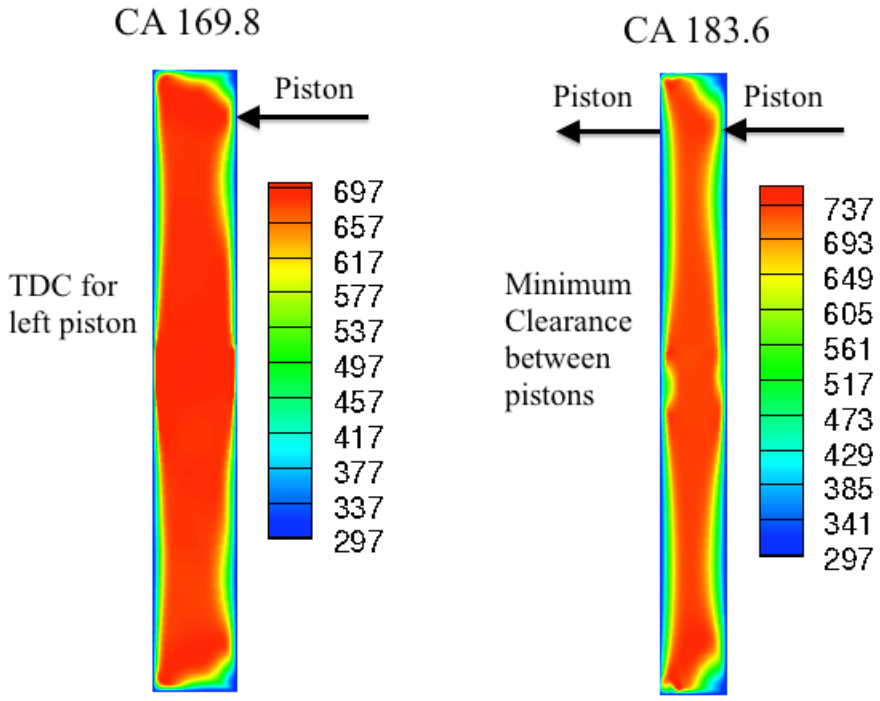

(b)

Figure 2.5: Temperature contours at the center plane Z=0 for the unequal stroke double piston RCM for rpm 2100 at (a) CA 120, (b) CA 169.8 and 183.6, (c) CA 191.2 and 210, and (d) CA 240.

Figure 2.5: (cont'd)

(c)

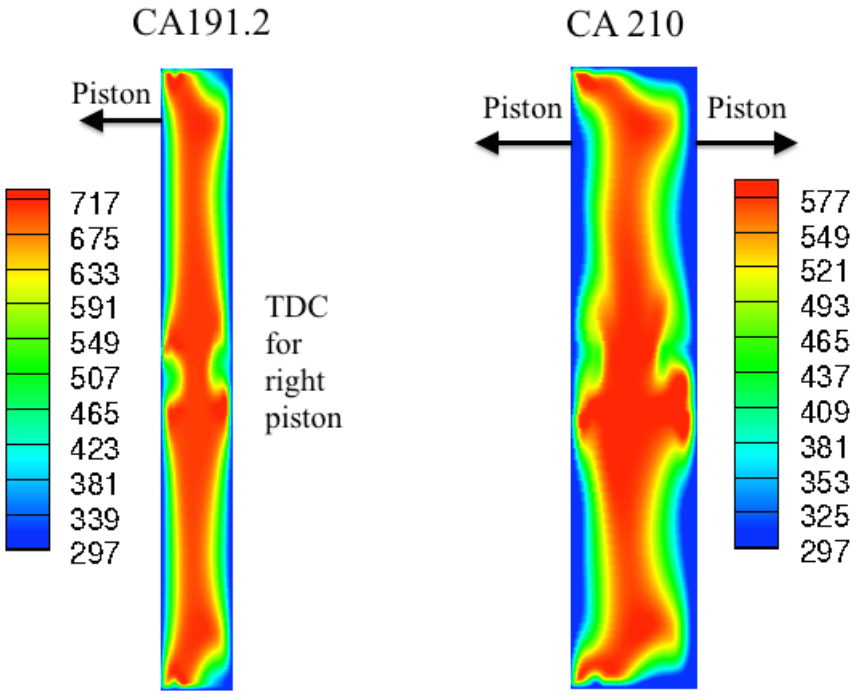

(d)

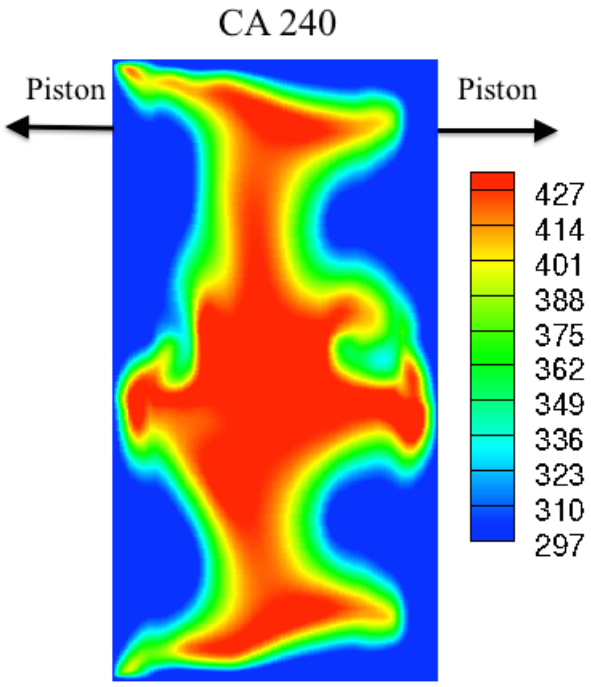

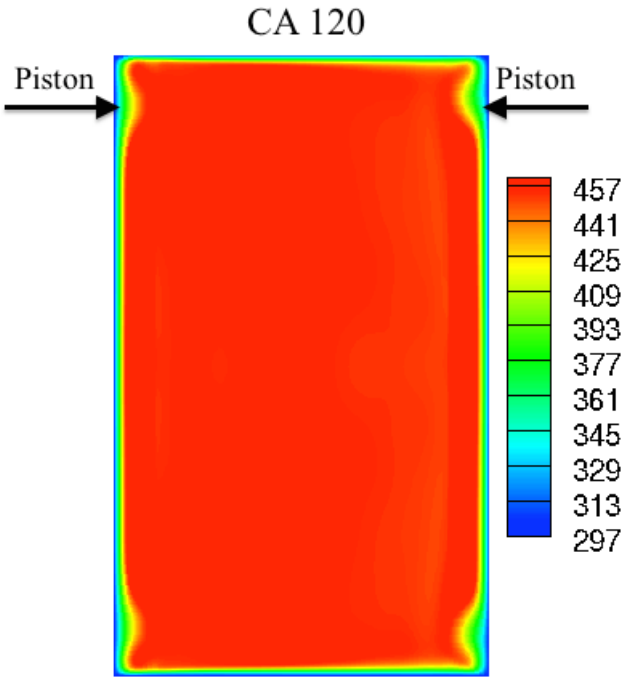

(a)

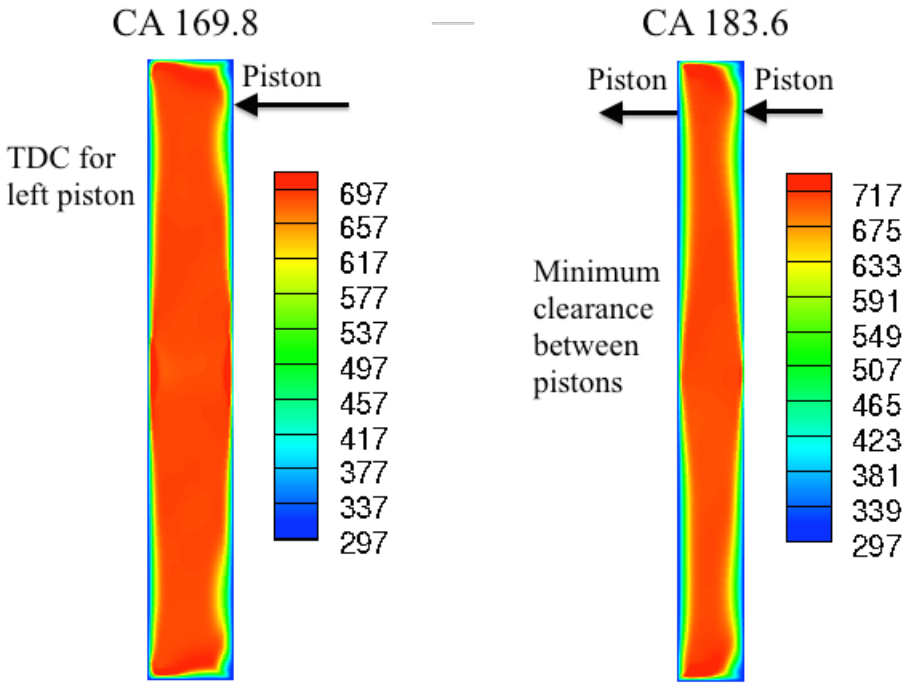

(b)

Figure 2.6: Temperature contours at the center plane Z=0 for the unequal stroke double piston RCM for rpm 3500 at (a) CA 120, (b) CA 169.8 and 183.6, (c) CA 191.2 and 210, and (d) CA 240.

Figure 2.6: (cont'd)

(c)

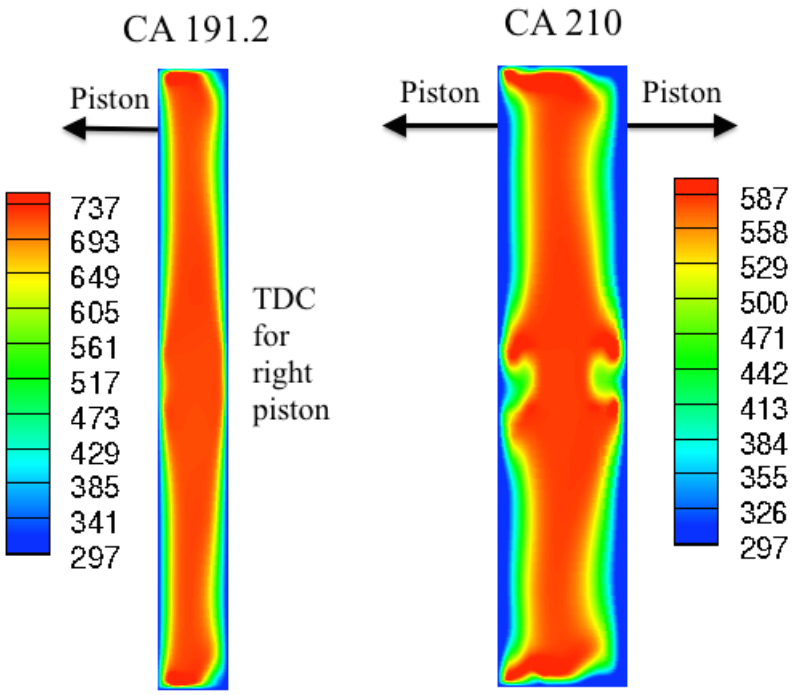

(d)

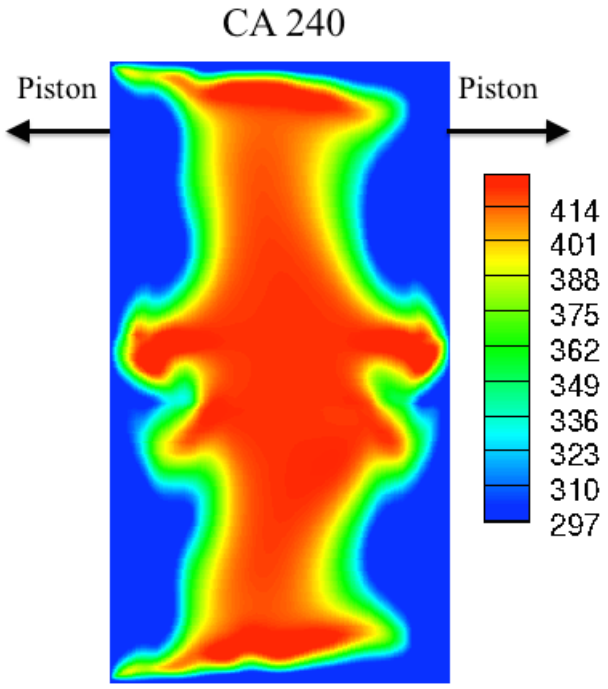

Chapter 3

LES/FMDF of Turbulent Flows and Spray Combustion in an Opposed-Piston Two-Stroke Engine

3.1 Introduction

Opposed-piston two stroke engines have recently generated some interest in industry due to their high power density and fuel economy. The opposed piston configuration is mechanically simpler compared to conventional four-stroke engines but flow scavenging is critically important in these engines. The flow in these engines is unsteady, turbulent and highly variable from one cycle to the other, suggesting that it can be much better predicted by LES. Traditionally, IC engine flows have been simulated with the RANS models, which provide information on the mean flow features, but the transient features and the large-scale vortical structures are lost due to averaging. The ability of LES models to capture these features has been recognized and various studies based on LES are now available in the literature (see Banaeizadeh et al. [34] for a brief review). Opposed-piston engines have a piston on both ends of the cylinder, with no cylinder head. These engines have been available for several decades with the most famous engine being the Junkers Jumo 205 diesel aviation engine

in the 1930s, and are still used today in marine diesel engines. Two-stroke opposed-piston engines have many thermodynamic advantages [164] including a high power density and high efficiency, with the additional advantage of simpler mechanical systems due to the absence of valve-trains and supporting mechanisms. The engine speed and effective stroke is higher as compared to four-stroke engines, with the same scavenging efficiency. Uniflow scavenging is employed in these engines, which means that the gas at the intake end of the cylinder replaces the exhaust gas at the other end of the cylinder. For proper operation of the engine, this scavenging process requires optimization and has been the subject of many numerical investigations. One of the first computational study of the scavenging process for two-stroke opposed-piston engines was carried out by Zhu et al. [165] using KIVA3, a code developed at Los Alamos National Laboratory. The effect of three operating and geometrical parameters namely the inclination angle of the intake ports, the stroke-to-bore ratio and the exhaust port time-area on the scavenging process was studied. The study emphasized the importance of these parameters on the scavenging and the hydrodynamics of the engines. They found that for engines with small bore to stroke ratios, the scavenging efficiency can be sufficiently improved by increasing the intake port inclined angle as the recirculation zones at the cylinder walls become smaller in size. The study was instrumental in asserting the important role of numerical simulations in engine design. A detailed description of the opposed-piston opposed-cylinder (OPOC) concept has been given in Hofbauer [166]. Several simulation tools were used in this study to optimize packaging, performance, kinematics and scavenging and the potential of the opoc concept was demonstrated. Franke et al. [167] carried out an optimization study of the combustion system layout using the commercial software STAR-CD, with the combustion modeling performed by the ECFM 3Z model. The dual side injection configuration was studied and it was found that this configuration poses several

challenges compared to the central injection configuration. Kalkstein et al. [168] carried out 1D simulations, using the commercially available tool GT-Power, and 3D simulations using STAR-CD, of the gas-exchange process interactively for optimization of the design parameters and fine-tuning of the intake/exhaust port heights. They found that a larger port height increases the scavenging efficiency due to the larger overlap between the intake and exhaust port opening timings, but also leads to a higher loss of fresh charge. A shorter port length, on the other hand, results in almost no fresh charge loss and increases the effective compression ratio, but decreases the scavenging efficiency. Venugopal et al. [169] compared experimental and numerical results for the effects of the injection pattern on piston thermal management for an Opposed-Piston, Two-Stroke (OP2S) diesel engine with special emphasis on the analysis of piston hot-spots. The commercial software CONVERGE was utilized to conduct simulations of different injection patterns characterized by two parameters, viz. the injector clocking angle and the injector spray angle. The injector clocking angle determines the circumferential rotation of the injector while the injection spray angle is the angle between the injector axis and the spray plumes. The RNG $k-\epsilon$ turbulence was employed but the intake and exhaust ports were not simulated, and only the closed cycle calculation was carried out. It was found that both the clocking angle and the spray angle could have a significant impact on piston temperatures. All of the computational studies mentioned have used RANS models with conventional or modified combustion models. But as argued before, the flow in opposed-piston two-stroke engines is expected to be much better predicted by LES models. A potent method for the LES of turbulent spray combustion is the two-phase FMDF ([34], [153]), which is an extension of the single-phase SGS FMDF model [121] to two-phase flows. FMDF represents the joint PDF of the SGS variables. An important feature of the FMDF formulation is that the reaction term appears in a closed form, making it suitable

for various types of reacting flows. In this chapter, LES of turbulent spray combustion in a generic single cylinder, opposed-piston, two-stroke engine configuration has been conducted with the two-phase filtered mass density function (FMDF) model developed at Michigan State University. The LES/FMDF is implemented via an efficient, hybrid numerical method in which the filtered compressible Navier-Stokes equations in curvilinear coordinate systems are solved with a high-order, multi-block, compact differencing scheme, and the spray and FMDF are implemented with stochastic Lagrangian methods. The effects of various geometric parameters, operating conditions and spray parameters on the flow evolution, turbulence, spray and combustion in the engine are studied. The LES/FMDF methodology has been described in details in Chapter 2 of this dissertation and is applied here to a generic single cylinder, opposed-piston, two-stroke engine.

3.2 Description of Engine Parameters and Computational Model

In the present study, the two-phase LES/FMDF model has been applied to an opposed piston two-stroke engine. The two-stroke engine considered here has two flat pistons, with unequal intake and exhaust strokes, the exhaust stroke being longer. The exhaust side has 12 equally spaced, equally sized ports. The 12 ports on the intake side have different sizes with varying gaps between them. In opposed piston engines, the port width and the gaps between the ports are controlled by the mechanical strength of the liner and the stiffness of the piston rings. In the engine studied here the length, viz. the dimension of the ports in the direction of movement of the piston, is higher for the exhaust ports as compared to the intake ports, while the circumferential width of the intake ports is higher. The exhaust side piston

Parameter	Value/Description
Bore/Intake Stroke Ratio	1.11
Bore/Exhaust Stroke Ratio	1.43
Compression Ratio	17:1
RPM	2000, 2800, 3500
Boost Pressure	1.18, 2.18
Intake Port Angle	7.5°, 15°
Wall Heat Transfer	Adiabatic, Heat Transfer

Table 3.1: Two Stroke Opposed Piston Engine Parameters

reaches the Top Dead Center (TDC) before the intake side piston and is advanced by a few crank angle degrees. The advance of the exhaust side piston and the longer exhaust ports lead to these ports opening before the intake ports, near the Bottom Dead Center (BDC). This leads to efficient "uniflow" scavenging, generating a highly unsteady, turbulent flow. This type of scavenging utilizes the maximum possible area of the cylinder for scavenging as compared to other types of scavenging and gives the optimum scavenging efficiency at any scavenging ratio. Uniflow scavenging is the most efficient method of scavenging for engines with large bore to stroke ratios but optimizing the scavenging process is more difficult than loop or cross scavenging.

Some of the operating and geometric parameters of the opposed piston configuration considered in this study are given in Table 3.1. Figure 3.1 shows the motion profiles of the two pistons.

3.2.1 Computational Domain and Mesh

The computational domain shown in Figure 3.2(a) is a block-structured grid with nearly 2.9 million grid points. The grid is divided into 72 blocks with 48 blocks representing the cylinder and 1 block for each port. An efficient parallel algorithm based on the MPI library

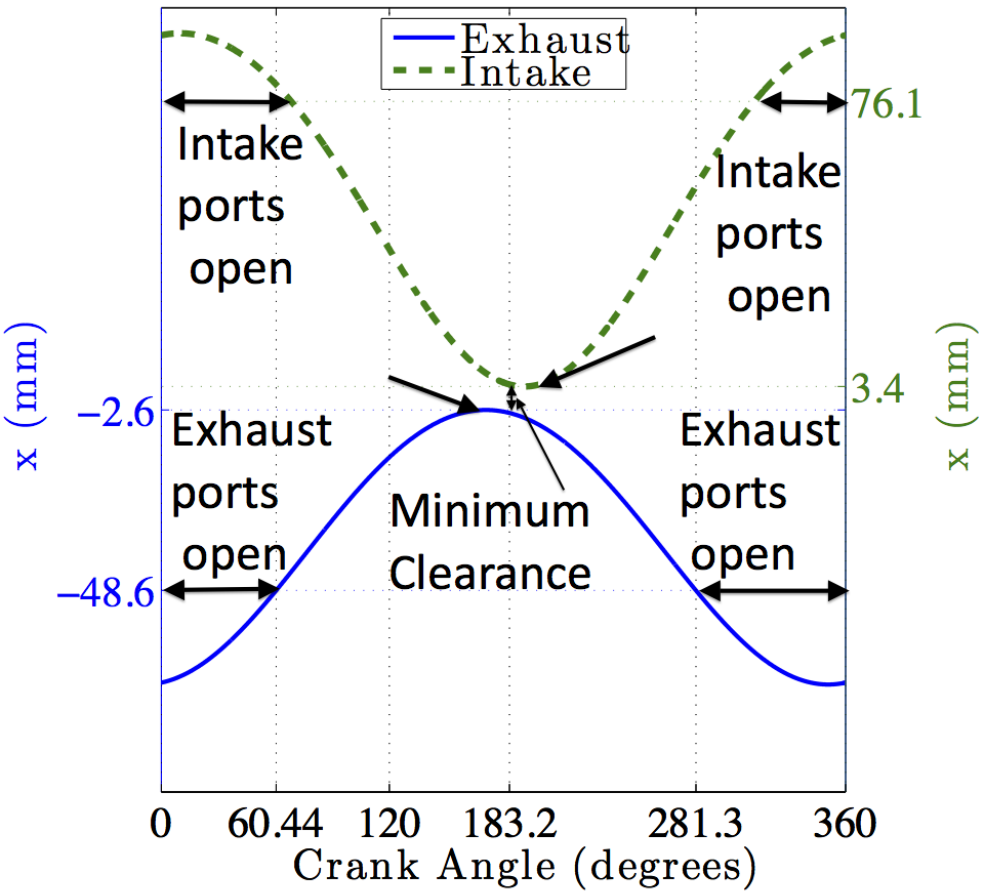

Figure 3.1: Piston profiles for the intake and exhaust ports. The pistons have different TDC and the exhaust piston reaches its TDC earlier than the intake piston.

is used to carry out the computations on the block-structured grid. Different processors carry out the numerical calculations for each block and the results are communicated across the common boundaries in an efficient manner. The movement of the pistons results in the opening and closing of the ports and the overlap regions between the cylinders and the ports do not remain aligned at all times. This requires some interpolation between the cylinder and port blocks, which is carried out here by the method of bilinear interpolation. Figures 3.2(b) and 3.2(c) show 2D cross sections of the mesh. The grid size varies from 0.1 mm to 1.5 mm, with grid compression near the walls. The cylinder grids are compressed/expanded

due to the motion of the pistons with the number of grids remaining constant.

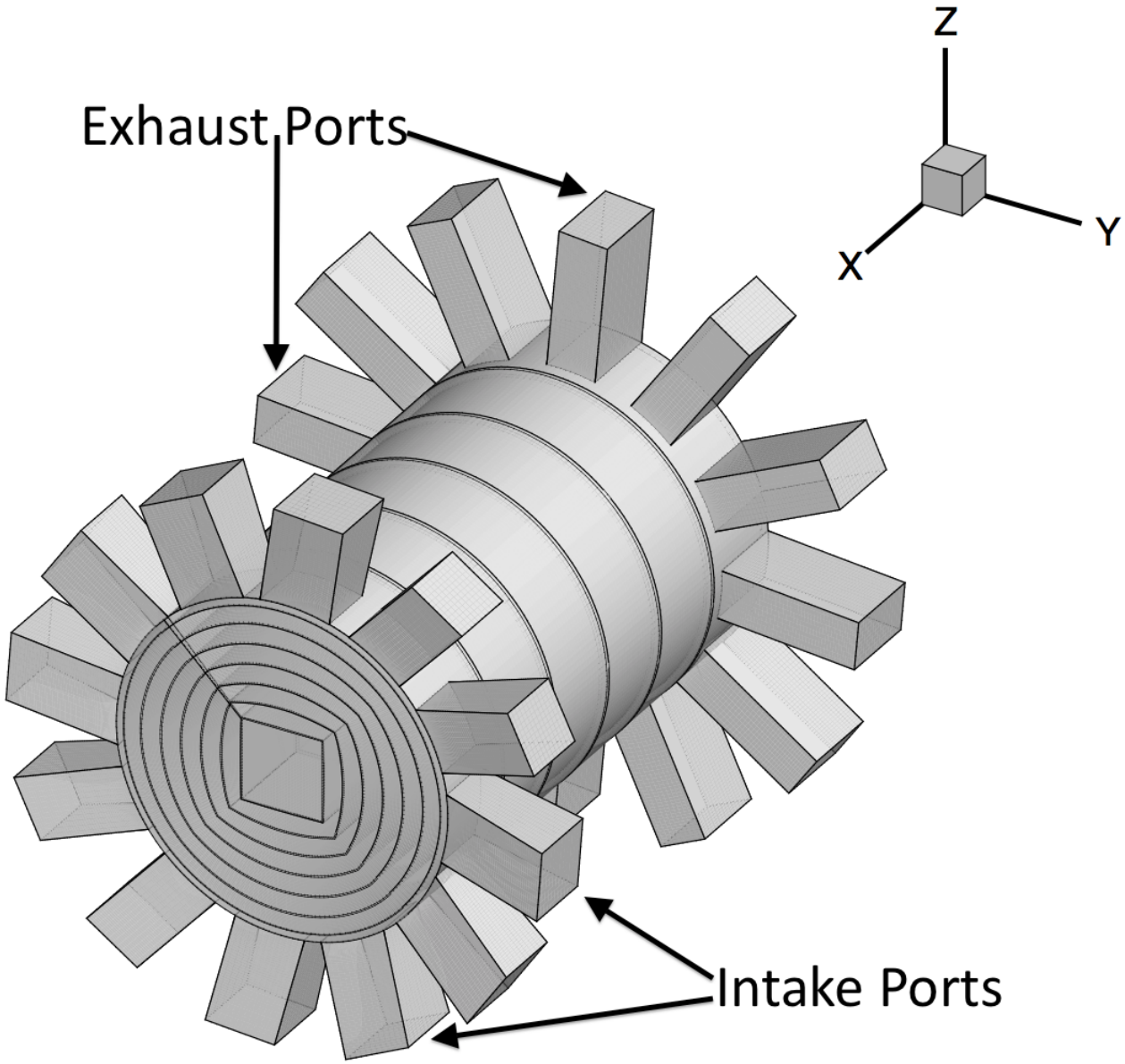

(a)

Figure 3.2: (a) 3D computational domain divided into 72 blocks, (b) 2D cross section of mesh through ports, parallel to cylinder axis, (c) 2D cross section of mesh perpendicular to the cylinder axis.

Figure 3.2: (cont'd)

(b)

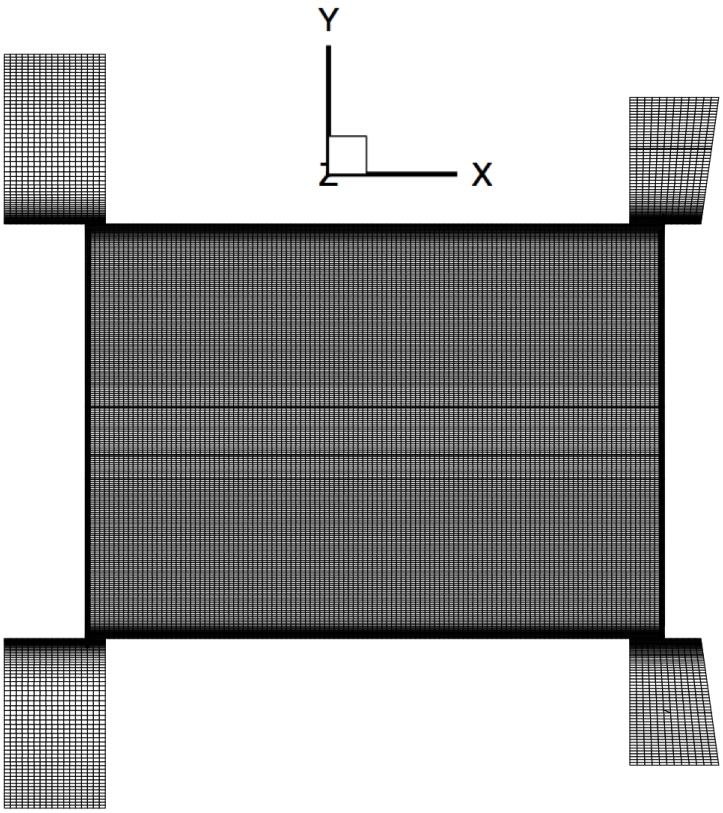

(c)

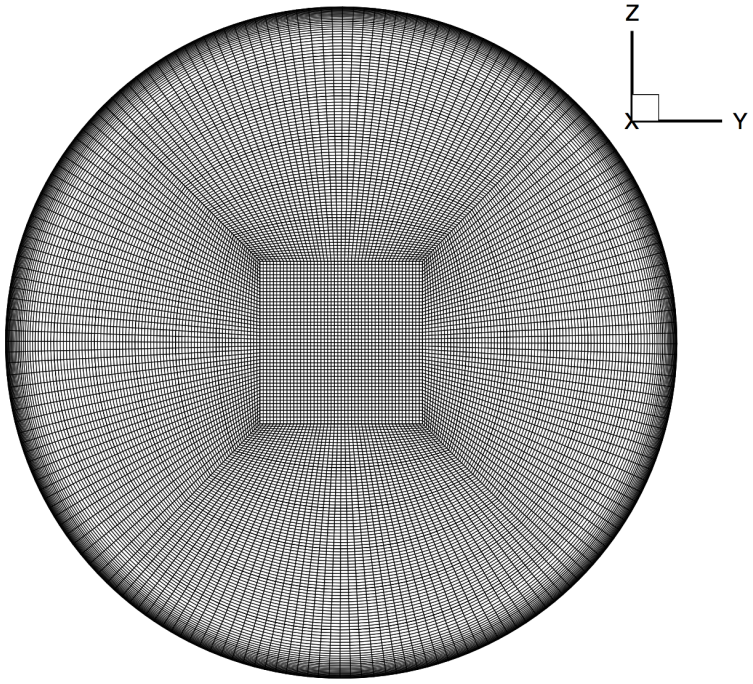

3.3 Results and Discussions: Non-reacting Flows without Spray

Three sets of simulations were carried out for the opposed piston engine: non-reacting flows without spray, non-reacting flows with spray and reacting flows with spray and combustion. The non-reacting flow simulations are considered to study the effect of different modeling and geometry parameters and operating conditions given in Table 3.1. The non-reacting spray simulations study the effect of different spray parameters on the evolution of spray using the LES/FMDF methodology, with the chemical reaction source term turned off. The reacting spray simulations have the spray and reaction terms turned on.

Several cases were simulated for non-reacting flows with different heat transfer models, intake port angles, and intake port back pressures. The primary purpose of these simulations is to study the effect of these parameters on the in-cylinder flow at different crank angles and its statistics, their likely effect on the evolution of the spray and the Cycle-to-Cycle Variations (CCV) in the flow. The mean features of flow for these different parameters have been compared with a baseline case. The baseline case employs a heat transfer model for the wall boundary conditions, has a port angle of 7.5°, runs with rpm of 3500 and has an intake port back pressure of 2 atm. Each of these models/parameters has been changed, keeping other simulation parameters the same, to elucidate the effect of the parameter on the overall evolution of the flow. The baseline case is discussed in detail first and the parameters described above are then changed to study their effects.

3.3.1 Baseline Case

The baseline case is a high rpm, medium boost, low swirl opposed-piston engine with heat transfer conditions at the cylinder liners and piston walls. For this case, the heat transfer boundary condition at walls is implemented using a convection-conduction model. The model calculates the inner wall temperature using a convection-conduction circuit. The temperature for the outer wall of the cylinder liner and piston is prescribed as a function of crank angle and the inner wall temperature is calculated based on a conduction resistance for the wall and an assumed convective heat transfer coefficient for the inner wall. The temperature of the inner wall is then used as a boundary condition for solving the energy equation at the wall boundary. The heat transfer model is described in detail below in Section 3.3.2. The boundary conditions at the intake and exhaust ports are pressure boundaries with prescribed pressure and temperature. The flow enters and exits the pressure boundaries normal to the boundary face; in other words the velocity vectors at the intake and exhaust ports are normal to the boundary face but the inflow/outflow velocity is not prescribed and floated. The exhaust ports are open directly to the atmosphere, while a boost pressure is applied at the intake ports to drive the flow. The boost pressure is calculated to give an effective boundary pressure of 2 atm. The boost pressure calculation is described in detail below in Section 3.3.4.

3.3.1.1 Cycle to Cycle Variations of Flow Variables

The exhaust ports start opening around crank angle of CA=281°, the intake ports open around CA=315°, and the top dead center (TDC), which is the minimum clearance between the pistons, is reached around CA=183.2°. Although the mean thermodynamic parameters

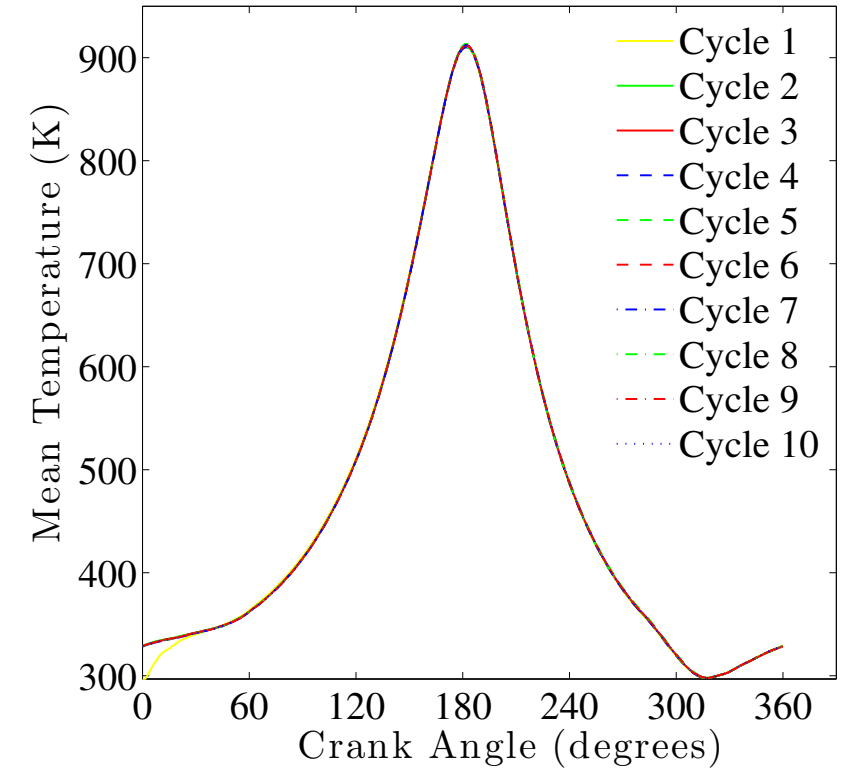

(a)

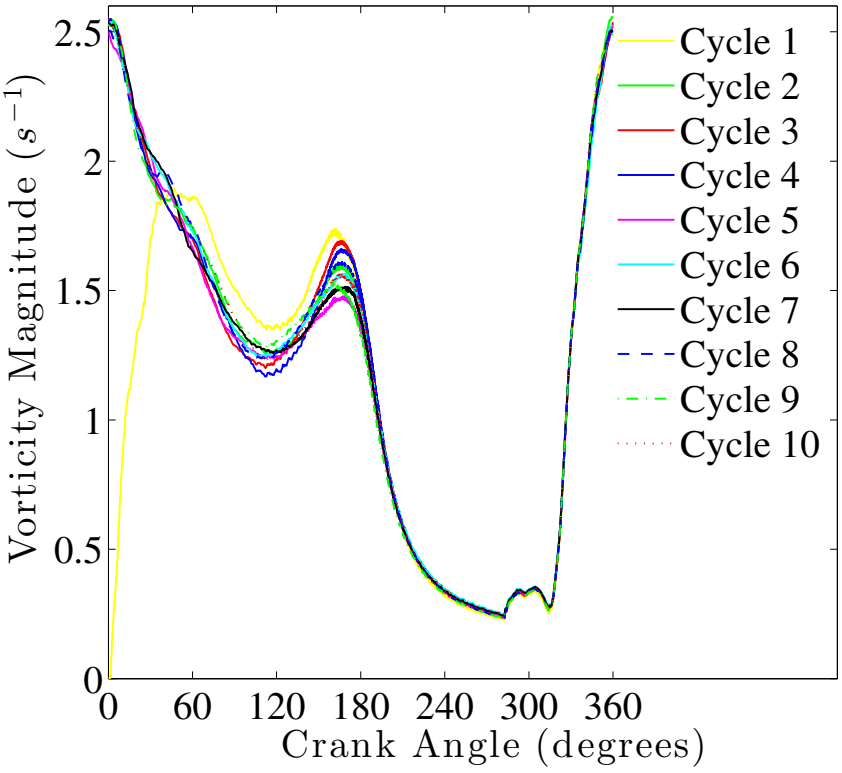

(b)

Figure 3.3: Cycle-to-Cycle Variation (CCV) for the baseline case, (a) Mean Temperature, (b) Mean Vorticity Magnitude.

of the flow become cycle-invariant after the first few cycles, more cycles need to be simulated to calculate the mean values and statistics of other parameters. Thus, ten complete cycles have been simulated for the baseline case. Figures 3.3(a) and 3.3(b) show cycle-to-cycle variations (CCV) of volume averaged temperature and vorticity magnitude, respectively, at different crank angles. There is no significant CCV in temperature; except for the first cycle, the results are pretty much the same for all cycles. As expected, the first cycle results for all variables are very different than those in later cycles due to initial condition effect. The mean vorticity magnitude has a minimum before the opening of the exhaust ports (around CA=281°) and increases significantly as the intake ports open (around CA=315°). It decreases during the first part of the compression stage (between about CA=70° to CA=120°) and increases again before reaching a local maximum at the TDC (around CA=183°), where it exhibits significant CCV.

Figure 3.4 shows the CCV of two large-scale flow variables: the swirl and the tumble. Swirl is defined the overall flow rotation around the axis of piston motion (x-axis) and is quantified by the swirl ratio, defined as,

$$SR_x = \frac{H_x}{2\pi M_x \omega_s}\,, \tag{3.1}$$

where H_x is the flow angular momentum around the x-axis, M_x is the moment of inertia around the x-axis with the origin as the center of mass of the fluid, and ω_s is the engine rotational speed in revolutions per second. Swirl is caused by the incoming flow possessing an angular momentum and is dependent on the angle of intake ports. Tumble is defined as the rotational flow around an axis perpendicular to the swirl axis, and is influenced by the shape of the ports and the piston. There are two tumble ratios, TR_y and TR_z, around the

y- and z-axes, respectively, defined as

$$TR_y = \frac{H_y}{2\pi M_y \omega_s} \tag{3.2}$$

$$TR_z = \frac{H_z}{2\pi M_z \omega_s} \tag{3.3}$$

The inclination of the intake ports in the current opposed piston configuration is favorable to the generation of a swirl-dominated flow. The swirl and tumble motions together assist the fuel vapor and air to mix better by creating large-scale fluid motions in the cylinder. There is significant CCV in the swirl ratio plot (Figure 3.4(a)) although the evolution of the flow is similar for all cycles. The swirl ratio increases significantly from a minimum as just when

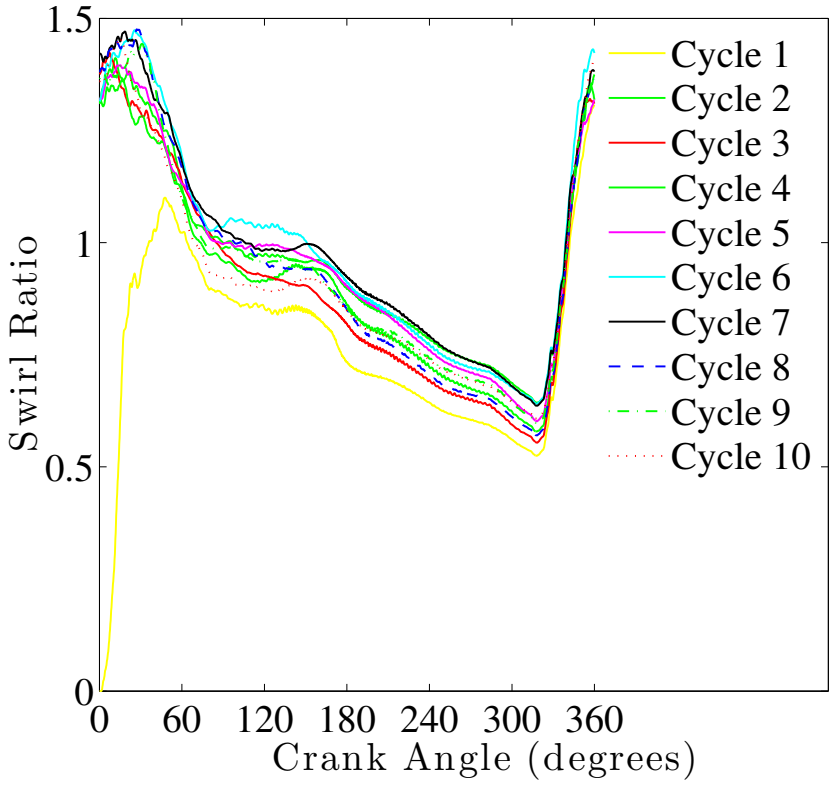

(a)

Figure 3.4: CCV of large scale flow features for the baseline case, (a) Swirl Ratio (SR_x), (b) Tumble Ratio y (TR_y), and (c) Tumble Ratio z (TR_z).

Figure 3.4: (cont'd)

(b)

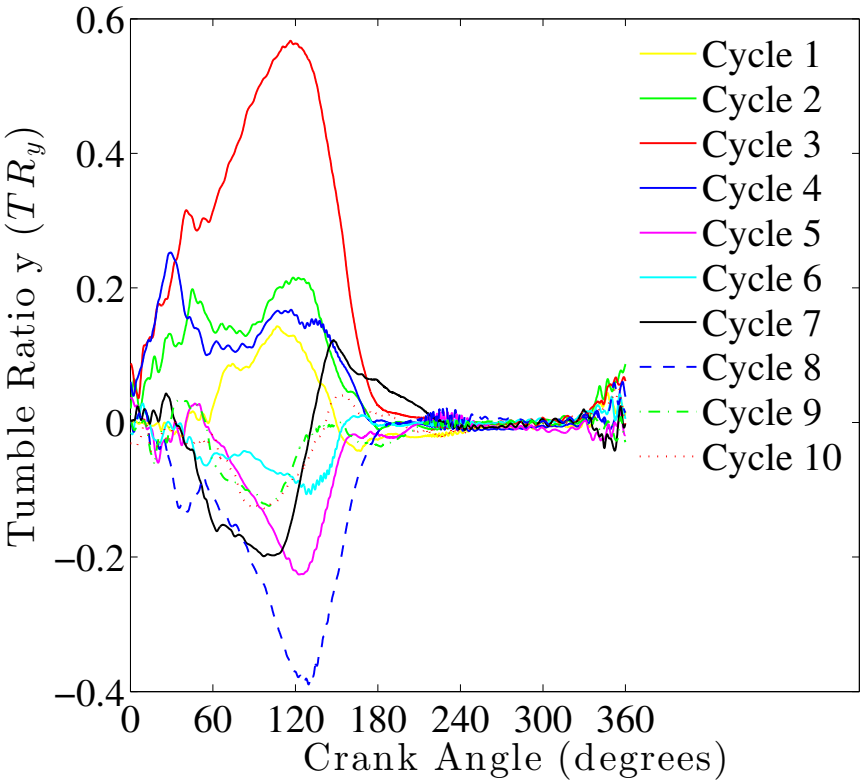

(c)

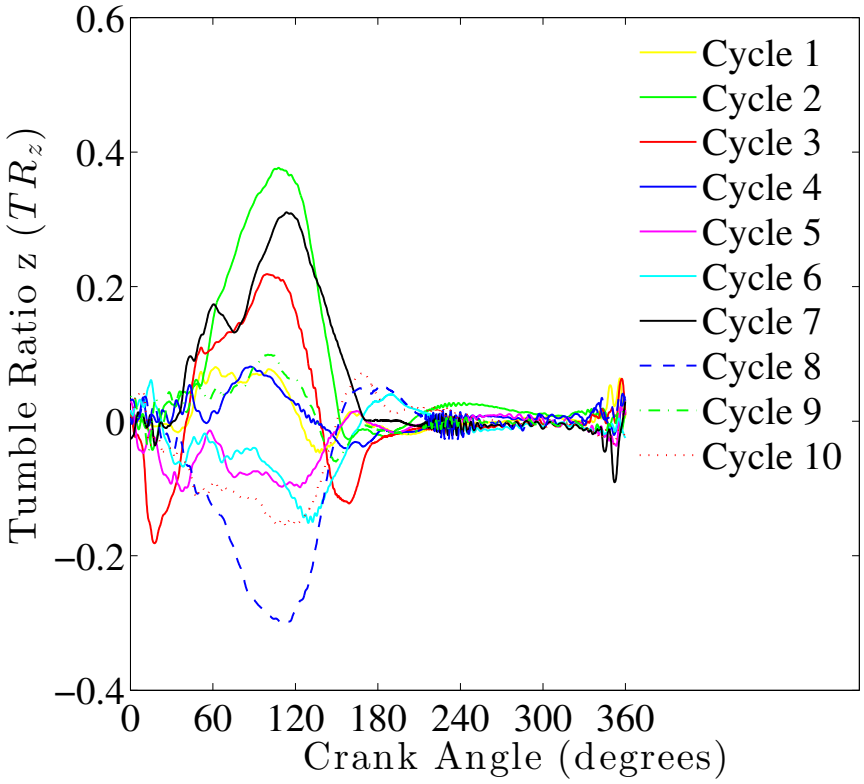

the intake ports start opening, this is due to the flow coming in at an angle with respect to the axis of the cylinder because of the inclination of the intake ports. The swirl ratio decreases as the intake ports close and the angular momentum of the flow decreases and the compression starts. There is a slight increase in the swirl near the TDC. As the radius of rotation decreases due to compression, the speed of rotation increases, causing the slight bump in the swirl ratio. However this increase is not comparable to that seen in cases with piston bowls, due to the absence of significant swirl-squish interaction. The TR_y and TR_z values in Figures 3.4(b) and 3.4(c) are lower in magnitude compared to the swirl values but the CCV is much more significant in tumble ratios especially between CA=0° to CA=180°. There is a significant increase in the tumble in the initial part of the compression stage (CA 70° to CA 120°) as the flow loses its rotational energy but 'tumble breakdown' occurs as the TDC is reached. By 'tumble breakdown', we refer to the conversion of large-scale fluid motion into small-scale flow/turbulence as the effective length scale decreases by the compression. The tumble ratios also change sign during a cycle and are very different from one cycle to another cycle, indicating the variable nature of the flow.

3.3.1.2 Turbulent Fluctuations of Flow Variables

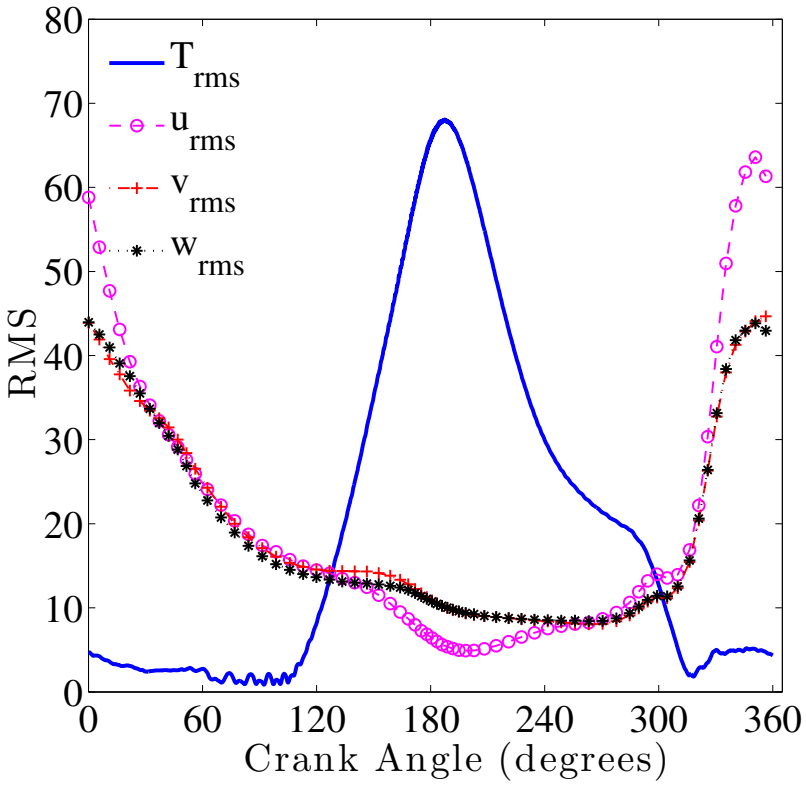

Figure 3.5: RMS of temperature and velocity components for the baseline case.

Figure 3.5 shows the rms of temperature and velocity components as a function of the crank angle. The rms values of all three velocity components increase as the exhaust ports start opening due to the higher fluid velocities near the exhaust ports. This change in rms would be higher in the case of reacting flow as the difference between the in-cylinder pressure and exhaust pressure would be higher which causes the velocity difference between the exhaust port area and the rest of the cylinder to be higher. The rms increases significantly to a maximum value as the intake ports open; this is due to the high velocities of the incoming flow created by the high pressure-gradient at the intake port boundaries. The rms values decrease continuously during the compression stroke as the velocity components become more uniform and less turbulent by the mixing of the incoming flow with the rest

of the cylinder. In summary, the flow-field is highly inhomogeneous and turbulent while the intake and exhaust ports are open but becomes more homogeneous during compression. In contrast, the rms of the temperature increases during compression, reaching a maximum at the TDC. Near the TDC, the fluid temperature in the interior of the cylinder increases due to compression, but the temperature near the walls is lower due to heat transfer to the colder outer walls, maintained at a fixed temperature. This results in significant variation in the temperature and leads to higher rms values. During expansion, the interior flow cools down and the in-cylinder temperatures become comparable to the wall temperatures, thus reducing the rms value. Figure 3.6 shows the overall flow turbulent intensity to substantially

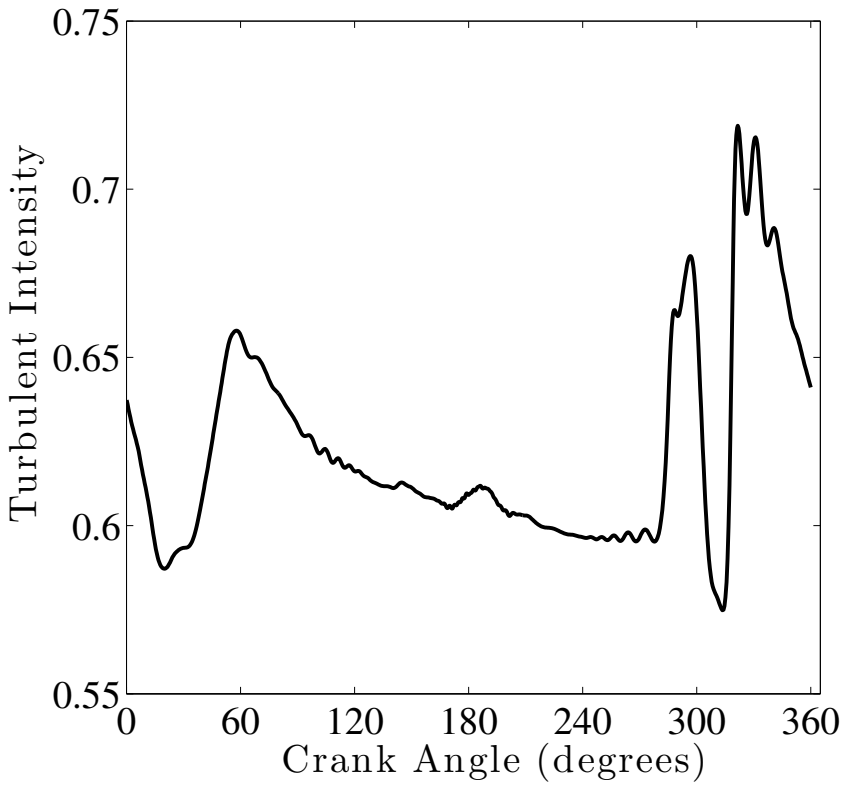

Figure 3.6: Turbulent Intensity for the baseline case.

increases when the intake ports open and to peak right at the opening of exhaust ports and right after the intake ports start closing. There is a slight bump in the turbulent intensity

at the TDC due to 'tumble breakdown'.

3.3.1.3 Flow Evolution

The 2D contours of the filtered velocity components at different planes are plotted in Figures 3.7-3.9 to illustrate the evolution of the flow. The axial velocity component u for different crank angles is shown in Figure 3.7 on a plane passing through two intake ports and parallel to the axis of the cylinder. In Figure 3.7(a), the intake ports are fully open and the exhaust piston is moving towards the TDC. At CA=60° (Figure 3.7(b)), all ports are closed and both pistons are moving towards the TDC. Note that both pistons are near the TDC at CA 180° (Figure 3.7(c)). The exhaust ports have started opening at CA 300° (Figure 3.7(d)), but there is no significant axial velocity as the pressure difference between the inner cylinder region and the exhaust port boundary is not high. In the presence of combustion, the velocities would be higher as the burned gases rush out of cylinder due to the higher pressure created by the combustion. The intake ports are partially open at CA 330° as shown in Figure 3.7(e) and due to the high boost pressure applied at the intake boundaries, a significant pressure gradient exists which causes high axial velocities in the incoming flow. The intake ports are completely open at CA 360° in Figure 3.7(f). The incoming fluid pushes out the existing air in the cylinder; in the case of a reacting simulation, the burned gases would be pushed out of the cylinder by the fresh incoming air. This illustrates the 'scavenging' action of the incoming air. This type of scavenging is known as 'uniflow scavenging' and is a characteristic feature of opposed-piston engines. Here, most of the scavenging is done by the action of the incoming air as compared to the cases when most of the exhaust exits the cylinder due to the pressure gradient between the inner cylinder and exhaust ports. Figure 3.8 shows the radial velocity component v (along the y-axis) on a plane passing

through the intake ports and perpendicular to the cylinder axis for different crank angles. In Figure 3.8(a) (CA=0°), the intake ports have been open for some time and a swirling motion exists in the cylinder due to the angle of the ports. The ports are nearly closed at CA=30° (figure 3.8(b)) and the swirling motion in the cylinder has decreased. The ports are completely closed at CA=180° and CA=300° (Figures 3.8(c) and 3.8(d) respectively). The intake ports are partially open by CA=330° and a significant swirling motion exists due to the high velocity fluid coming in at an angle. Figure 3.8(f) shows the radial velocity contours at CA=360° when the ports are almost completely open and a significant swirling motion still exists. Figure 3.9 shows the radial velocity component along the y-axis at TDC on a plane perpendicular to the cylinder axis, near the center of the cylinder. A significant swirling motion exists at CA=0° and CA=30° (Figures 3.9(a) and 3.9(b), respectively) when the intake ports are open, however the swirl magnitude in the cylinder is lower than in the regions near the ports. As the ports close and the gas in the cylinder gets compressed, the swirling motion decreases. Some swirling flow however does exist near the TDC as seen in Figure 3.9(c) (CA=180°), which can be useful in enhancing the mixing of evaporated vapor in the outer regions of the cylinder. The swirling motion completely disappears at CA =300° (Figure 3.9(d)). Figures 3.9(e) and 3.9(f) show that as the intake ports open again, the swirl increases again.

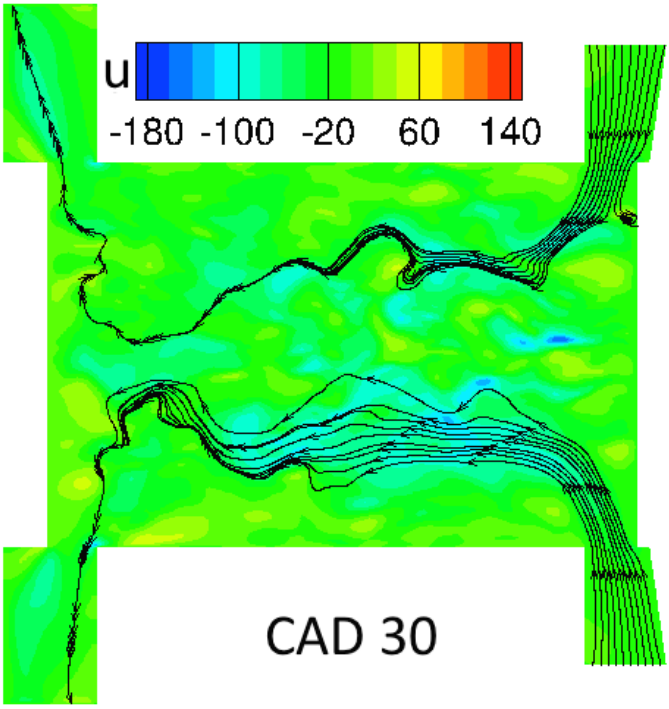

(a)

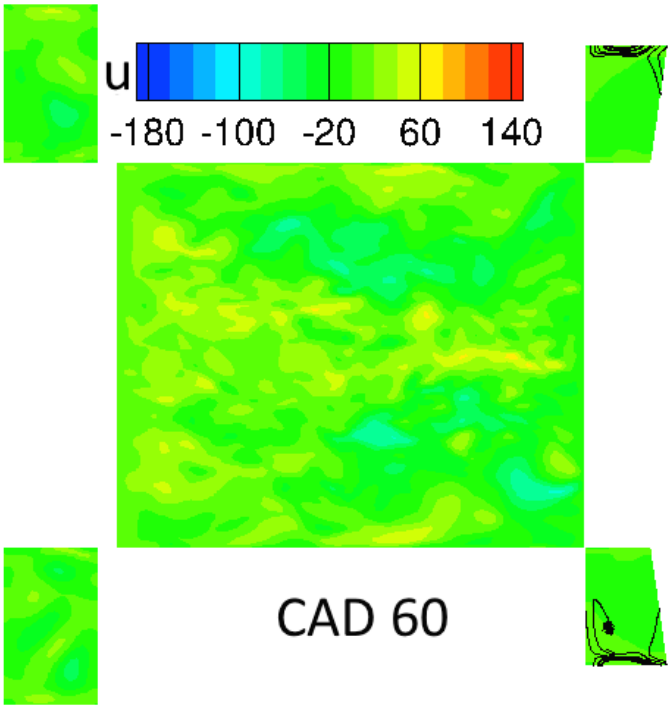

(b)

Figure 3.7: 2D contours of axial velocity (u) on a plane through two intake ports, parallel to cylinder axis (a) CA 30°, (b) CA 60°, (c) CA 180°, (d) CA 300°, (e) CA 330°, and (f) CA 360°.

Figure 3.7: (cont'd)

(c)

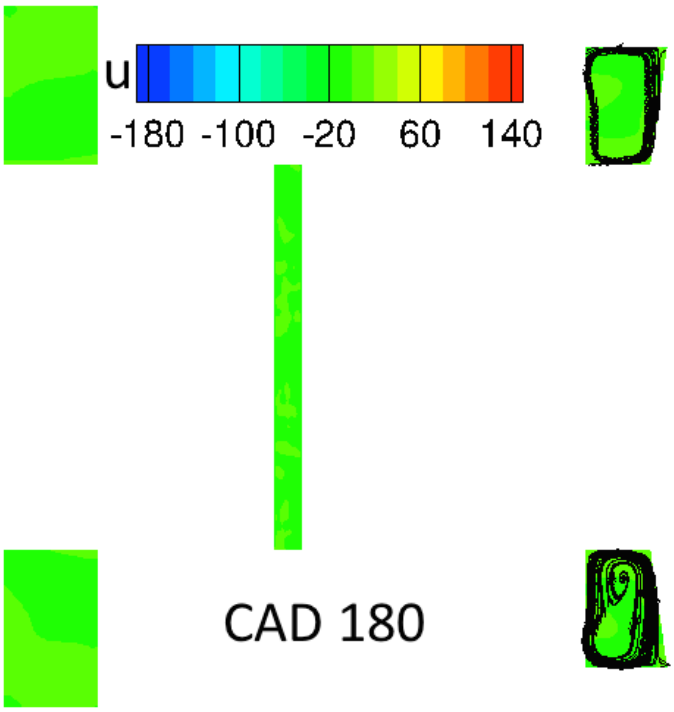

(d)

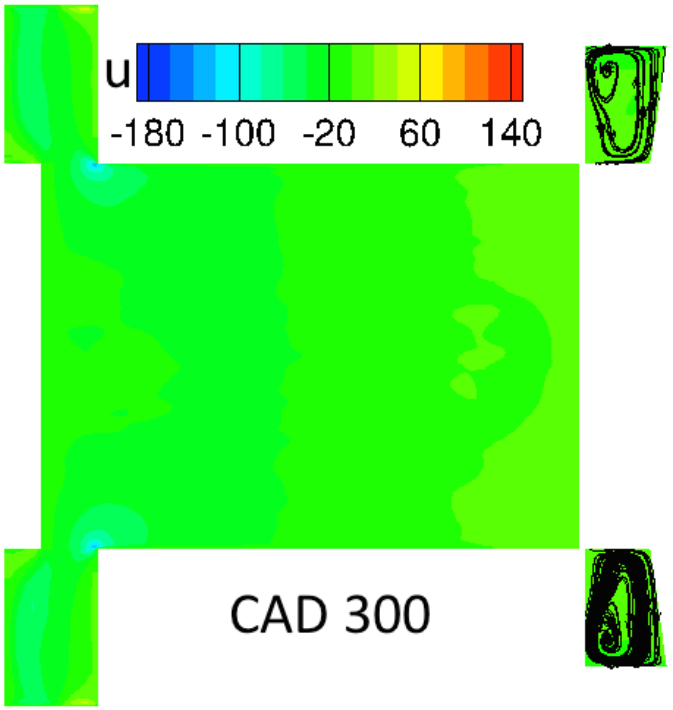

Figure 3.7: (cont'd)

(e)

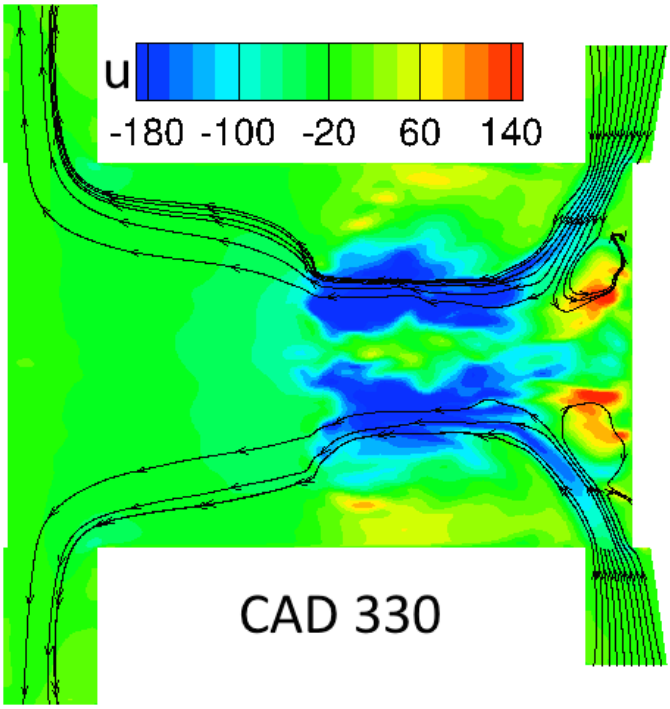

(f)

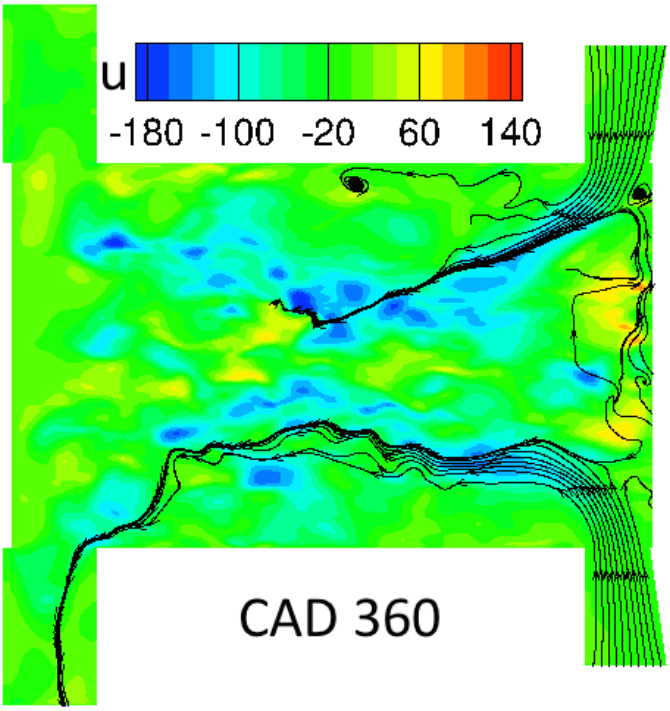

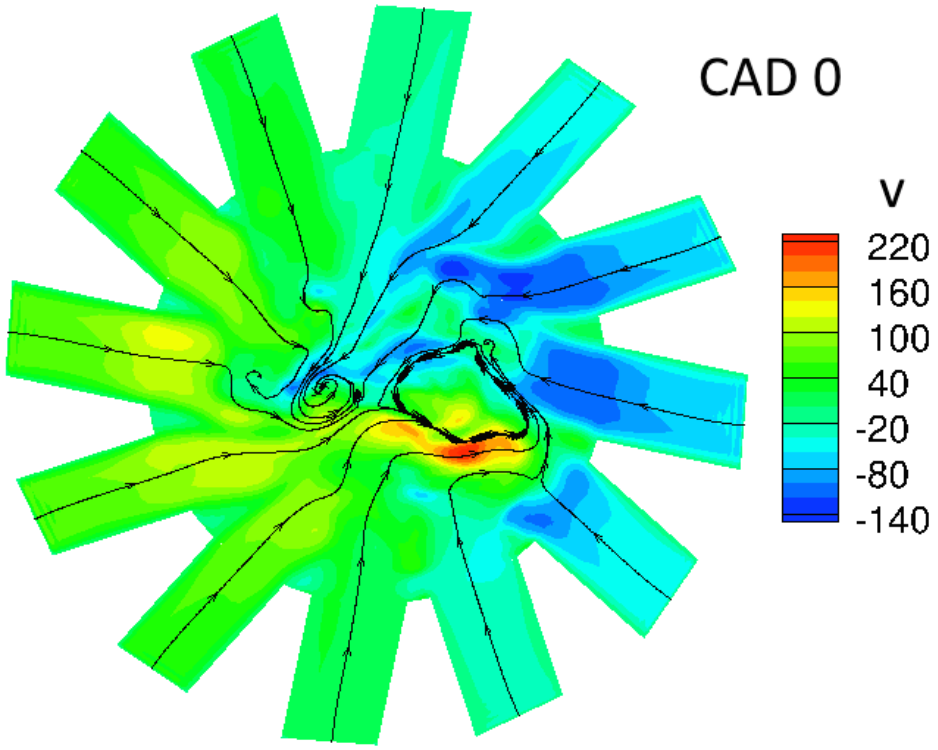

(a)

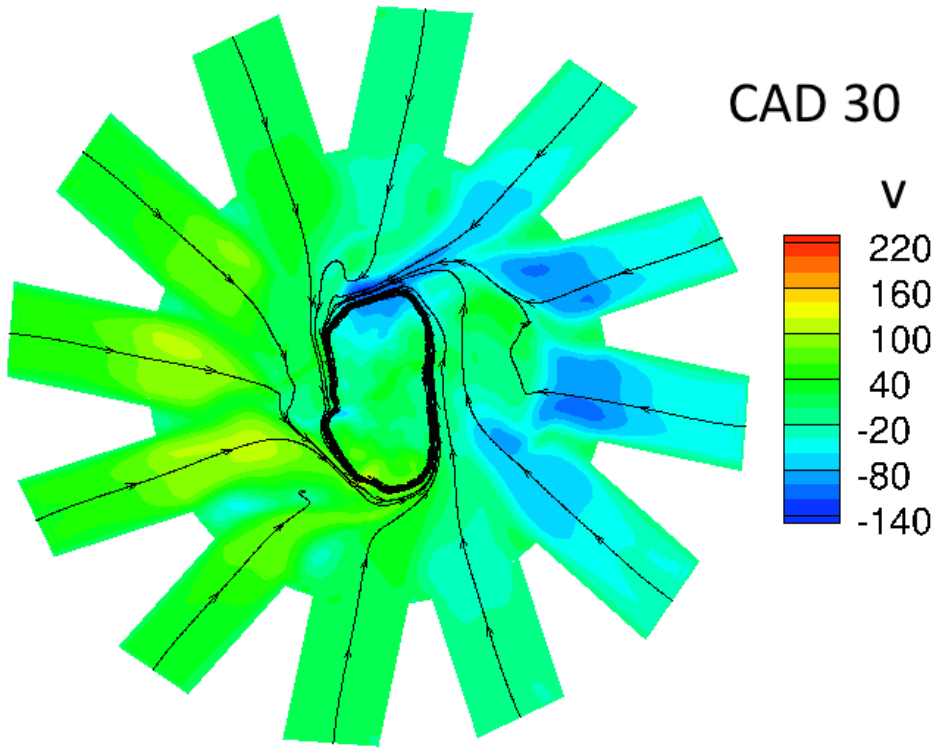

(b)

Figure 3.8: 2D contours of radial velocity y-component (v) on a plane through intake ports, perpendicular to cylinder axis (a) CA 0°, (b) CA 30°, (c) CA 180°, (d) CA 300°, (e) CA 330°, and (f) CA 360°.

Figure 3.8: (cont'd)

(c)

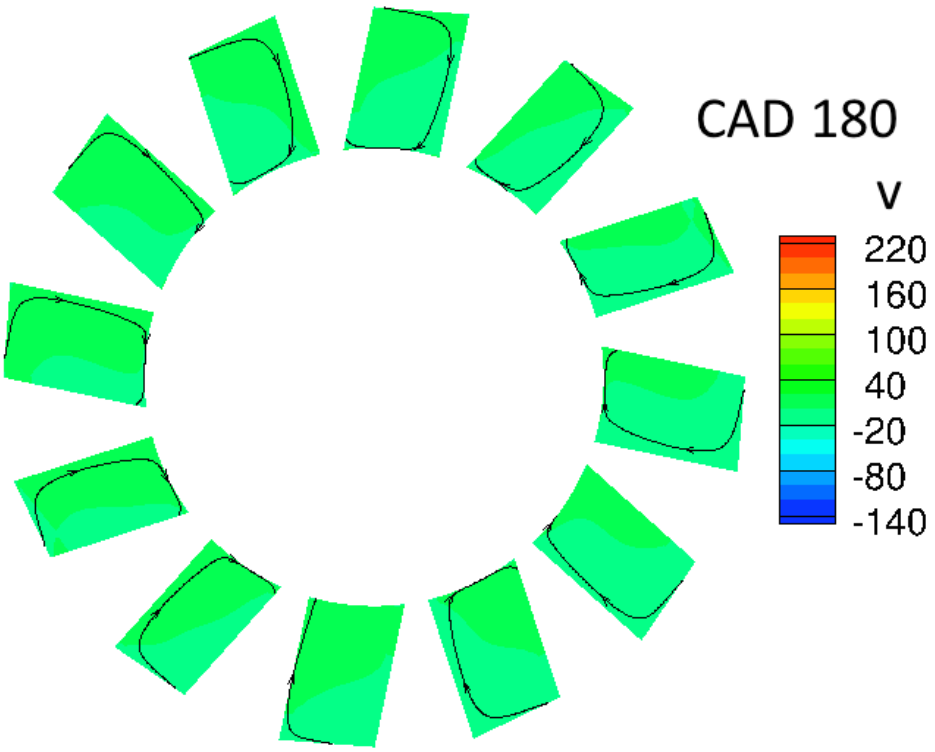

(d)

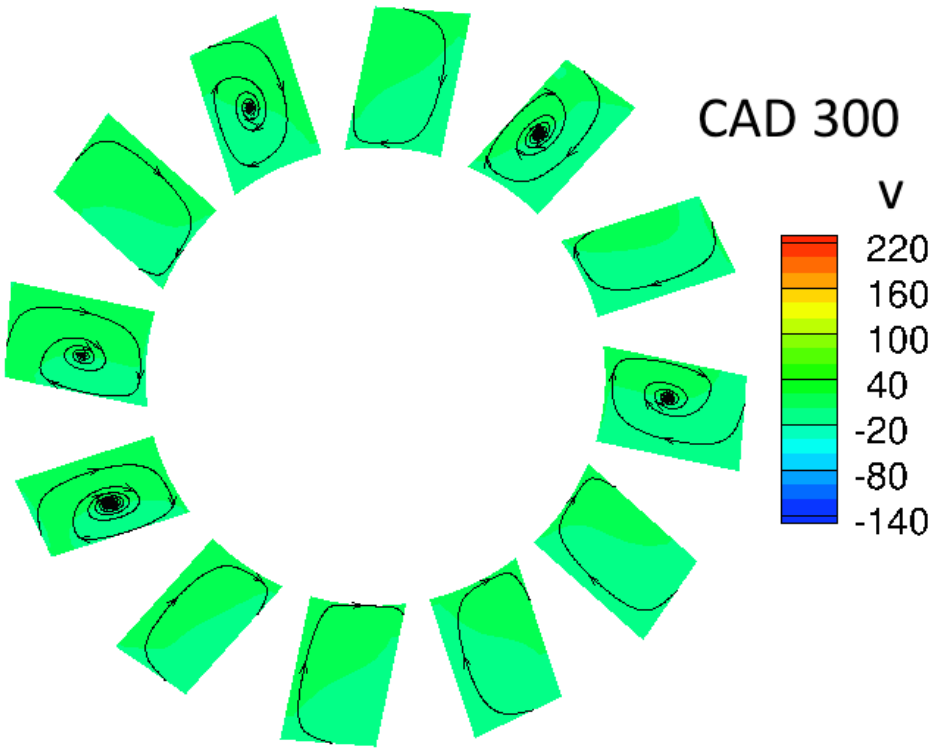

Figure 3.8: (cont'd)

(e)

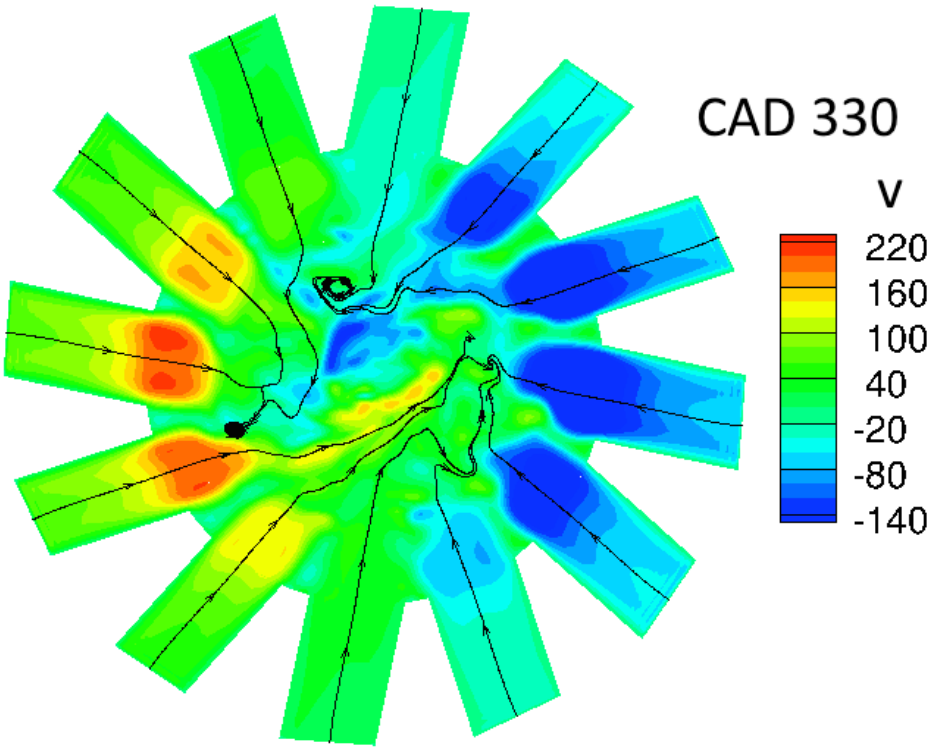

(f)

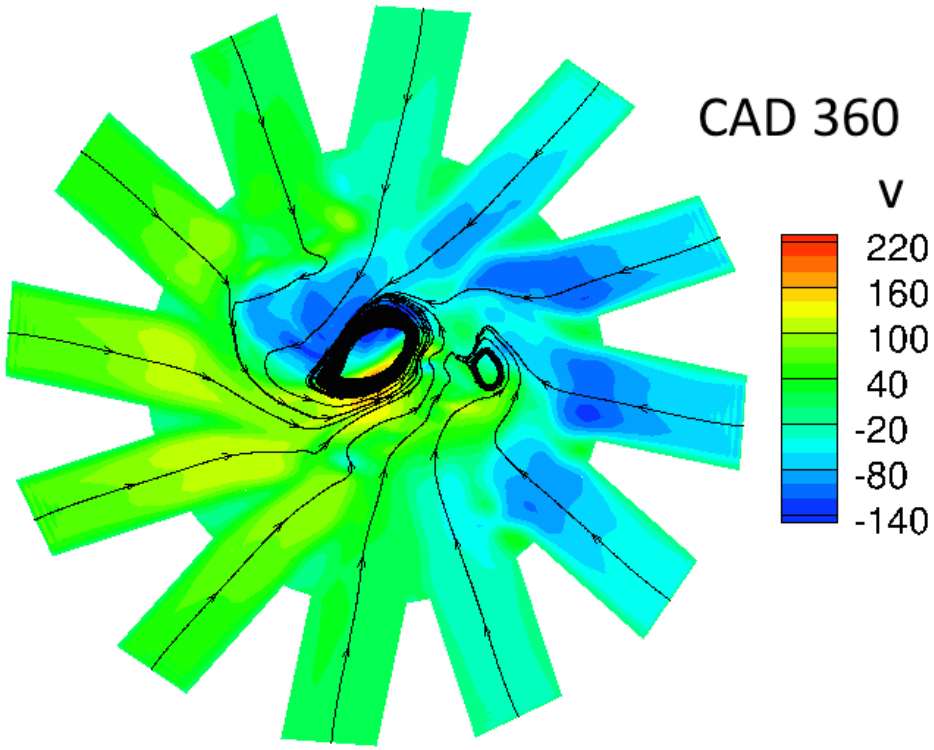

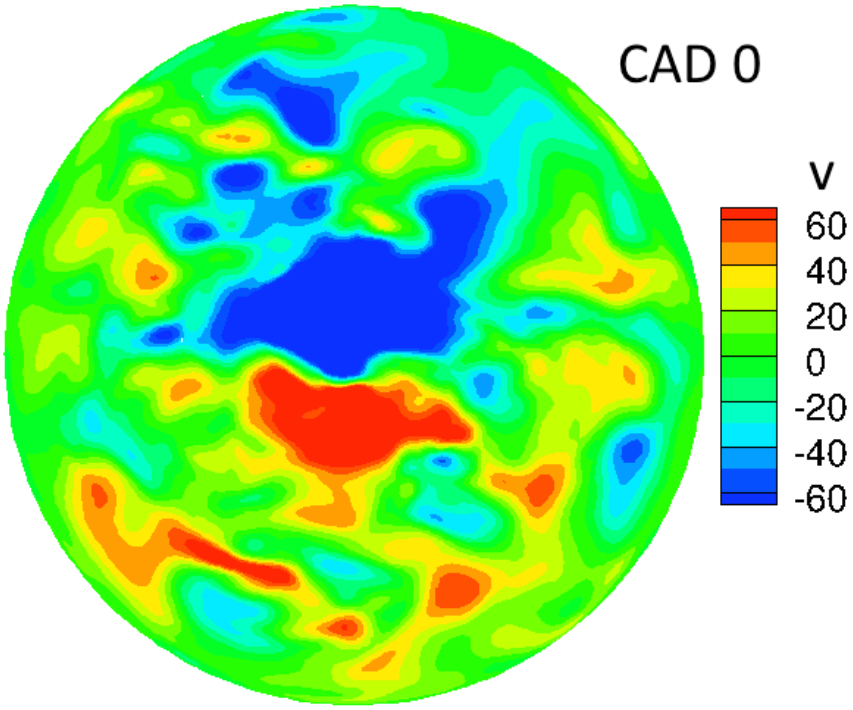

(a)

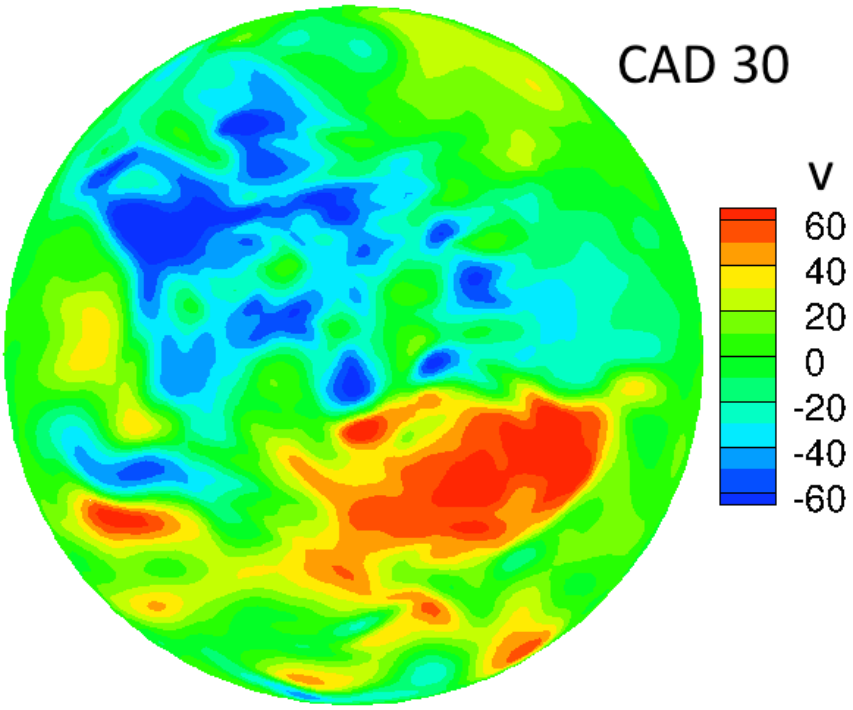

(b)

Figure 3.9: 2D contours of radial velocity y-component (v) on a plane through the cylinder and perpendicular to cylinder axis (a) CA 0°, (b) CA 30°, (c) CA 180°, (d) CA 300°, (e) CA 330°, and (f) CA 360°.

Figure 3.9: (cont'd)

(c)

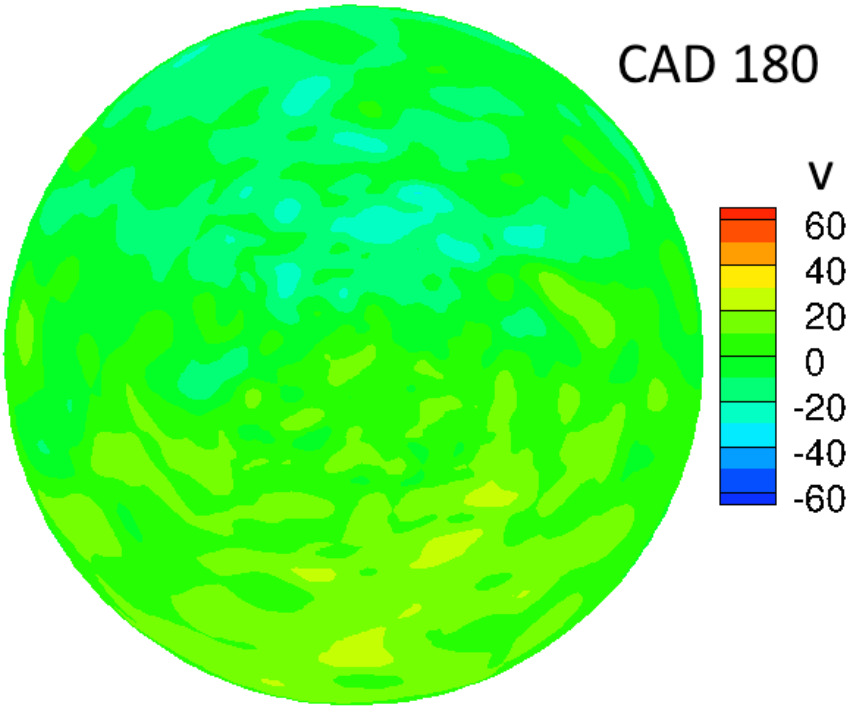

(d)

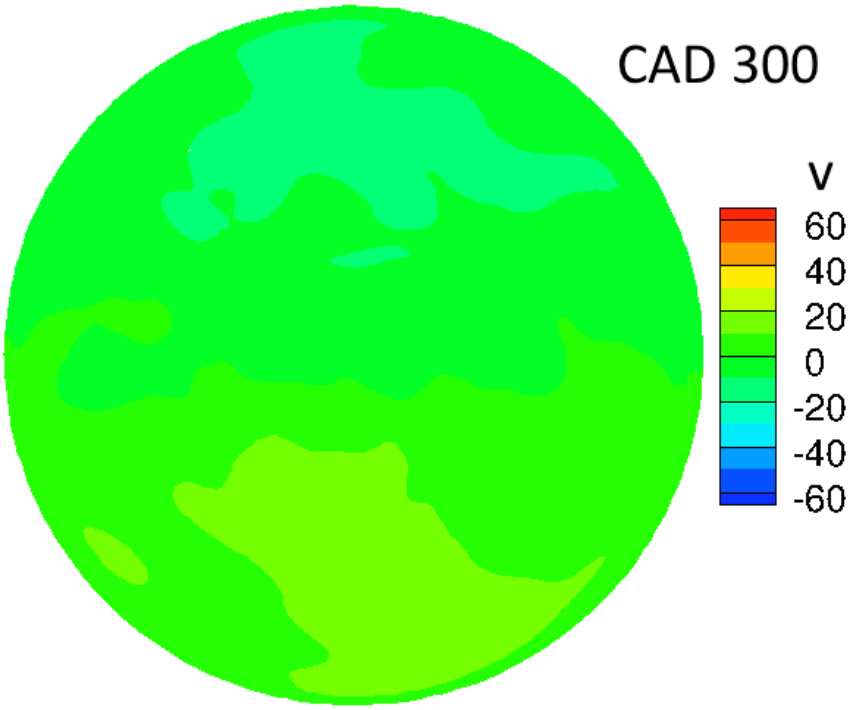

Figure 3.9: (cont'd)

(e)

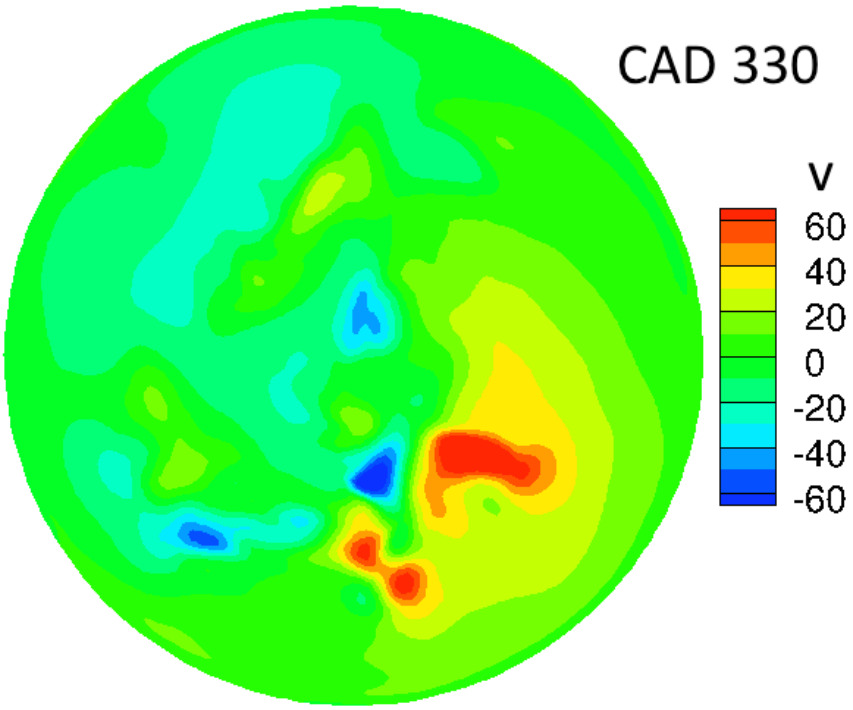

(f)

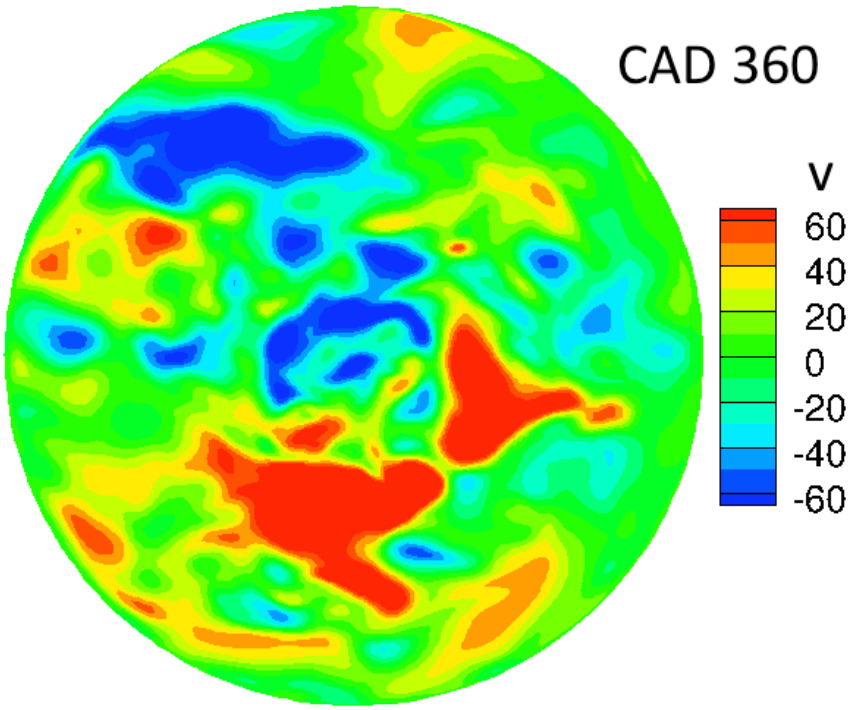

3.3.1.4 Flow in Different Regions of Cylinder

In order to understand the effect of variably sized and unequally spaced intake ports on the flow and also to quantity the flow inhomogeneity and turbulence levels inside the cylinder, the cylinder was divided into 13 different zones as shown in Figure 3.10. Zones 1 to 12 correspond to the regions near the 12 intake ports and the flow in these zones is expected to be likely influenced by the shape/size of the corresponding ports and the incoming flow through the ports. Zone 13 is a square zone in the center of the cylinder. The turbulent intensity of the flow in the 13 selected zones is shown in Figure 3.10(b) as a function of the crank angle. The overall trend in the first 12 zones is similar but there are significant differences in the calculated turbulent intensities for different zones. This is shown by the envelope of the intensity values in these 12 zones, illustrated by the thick dark lines. The turbulent intensities vary between 3-10%; the difference between the intensities is the smallest at CA=300°, a few degrees before the intake ports open. The maximum difference between the intensities is at CA=30°, when the intake ports are almost completely closed; zone 6 has the lowest turbulent intensity while zone 9 has the highest turbulent intensity at this crank angle. Zone 13, on the other hand, follows a slightly different trend. While the turbulent intensity in the rest of the cylinder decreases continuously as compression starts, that in zone 13 remains nearly constant with only minor variations. However, zone 13 experiences a drop in the turbulent intensity just before the ports open and a significant increase as the intake ports open, similar to the trends observed in other zones. Figure 3.10(b) indicates that the flow in regions close to ports is highly inhomogeneous at the end of the intake stroke but is more homogeneous before the intake ports open. The maximum difference in the turbulence levels in the cylinder occurs after the end of the compression stage, when

the center of the cylinder still has significant turbulence while the rest of the cylinder has the lowest turbulent intensity values in the entire cycle. Figure 3.10(c) shows the volume-averaged vorticity magnitude for the 13 zones as a function of the crank angle. All the zones show a similar trend to that of turbulent intensity, with the mean vorticity magnitude having a minimum just before the opening of the exhaust ports, a significant increase in vorticity as the intake ports open, a decrease during the first part of the compression stage (between CA=70° to CA=120°) and an increase again before reaching a local maximum at TDC. Zone 13 has a relatively higher vorticity magnitude compared to the rest of the zones, particularly during the opening of the intake ports.

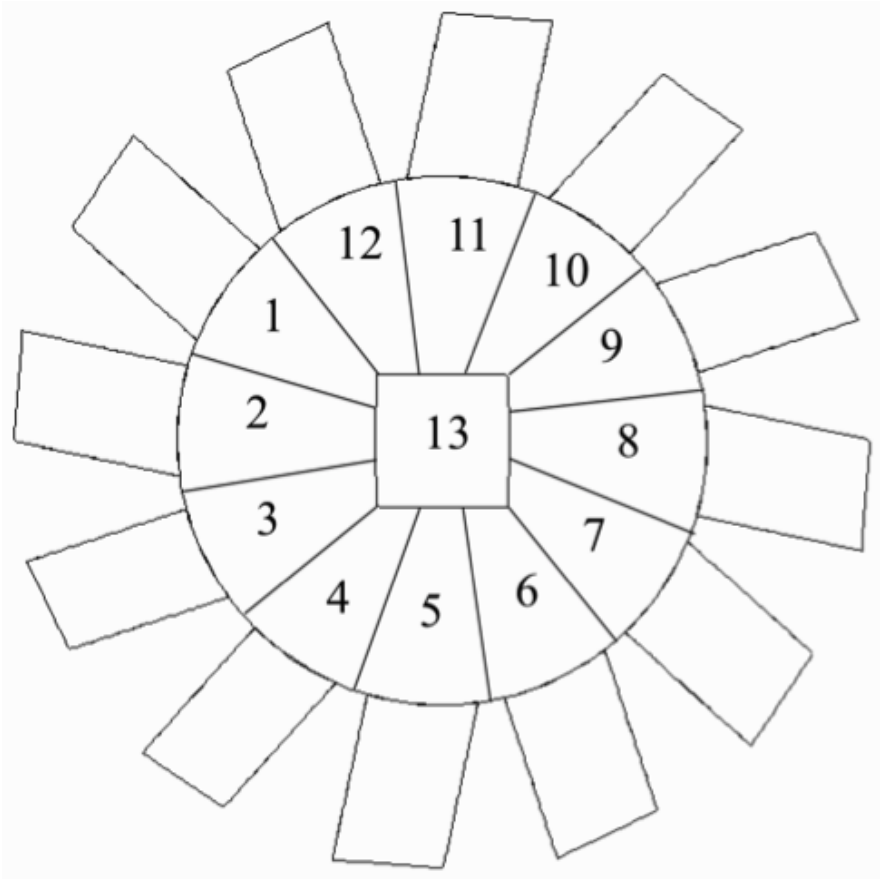

(a)

Figure 3.10: (a) Cylinder divided into 13 different zones, and (b) Turbulent intensity, (c) Vorticity magnitude, in different zones in the cylinder as a function of the crank angle.

Figure 3.10: (cont'd)

(b)

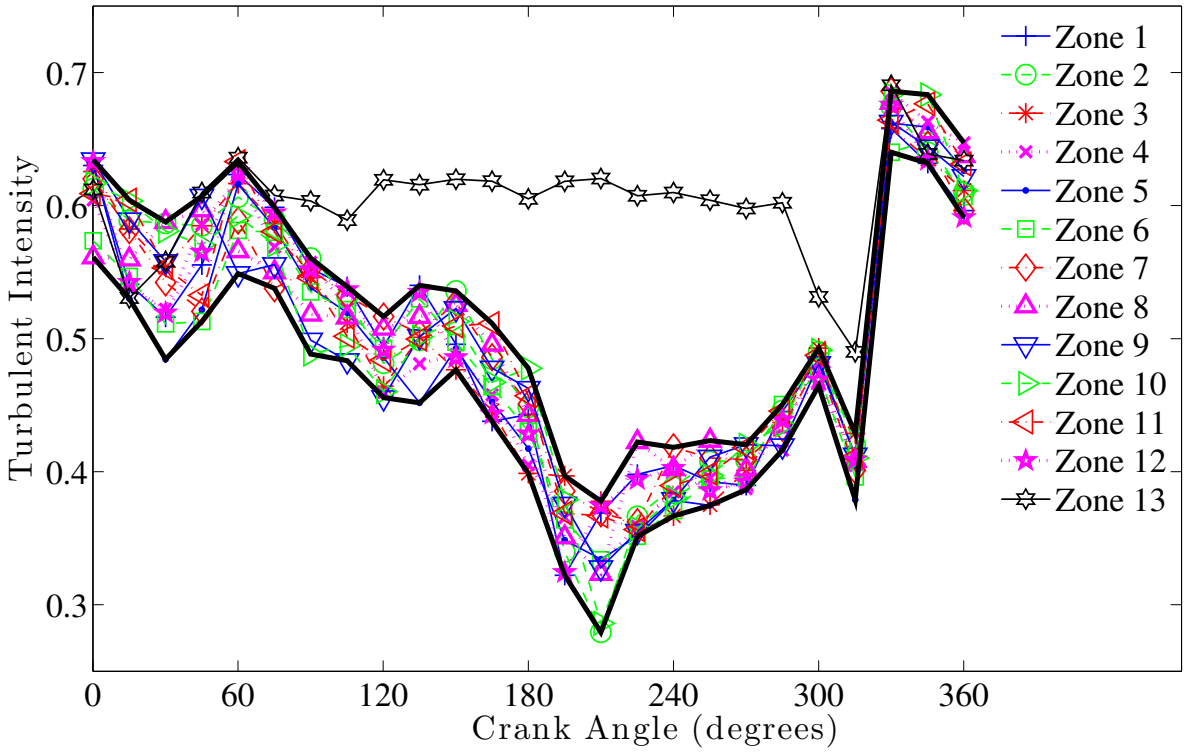

(c)

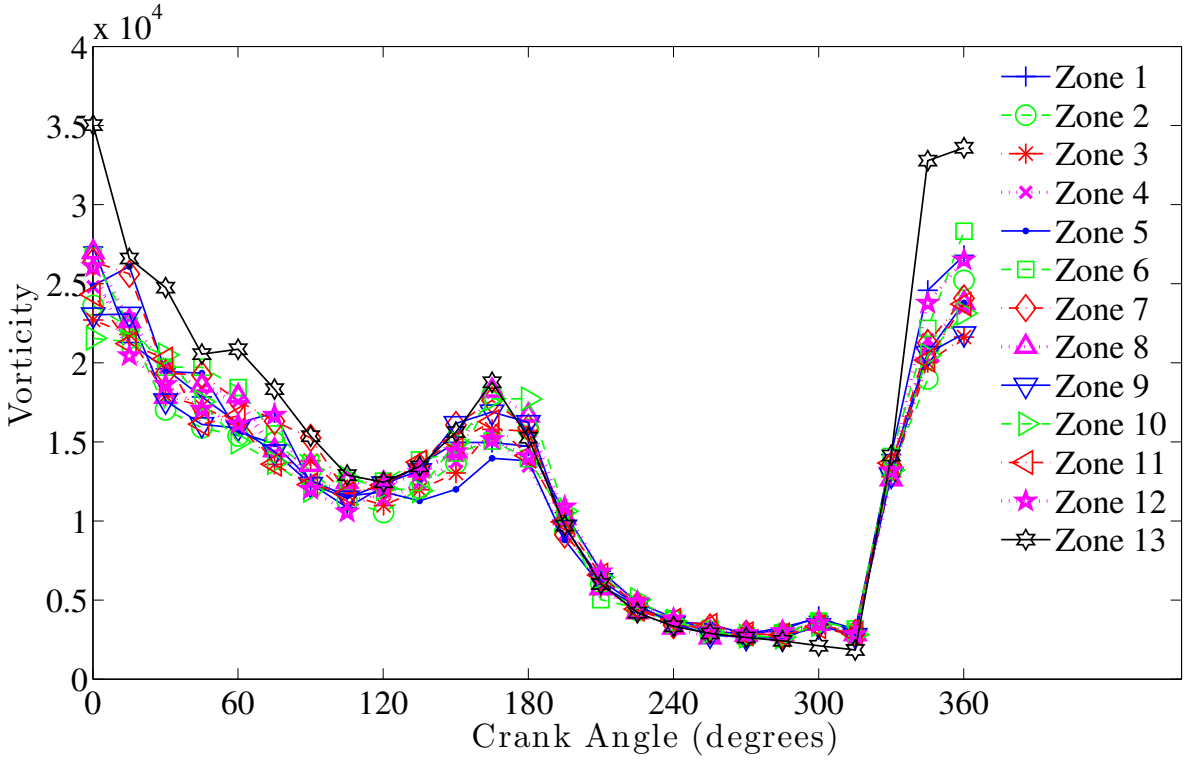

3.3.1.5 Cycle to cycle variation and mean velocity behavior

Figures 3.11(b), 3.11(c). and 3.11(d) show the CCV and mean values of the velocity components on z=0 line at plane x=0 at CA=150° (see Figure 3.11(a)). At this crank angle, all the ports are closed and the gas inside the cylinder is being compressed. There is significant swirl and some tumbling motion and considerable CCV in the velocity components. The mean u velocity profile has a peak near the center, with the magnitude nearly approaching zero at other locations. The mean radial (v-component) velocity changes sign near the center with two peaks about 20% of the distance from the wall on either side, illustrating the swirling nature of the flow. Similarly, the mean w-velocity component changes sign near the center of the cylinder, although the change in sign and magnitude of the w-velocity is slightly monotonic as compared to the v-velocity.

Figure 3.12 shows the velocity vectors, colored by the velocity magnitude, at a plane passing through the ports, parallel to the axis of the cylinder, and at a crank angle of 30° for cycles 1 to 10 (Figures 3.12(a) - 3.12(e)) and their (cyclic) mean (Figure 3.12(f)) values at the sane plane and crank angle. At this crank angle, the intake ports are almost completely open and have been open for some time. Two incoming jets of fresh air can be observed in the visible ports; there would be similar jets for the ports not seen in Figure 3.12. Due to initial condition effects, the velocity magnitudes at this plane are the highest in the first cycle. The maximum velocity magnitude for the rest of the cycles is nearly the same and occurs in the exhaust ports. The outgoing jets have been scavenged out of the cylinder by the incoming fresh air jets and exit at high velocities due to the high pressure-gradient existing between the opposite ends of the exhaust ports. The incoming jets create small vortices near the corners and in the region between the jets near the intake piston. As the

jets collide, the nearly uniform velocity vectors become distorted and several small vortical motions are generated in the region surrounding the jets. The nearly undisturbed portions of the jets seem to have penetrated, both radially and axially, to different extents at different cycles. Also, there are considerable differences in the velocity fields in the regions after the colliding jets. Figure 3.12(f) shows the mean velocity vectors for cycles 1 to 10. The jets collide smoothly and many of the small vortices near the colliding jets are been averaged out in the mean plot. A similar velocity field would be expected to be obtained by RANS simulation. This illustrates the importance of LES in elucidating the details of the flow. Similarly, Figure 3.13 shows the velocity vectors, colored by the velocity magnitude, at a plane passing through the ports and perpendicular to the cylinder axis, at CA=30° for cycles 1 to 10 (Figures 3.13(a) -3.13(e)). The cyclic mean velocity contours are also shown in Figure 3.13(f). The incoming jets from each port have high angular momentum due to the port angle and collide near the center of the plane. A significant non-uniform swirling motion exists, the shape, location and magnitude of which varies considerably from one cycle to another. Also, there is a considerable CCV in the velocity fields near each individual port. Figure 3.13(f) shows the mean values obtained from averaging of cycles 1 to 10. Evidently, the velocity fields near the ports are quite similar, and there is a swirling motion near the center of the plane.

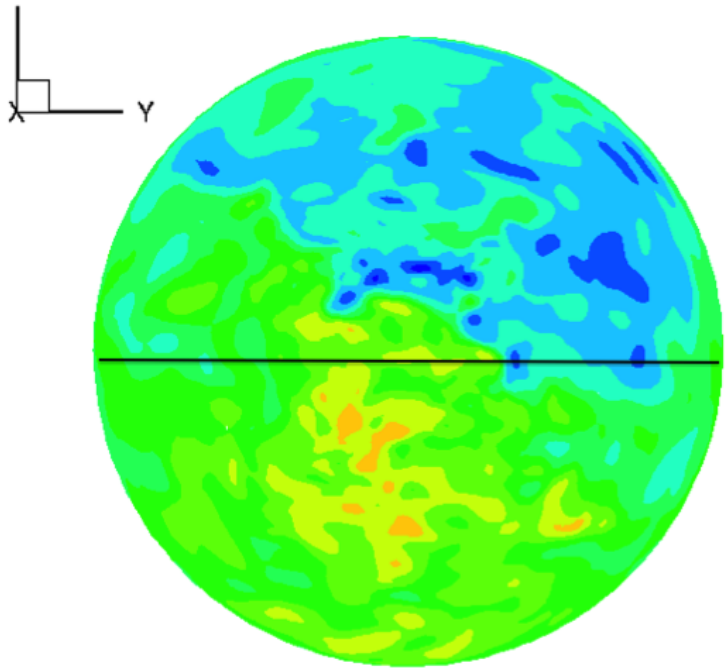

(a)

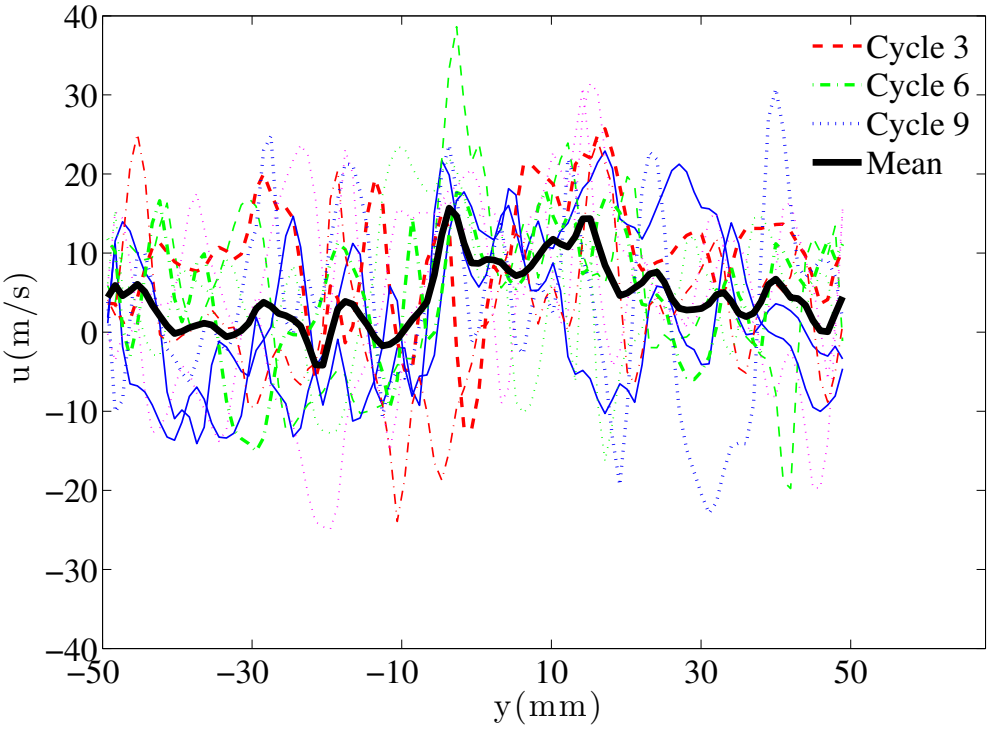

(b)

Figure 3.11: (a) Cross section at x=0, CA 150°, Line z=0. Velocity magnitudes at line z=0, plane x=0, Crank Angle 150° for ten cycles and their mean (shown by thick line), (b) u (axial) velocity, (c) v (radial) velocity, and (d) w (radial) velocity.

Figure 3.11: (cont'd)

(c)

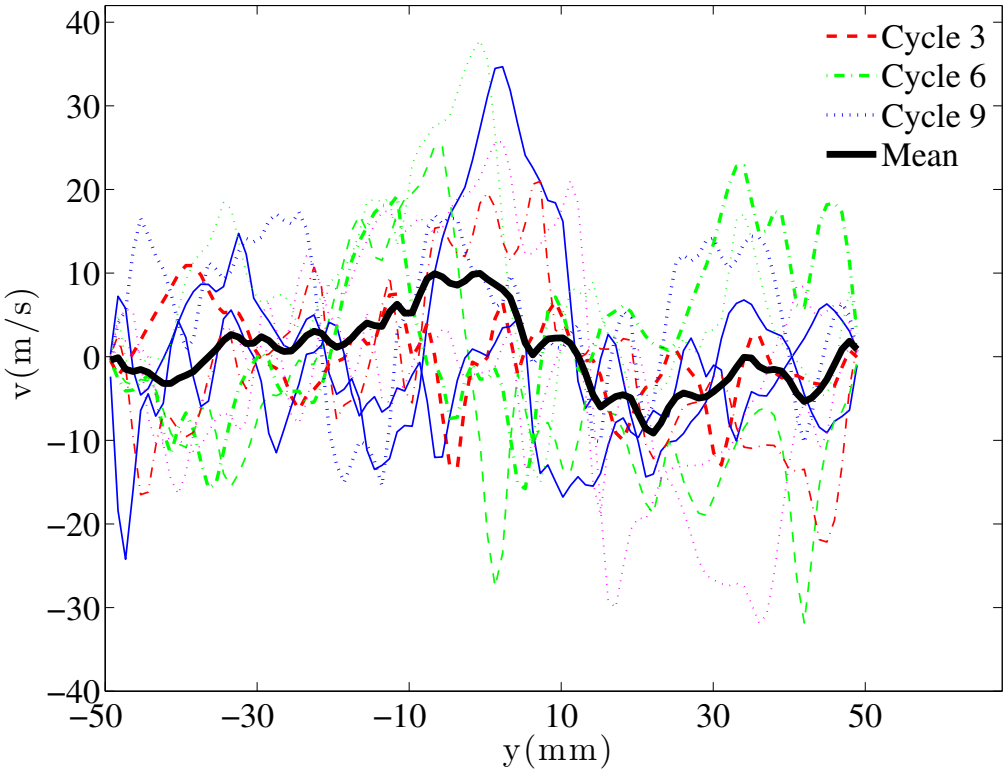

(d)

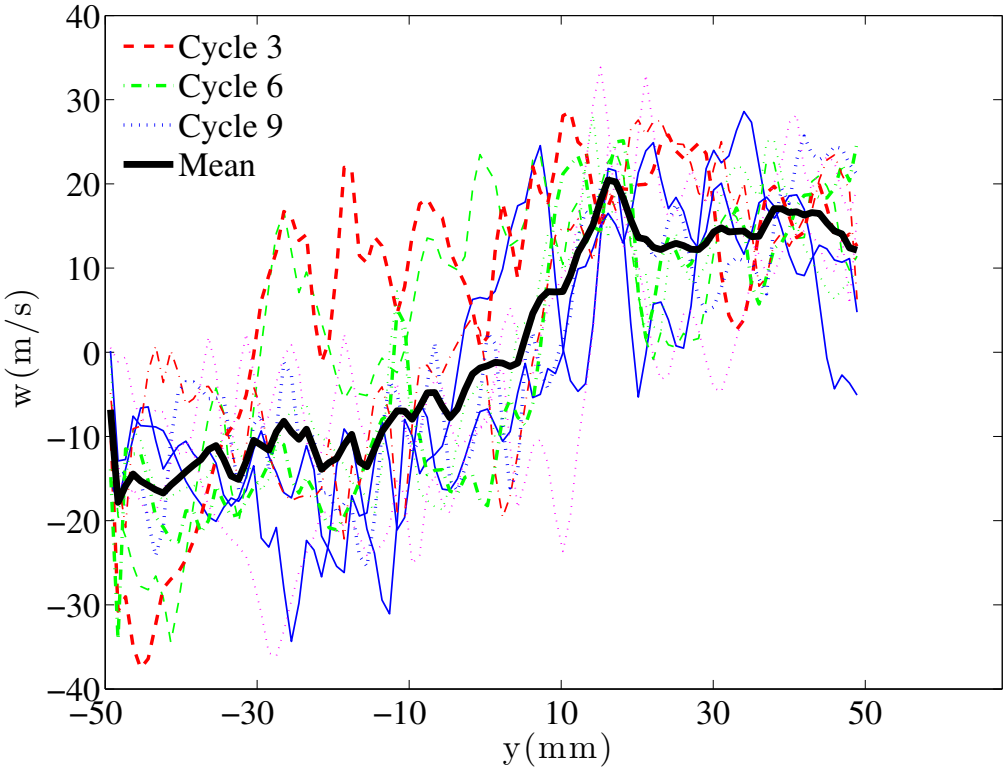

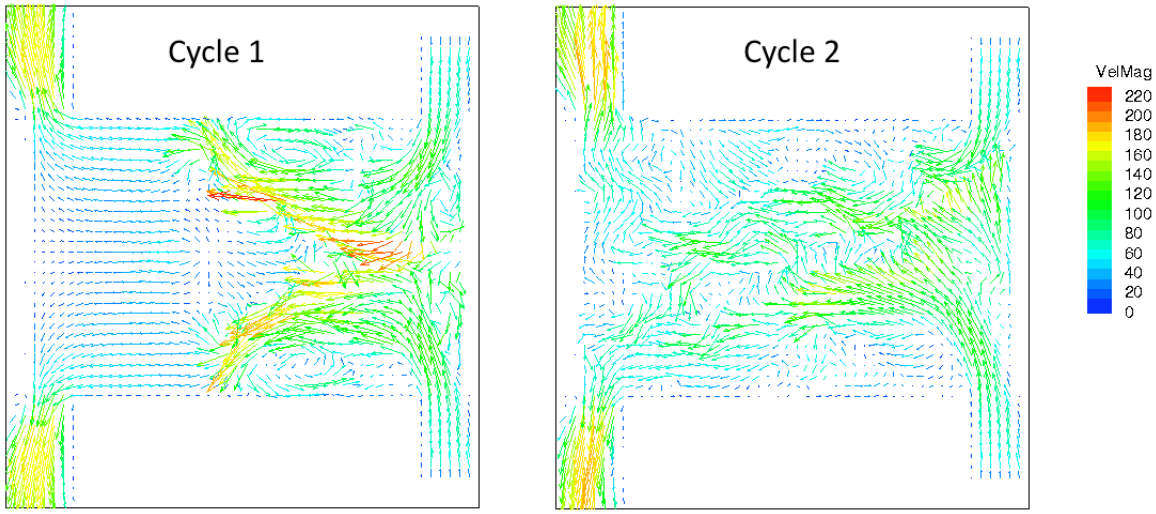

(a)

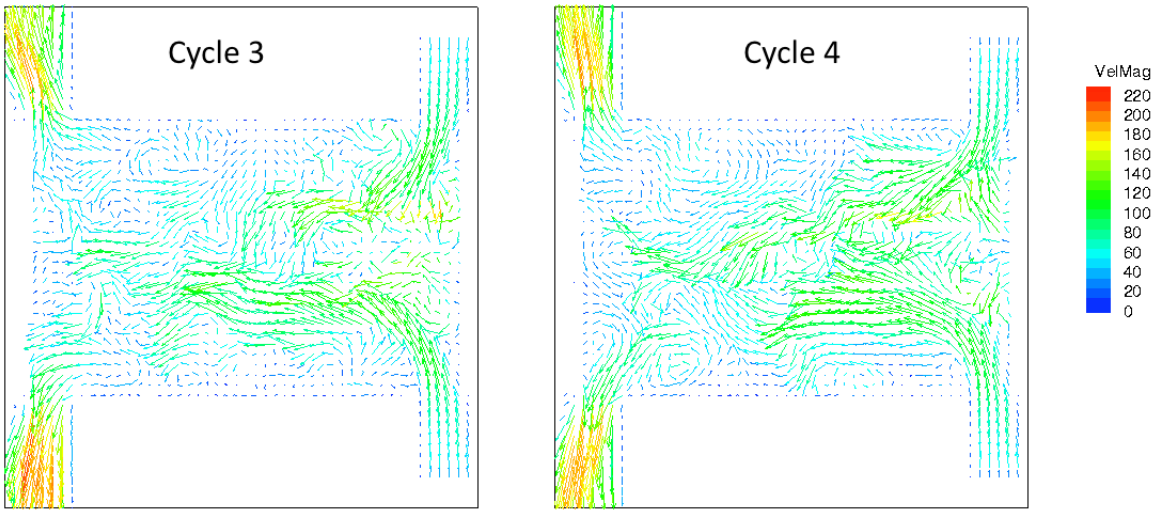

(b)

Figure 3.12: Velocity Vectors, colored by velocity magnitude, at a plane through the ports, parallel to the cylinder axis and at CA 30°, (a) Cycles 1 and 2, (b) Cycles 3 and 4, (c) Cycles 5 and 6, (d) Cycles 7 and 8 , (e) Cycles 9 and 10, and (f) Mean of 10 cycles.

Figure 3.12: (cont'd)

(c)

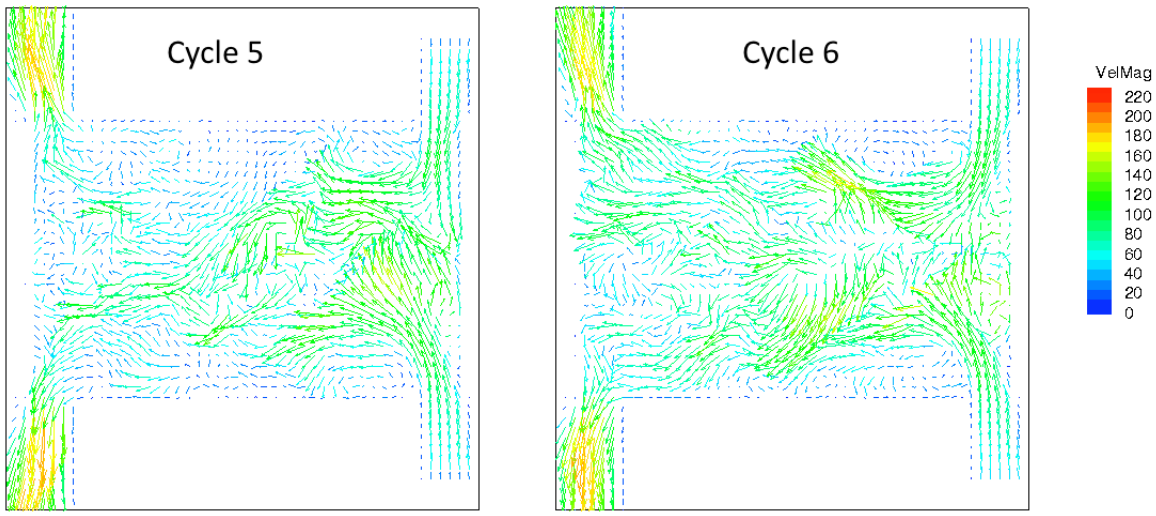

(d)

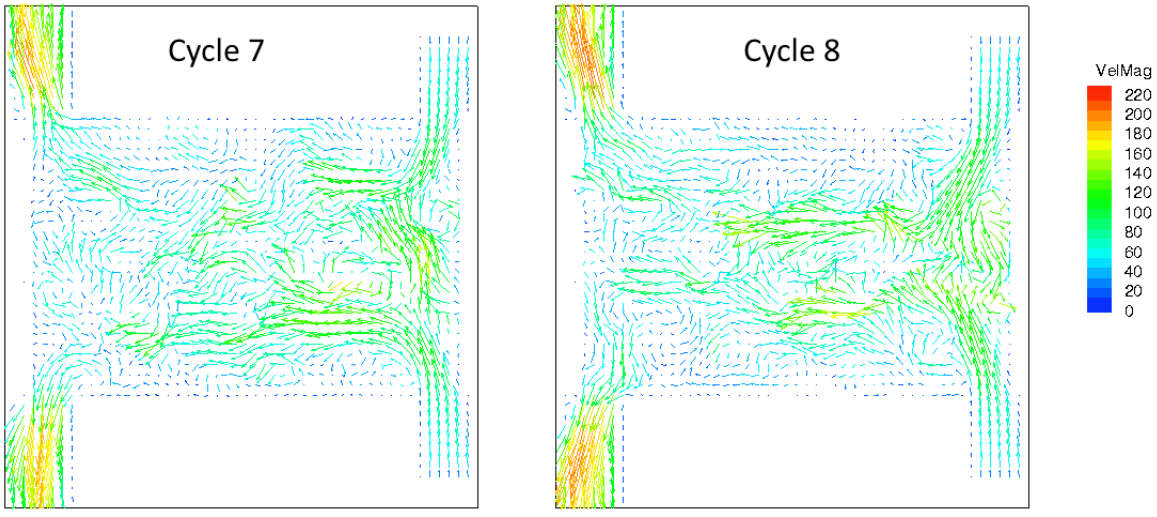

Figure 3.12: (cont'd)

(e)

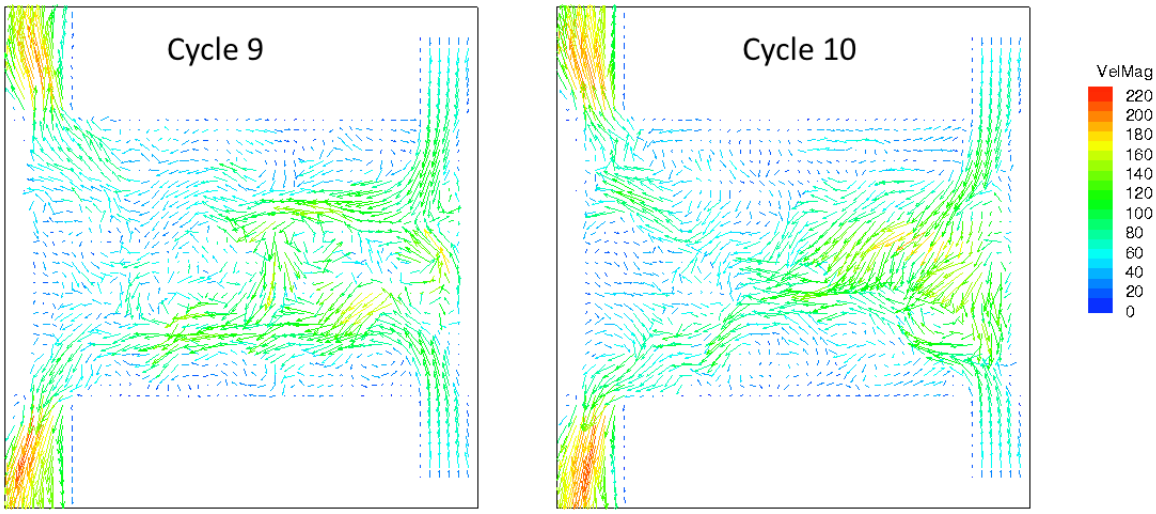

(f)

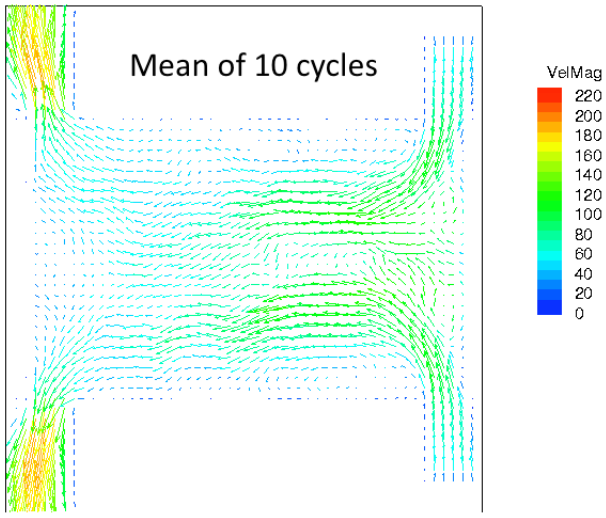

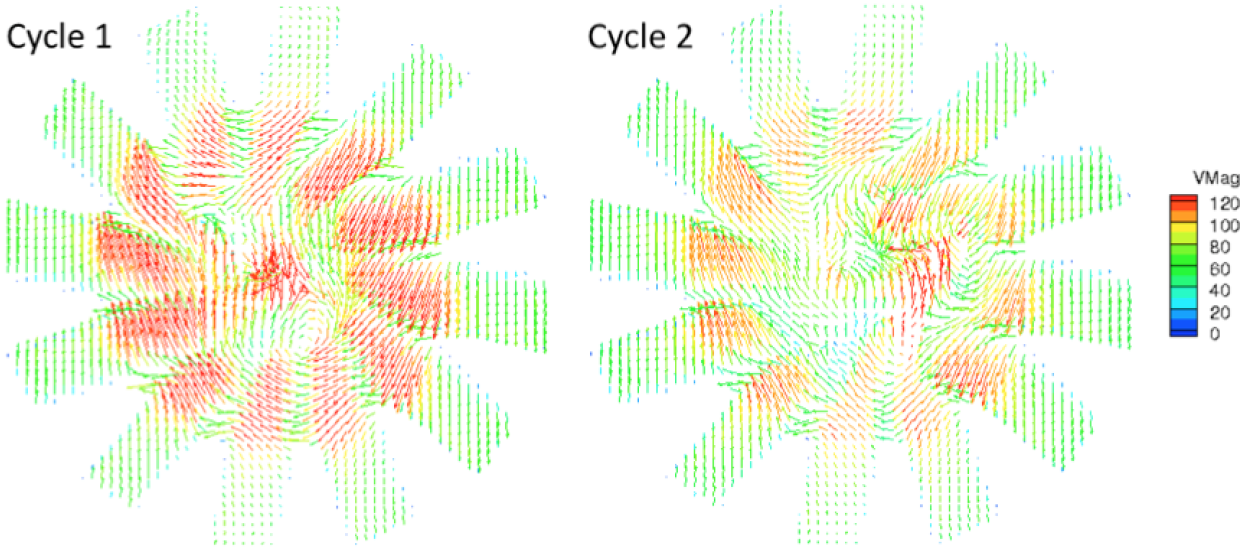

(a)

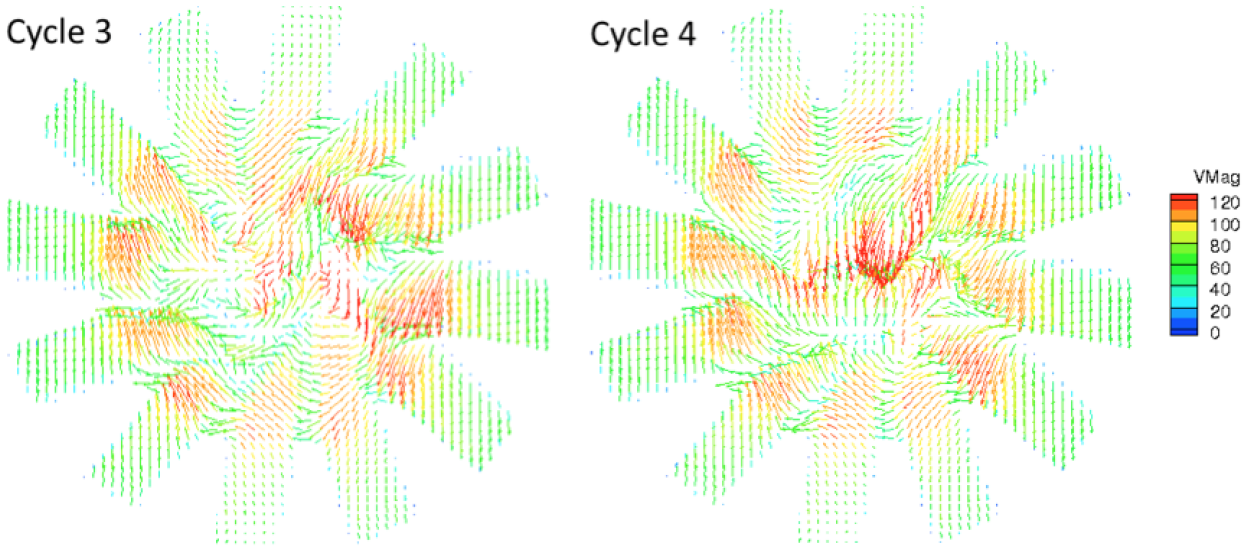

(b)

Figure 3.13: Velocity Vectors, colored by velocity magnitude, at a plane through the intake ports, Crank Angle 30 CA 30°, (a) Cycles 1 and 2, (b) Cycles 3 and 4, (c) Cycles 5 and 6, (d) Cycles 7 and 8, (e) Cycles 9 and 10, and (f) Mean of 10 cycles.

Figure 3.13: (cont'd)

(c)

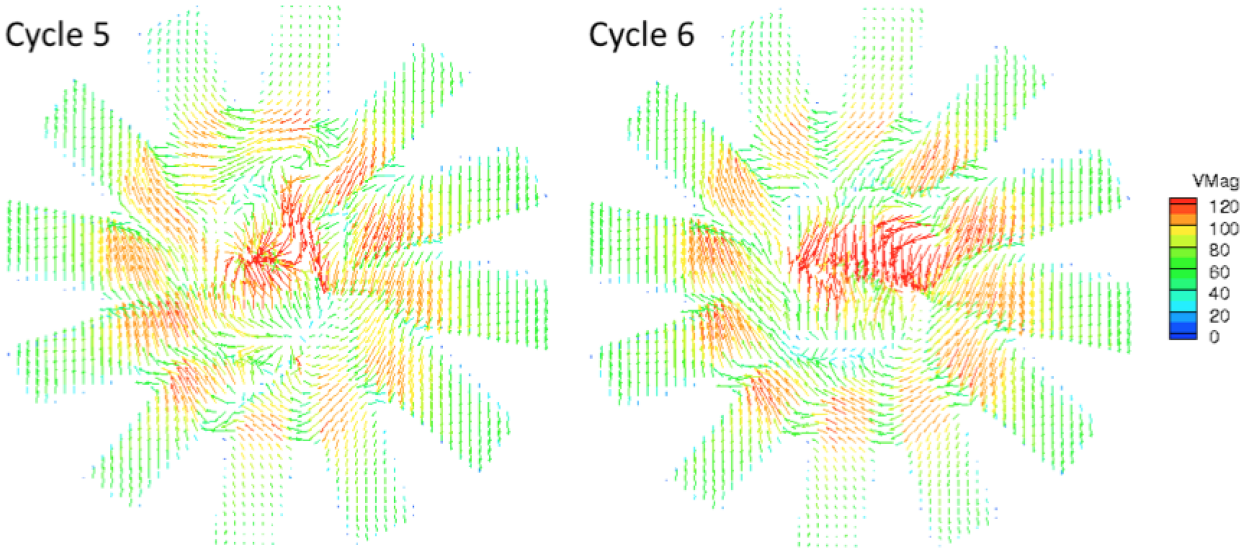

(d)

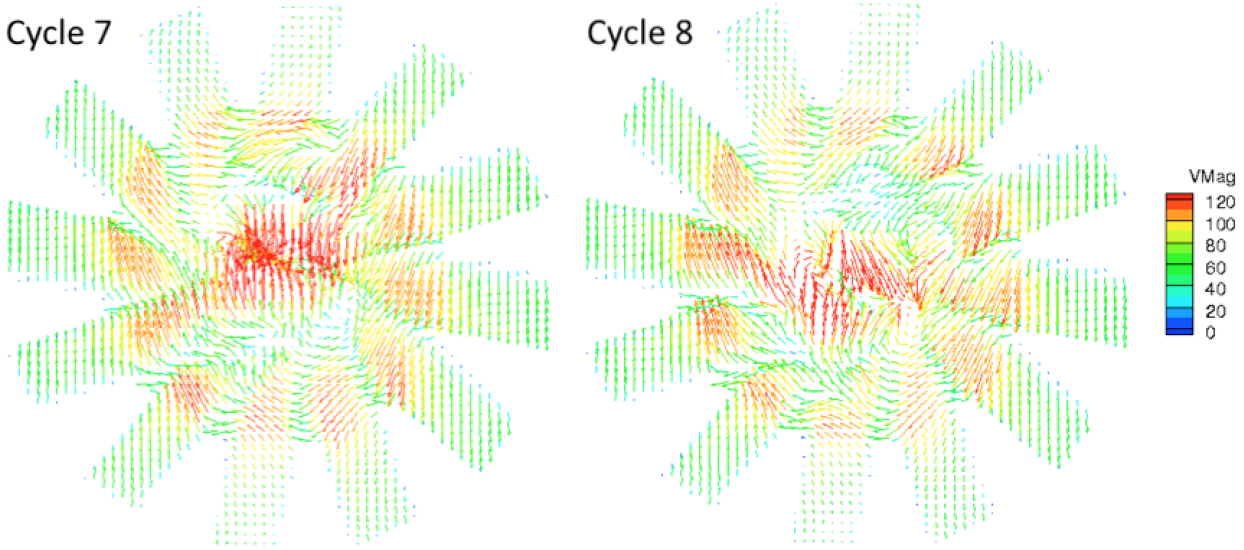

Figure 3.13: (cont'd)

(e)

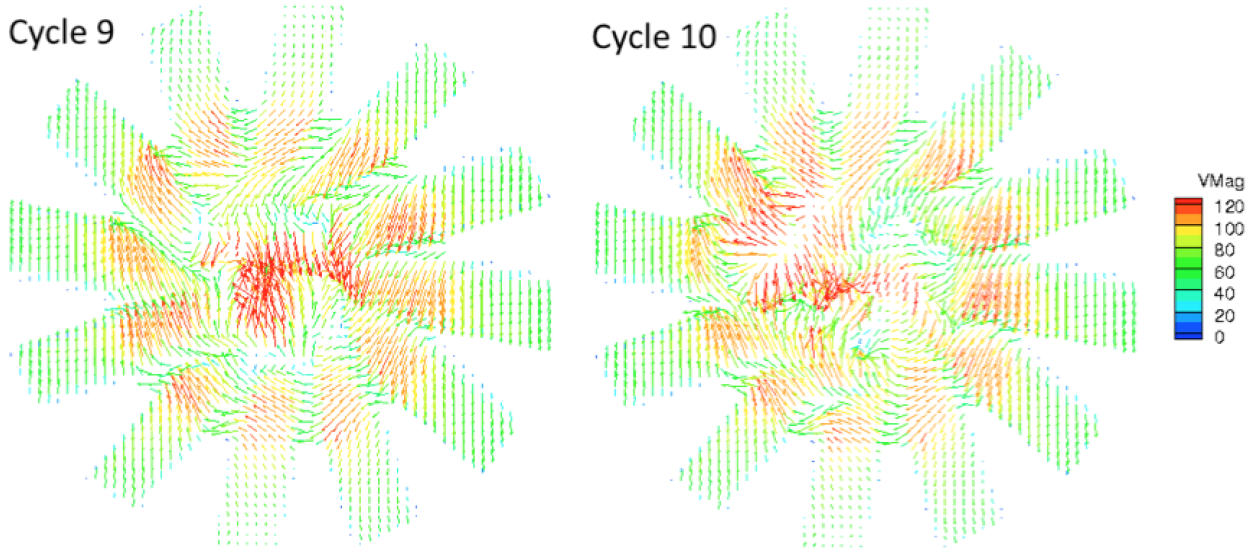

(f)

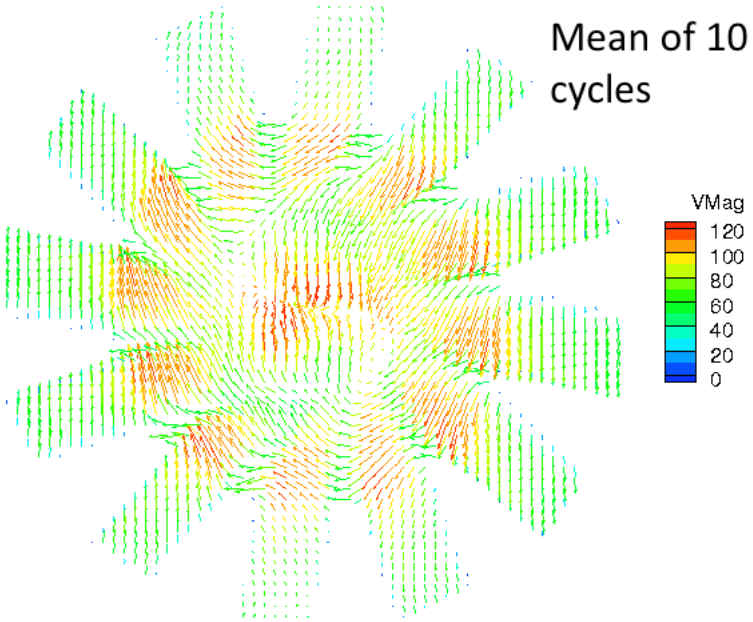

3.3.2 Effect of Heat Transfer Model

The heat transfer from the cylinder interior to the walls, particularly during compression and combustion is important to the overall energy balance and generates a thermal field in the metal parts which is of significant importance for determining the structural durability of these parts. Additionally the heat transfer model for the cylinder liner and piston walls can have a significant influence on the flow and temperatures inside the cylinder. The temperature wall boundary condition can be treated in several different ways; studies have been carried out assuming isothermal or adiabatic conditions. Ideally, a detailed analysis of the heat transfer would involve a combination of 1D and 3D tools and Conjugate Heat Transfer (CHT) models, but is beyond the scope of this study. Assuming isothermal conditions for the outer wall surfaces is reasonable since the temperature of these surfaces is maintained using a coolant circuit, but constant temperature assumption for the interior walls can lead to numerical issues and spurious results. Adiabatic boundary conditions can lead to over-predicted interior temperatures. However in this study, in the absence of experimental temperature results, adiabatic boundary conditions provide a means to validate the mean temperature values by comparing them to 0-D theoretical results. For an adiabatic flow, one can assume that

$$PV^k = constant$$

where P is the average in-cylinder pressure, V is the cylinder (trapped mass) volume and k is the adiabatic constant for the fluid. For the closed portion of the cycle (with both the intake and exhaust ports closed), the trapped mass inside the cylinder does not change and the adiabatic relation between the pressure and volume inside the cylinder may be assumed to hold. Figure compares the cylinder pressure obtained from the closed cycle simulation (with

adiabatic boundary conditions) with the pressure obtained using the adiabatic assumption. The two curves match indicating that the numerical errors in the simulation due to grid movement, compression, processor communication, etc. are minimal.

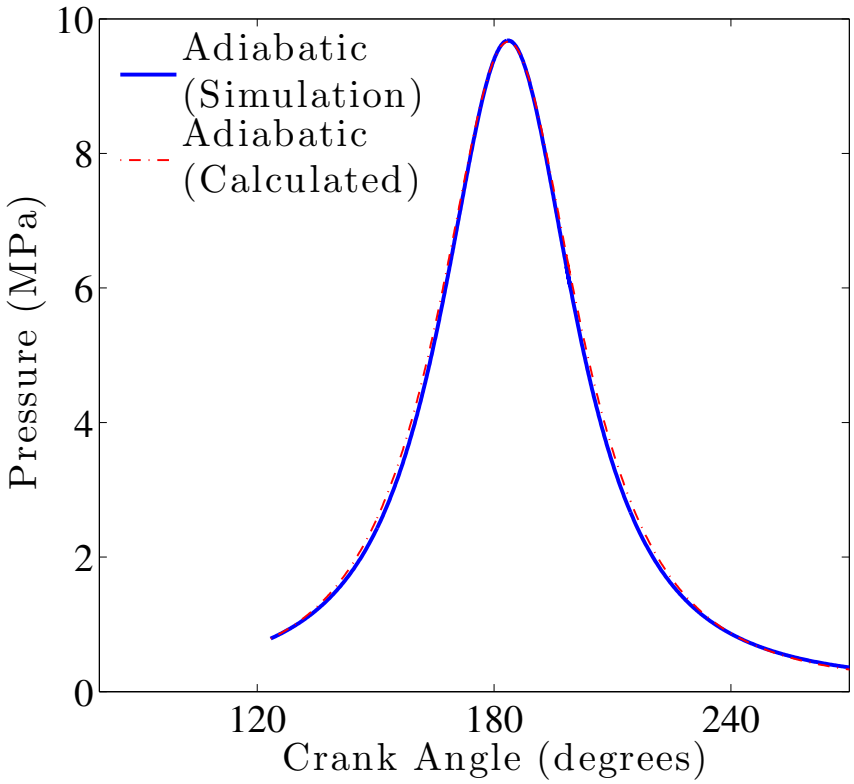

Figure 3.14: Comparison between the pressures obtained using adiabatic wall boundary condition and the adiabatic relation $PV^k = constant$ during the closed portion of the cycle.

In addition to adiabatic condition, simulations with wall heat transfer are also considered. The heat transfer model used in this study utilizes the energy balance for the inner wall to calculate the inner wall temperature based on the thermal conductance of the wall and the mean heat transfer coefficient inside the cylinder. Figure 3.15(a) illustrates the energy balance used to calculate the inner wall temperature. Here T_g is the mean gas temperature inside the cylinder, T_{wi} is the temperature of the inner wall, T_{wo} is the prescribed temperature at the outer wall, h_g is the mean convection heat transfer coefficient for the gas, k is the thermal conductivity for the metal wall, Δx_w is the thickness of the wall and Q is the

heat flux. Applying the energy balance, we get,

$$Q = \frac{kA(T_{wi} - T_{wo})}{\Delta x_w} = h_g A(T_g - T_{wi}) \tag{3.4}$$

Thus, the temperature of the inner wall is given by

$$T_{wi} = \frac{h_g T_g + (k/\Delta x_w)\, T_{wo}}{h_g + (k/\Delta x_w)} \tag{3.5}$$

The mean convective heat transfer coefficient is calculated as

$$h_g = \frac{Nu_g k_g}{D}\,, \tag{3.6}$$

where k_g is the gas thermal conductivity, D is the cylinder diameter, and Nu_g is the mean Nusselt number calculated as $Nu_g = 0.035Re^{0.8}$, where Re is the mean Reynolds number. Figure 3.15(b) compares the temperature profiles obtained using the adiabatic and wall heat transfer boundary conditions. For the heat transfer case, the outer walls of the cylinder liner and piston are assigned temperatures of $175°C$ and $200°C$, respectively. In order to ensure that there is no heat transfer from the walls to the interior, the walls are assigned a temperature equal to the mean temperature of the cylinder gas, as long as this temperature is below the values prescribed above. When the gas temperature rises due to compression and/or combustion, and exceeds the given temperature value, the prescribed value is assigned to the cylinder walls. The assigned wall temperature boundary conditions are shown in Figure 3.15(c). As can be seen in Figure 3.15(b), the peak temperature obtained for the heat transfer case is lower due to the energy loss to the outer walls, however the difference between the two cases would be much greater in a reacting case. The temperatures for

the cases with adiabatic or conductive walls are nearly the same before the compression stage, with the peak temperature obtained at the end of the compression. After the TDC, the adiabatic case exhibits a higher temperature as expected. Figure 3.15(d) shows the rms of the temperature for the two cases. The rms for the adiabatic case is very low as the temperature is nearly uniform in the cylinder interior and near the cylinder walls. In sharp contrast to the adiabatic case, the lower prescribed outer wall temperature creates a significant temperature gradient near the wall, thus a much higher rms value in the case of the heat transfer model.

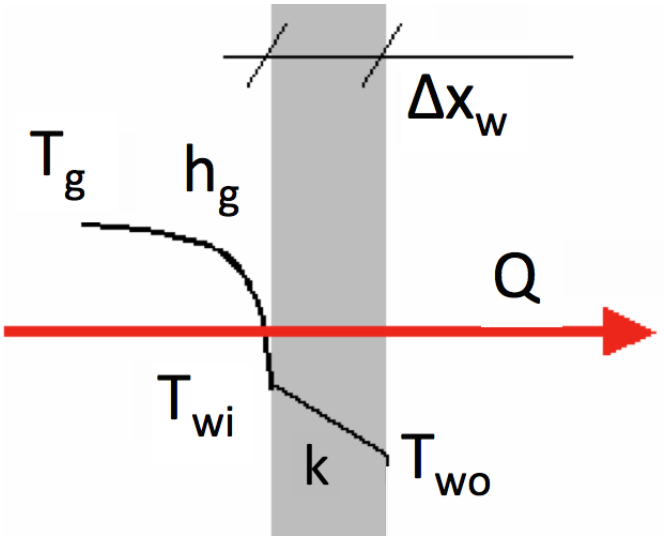

(a)

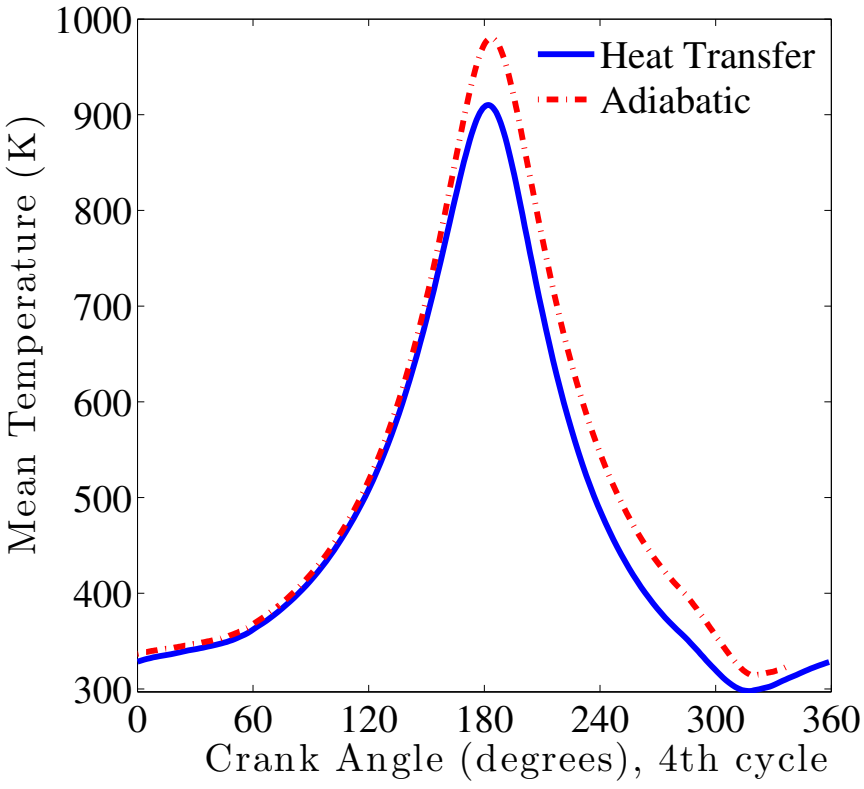

(b)

Figure 3.15: (a) Energy balance for the wall, (b) Mean Temperature comparison between adiabatic and wall heat transfer boundary conditions, (c) Wall temperature boundary conditions for the cylinder walls and piston for the heat transfer case, and (d) Temperature rms comparison between adiabatic and wall heat transfer boundary conditions.

Figure 3.15: (cont'd)

(c)

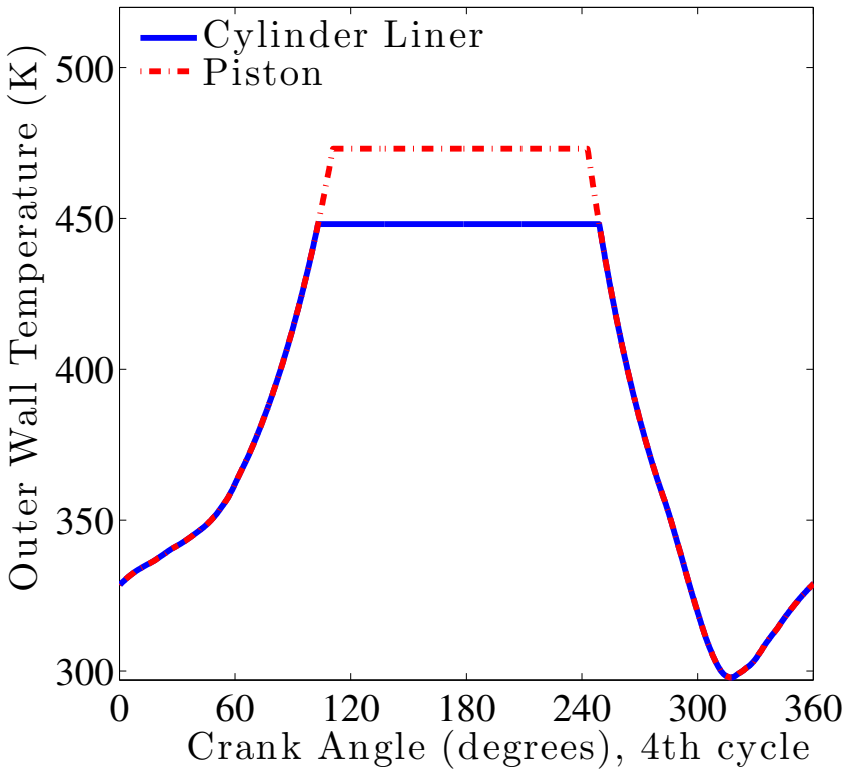

(d)

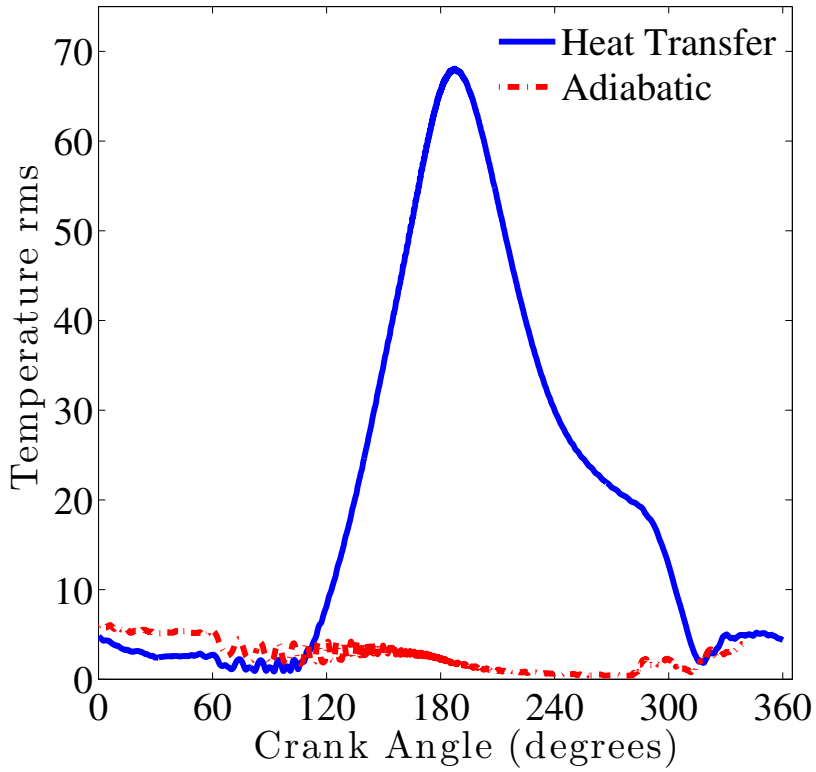

3.3.3 Effect of Port Angle

The swirl orientation or port angle of the intake ports depends upon many factors including the bore to stroke ratio and its value lies in the range 5 to 20° [170]. As the name suggests, the swirl orientation angle would be expected to have an effect on the magnitude of the swirl ratio, which is an important parameter in the design of internal combustion engines due to its potential effect on fuel-air mixing, combustion efficiency and emissions. In order to understand the effect of the port angle on various flow features, two different port angles were simulated, the baseline case, which has a port angle of 7.5°, and another geometry with a port angle of 15°. Other simulation parameters were kept the same. There is no difference in the mean temperature profiles for the two port angle geometries (Figure 3.16(a)) since the trapped mass, and hence the temperature, is controlled by the pressure differences, which do not change with the port angle. The swirl ratio follows similar trends in both cases as seen in Figure 3.16(b), however the peak value is about 80% higher in the case with port angle of 15°. As can be observed in Figures 3.16(c) and 3.16(d), the tumble ratio magnitudes do not differ significantly. The signs are opposite but this can be accounted for by the CCV in tumble ratios observed previously.

Figure 3.17 compares the rms values of temperature and velocity components. As expected, the temperature rms values are nearly the same for all crank angles, except at the TDC when the higher port angle has a slightly lower rms. This can be explained by the mean Nusselt (Nu) number and the heat transfer coefficient for the two cases shown in Figures 3.17(e) and 3.17(f), respectively. The case with port angle of 15° has a relatively higher mean in-cylinder velocity leading to a higher Nu, and consequently a higher heat transfer coefficient. Consequently, at the TDC the higher heat transfer coefficient generates more

uniform temperature field near the walls and hence a lower temperature rms. The rms of the u-velocity (Figure 3.17(b)) is nearly the same for both cases except during the opening and closing of the intake ports, when the second case has slightly higher velocities. The rms of the radial velocity components is about $15 - 20\%$ higher for the higher port angle case as depicted in Figures 3.17(c) and 3.17(d). This is due to the higher angular momentum of the incoming jets. In summary, the primary effect of increasing the port angle is increasing the swirl ratio, which in turn can affect the turbulence levels and mixing. In general, a larger parametric study would be required to determine the optimum port angle for the proposed application. For this study, the geometry with port angle 7.5° is used as the baseline case.

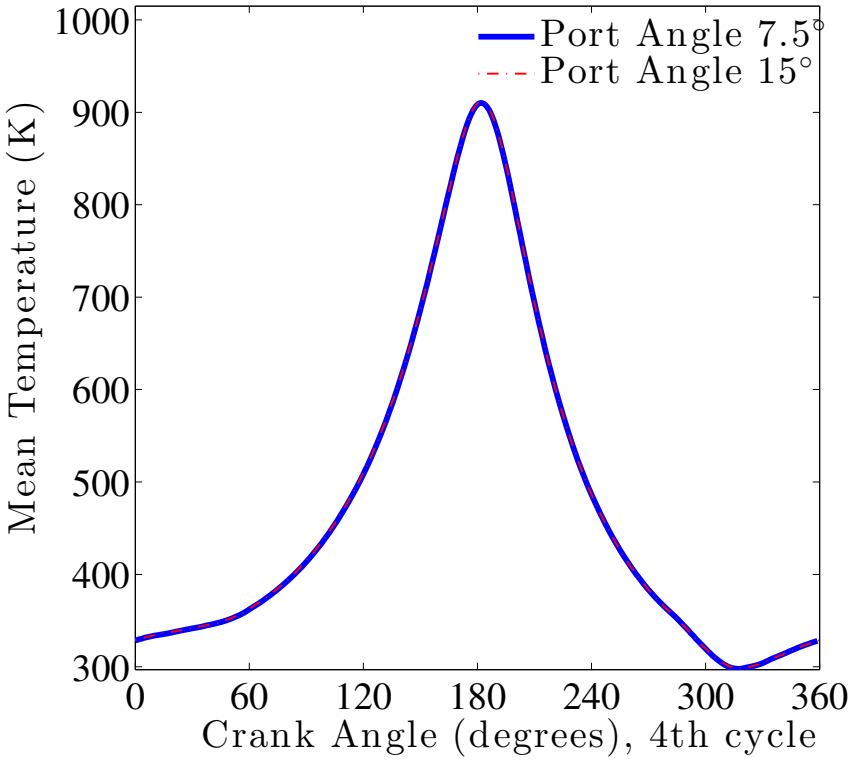

(a)

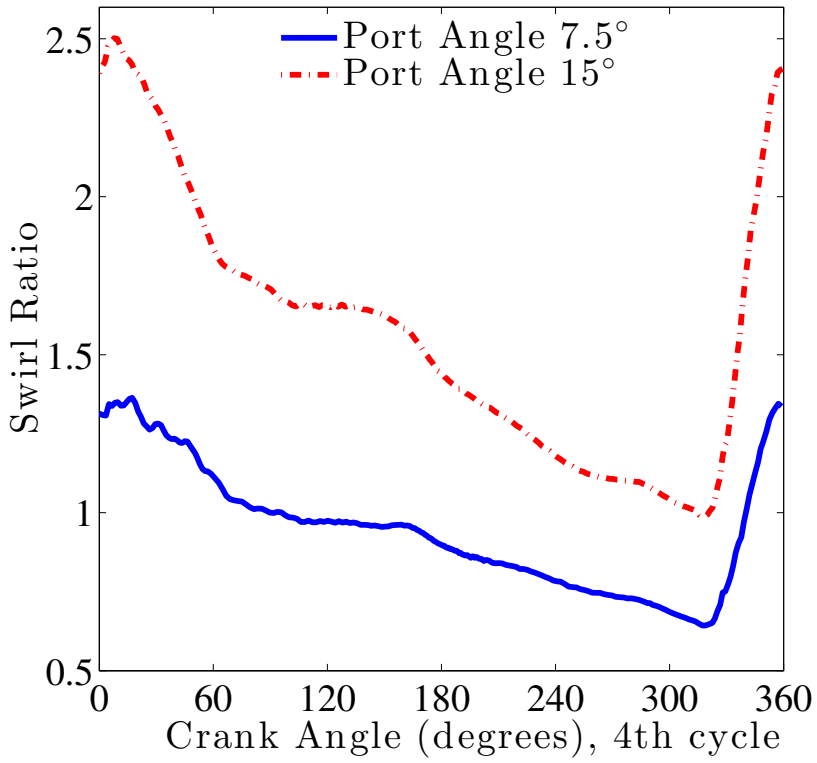

(b)

Figure 3.16: Comparison between the mean flow features for different port angles, (a) Mean Temperature, (b) Swirl Ratio (SR_x), (c) Tumble Ratio y (TR_y), (d) Tumble Ratio z (TR_z).

Figure 3.16: (cont'd)

(c)

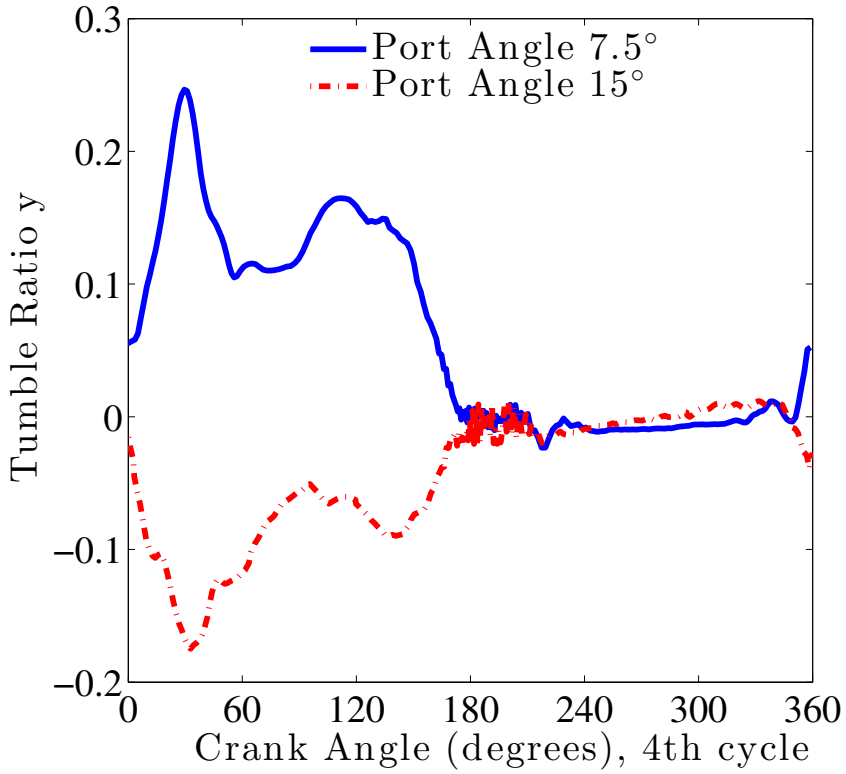

(d)

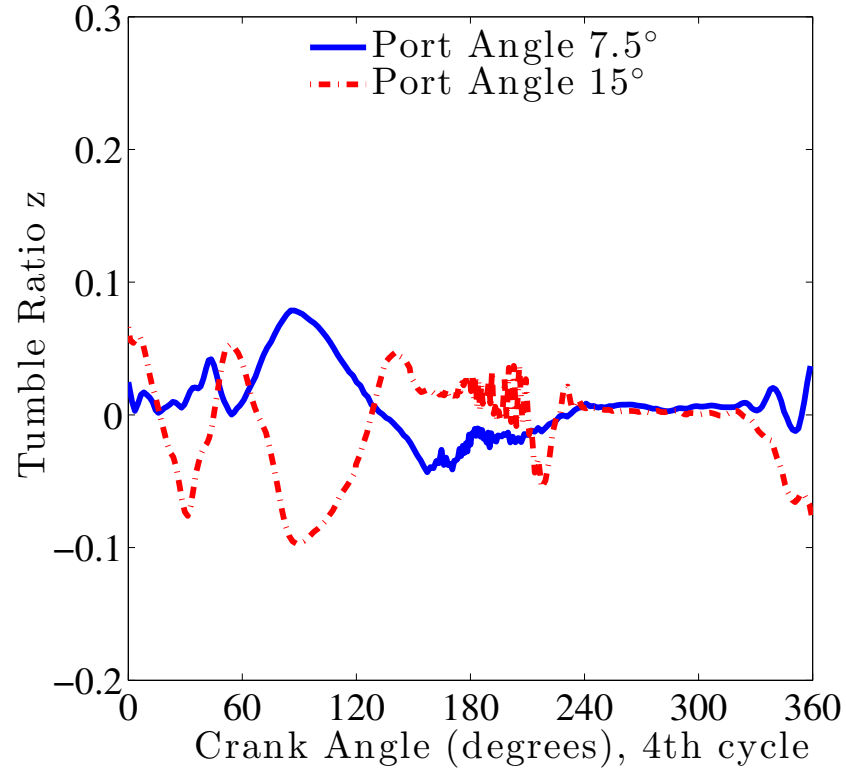

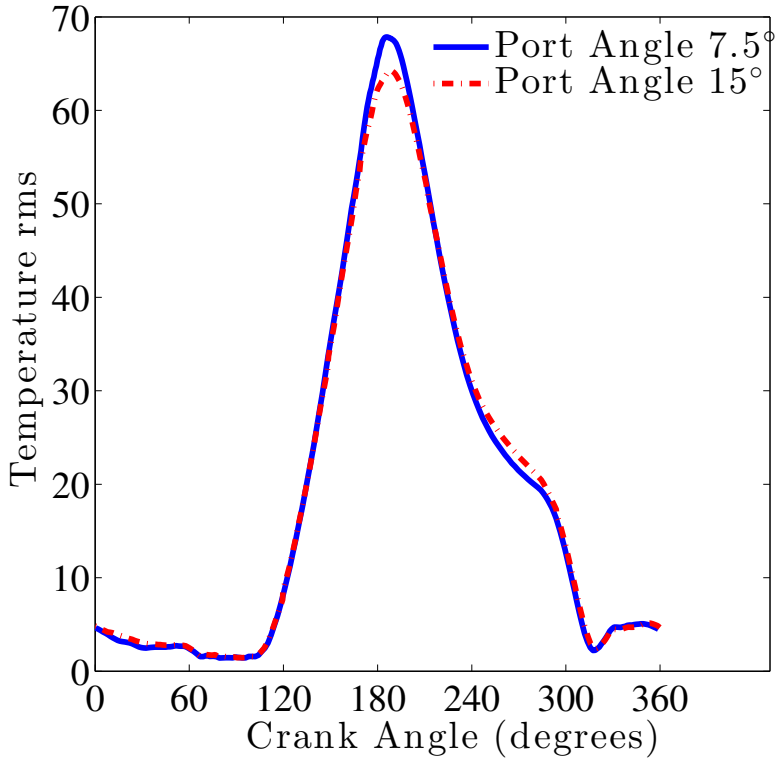

(a)

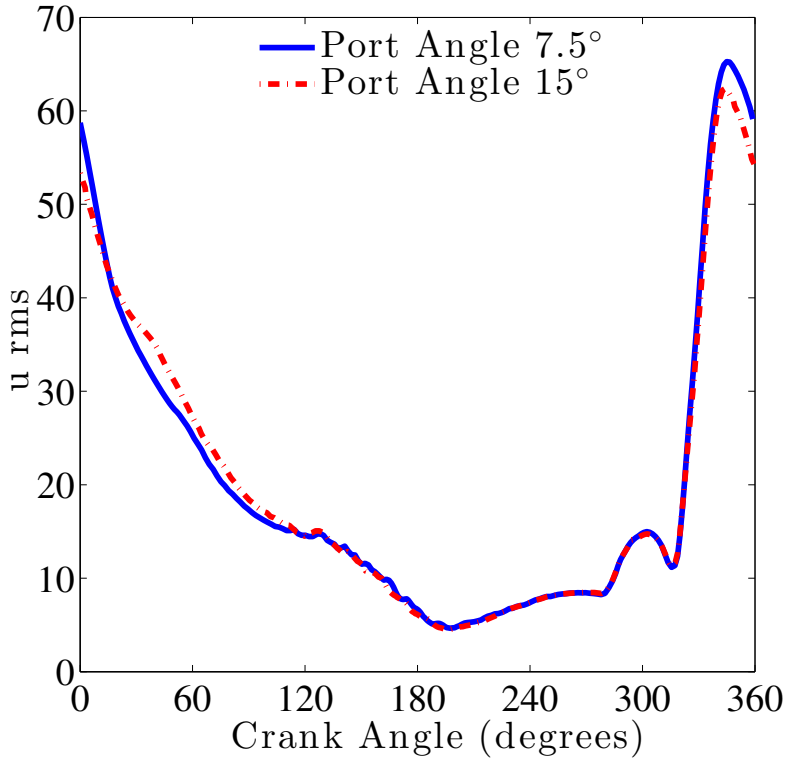

(b)

Figure 3.17: Comparison between the rms values for different port angles and heat transfer coefficients, (a) Temperature rms, (b) u rms, (c) v rms, (d) w rms , (e) Mean Nusselt number, (f) Mean heat transfer coefficient.

Figure 3.17: (cont'd)

(c)

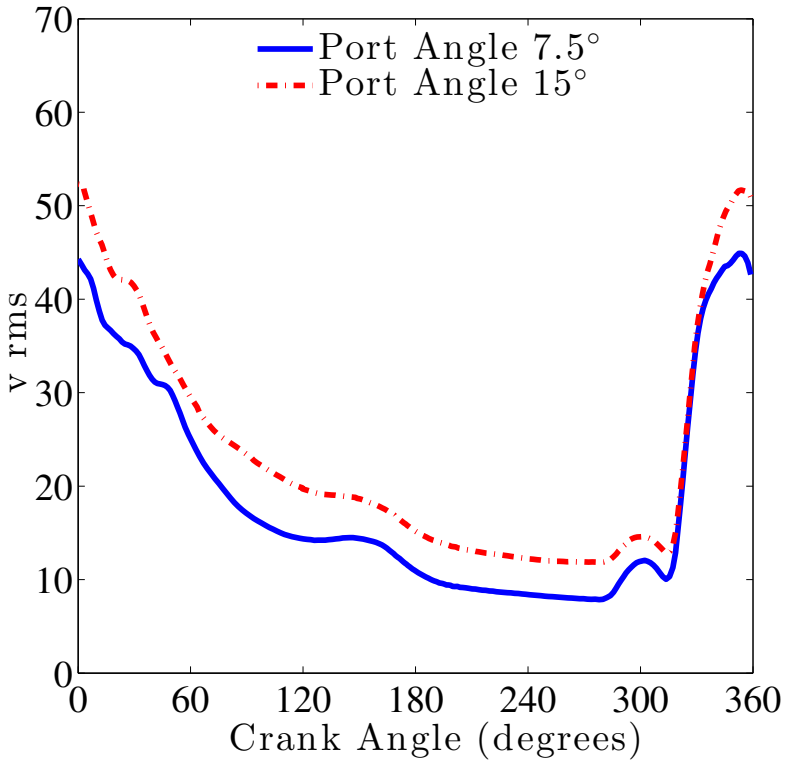

(d)

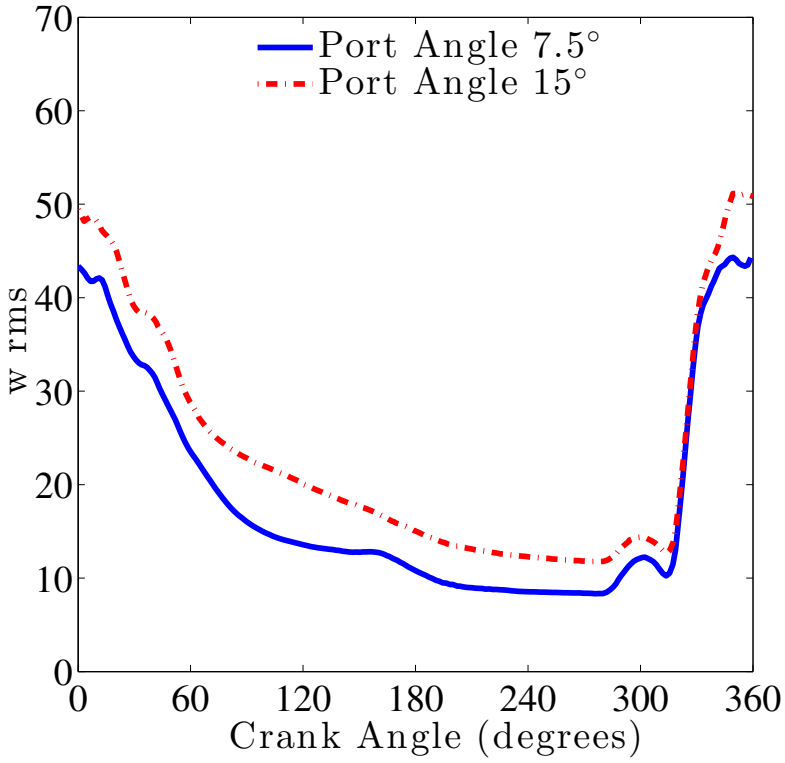

Figure 3.17: (cont'd)

(e)

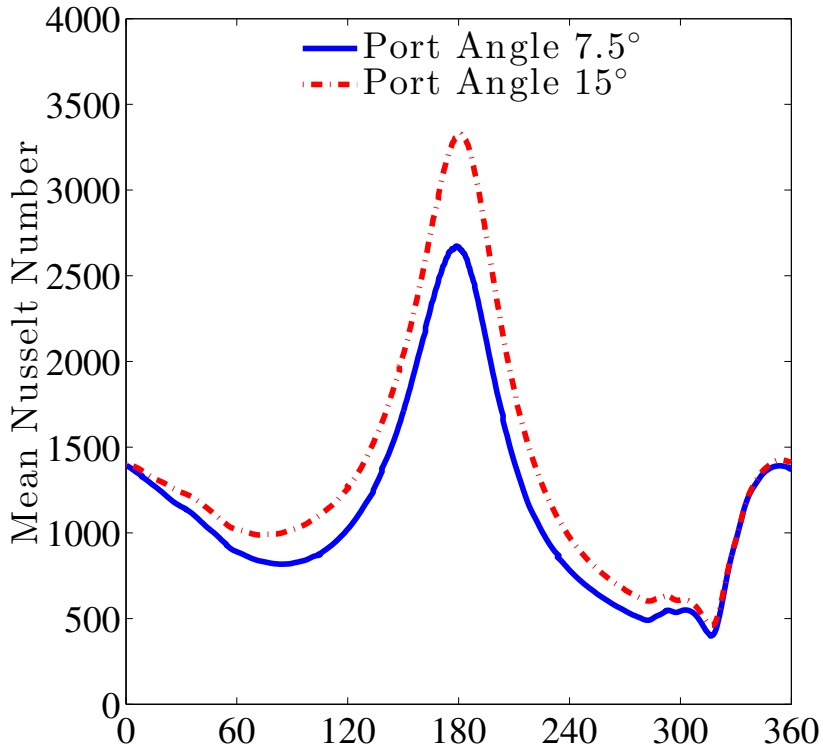

(f)

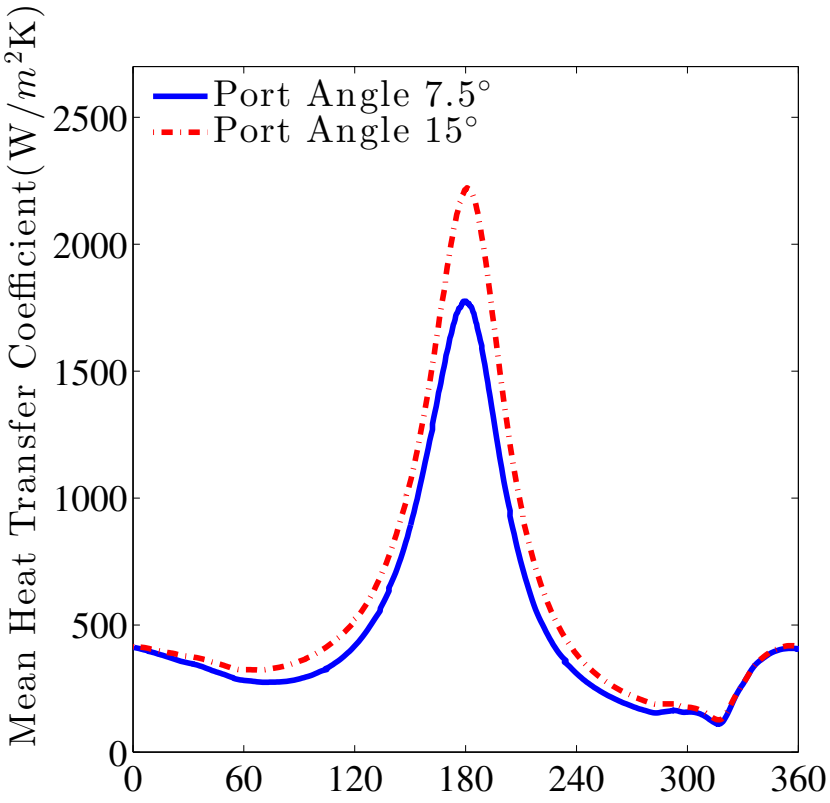

3.3.4 Effect of Backpressure

Turbocharging is a common technique employed to increase the efficiency and power of the internal combustion energy by forcing extra air into the combustion chamber. Increasing the pressure difference between the cylinder and intake ports forces more air into the engine as compared to a "naturally charged" engine and proportionately more fuel can be added to the system to increase the power output. The boost pressure or the excess pressure above atmospheric pressure that is applied to the intake ports is limited by the thermal and mechanical considerations for the system. As the pressure of the intake air is increased its temperature also increases, thus reducing the density and consequently the availability of oxygen for combustion. This necessitates the use of intercoolers after the turbocharger to cool down the air. While simulating the boosted operation of an engine, it is necessary that sufficient precautions are taken to ensure that correct temperature and pressure boundary conditions are applied. Two boost pressure conditions are included in this study. The various parameters of the turbocharger and intercooler are selected such that the effective pressures at the intake port boundaries are 2 atm and 3 atm, respectively, for the two cases considered in this study. The following process was utilized here to calculate the intake temperature for the two boosted conditions considered. Assuming that the pressure drop in the intercooler is 0.18 atm, the pressure at the intercooler exit is $P_f = 1 + B - 0.18$, where B is the boost pressure. The pressure ratio of the turbocharger is thus $P_{tc} = 1+B$. The output temperature of the turbocharger, $T_{out,tc}$ or the input temperature of the intercooler, $T_{in,intc}$, is thus given by

$$T_{in,intc} = T_{out,tc} = T_{in,tc}\left(1 + \frac{P_{tc}^{0.286} - 1}{\eta_{tc}}\right) \tag{3.7}$$

where η_{tc} is the efficiency of the turbocharger. If the efficiency of the intercooler is η_{intc}, the output temperature of the intercooler, $T_{out,tc}$ is given by,

$$T_{out,intc} = T_{in,intc} - \eta_{intc}(T_{in,intc} - T_{in,tc})$$

$$= T_{in,tc}\left[1 + \frac{(q - \eta_{intc})}{\eta_{tc}}(P_{tc}^{0.286} - 1)\right] \tag{3.8}$$

For the purpose of this study, it is assumed that the efficiency of both the turbocharger and intercooler is 60%. Thus, assuming that intake temperature of the air at the turbocharger is 300 K. Thus, the conditions in the two cases simulated are,

Case 1: Pressure at intake port = 2 atm $B = 1.18, P_d = 0.18atm, \eta_{tc} = 0.60, \eta_{intc} = 0.60, T_{in,tc} = 300K$ $T_{out,intc} = 349.94K$.

Case 2: Pressure at intake port = 3 atm $B = 2.18, P_d = 0.18bar, \eta_{tc} = 0.60, \eta_{intc} = 0.60, T_{in,tc} = 300K$ $T_{out,intc} = 378.44K$

Figure 3.18(a) compares the mean temperature inside the cylinder for the two cases. Since the total mass of the trapped air is higher for the higher boost pressure and the temperature of the incoming air is also slightly higher, the mean temperature achieved at the TDC is also higher. This indicates that the temperature and pressure inside the cylinder after combustion would also be higher, which can lead to combustion instabilities and higher emissions, limiting the amount of boost that can be applied to an engine. Figure 3.18(b) compares the swirl ratio for the two cases and it can be seen that applying a higher boost pressure leads to significantly higher swirl inside the cylinder. This is due to the higher overall momentum and angular momentum of the incoming flow due to the existence of higher pressure-gradients. This can potentially have a positive effect on mixing and combustion, and can offset some of the disadvantages of a higher combustion temperature. The tumble

ratios are also higher in the higher boost pressure case, as seen in Figures 3.18(c) and 3.18(d), and this can also enhance mixing and combustion.

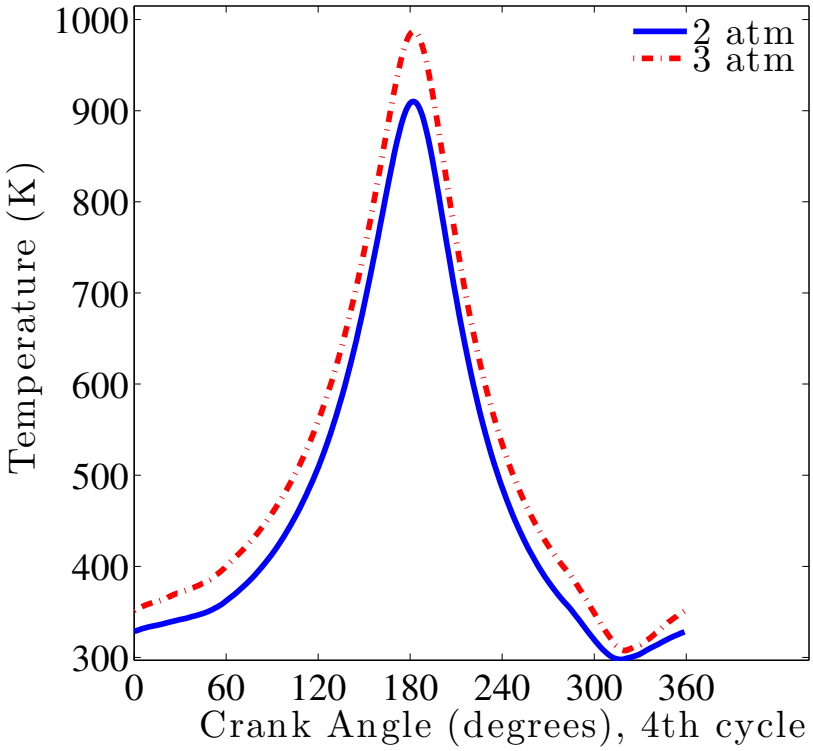

(a)

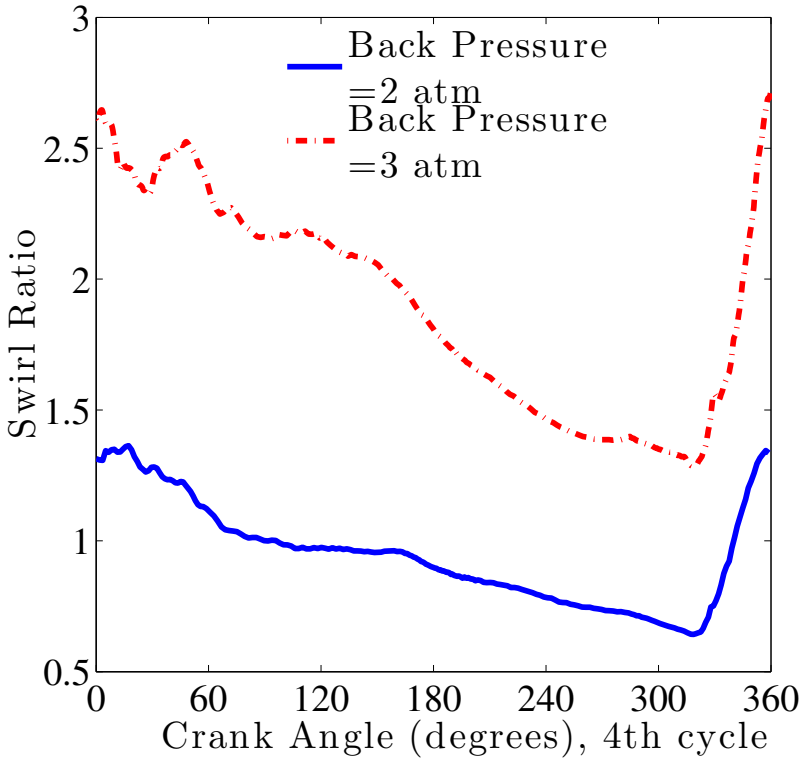

(b)

Figure 3.18: Comparison between the mean flow features for different back pressures, (a) Mean Temperature, (b) Swirl Ratio (SR_x), (c) Tumble Ratio y (TR_y), (d) Tumble Ratio z (TR_z).

Figure 3.18: (cont'd)

(c)

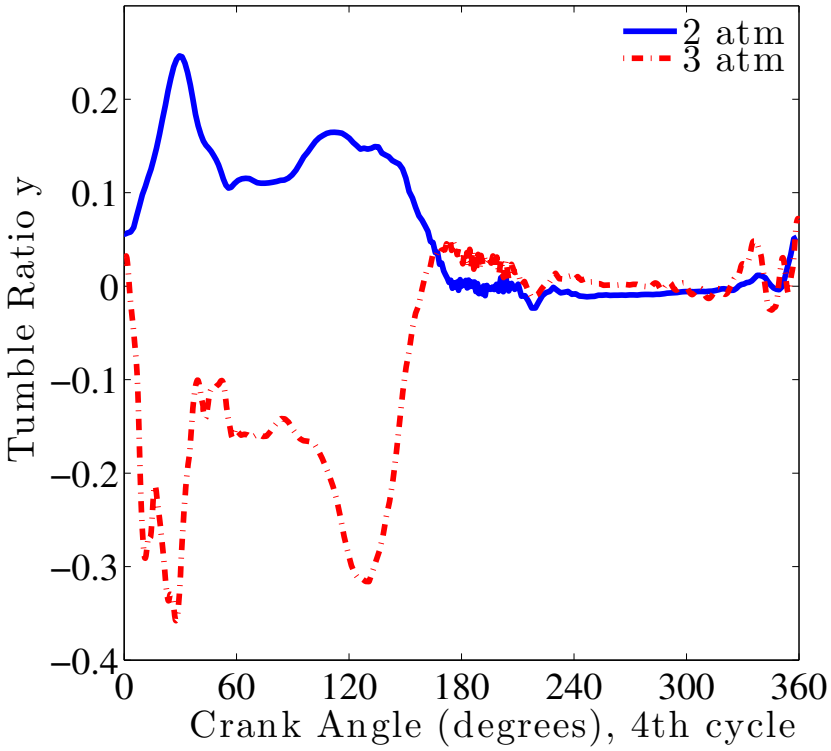

(d)

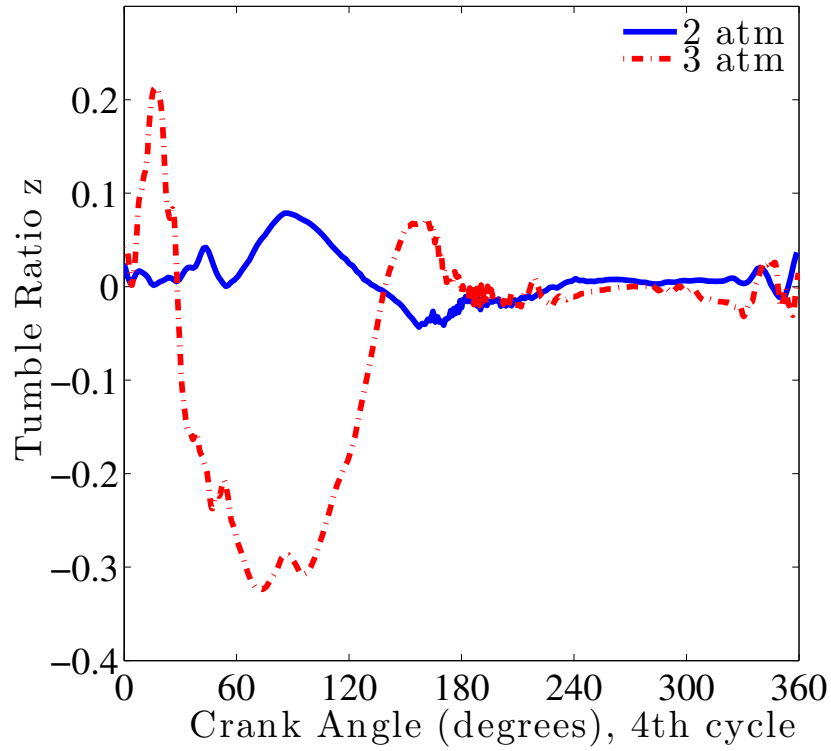

The temperature rms values and mean heat transfer coefficients are compared for the two boost pressures in Figures 3.19(a) and 3.19(b), respectively. A back pressure of 3 atm leads to a heat transfer coefficient which is about 90% higher than that seen in the lower back pressure case, thus causing a lower temperature rms near the TDC. Due to higher pressure difference between the cylinder and the intake ports, the velocity of the incoming jets is higher for the higher boost pressure, resulting in more variation in the velocities in the cylinder and increased rms values for the velocity components as seen in Figures 3.19(c), 3.19(d) and 3.19(e). In summary, applying a higher back pressure increases the mean temperatures, turbulence and mixing, but is limited by the potential onset of combustion instabilities and higher emissions.

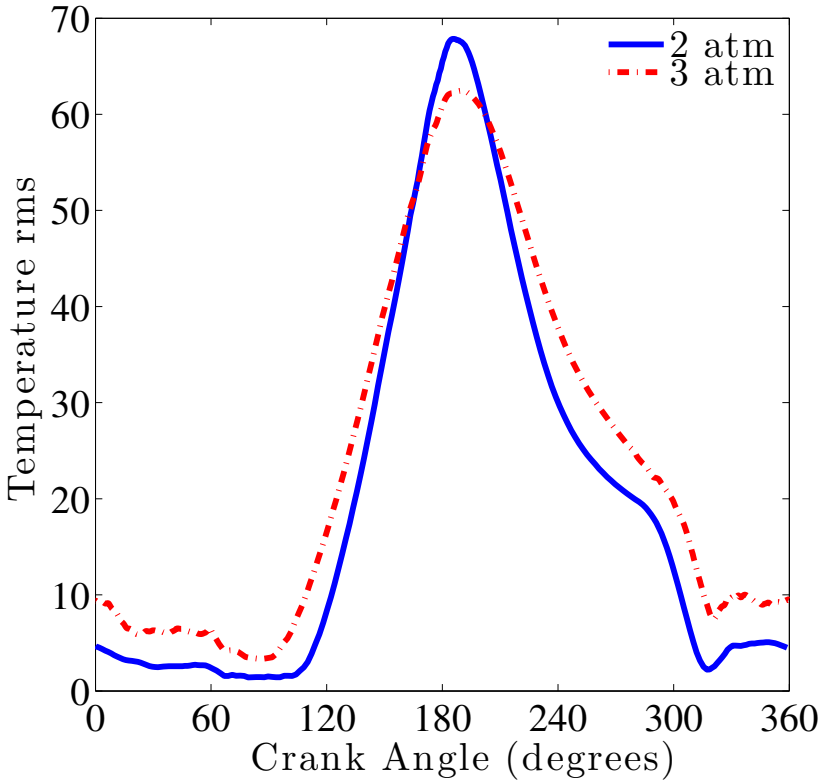

(a)

Figure 3.19: Comparison between different back pressures, (a) Temperature rms, (b) Mean heat transfer coefficient, (c) u rms, (d) v rms, (e) w rms.

Figure 3.19: (cont'd)

(b)

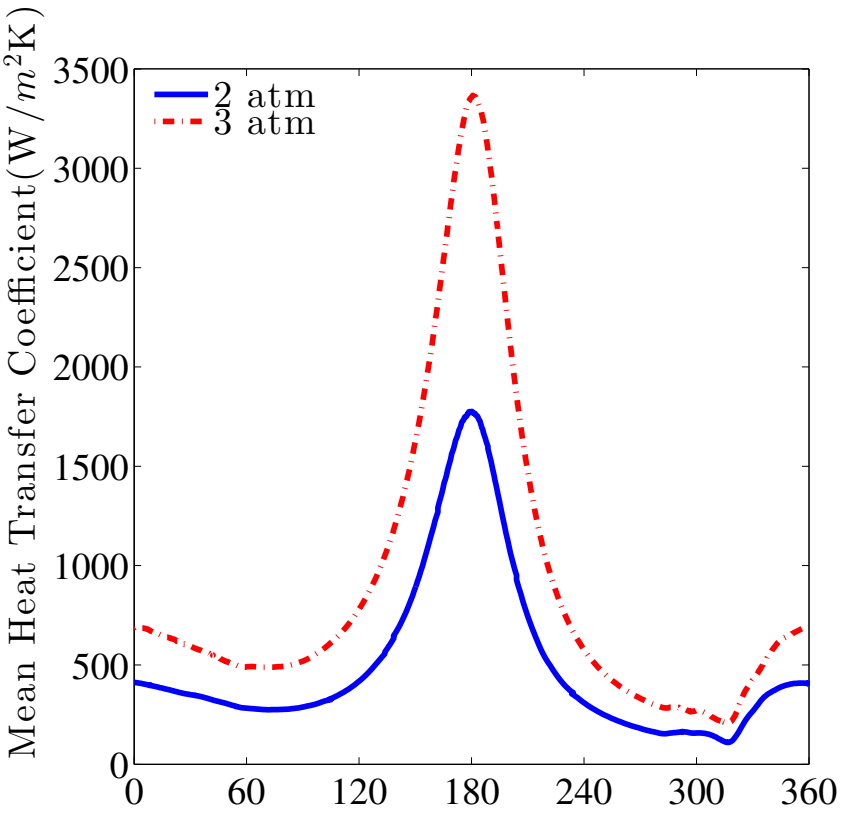

(c)

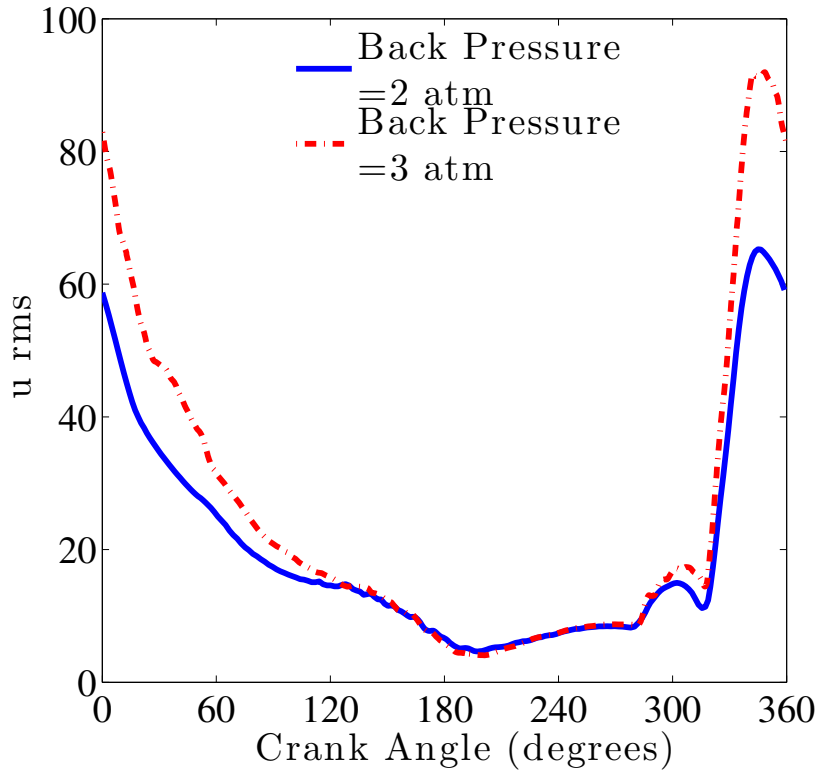

Figure 3.19: (cont'd)

(d)

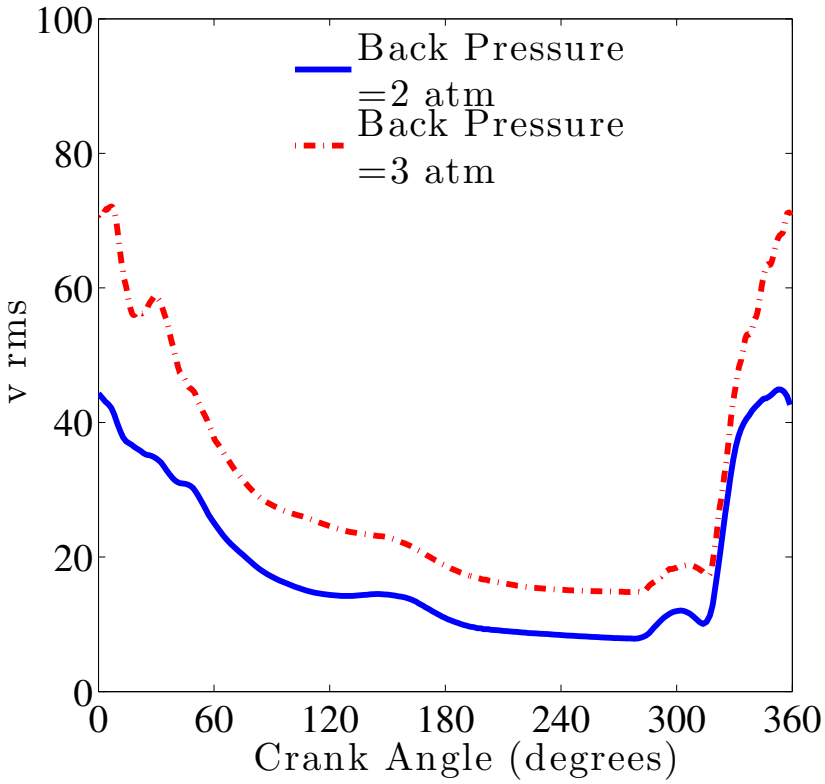

(e)

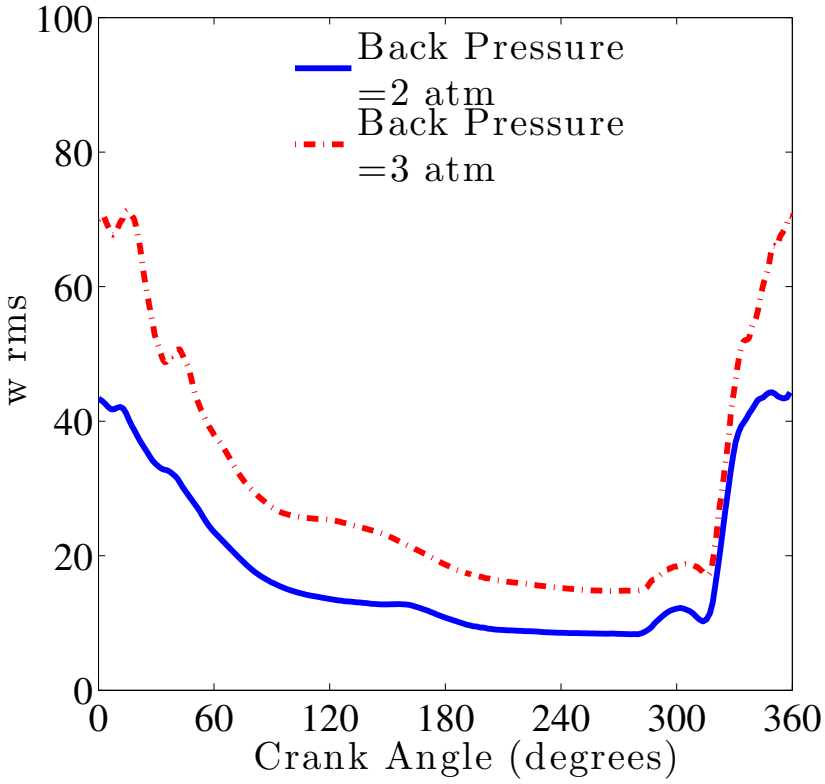

3.4 Results and Discussions: Non-reacting Flows with Sprays

Spray and combustion of n-dodecane is studied for the opposed-piston configuration using the two-phase compressible scalar LES/FMDF model previously described in Chapter 2 of this dissertation. N-dodecane is used here as a surrogate for diesel. The injector parameters, namely the injector orientation with respect to the pistons and cylinder walls and the spray angles need to be optimized to ensure proper fuel-air mixing and minimal interaction of the spray plume with the walls. For the opposed piston engine, the spray requirements differ from conventional diesel engines as detailed in the study by Hofbauer [166]. The nozzle tip needs to be mounted at the border of the combustion chamber instead of the center of the chamber and the spray orientation is rotated 90 degrees as compared to the conventional engines, in which case it points in the direction of the piston. The number of nozzle holes and hole diameter are limited by the bowl geometry and sprays are directed from the high charge density outer regions to the low charge density chamber center. The injector configuration best suited for the opposed piston engines is the side configuration in which the fuel is injected in the high charge density outer regions and penetrates into the center of the chamber. This requires relatively large nozzle diameters. Since the side injection configuration results in the main direction of the injection being towards the center of the combustion chamber, the in-cylinder swirl plays an important role in the fuel penetration and its mixing in other regions of the cylinder and is generally kept low in magnitude. In the study by Hofbauer [166], several injector configurations were tested to optimize the air-fuel mixture formation with two controlling parameters, the air utilization, which was maximized and the wall-fuel

contact, which was minimized. Two side injectors, each with 3-hole nozzles, were found to be better, compared to two side injectors with four nozzles. In order to avoid contact between the two middle sprays from opposite injectors, these sprays were inclined by 5°. The outer sprays were inclined by an additional 7° to make the spray flatter and to ensure better mixture distribution in the cylinder. In this study, a similar injector configuration with two opposite side mounted injectors is used and is shown in Figure 3.20(b). The injector location and the spray orientation differ from the spray angles discussed above and are given in Table 3.2. The parameters Tiltxy and Tiltyz in this table give the angles of the spray on the xy and yz planes as shown in Figure 3.20(c). The parameters x_{inj}, y_{inj}, and z_{inj} specify the location of the nozzle from the coordinate system origin and as shown in Figure 19(b).Various injection parameters described in Table 3.3 have been studied for the non-reacting sprays. The effect of the nozzle diameter, injection pressure and temperature of injection on the spray evolution have been of considerable interest to the engine research community in the past. Siebers [42] studied the effect of various spray parameters on the liquid penetration length of the fuel in a closed combustion chamber with quiescent conditions. Details of the experiment have been described in Chapter 1 of this dissertation. Validation studies of the spray models used in this study have also been presented earlier in Chapter 1. The computational model has been tested for a wide range of ambient conditions and for a variety of fuels including single component and multicomponent fuels with 2 to 8 species. The spray models used in this study are presented in Table 3.4, while Table 3.5 gives details of various cases studied with different nozzle and injection parameters, viz. the nozzle hole diameter, the injection pressure, the injected liquid temperature, the injection duration and the cone angle of the spray for each individual nozzle hole.

The start of injection (SOI) is at CA=160° and the duration of injection is varied with the

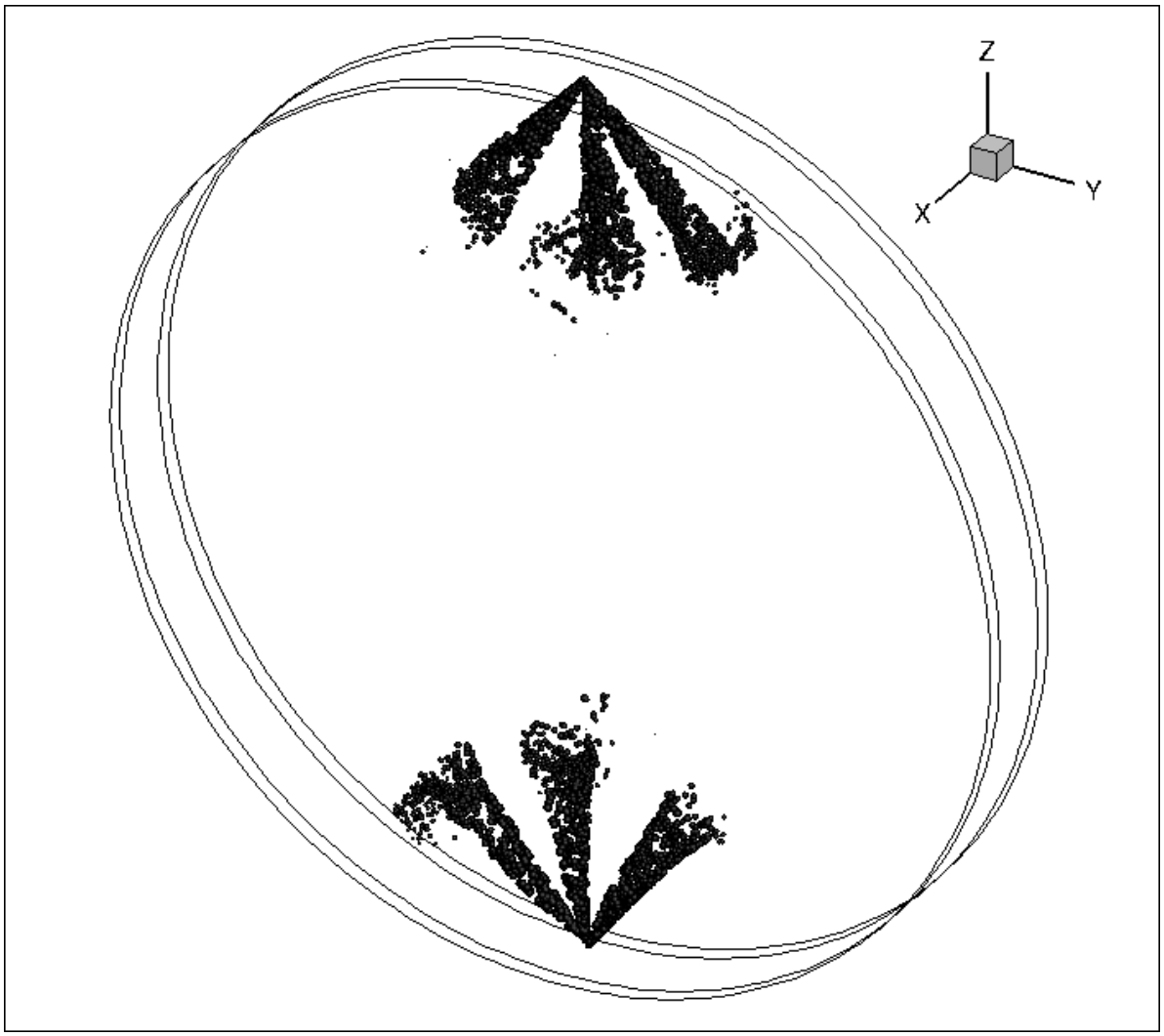

(a)

Figure 3.20: Injector and spray orientation for the current configuration, (a) 3D view of the spray orientation, (b) and (c) Definition of nozzle location and spray orientation parameters presented in Table 3.2.

spray parameters such that the total fuel mass injected remains to be the same in all studied cases. Additionally, the engine operating parameters are the same as the baseline case in the non-reacting flow simulations with an rpm of 3500, wall heat transfer, 7.5° port angle, back pressure 2 atm. The spray and combustion simulations are carried out in the fourth cycle, after three non-reacting flow cycles. The ambient conditions in the combustion chamber for all the sprays are the same, however since the injection durations are different, and the

Figure 3.20: (cont'd)

(b)

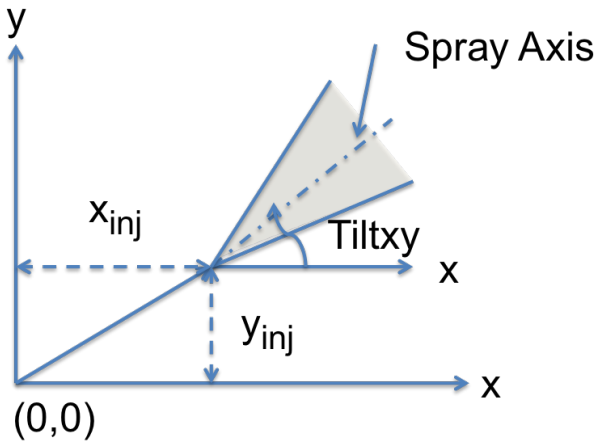

(c)

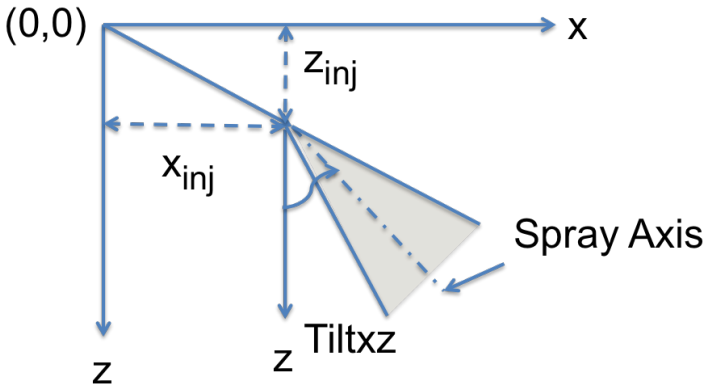

cylinder gas is being compressed during injection, the conditions of sprays are not quite the same. A goal of our spray investigations is to study the effect of the spray parameters on the liquid penetration length. The liquid penetration length is defined as the maximum axial penetration distance of the liquid from the nozzle during the injection process. The numerical spray length is defined as the distance from the nozzle hole to the axial location before which most of the mass of the liquid jet is located. In this study, this length is taken to be the distance from the nozzle before which 99% of the liquid mass exists. Since there are six nozzle holes, the liquid penetration length considered us considered to be the average

Nozzle No.	**Tiltxy(°)**	**Tiltyz(°)**	x_{noz} **(mm)**	y_{noz} **(mm)**	z_{noz} **(mm)**
1	3	40	2	0.5	48.5
2	0	3	1.5	0	48.5
3	-3	-40	1	-0.5	48.5
4	5	145	2	0.5	-48.5
5	0	185	1.5	0	-48.5
6	-3	225	1	-0.5	-48.5

Table 3.2: Nozzle location and spray orientation parameters

Parameter	**Value/Description**
Nozzle Diameter	100 μm,180 μm, 246 μm
Injection Pressure	72 MPa, 138 MPa, 150 MPa
Fuel Injection Temperature	293 K, 373 K, 436 K
Injector Configuration	2 side injectors with 3-hole nozzles

Table 3.3: Injection parameters

of the liquid length computed for each hole.

Physical Phenomenon	**Model**
Primary Atomization	Blob Model
Secondary Breakup	KH-RT Model
Drag	Dynamic Drag with droplet distortion
Evaporation	Multicomponent Evaporation model

Table 3.4: Spray models

S. No.	**Nozzle Diameter** (μm)	**Injection Pressure (MPa)**	**Fuel Temperature (K)**	**Injection Duration (Crank Angle)**	**Cone Angle** ($^\circ$)
1	246	138	293	10	14.98
2	246	138	373	10.42	15.27
3	246	138	436	10.83	15.54
4	180	138	436	20.49	14.73
5	180	150	436	19.65	14.73
6	180	72	436	28.37	14.73
7	100	138	293	59	13.38
8	100	138	373	61.48	13.63
9	100	138	436	63.90	13.87

Table 3.5: Details of injection parameters

3.4.1 Variation of penetration length with nozzle diameter

Spray experiments, including those of Siebers [42], indicate that the spray or liquid penetration length increases linearly with the nozzle diameter. Figure 3.21(a) shows the evolution of the liquid length with the crank angle for three different nozzle diameters. The injection pressure is kept fixed at 138 MPa and the temperature of the injected liquid is kept at 436 K for the simulated cases. The evolution of the liquid length is tracked until one of the three conditions is met: completion of the injection process or one of the sprays hits the cylinder wall or the liquid jet achieves a pseudo-steady state. If the jet hits the wall, the liquid length becomes constant and the penetration length definition does not hold well. The third condition, viz. the liquid jet achieving a steady state, is the desired condition for defining the liquid length. Experimental results of Siebers [42] show that the pseudo-steady state is achieved 0.5-1.0 ms after the SOI for most spray parameters and ambient conditions. The time taken to achieve the steady state condition increases with increasing ambient gas density and pressure. For the case with nozzle diameter 246 μm, the injection duration is 10.83 CA or 0.52 ms. In figure 3.21(a), the liquid jet does not seem to reach steady state condition before the end of injection. For the nozzle diameter of 180 μm, the injection duration is 20.49 CA or 0.97 ms, longer than that considered in the previous case. Yet, the liquid jet does not achieve steady state condition, although there are indications that it may have done so if the injection duration was slightly longer. The only spray achieving the pseudo-steady state is the one with nozzle diameter of 100 μm; the injection duration is 63.90 CA or 3.04 ms in this case. This provides ample time for the jet penetration to achieve equilibrium. Another issue that needs to be studied here is the effect of changing the ambient gas conditions results in this study is the effect of changing ambient conditions

on the liquid penetration length. In Siebers' [42] setup, the liquid length measurements were conducted in a closed combustion chamber with quiescent conditions and the ambient temperature and density or pressure conditions did not change so much. In the opposed piston engine simulations, the ambient conditions for the spray change due to the compression of the gas and since the spray is injected near the TDC, the variation in these conditions is particularly significant. Figure 3.21(b) shows the variation of the ambient mean temperature and density with the crank angle for the sprays studied here. There is a significant variation in both variables, particularly in density, during the injection process for all the cases considered in this section. The temperature, density and pressure increase by about 12%, 54% and 72%, respectively, during the injection process for the case with nozzle diameter of 246 μm. The corresponding increases for the case with nozzle diameter of 180 μm are about 18%, 96% and 131%, respectively. This high variation in ambient conditions influences the penetration length significantly. Figure 3.21(c) compares the liquid penetration lengths for injectors with different nozzle diameters. The injection pressure is fixed at 138 MPa, and the injected droplet temperature is varied from 293 K to 436 K. The penetration lengths are the highest for temperature 293 K and decrease as the injection temperature increases. The penetration length increases monotonically as the nozzle diameter increases. The injected mass flow rate increases with the square of the nozzle diameter but the amount of air entrained is a linear function of the nozzle diameter, assuming all other conditions are fixed. Entrained air increases with the square root of the gas density, thus there is a continuous increase in the entrained air with increasing crank angle until the TDC is reached. The deviation from the expected experimental trends with fixed ambient conditions can be explained to be due to the variation in ambient conditions and the injection period not being long enough to establish the pseudo-steady condition, as discussed previously.

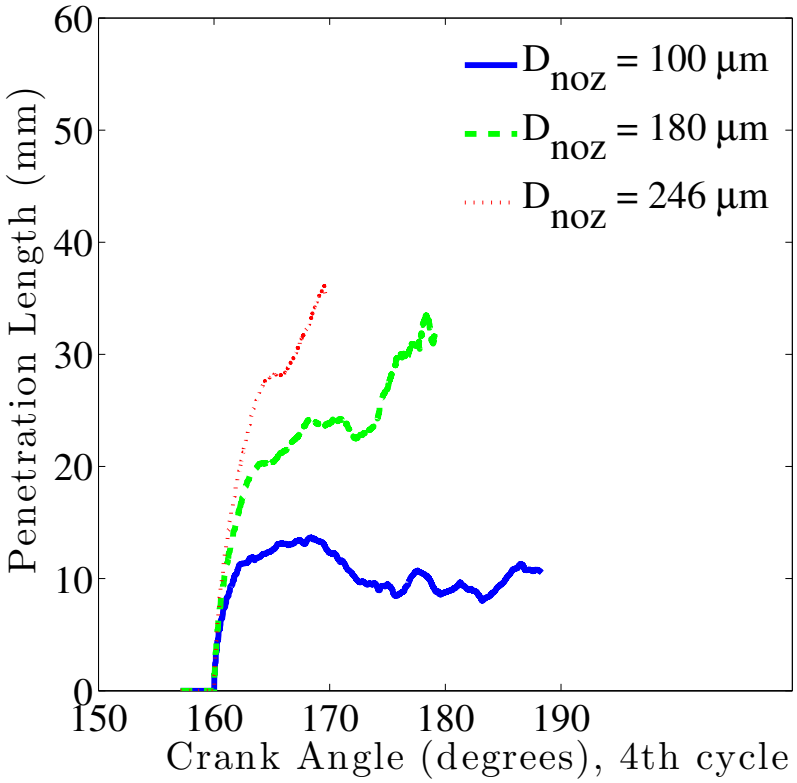

(a)

Figure 3.21: (a) Evolution of penetration length with crank angle for different nozzle diameters. Injection Pressure = 138 MPa, Injection temperature = 436 K, (b) Variation of ambient conditions for the spray with crank angle, (c) Variation of penetration length with nozzle diameter for different injection temperatures with the injection pressure fixed at 138 MPa.

Figure 3.21: (cont'd)

(b)

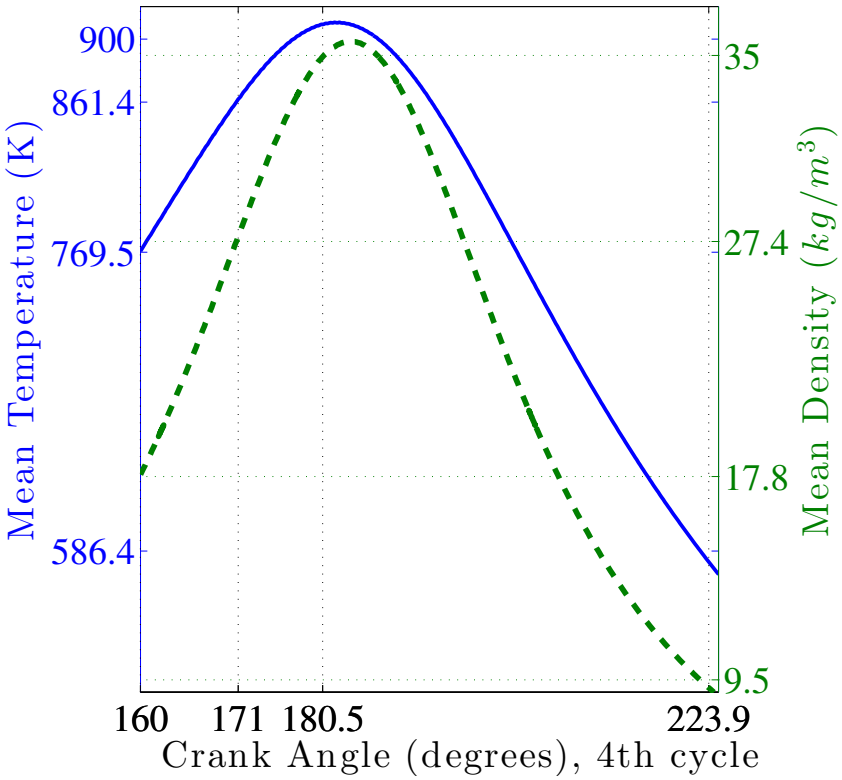

(c)

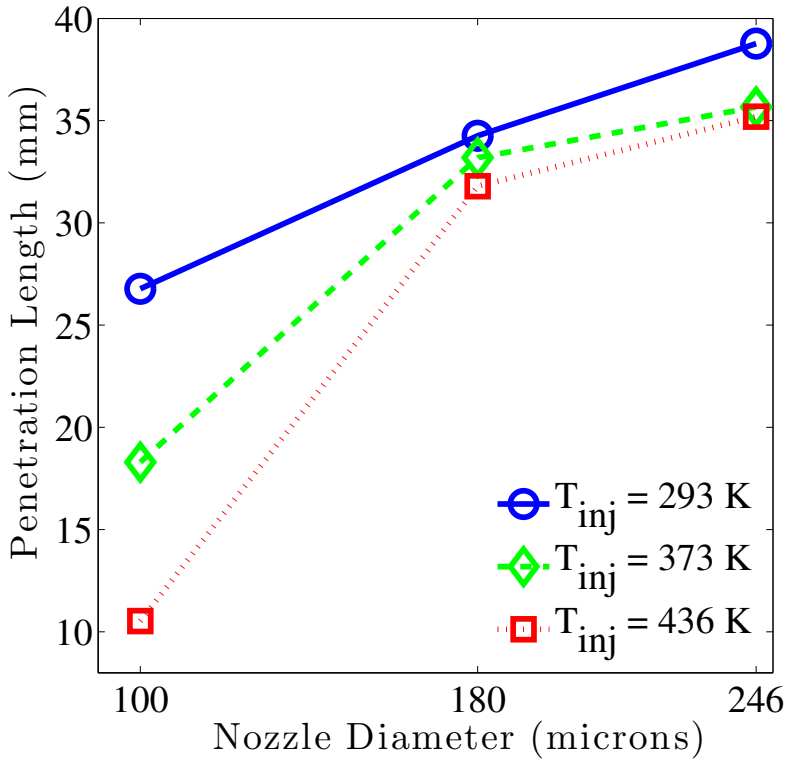

3.4.2 Variation of penetration length with injection pressure

The mass flow rate of the injected spray is a linear function of the injected liquid or droplet velocity, which increases with an increase in the injection pressure. The entrained air also increases linearly with the injection pressure as it has a similar dependence on the injected droplet velocity as the mass flow rate has. Since the penetration of the liquid is mixing controlled, the liquid length is not expected to increase with injection pressure and this has been observed experimentally by Siebers [42]. Although, the evaporation rate increases with the injection pressure, it is matched by a corresponding increase in the rate of injection of the liquid. Figure 3.22(a) shows the liquid length at different crank angles for different injection pressures. The nozzle diameter and injection temperature are kept fixed at 180 μm and 436 K, respectively. In all the cases, the spray nearly achieves pseudo-steady state condition before the injection stops. The evolution of the liquid length is nearly the same for all cases simulated, although the spray gets closer to a pseudo-steady state condition for injection pressure of 72 MPa since the injection period for this injection pressure is higher than other pressures (nearly 28° CA as compared to 20.5° CA and 19.6° CA for injection pressures of 138 MPa and 150 MPa, respectively). Figure 3.22(b) compares the calculated penetration lengths for the three different injection pressures. There is a slight increase in the liquid length with injection pressure which is consistent with the experimental studies (see Siebers [42]), even though there is a more pronounced increase with injection pressure in numerical results. This can be explained by the injection process stopping before a steady state condition is achieved as discussed earlier. Since the liquid length reaches a maximum before decreasing back to a steady state value, and since injection ends earliest for the 150 MPa case, the liquid length is the highest for this case. The penetration length drops to

a lower value at lower injection pressures as they progress more towards a steady state condition.

3.4.3 Variation of penetration length with injection temperature

Figure 3.23(a) shows the variation of the liquid penetration length with the injection temperatures for the nozzle diameter and injection pressure fixed at 246 μm and 138 MPa, respectively. The energy required to heat and vaporize the fuel decreases as the temperature increases. Hence, the length to which the liquid jet needs to penetrate and to entrain the required amount of energy also decreases. In all three cases considered here, the injection stops before a steady (or pseudo-steady) length is reached, but there is a clear trend of lower liquid penetration length with higher liquid temperature. It can also be seen that the penetrated length is the same for a few crank angles after the SOI in all three cases, but when a sufficient amount of gas has been entrained, the higher temperature jets evaporate faster and thus their penetration will be lower. The 436 K jet not only evaporates faster but also experience longer injection because of the lower density of the fuel at this temperature and thus the non-steady state liquid penetration length condition. Figure 3.22(b) compares the variation of liquid penetration lengths with temperature for three different nozzle hole diameters, with the injection pressure fixed at 138 MPa. The liquid length decreases with temperature for all the cases, as has been observed experimentally by Siebers [42]. The slight deviation in the trends for the larger nozzle diameters is due to the issues discussed previously, namely the short injection period and the continuous change in ambient temperature and density conditions. Evidently, the decrease in penetration length with temperature is much stronger in the case having the smallest nozzle diameter due to the smaller droplets evaporating faster for the higher temperatures.

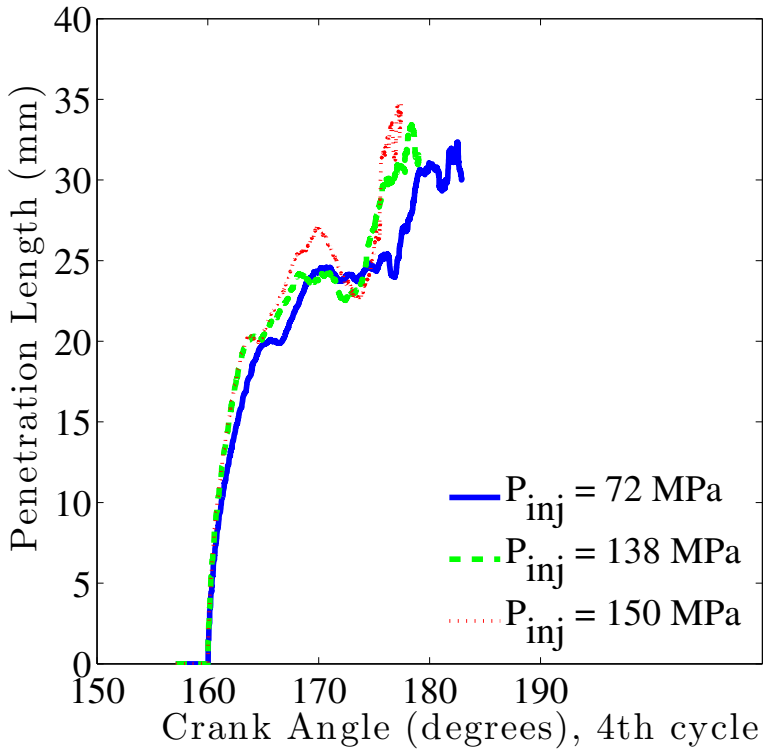

(a)

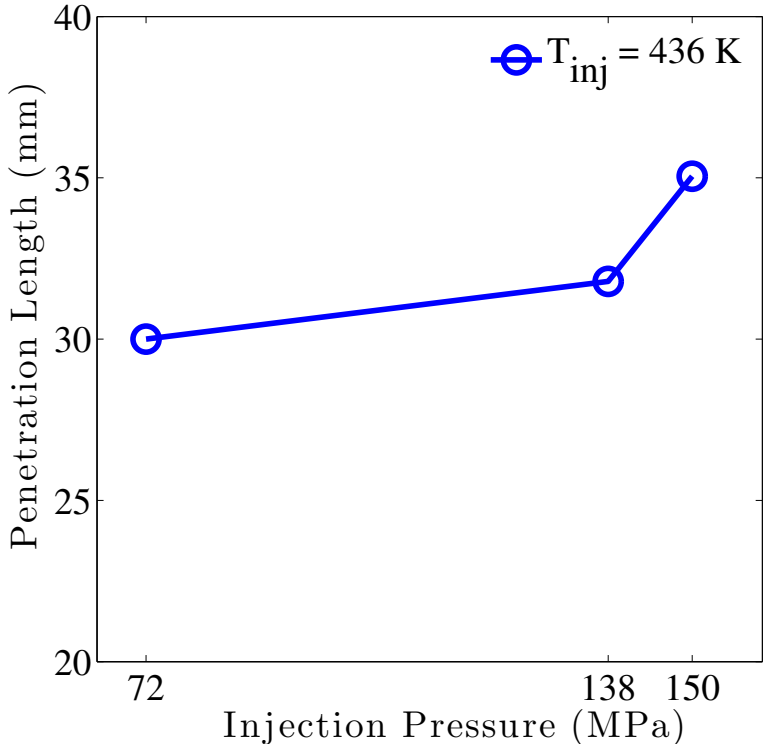

(b)

Figure 3.22: (a) Evolution of penetration length with crank angle for different injection pressures, (b) Variation of penetration length with injection pressures. Nozzle Diameter = 180 μm, Injection temperature = 436 K.

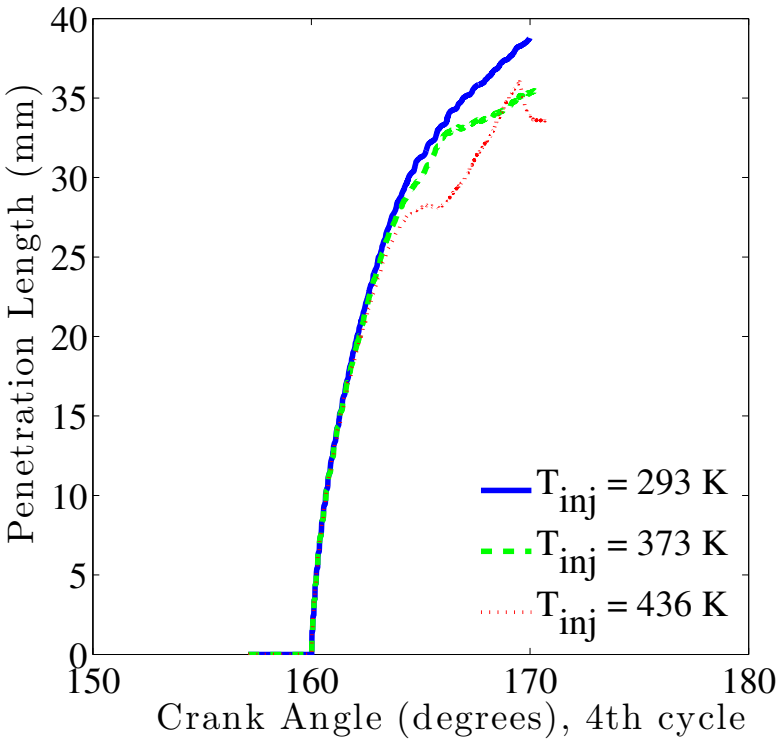

(a)

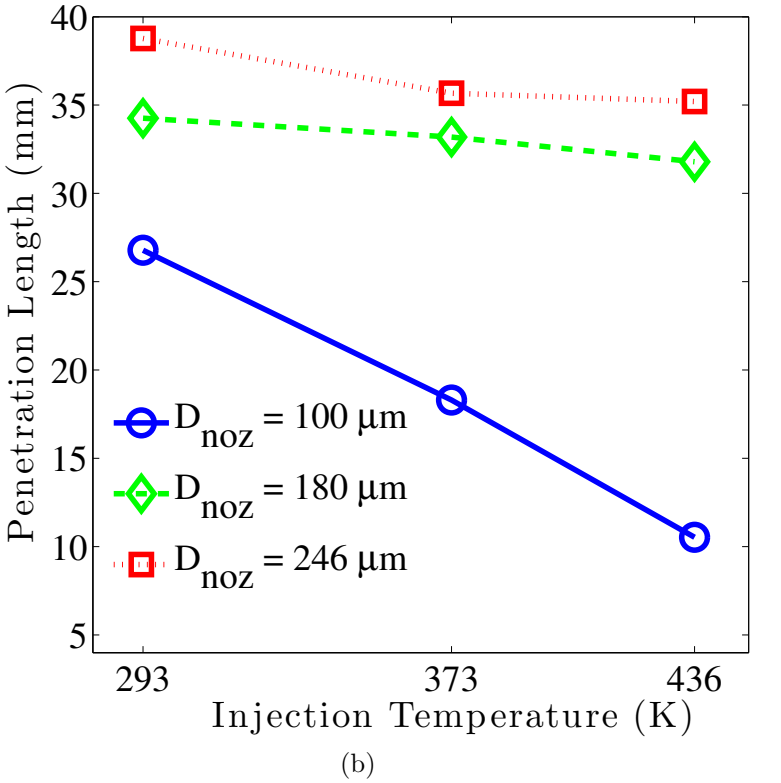

(b)

Figure 3.23: (a) Evolution of penetration length with crank angle for different injection temperatures. Nozzle Diameter = 246 μm, Injection pressure = 138 MPa, (b) Variation of penetration length with fuel injection temperature for various nozzle diameters. Injection pressure = 138 MPa.

Figure 3.24(a) depicts 3D isosurfaces of the vorticity magnitude the middle of the injection period at CA=166°. The vorticity field shows the complex turbulent flow generated by the high pressure spray in the gas flow. The flow and turbulence generated by the spray are important features of these types of sprays [62, 63] and are expected to have a significant effect on the spray evolution and fuel-air mixing. Figure 3.24(b) shows the isosurfaces of temperature at CA=166°. Figures 3.24(c)-3.24(e) show the isosurfaces of the evaporated fuel at three crank angles and further illustrate the complex turbulent flow.

Figure 3.25 shows the variation of the spray and the evaporated fuel mass fractions with crank angle for a nozzle diameter of 246 μm. The injection pressure is 138 MPa and the injected fuel temperature is 436 K. The SOI is at CA=160° and the injection stops at CA=170.83°. The contour plots in Figure 3.25 at the x=1.5 mm plane passing through the middle injector on each side. Initially, when the spray jets from the six nozzle holes start penetrating into the gas, the rate of evaporation is low as the large drops or droplets are heating up before breakup and evaporation. However, in the case considered here, there is some evaporation as the initial liquid temperature is relatively high and also very small droplets are stripped off from the surface of large droplets due to Kelvin-Helmholtz (KH) waves. These droplets evaporate quickly, however since their overall mass fraction is very low, the evaporated fuel cannot be seen in the contour plots shown in Figure 3.25(a) (CA=162°) due to the high contour levels used. As the jet penetrates further, the larger droplets start breaking into a significant number of small droplets (3-10 μm) due to Rayleigh-Taylor (RT) breakup. These small droplets heat up and evaporate quickly. Also, due to the high spray momentum, there is an increase in the gas temperature near the tip of the spray, which speeds up the rate of evaporation of small droplets. This results in relatively large mass fraction of evaporated fuel near the tip of the spray as seen in Figure 3.25(b) (CA=164°). With further

penetration and breakup of the spray, the rate of evaporation increases and the vapor plumes in the front of the liquid jets spread as seen in Figures 3.25(c) and 3.25(d) at CA 166° and 168°, respectively. These vapor plumes which have high velocities due to the momentum imparted by the spray, start interacting with the vapor plumes of neighboring sprays and merge as seen in Figures 3.25(d) and 3.25(e). As the injection stops, the vapor plumes start losing their momentum and get entrained by the swirling motion of the surrounding gas. This promotes the uniform mixing of the evaporated fuel throughout the cylinder. For the current geometry and operating conditions, Figure 3.25 seems to show that the spray orientation, injection parameters, amount of fuel injected and swirl and tumble are not optimum for a good mixing. A detailed study and optimization is generally required to achieve uniform mixing and combustion; this is beyond the scope of the current study.

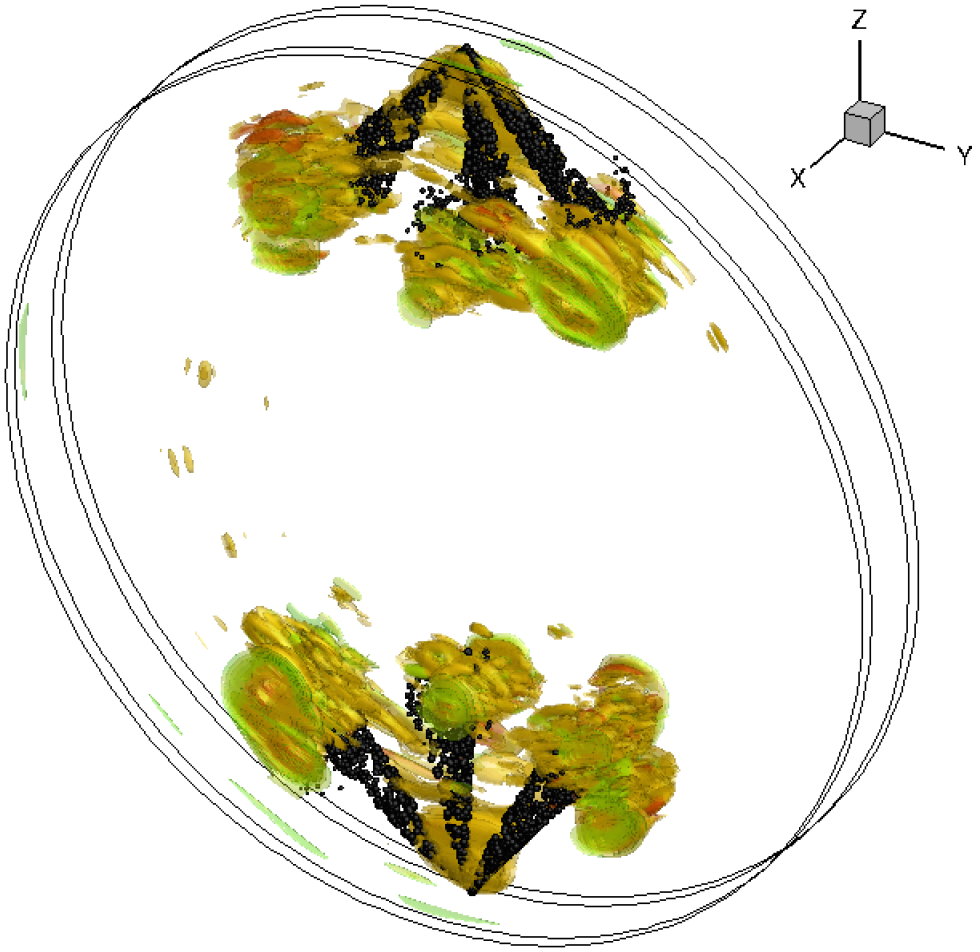

(a)

Figure 3.24: (a) Vorticity isosurfaces at CA 166°, (b) Temperature isosurfaces at CA 166°, (c) Mass fraction isosurfaces at CA 166°, (d) Mass fraction isosurfaces at CA 170°, (e) Mass fraction isosurfaces at CA 173.4°. Nozzle Diameter 246 μm, Injection Pressure 138 MPa, Injected fuel temperature 436 K.

Figure 3.24: (cont'd)

(b)

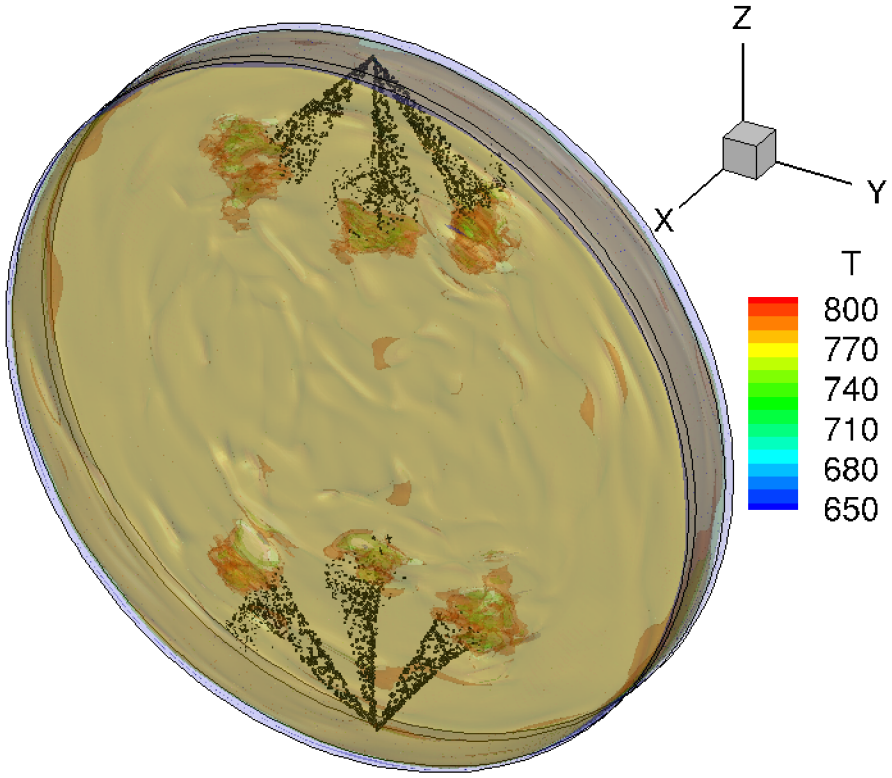

(c)

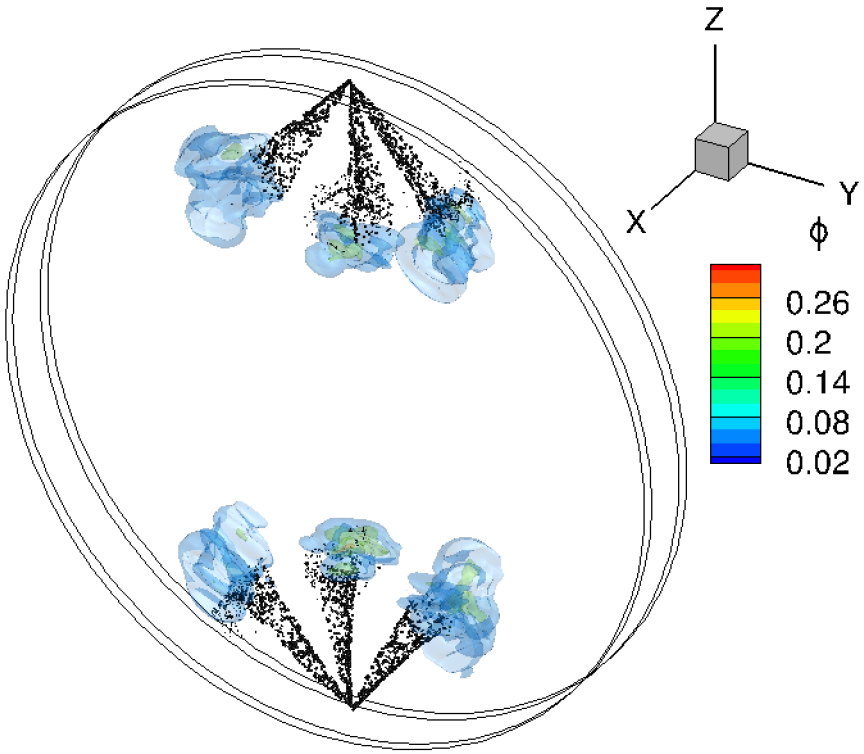

Figure 3.24: (cont'd)

(d)

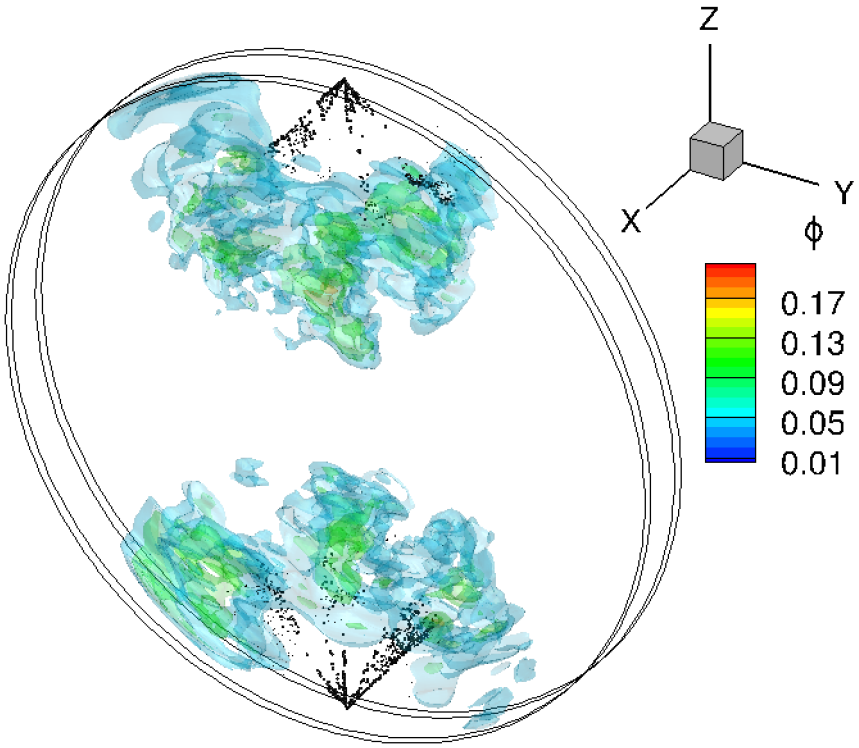

(e)

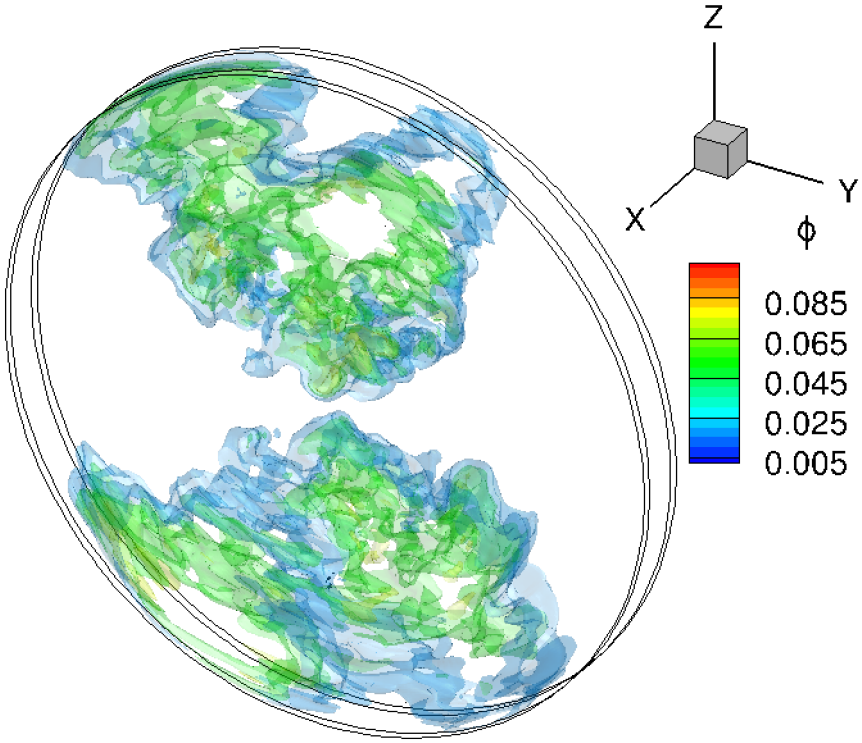

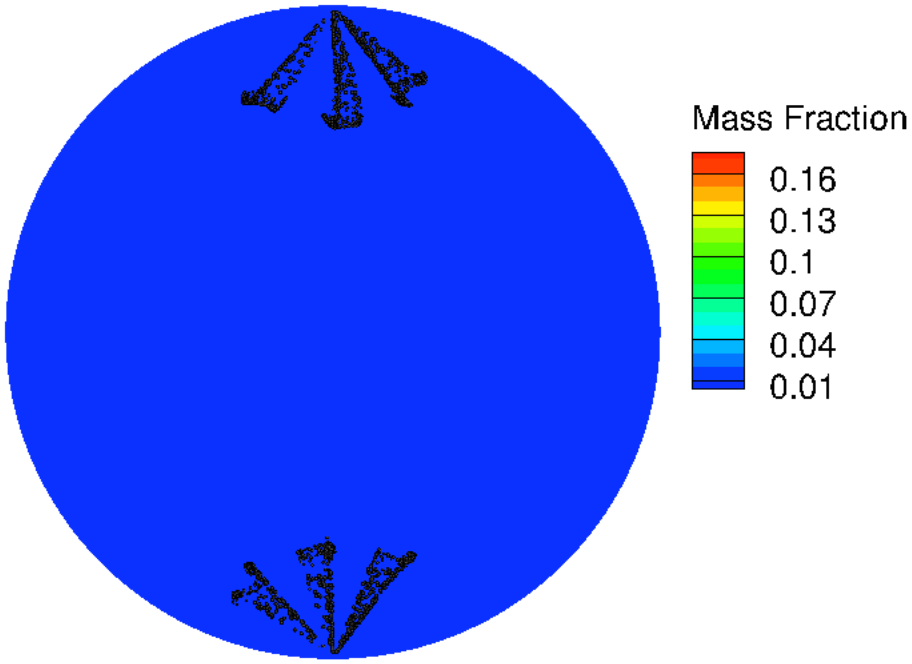

(a)

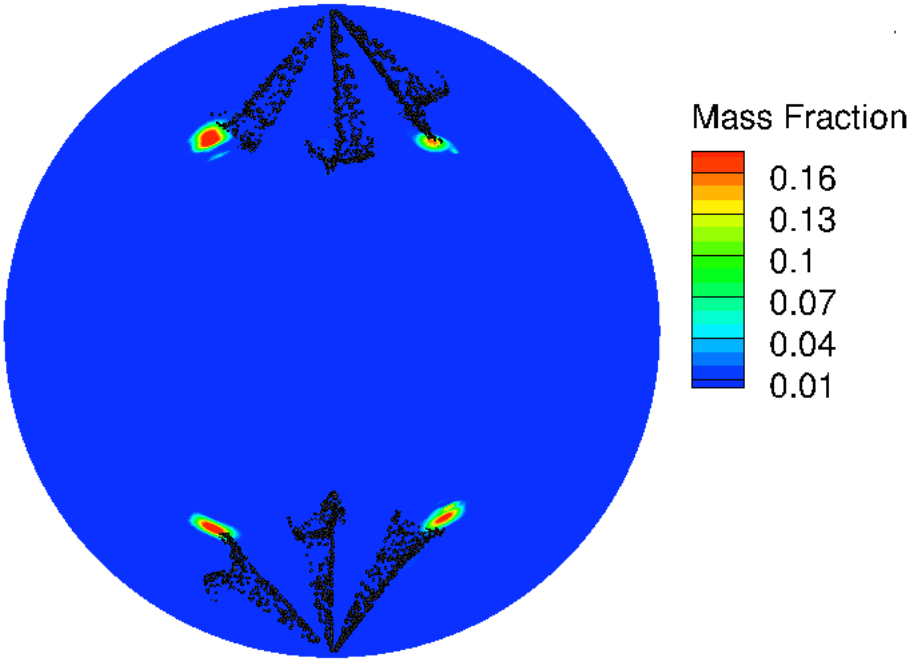

(b)

Figure 3.25: Evolution of the spray and the evaporated fuel mass fractions with crank angle for nozzle diameter 246 μm, injection pressure 138 MPa, fuel temperature 436 K, (a) CA 162°, (b) CA 164°, (c) CA 166°, (d) CA 168°, (e) CA 170°, (f) CA 171°, (g) CA 172°, (h) CA 173°.

Figure 3.25: (cont'd)

(c)

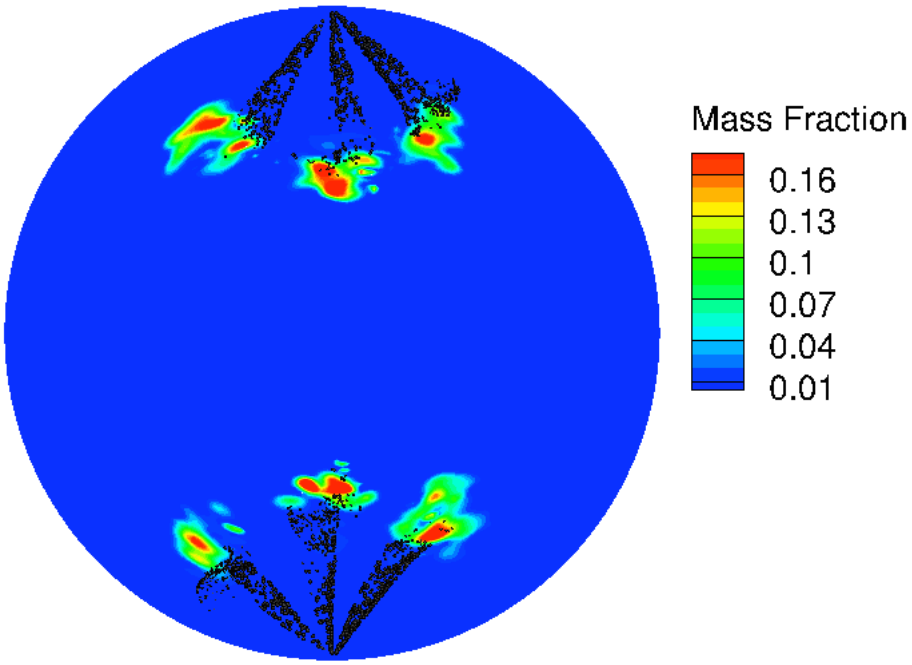

(d)

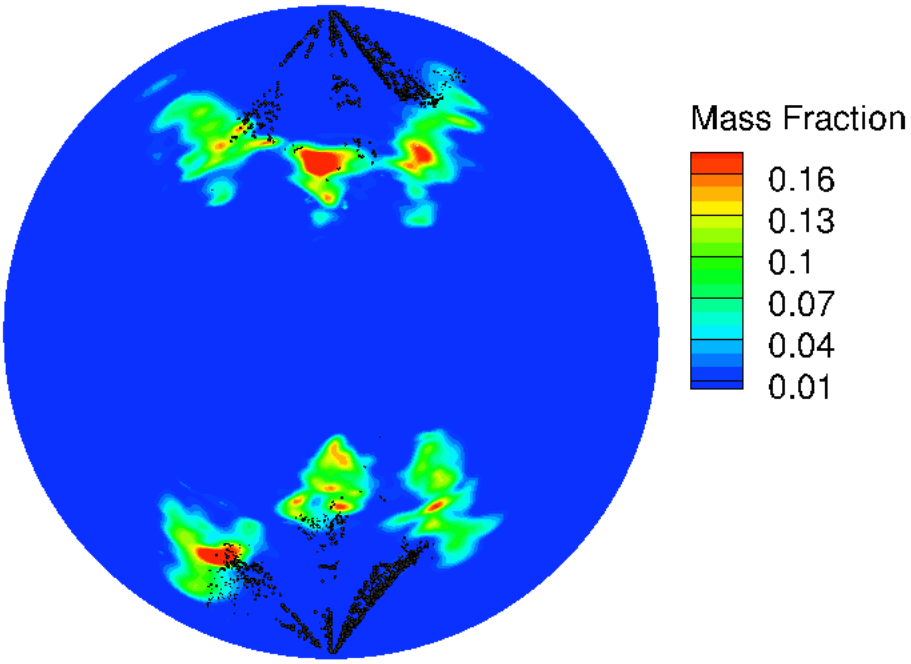

Figure 3.25: (cont'd)

(e)

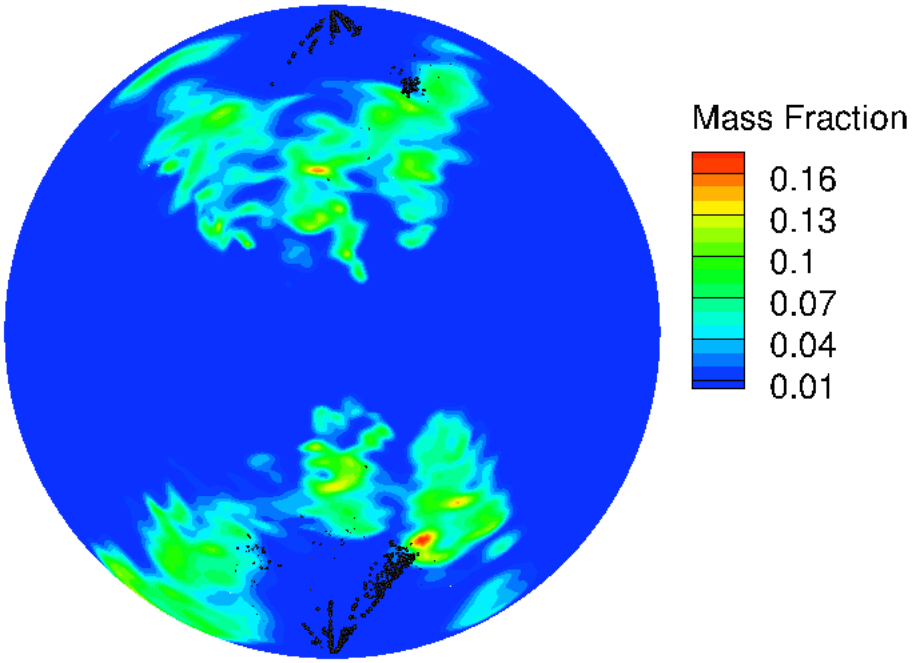

(f)

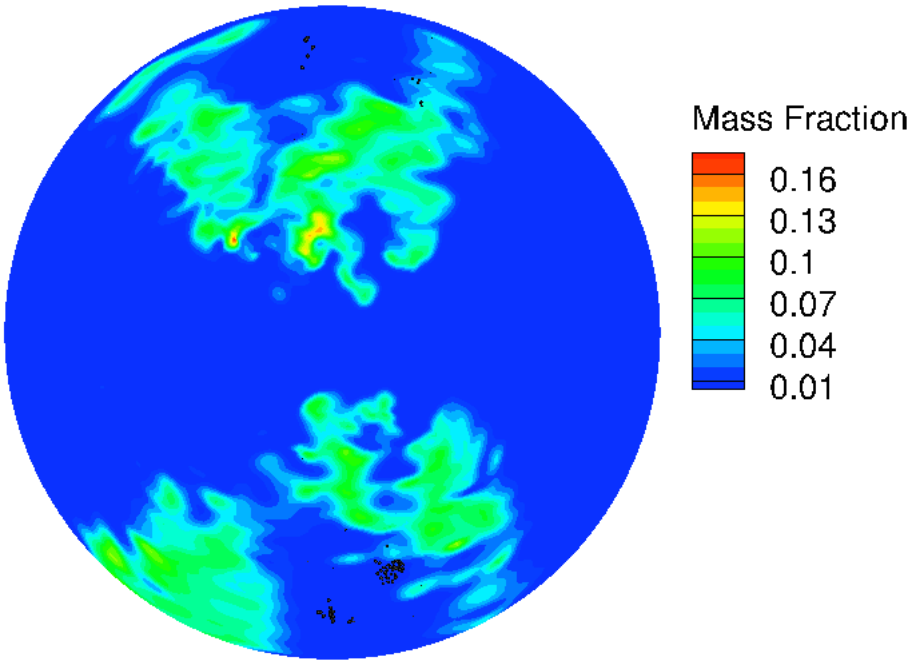

Figure 3.25: (cont'd)

(g)

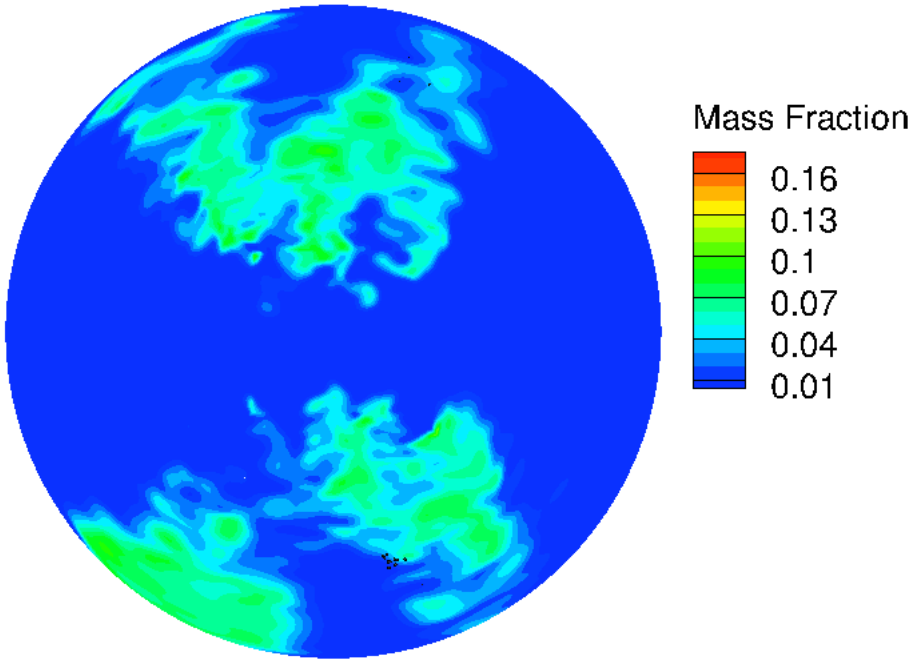

(h)

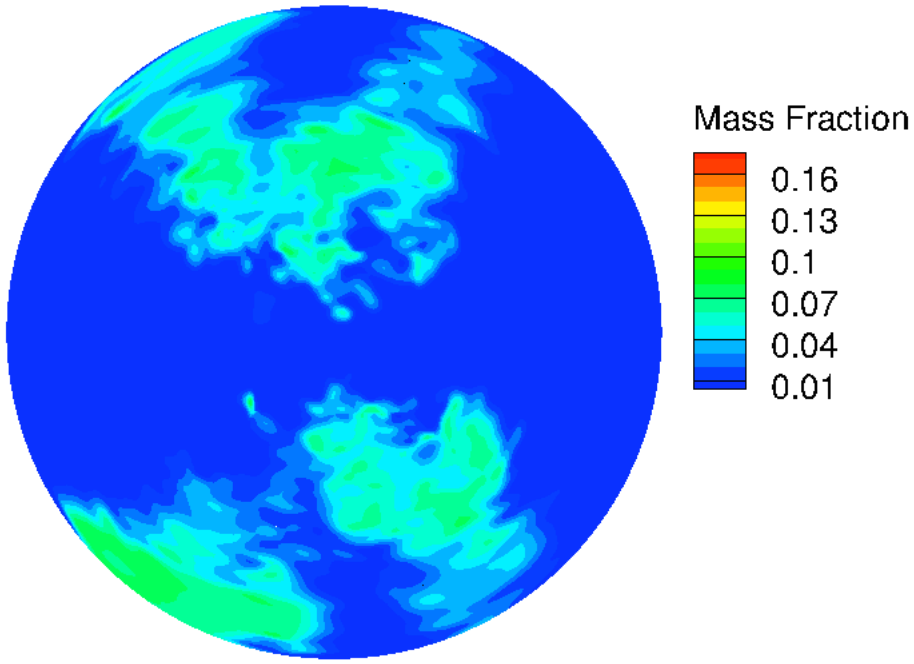

3.4.4 Consistency of LES and FMDF components

It has been discussed previously in Chapter 2 that some of the filtered variables like temperature and species mass fraction can be computed from both the LES and FMDF parts of the hybrid LES/FMDF formulation. This provides an opportunity for checking the numerical accuracy of the LES/FMDF methodology and its numerical solvers. It is expected that if the variables are obtained independently using different numerical methods and their values are still consistent with each other, the LES/FMDF solution can be stated to be numerically accurate. Figure 3.26 compares the mass fractions of the evaporated fuel obtained using the hybrid LES/FMDF methodology. The values obtained by solving the filtered LES equations by the Finite Difference (FD) grid are shown on the x-axis while the values obtained by solving the FMDF equations using the Monte Carlo (MC) methodology are shown on the y-axis. Ideally, the evaporated fuel mass fractions obtained by both methods should be perfectly correlated. Deviation from perfect correlation can be due to several factors including finite difference grid resolution, source terms due to spray, the number of MC particles, etc. Figure 3.26(b) shows the scatter plot of the LES and FMDF mass fraction at CA 164°, four crank angle degrees after the start of injection. The correlation coefficient (R) in this case is 0.9712. The predicted values differ at the higher range of mass fractions (0.1-0.2). This is due to the higher mass fraction gradients at the tip of the spray where faster evaporation occurs. The high order finite difference scheme generates overshoots and undershoots in regions of high gradients due to the limited grid resolution. The FMDF part is non diffusive, free from these overshoots/undershoots, and more accurate in these regions. The overall consistency can be improved by increasing the resolution of the finite difference grid at the cost of higher computational time. The comparison between the temperature components

at CA=164° is shown at Figure 3.30(a) and there is a high level of consistency between them. At later crank angles, the evaporated fuel vapor mixes with the ambient gas and the distribution of the fuel becomes more uniform. Figures 3.28(a), 3.28(b) and 3.29(a), 3.29(b) demonstrate the consistency between the two components of LES/FMDF at CA=170° and 173.4°, respectively. At the end of the injection period (CA 170°), some droplets are still undergoing breakup and regions of high mass fraction gradients exist, but overall there is a more uniform mixture. At CA=173.4°, only small droplets are left, the overall rate of evaporation is significant and the mixture is quite uniform. There is a slight improvement in consistency at this crank angle, especially in the higher mass fraction range. In case of the temperature components the consistency at CA=173.4 (Figure 3.30(a)) is lower compared to earlier crank angles because of wall heat transfer effects. Figures 3.31(a), 3.31(b) and 3.31(c) compare the LES and FMDF profiles along three different lines on the y-z plane, obtained by averaging along the axis of the cylinder. The profiles at y=-15 mm, y=0 mm and y=15 mm match quite well; expect for some slight overshoots/undershoots in the finite difference results. There is a high level of consistency between the Eulerian/LES and Lagrangian/FMDF components of the hybrid LES/FMDF methodology.

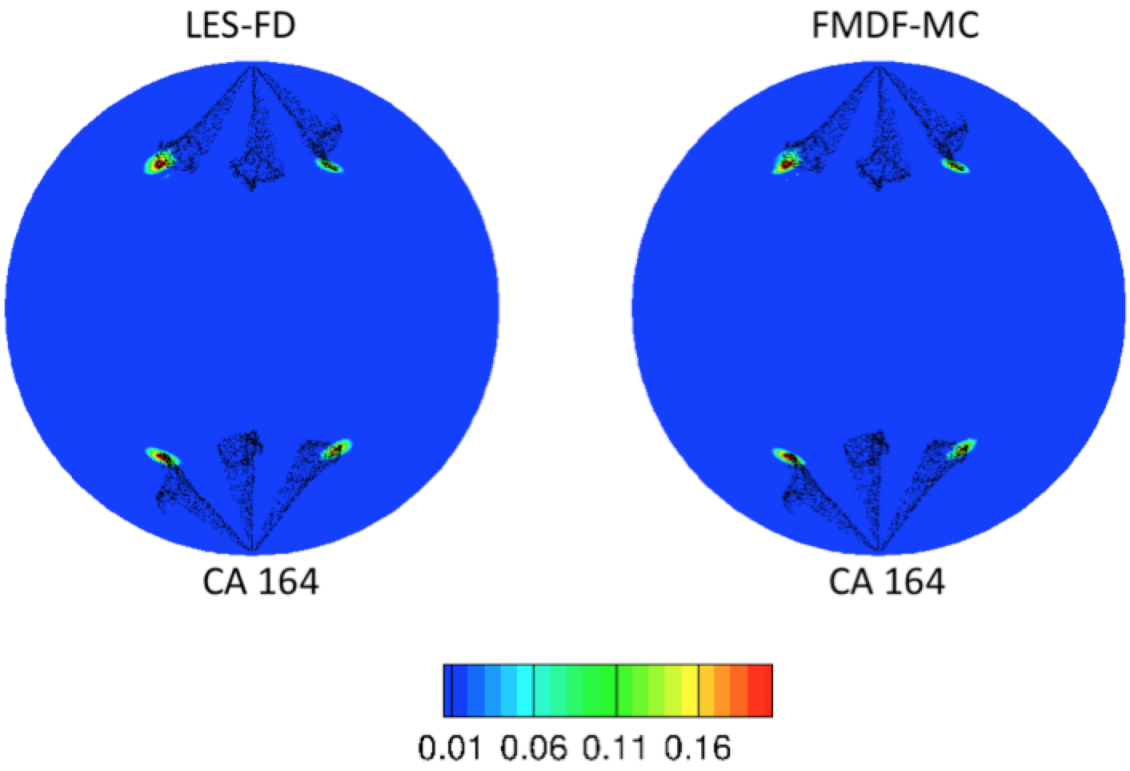

(a)

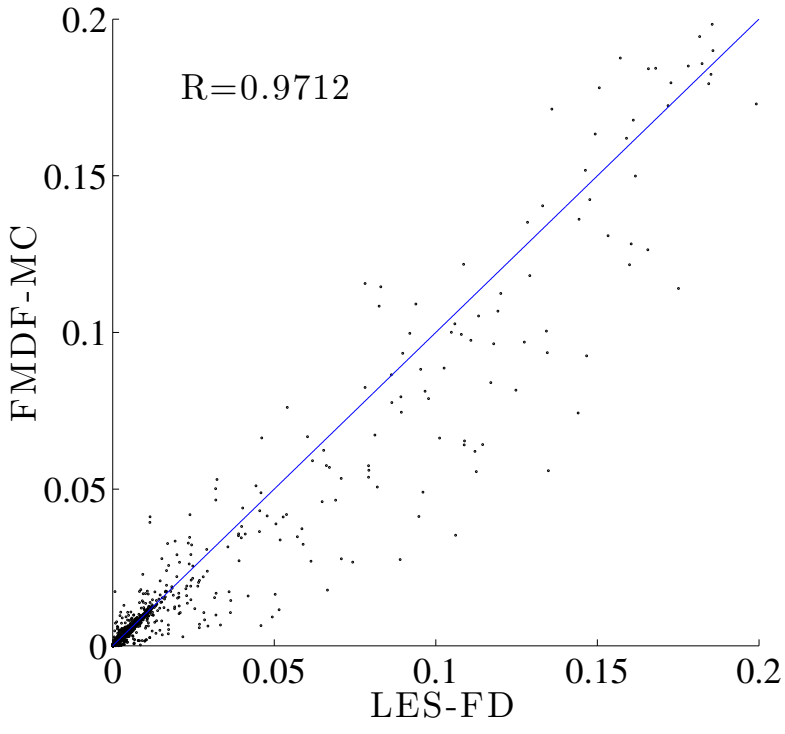

(b)

Figure 3.26: (a) Comparison between the evaporated fuel mass fractions obtained from LES and FMDF at CA 164°, (b) Correlation between the evaporated fuel mass fractions obtained from LES and FMDF at CA 164°.

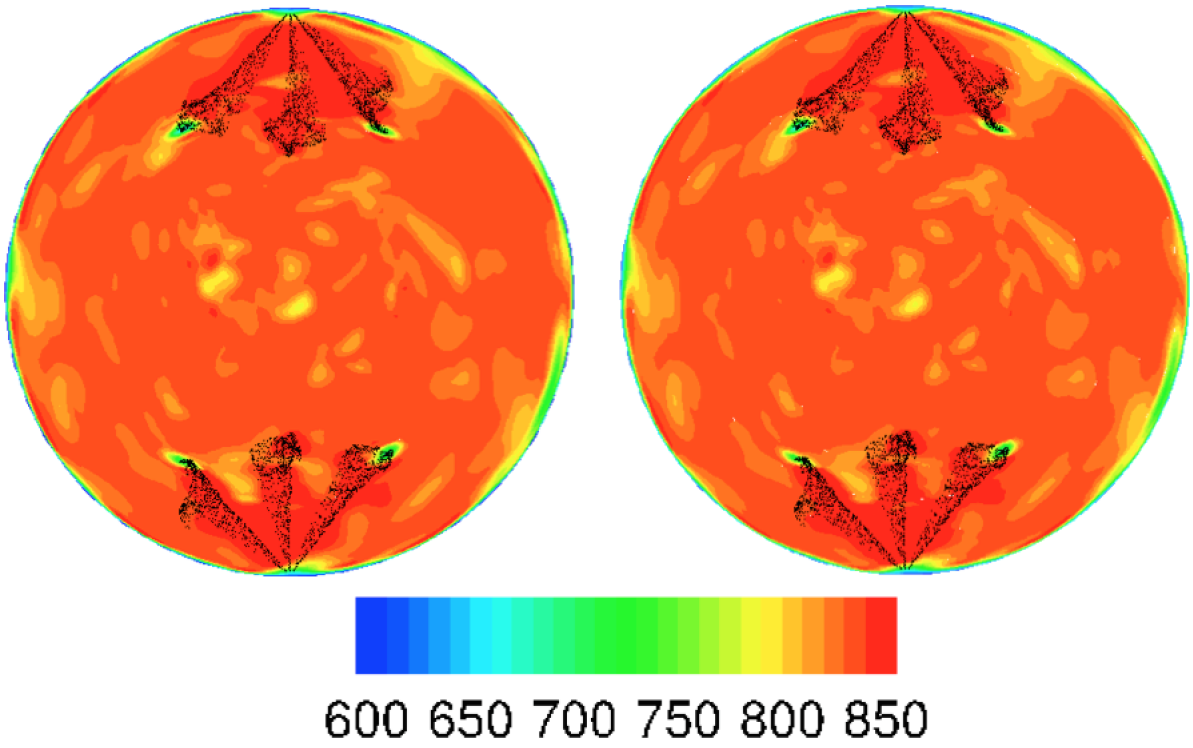

(a)

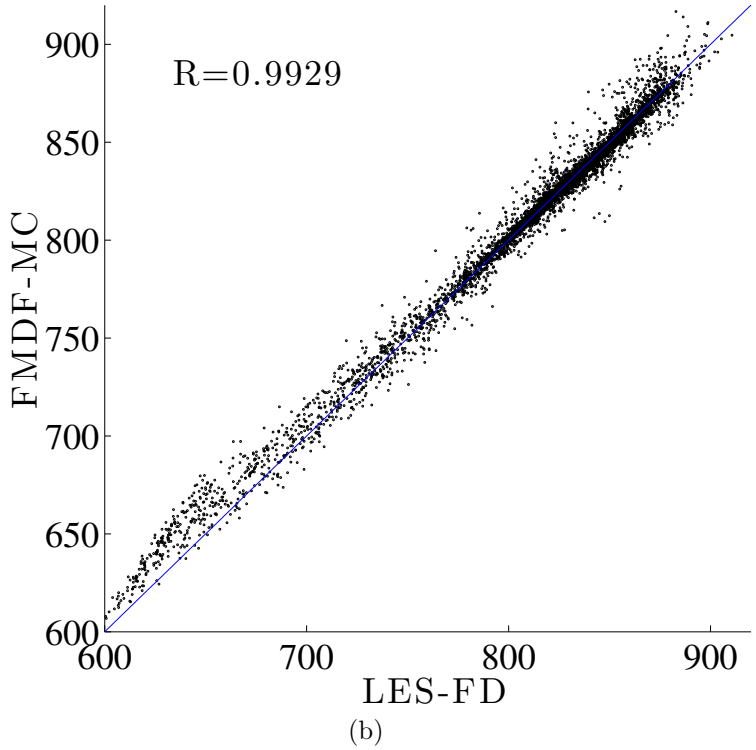

(b)

Figure 3.27: (a) Comparison between the temperatures obtained from LES and FMDF at CA 170°, (b) Correlation between the temperatures obtained from LES and FMDF at CA 170°.

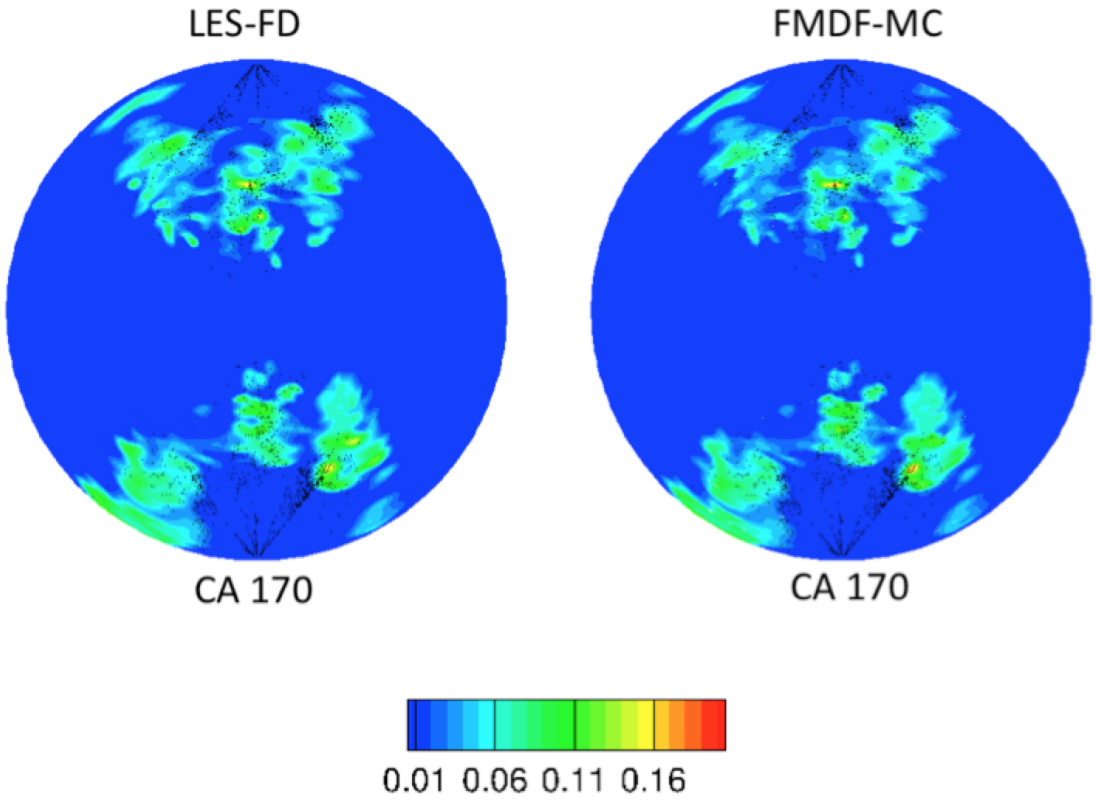

(a)

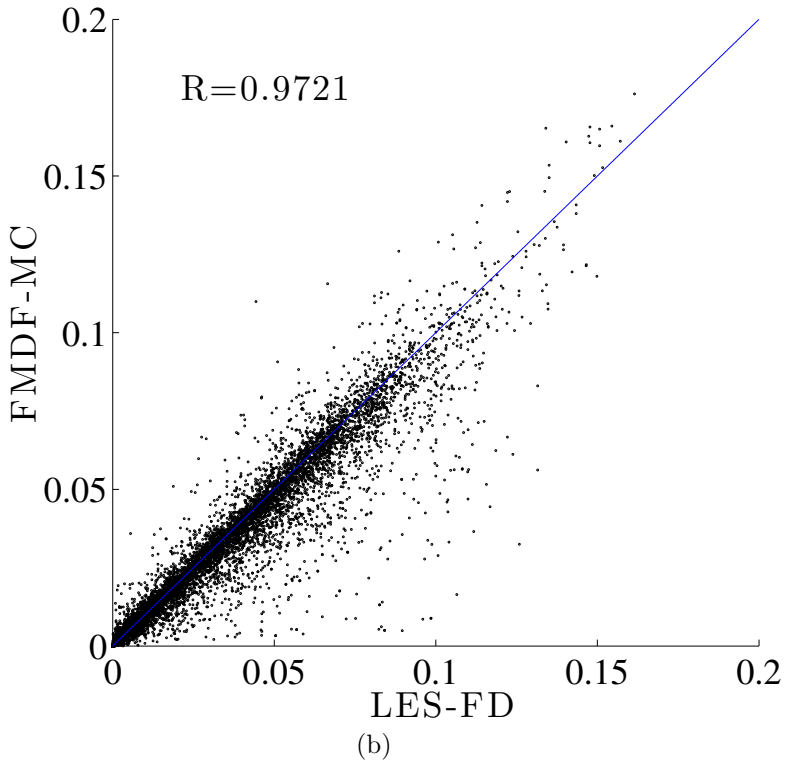

(b)

Figure 3.28: (a) Comparison between the evaporated fuel mass fractions obtained from LES and FMDF at CA 170°, (b) Correlation between the evaporated fuel mass fractions obtained from LES and FMDF at CA 170°.

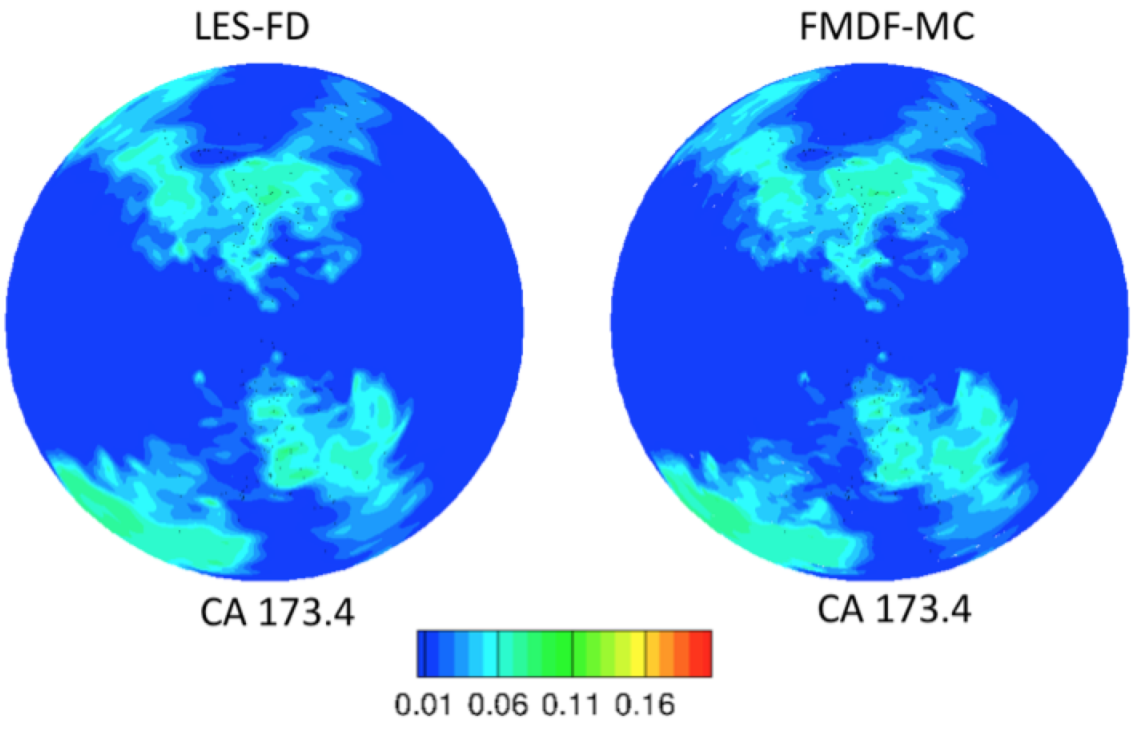

(a)

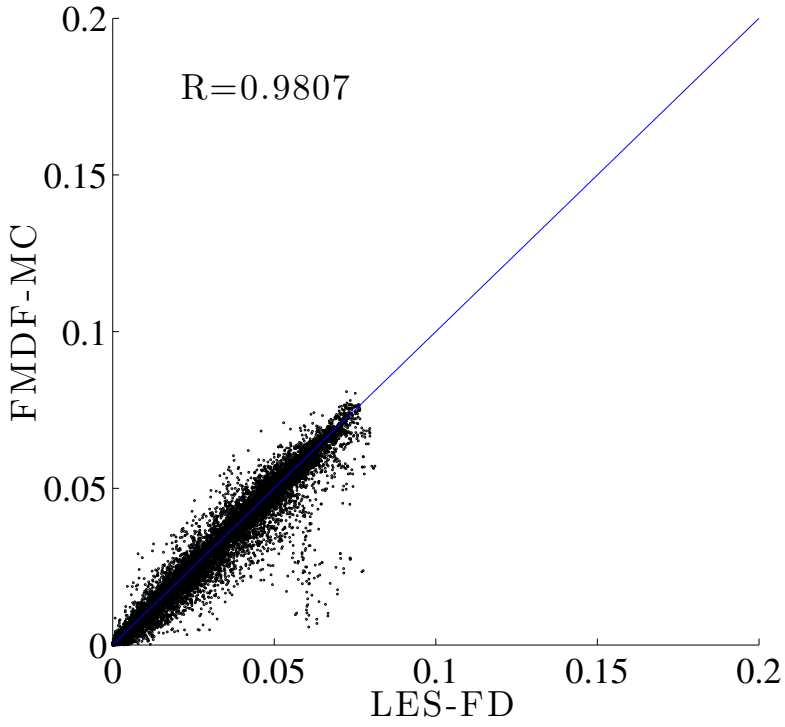

(b)

Figure 3.29: (a) Comparison between the evaporated fuel mass fractions obtained from LES and FMDF at CA 173.4°, (b) Correlation between the evaporated fuel mass fractions obtained from LES and FMDF at CA 173.4°.

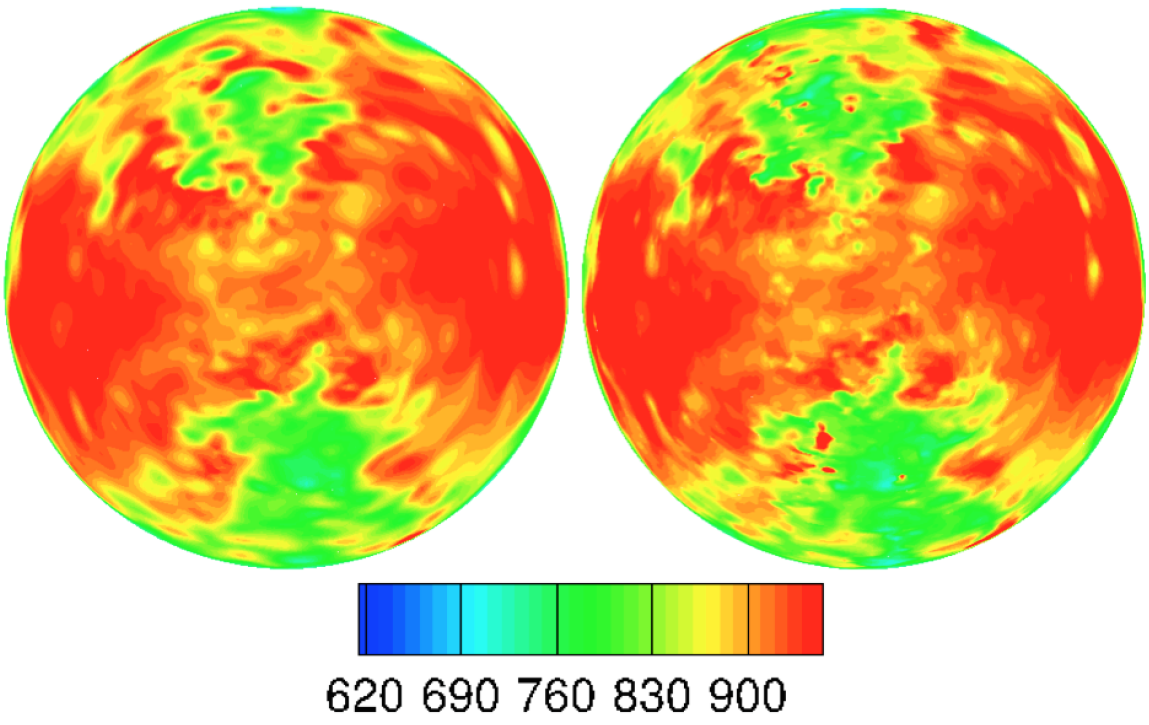

(a)

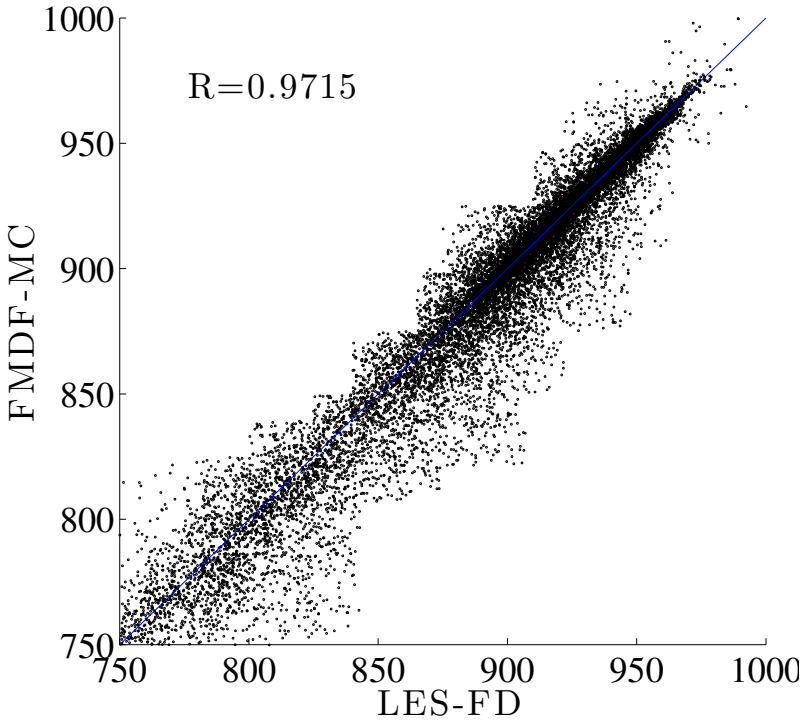

(b)

Figure 3.30: (a) Comparison between the temperatures obtained from LES and FMDF at CA 173.4°, (b) Correlation between the temperatures obtained from LES and FMDF at CA 173.4°.

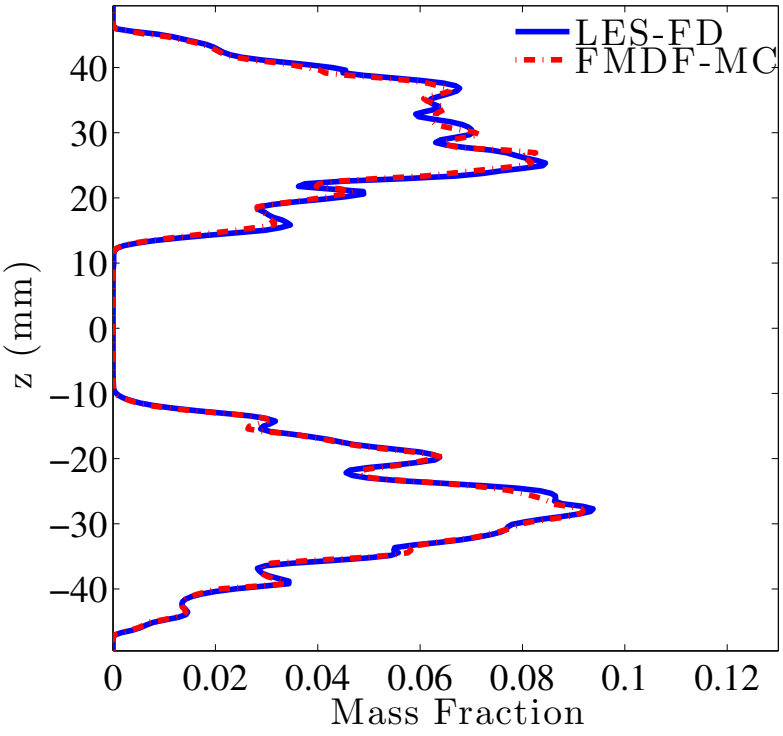

(a)

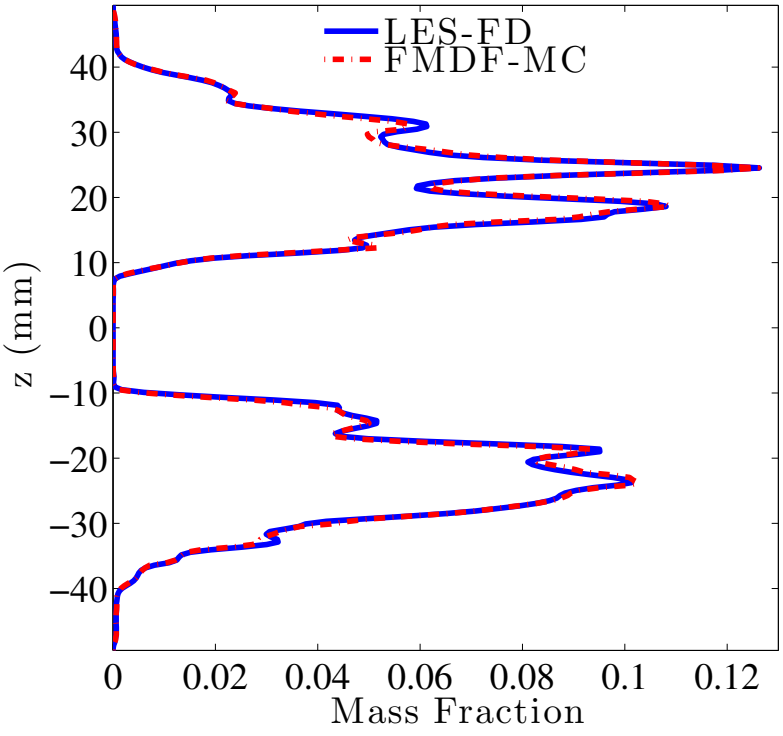

(b)

Figure 3.31: Comparison between the axially averaged values of evaporated fuel mass fractions obtained from LES and FMDF at different locations on the y-z plane (a) y = -15 mm, (b) y =0 mm, (c) y = 15 mm.

Figure 3.31: (cont'd)

(c)

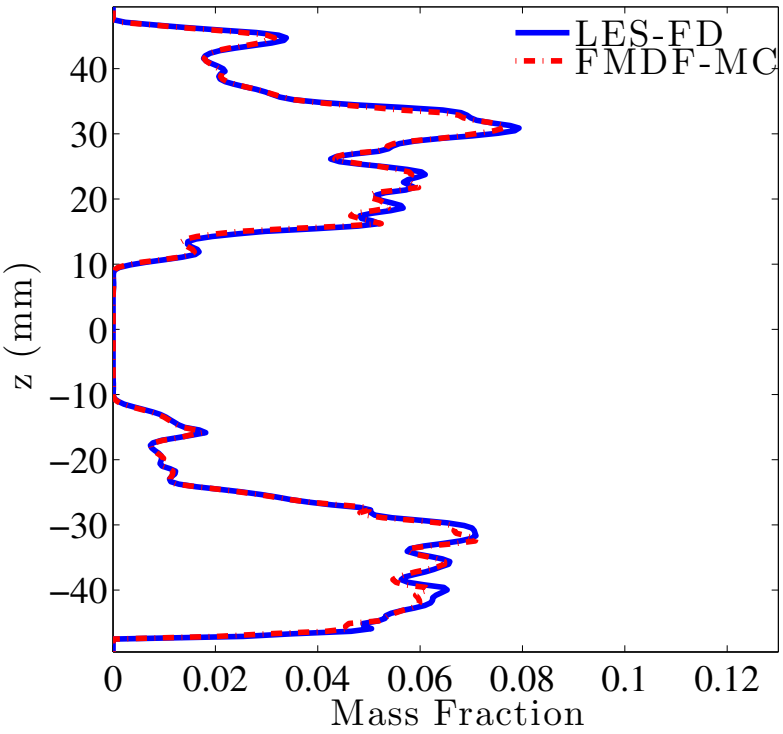

3.4.5 Multicomponent Fuel

Spray simulations have also been carried out for a bicomponent fuel, which is used as surrogate fuel for diesel. The fuel has the composition of 70% n-decane and 30% α-methylnaphthalene and is one of the several fuels studied in the first chapter of this dissertation. Figure 3.32 shows the evolution of the liquid lengths computed based on the two components and the mean liquid length vs. the crank angle. The liquid length of the less volatile α-methylnaphthalene is higher than that for n-decane as expected and the mean length of the 2-species fuel is nearer to that of n-decane. The multicomponent evaporation model discussed in Chapter 1 of this dissertation can be applied to any number of species and any multicomponent fuels.

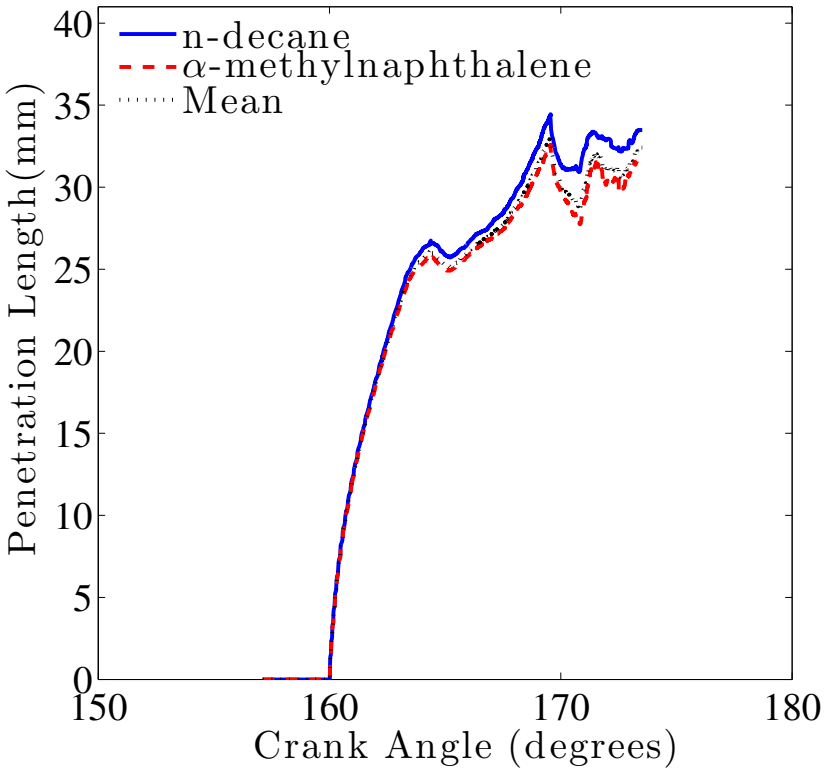

Figure 3.32: Evolution of the liquid length of the individual bicomponent fuel species and their mean. Nozzle diameter 246 μm, Injection Pressure 138 MPa, Injected fuel temperature 436 K.

3.5 Results and Discussions: Reacting Flows with Sprays

Reacting flow simulations have also been carried out with n-dodecane as the diesel surrogate and a global 1-step mechanism for the chemical reactions. Results are presented only for the case with nozzle diameter of 180 μm, injection pressure of 138 MPa and fuel injection temperature of 436 K. The spray configuration has been simplified with only a single nozzle (Figure 3.33(a)) and the grid resolution has been increased locally in the spray and combustion region (Figure 3.33(b)). As discussed previously, there is a redundancy of the filtered values of variables like temperature and species mass fraction obtained by LES-FD and FMDF-MC and this gives an opportunity to check the numerical accuracy of the hybrid LES/FMDF methodology for reacting flows. Figures 3.34(a) and 3.34(b) compare the temperatures obtained by the LES-FD and FMDF-MC components of the LES/FMDF at CA=183.21°. Figure 3.34(c) shows the correlation between the two components. There is good consistency between the results obtained from the two methods. The flow velocities and turbulence generated due to high-pressure injection is much higher than the magnitude of the swirling flow. Auto-ignition occurs on each side near the injector and the flame first propagates towards the center of the cylinder as the evaporated fuel carried by the momentum of the injected spray is ignited. The flame then starts spreading towards the cylinder walls as some of the evaporated vapor is spread radially towards the wall due to the swirling motion generated by the intake flow. It should be noted that the single-step global mechanism significantly under-predicts the chemical ignition delay and over-predicts the rate of reaction and flame temperature. This mechanism has been used here only to establish the consistency and the numerical accuracy of the LES and FMDF for reacting flows. With a better description of the chemical kinetics, we can expect the auto-ignition to occur further

downstream of the injector, nearer to the center of the cylinder. The consistency is also expected to improve due to better prediction of reaction rates compared to the high rates predicted by the global mechanism leading to large reaction source terms and consequently numerical undershoots and overshoots. The LES/FMDF methodology is capable of utilizing any description of the chemical kinetics including global or reduced kinetic models with direct ODE or ISAT solvers. Besides the use of complex multistep mechanisms, an approach often utilized is to use ignition delay correlations to calculate the ignition delay for the conditions existing in the cylinder. Examples of such correlations [171], [172] are:

$$\tau_{ID} = 2.4\phi^{-0.2} P^{-1.02} e^{Ea/R_u T}, \tag{3.9}$$

where τ_{ID} is the ignition delay in ms, ϕ is the fuel-air equivalence ratio, P is the pressure in bar, T is the temperature in K, and E_a/R_u is the activation energy.

$$\tau_{ID} = 9.4x10^{-12} P^{-0.55} X_{O_2}^{-0.63} C^{-0.5} e^{\frac{46550}{RT}}, \tag{3.10}$$

where τ_{ID} is the ignition delay in s, P is the pressure in atm, X_{O_2} is the mole fraction of O_2, C is the number of carbon atoms in the n-alkane, T is the temperature in K, and $46550/R$ is the activation energy with R in $cal/molK$. These correlations have the limitation of being developed for a fixed range of operating conditions, fuels etc. but can be used in lieu of a detailed mechanism. Some efforts were made in this study to incorporate the use of these ignition delay correlations for diesel combustion with the LES/FMDF methodology, but more work needs to be done, this would be the subject of future studies. Efforts are also currently ongoing to implement more detailed kinetic models with the insitu adaptive tabulation (ISAT) method.

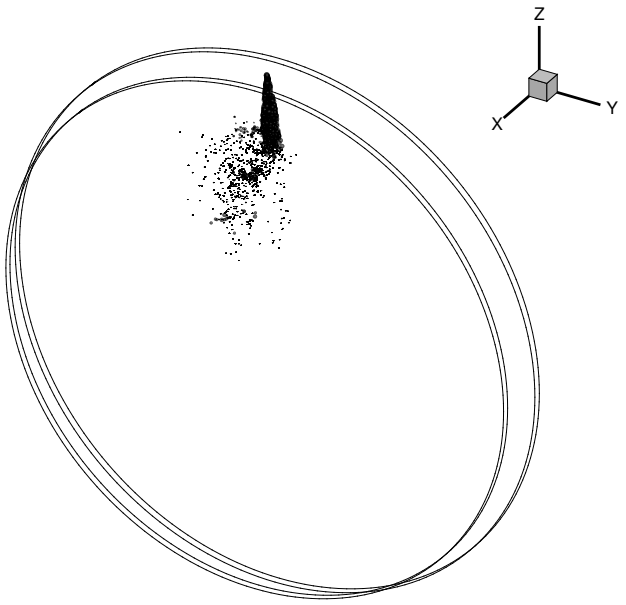

(a)

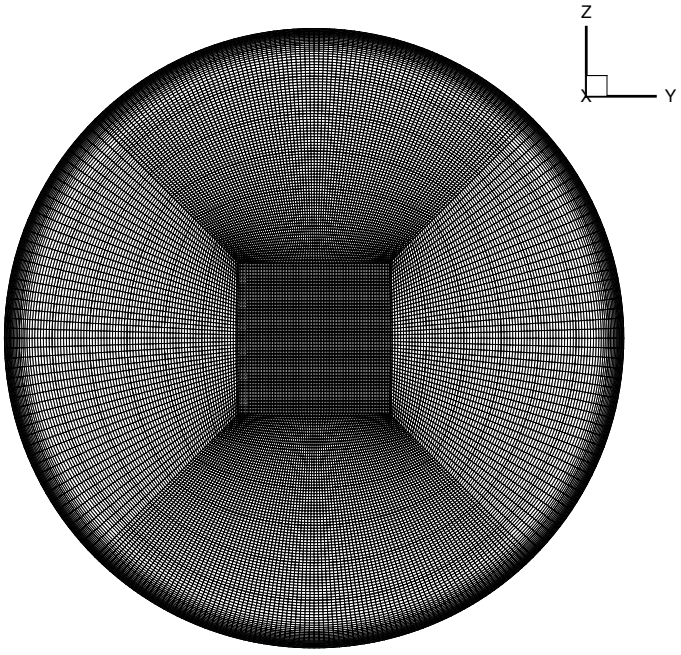

(b)

Figure 3.33: (a) Spray orientation for combustion simulations with 1 nozzle hole, (b) Fine grid with grid refinement in the spray and combustion regions.

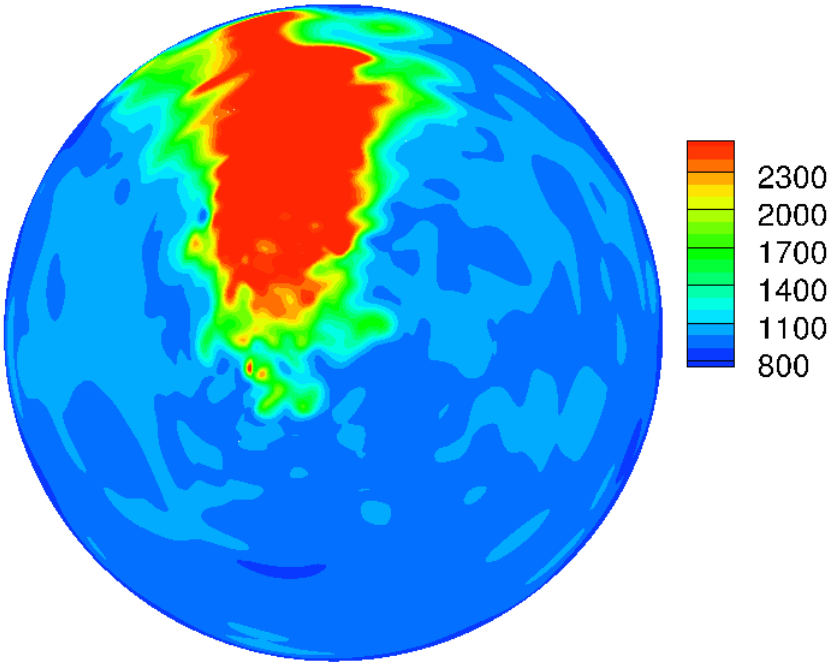

(a)

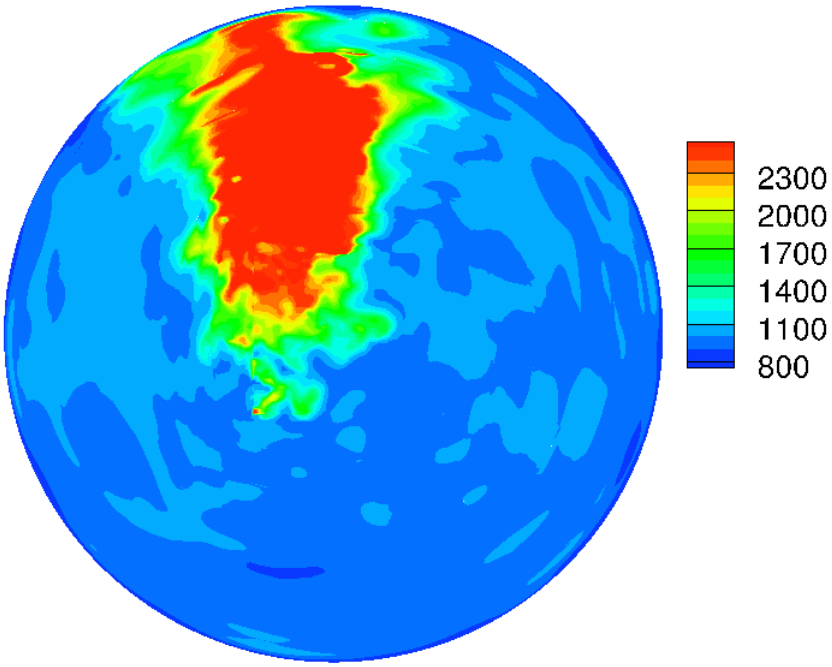

(b)

Figure 3.34: Temperature contours predicted on a plane through the mid-section of the cylinder by (a) LES-FD, (b) FMDF-MC components of the LES/FMDF methodology in the opposed-piston two-stroke engine at CA 183.21°, (c) correlation between the temperatures obtained from LES-FD and FMDF-MC.

Figure 3.34: (cont'd)

(c)

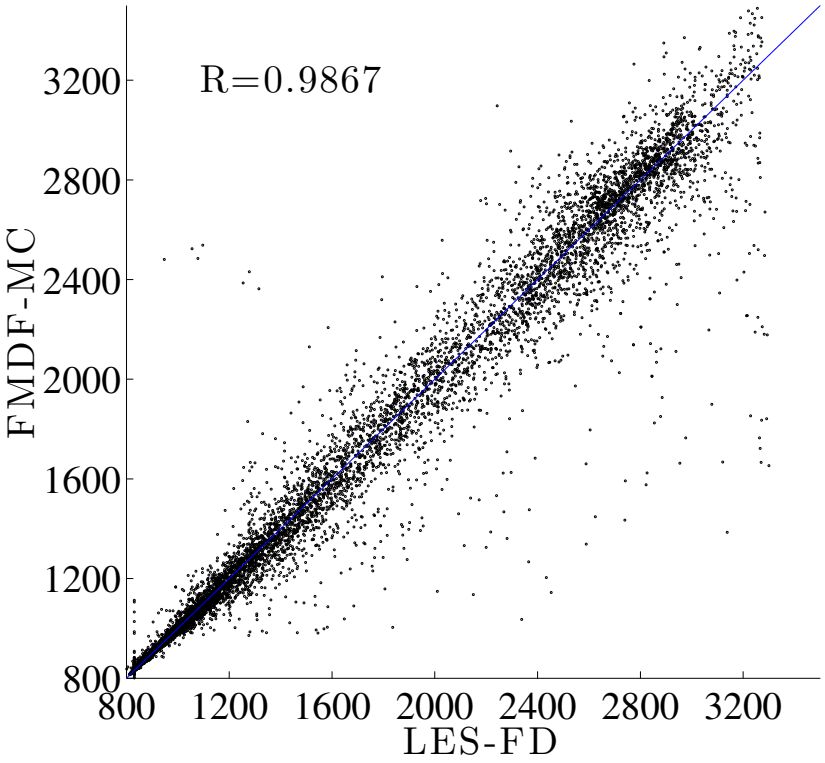

3.6 Summary and Conclusions

Large-eddy simulations of turbulent flow, spray and combustion in an opposed piston two-stroke engine is carried out via the compressible two-phase scalar filtered mass density function (FMDF) methodology. The cycle-to-cycle variations (CCV) in the flow variables like swirl and tumble are found to be significant, while those in the thermodynamic variables like temperature are negligible. The flow field is highly turbulent while the intake and exhaust ports are open and becomes more homogeneous in the compression stage. LES is able to capture the scavenging action, vital to the operation of the two-stroke engine, and the swirling flow generated by the intake ports. The effects of various modeling assumptions, geometry and operating parameters like the heat transfer model, the intake port angle and the intake backpressure on the operation of the engine have been studied. The heat transfer model used in some of our simulations is important as it affects the mean temperature inside the cylinder and also the heat flux to the metal parts during combustion. The intake port angle determines the amount of swirl generated in the cylinder and thus plays an important role during the mixture formation process. The magnitude of the intake backpressure not only affects the trapped mass inside the cylinder, but also the large-scale flow features like the swirl and tumble ratios. Higher backpressures can increase the efficiency but are limited by considerations related to high operating temperatures. The two-phase compressible LES/FMDF model has been applied successfully to simulate non-reacting turbulent spray for single-component and multi-component fuels. The Eulerian and Lagrangian components of the hybrid LES/FMDF methodology were found to be consistent with each other, thus validating the numerical accuracy of the LES/FMDF. The single component fuel simulations were carried out for n-dodecane, which is used as a surrogate for diesel using the multicom-

ponent evaporation model with variable properties. The effect of various spray parameters like the nozzle hole diameter, the injection pressure and the injected fuel temperature were also studied. In the absence of experimental results for the two-stroke opposed piston engine, the results of these simulations could not be validated quantitatively but the results available in literature for similar conditions were reproduced qualitatively. Simulations were also carried out for a bi-component fuel using the multicomponent evaporation model developed in this dissertation and the capability of the model was demonstrated. Combustion simulations were carried out for the opposed piston engine with n-dodecane as fuel and a global 1-step mechanism for the combustion chemistry. The consistency of the LES and FMDF components of the hybrid LES/FMDF solver was demonstrated. Quantitative prediction of combustion in diesel engines requires the use of better kinetic models and such models would be implemented in future studies.

APPENDIX

UNIFAC model, Biofuel species and properties, and MC Chemistry Parallelization and Optimization

This appendix describes the UNIFAC model used for calculating the activity coefficients, biofuel composition and their properties and the load balancing procedure for optimizing the Monte Carlo chemistry parallelization.

A.1 UNIFAC model

The UNIFAC method conceptualizes the liquid mixture to be a solution of the structural units or subgroups comprising the liquid molecules. The activity coefficients depend on the relative volume R_k and the relative surface area Q_k, which are properties of the subgroups, and on the subgroup interaction parameters a_{db}. The activity coefficient is composed of a combinatoric part (C), which represents the effect of the excess entropy, and a rest part (R), which represents the contribution of the excess enthalpy, and is defined as,

$$ln\gamma_k = ln\gamma_k^C + ln\gamma_k^R \tag{A.1}$$

where,

$$ln\gamma_k^C = 1 - J_k + lnJ_k - 5q_k(1 - J_k/L_k) \tag{A.2}$$

$$ln\gamma_k^R = q_k(1 - lnL_k) - \sum_{b=1,N_g} \left(\theta_b \frac{s_{bk}}{\eta_b} - G_{bk} ln \frac{s_{bk}}{\eta_k} \right) \tag{A.3}$$

$$J_k = \frac{r_k}{\sum_{c=1,N_{sp}} r_c X_{l,s,c}}; L_k = \frac{q_k}{\sum_{c=1,N_{sp}} q_c X_{l,s,c}} \tag{A.4}$$

$$r_k = \sum_{b=1,N_g} \nu_b^{(k)} R_b; q_k = \sum_{b=1,N_g} \nu_b^{(k)} Q_b \tag{A.5}$$

$$G_{bk} = \nu_b^{(k)} Q_b; \theta_b = \sum_{k=1,N_{sp}} G_{bk} X_{l,s,k}; s_{bk} = \sum_{d=1,N_g} G_{dk} \tau_{db} \tag{A.6}$$

$$\eta_{b=1,N_g} = \sum_b s_{bk} X_{l_s,k}; \tau_{db} = exp(-a_{db}/T_s) \tag{A.7}$$

Here, N_{sp} is the number of species, N_g is the number of subgroups and, $\nu_b^{(k)}$ is the number of subgroups of type b in a molecule of species k.

A.2 Biofuel Properties

Liquid Density (Rackett Equation)

$$V_s = V_s^R(0.29056 - 0.08775\omega)^{\phi} \tag{A.8}$$

$$\phi = (1 - T/T_c)^{2/7} - (1 - T_r/T_c)^{2/7} \tag{A.9}$$

Liquid Specific Heat (Corresponding States Method)

$$\frac{C_p^r}{R} = \frac{C_p - C_p^0}{R} = 1.586 + \frac{0.49}{1 - T_r} + \omega\left[4.2775 + \frac{6.3(1 - T_r)^(1/3)}{T_r} + \frac{0.4355}{1 - T_r}\right] \tag{A.10}$$

Vapor Specific Heat (Joback Method)

$$\begin{aligned} C_p^0(T) =& \left\{ \sum_k N_k C_{pAk} - 37.93 \right\} + \left\{ \sum_k N_k C_{pBk} + 0.210 \right\} T \\ &+ \left\{ \sum_k N_k C_{pCk} - 3.91e-04 \right\} T^2 + \left\{ \sum_k N_k C_{pDk} + 2.06e-07 \right\} T^3 \end{aligned} \tag{A.11}$$

Vapor Pressure (Riedel Corresponding States Method)

$$lnP_{vp} = A^+ - \frac{B^+}{T_r} + C^+ lnT_r + D^+ T_r^6 \tag{A.12}$$

$$A^+ = -35Q, B^+ = -36Q, C^+ = 42Q + \alpha_c, D^+ = -Q, Q = K(3.758 - \alpha_c) \tag{A.13}$$

$$\alpha_c = \frac{3.758K\psi_b + ln(P_c/1.01325)}{K\psi_b - lnT_{br}} \tag{A.14}$$

$$\psi_b = -35 + \frac{36}{T_{br}} + 42lnT_{br} - T_{br}^6 \tag{A.15}$$

Enthalpy of Vaporization (Law of Corresponding States)

$$\frac{H_v}{RT_c} = 7.08(1 - T_r)^0.354 + 10.95\omega(1 - T_r)^0.456 \tag{A.16}$$

Surface Tension (Sastri and Rao Method)

$$\sigma = KP_c^x T_b^y T_c^z \left[\frac{1 - T_r}{1 - T_{br}}\right]^m \tag{A.17}$$

A.3 Biofuel Species

The various biofuel species considered in this study and their chemical formulae and structure are given in Table A.1. The UNIFAC Groups for the various biofuel species are given in Table A.2 and their $R - Q$, a and c interaction parameters are given in Tables A.3-A.6.

Name	**Formula**	**Structure**
Methyl Oleate (MO)	$C_{19}H_{36}O_2$	$CH_3-(CH_2)_7-CH=CH-(CH_2)_6-CH_2COO-CH_3$
Dibutyl Succinate(DBS)	$C_{12}H_{22}O_4$	$CH_3-(CH_2)_3-OOCCH_2-CH_2COO-(CH_2)_3-CH_3$
2-EthylHexyl Nonanoate (2-EHN)	$C_{17}H_{34}O_2$	$CH_3-(CH_2)_3-(C_2H_5)CH-CH_2-OOCCH_2-(CH_2)_6-CH_3$
Butyl Nonanoate (BN)	$C_{13}H_{26}O_2$	$CH_3-(CH_2)_3-OOCCH_2-(CH_2)_6-CH_3$
Iso-Butyl Nonanoate (iBN)	$C_{13}H_{26}O_2$	$CH_3-(CH_2)_2-CH_2COO-CH_2-(C_2H_5)CH-(CH_2)_3-CH_3$
2-EthylHexyl Butyrate (2-EHB)	$C_{12}H_{24}O_2$	$CH_3-(CH_3)CH-CH_2-OOCCH_2-(CH_2)_6-CH_3$
Methyl Butanoate (MB)	$C_5H_{10}O_2$	$CH_3-CH_2-CH_2COO-CH_3$

Table A.1: Biofuel species chemical formulae and structure

Species	**CH_3**	**CH_2**	**CH**	**HC = CH**	**CH_2COO**
MO	2	13	0	1	1
DBS	2	6	0	0	2
2-EHN	3	11	1	0	1
BN	2	9	0	0	1
iBN	3	7	1	0	1
2-EHB	3	6	1	0	1

Table A.2: Biofuel Species and their UNIFAC groups

UNIFAC Group	Group No.	R_k	Q_k
CH_3	1	0.6325	1.0608
CH_2	2	0.6325	0.7081
CH	3	0.6325	0.3554
$HC = CH$	4	1.2832	1.2489
$CH_2 - COO$	5	1.2700	1.4228

Table A.3: Biofuel Species and their UNIFAC R-Q interaction parameters

a_{mn}	1	2	3	4	5
1	0	0	0	189.66	98.656
2	0	0	0	189.66	98.656
3	0	0	0	189.66	98.656
4	-95.418	-95.418	-95.418	0	980.74
5	632.22	632.22	632.22	-582.82	0

Table A.4: Biofuel Species and their UNIFAC a interaction parameters

b_{mn}	1	2	3	4	5
1	0	0	0	-0.2723	1.9294
2	0	0	0	-0.2723	1.9294
3	0	0	0	-0.2723	1.9294
4	0.06171	0.06171	0.06171	0	-2.4224
5	-3.3912	-3.3912	-3.3912	1.6732	0

Table A.5: Biofuel Species and their UNIFAC b interaction parameters

c_{mn}	1	2	3	4	5
1	0	0	0	0	-0.003133
2	0	0	0	0	-0.003133
3	0	0	0	0	-0.003133
4	0	0	0	0	0
5	0.003928	0.003928	0.0039280	0	0

Table A.6: Biofuel Species and their UNIFAC c interaction parameters

A.4 MC Chemistry Parallelization and Optimization

Large Eddy Simulation (LES) of chemically reacting flows via the Filtered Mass Density Function (FMDF) formulation involves integration of the chemical reaction equations for millions of nearly uniformly distributed Lagrangian Monte Carlo (MC) particles. In many cases, particles in the colder regions do not undergo any reaction at all while the chemical reaction equations need to be integrated for a varying number of particles in other regions of the flow. This causes imbalance in the computational load on various processors in the case of a uniform domain decomposition of the finite difference computational mesh. The imbalance in the computational load leads to a lower efficiency in the case of large scale parallel computations since the low load processors remain idle while the processors with larger number of MC particles undergoing reaction computations are busy. The aim here is to develop a load balancing algorithm to overcome the load imbalance and achieve higher efficiency for parallel computations.

A.4.1 Load Balancing Procedure

The basic steps of the load balancing procedure applied here are as follows:

1. The load information of each processor is utilized to calculate a load transfer matrix which contains information about the particle communication to be carried out between different processors to achieve a balanced load.

2. This matrix is then communicated to each processor and MC particle data transfer takes place using the load transfer matrix to achieve uniform load on all processors.

3. Once load balance is achieved, the combustion calculation is carried out and the updated MC particle information is sent back to the originating processor.

4. The procedure is repeated again at the next time step.

This procedure significantly reduces the total simulation time by reducing the idle time of the lower load processors. Various methods can be used to calculate the load transfer matrix and are described in the following sections. An important consideration in all these algorithms is that since the MC particles have to be communicated back to their originating processors, the algorithms should not only achieve load balancing but also seek to minimize the data redistribution and communication costs. Before the various load balancing algorithms are described, definitions of some basic terms used in the study are presented.

A.4.1.1 Definitions

Definitions of some of the terms used in the load balancing algorithm are as follows:

Vertex(V) —Each vertex on a processor graph represents a processor.

Edge(E) —Two processors form an edge if they share a common boundary and/or communicate MC particles with each other.

Processor Graph(G) —G=(V,E) Graph representing the set of vertices and their associated edges in the computational domain.

MaxEdge —Maximum number of communication partners for a vertex/processor.

Edge-cut —Total number of communications between different processors in the load balancing algorithm.

MaxMC —Maximum of the sum of MC particles migrating into or out of a domain or processor.

TotalMC —Sum of the total number of MC particles that migrate into or out of domains or processors.

An optimum load balancing algorithm should aim to achieve a balanced load such that

MaxEdge, Edge-cut, MaxMC and TotalMC are all minimized, thus minimizing the total data redistribution cost, while the load balance calculation itself is also minimized. However, various algorithms tend to minimize one or more of these parameters.

A.4.1.2 Cut-Paste Repartitioning

The simplest algorithm for load balancing is the cut-paste repartitioning method, which perturbs the initial distribution of the MC particles just enough to achieve a balanced load. This method optimally minimizes the data redistribution (MaxMC and TotalMC) but results in a larger Edge-cut, while MaxEdge is a variable parameter. The basic algorithm consists of the following steps:

1. Excess MC particles in overloaded processors are communicated to one or more underloaded processors, irrespective of whether the sub-domains represented by the processors are adjacent or not, to fulfill their deficit. This process is continued until the positive deficit on the overloaded processor becomes zero.

2. The underloaded processors receive particles from one or more overloaded processors until their deficit becomes zero.

3. The process is carried out for all processors until load balance is achieved.

A.4.1.3 Flow-Diffusion Method

The Flow-Diffusion method is based on the algorithm proposed in [173]. This method attempts to minimize the norm of the data movement between processors to achieve load balancing and is a global diffusion method. In this method, overweight processors export MC particles to adjacent processors, which may further communicate particles to their neighboring processors in order to achieve a global balance, while trying to minimize the edge-cut.

Let (V, E) is the processor graph for p connected processors, with $V = (1, 2, .., p)$ being the set of vertices, each representing a processor and E is the set of edges. An edge is formed by two processors i and j if they share a boundary and communicate with each other. If l_i is the load on a processor, the average load per processor is,

$$\bar{l} = \frac{\sum_{i=1}^{p} l_i}{p} \tag{A.18}$$

If δ_{ij} is the amount of load to be sent form processor i to processor j, the load balancing algorithm should make the load on each processor equal to the average load, that is,

$$\sum_{j|(i,j)\in E)} \delta_{ij} = \frac{l_i - \bar{l}}{p}, i = 1, 2, ..., p \tag{A.19}$$

If A is the matrix associated with 3.6, x is the vector of δ_{ij}s and b is the right-hand side, minimizing the Euclidean norm of the data movement between processors requires that $\frac{1}{2}x^T x$ be minimized subject to $Ax = b$. This leads to the system of equations,

$$L\lambda = b, \tag{A.20}$$

where $L = AA^T$, and λ is the vector of Lagrange multipliers. The algorithm for balancing the loads then becomes,

1. Find the average load, and thus the right-hand side of 3.6.

2. Solve equation 3.6 to obtain λ.

3. Determine the amount of load to be transferred between processors. The load that processor i communicates to processor j is $\lambda_i - \lambda_j$. A positive difference implies that processor i sends MC particles to processor j, while a negative difference means that processor i receives

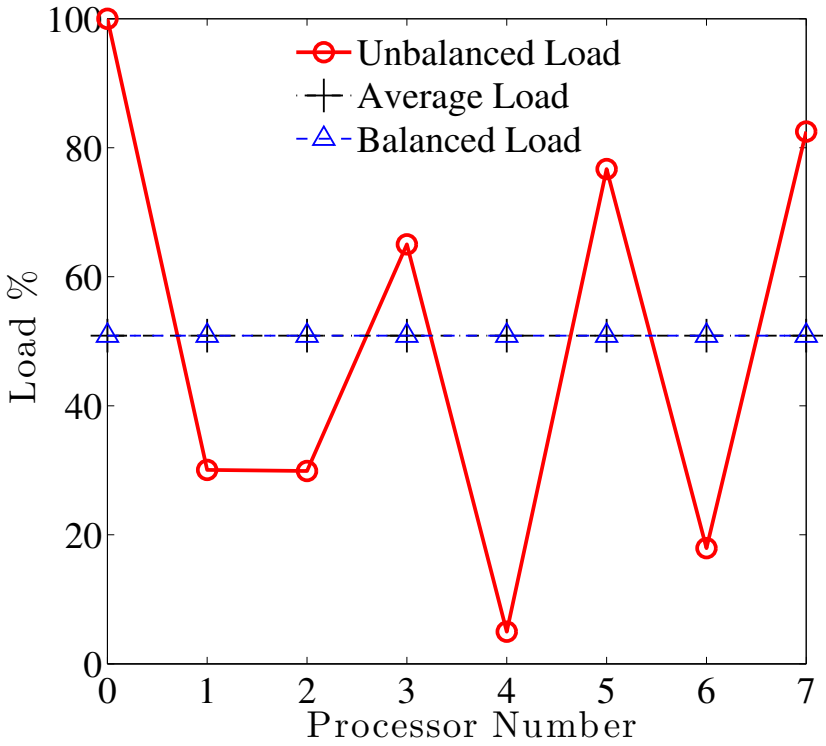

Figure A.1: Random load distribution for 8 processors.

particles from j.

A.4.2 Load balancing for a random load distribution

Figure A.1 represents a randomly generated load distribution for an 8 processor domain with the Monte Carlo particles distributed equally among the processors. The average load on the processors is about 50%. The load balancing algorithms discussed earlier were applied to the load balancing problem.

Figure A.2 compares the strong scaling obtained by applying the cut-paste repartitioning and the flow-diffusion methods for different number of processors (8-128) and Monte Carlo particles (8 million - 64 million). Strong scaling is defined as the scaling obtained when the problem size is kept fixed and the number of processors is increased. Ideal speedup in

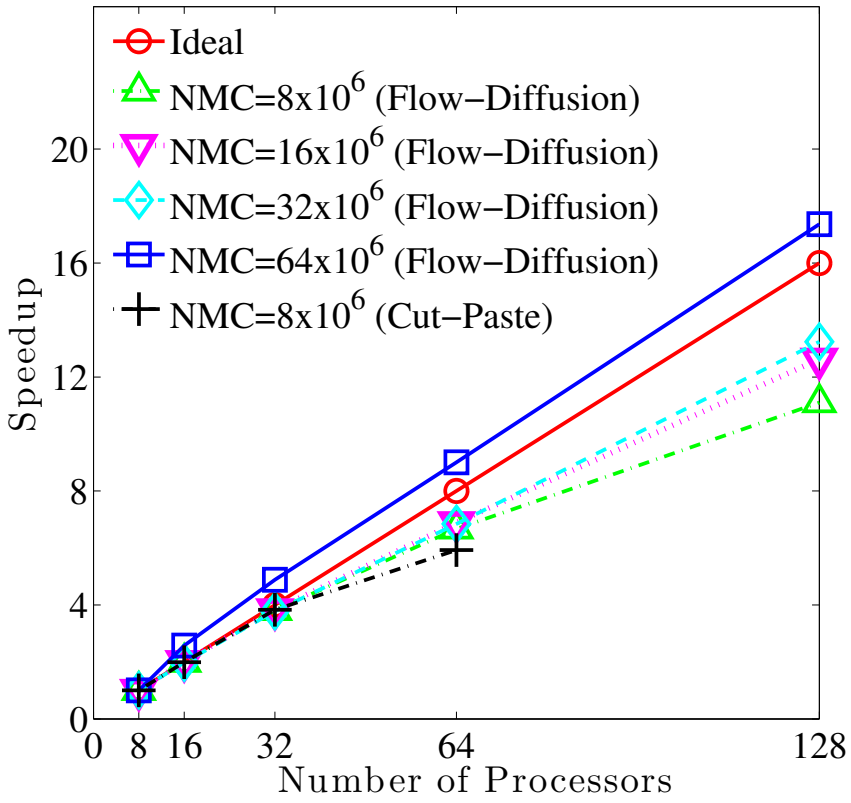

Figure A.2: Strong scaling for Cut-paste repartitioning and Flow-Diffusion methods. NMC=Total number of MC particles, distributed equally among processors.

this case is defined as the speedup obtained when computation time decreases linearly with increase in the number of processors. This implies that the computation time is halved when the number of processors is doubled, becomes a quarter when the number of processors is quadrupled, and so on. In these simulations, the cut-paste repartitioning method is applied without any modification. However, for the flow-diffusion method, the requirement that MC particle communication should only take place physically connected sub-domains is relaxed. This implies that processor graph for the flow-diffusion method need not be based on the actual physical domain connectivity but can be modified to achieve a smaller path for the diffusion calculation. As shown in Figure A.2, although the cut-paste repartitioning scales almost linearly up to 32 processors, the speedup is far from ideal for the 64 processor case. The flow-diffusion method gives better scaling as the number of processors is increased, although the scaling is still not linear for smaller size problems. For the case with NMC=64 million, where NMC is the total number of Monte Carlo particles in the computation, the scaling appears to be better than linear. This is probably due to the fact that the problem size is too big for the 8 processor case and the communication time to achieve load balance increases due to network bandwidth limitations. If the 16 processor is considered as the base case, the scaling is almost linear. Figure A.3 shows the weak scaling for the flow-diffusion method. Weak scaling is defined as the scaling obtained when the problem size increases proportionally to the increase in the number of processors. Thus, the number of MC particles per processor (NMC_p) is kept constant but the number of processors is increased leading to a bigger problem size. Ideal speedup in this case is 1, which means that the total computational time remains same if the problem size is increased as long as the number of particles per processor is same. The speedup is nearly ideal for 16 processors but deviates from ideal as number of processors increases. Also, the speedup is better for smaller

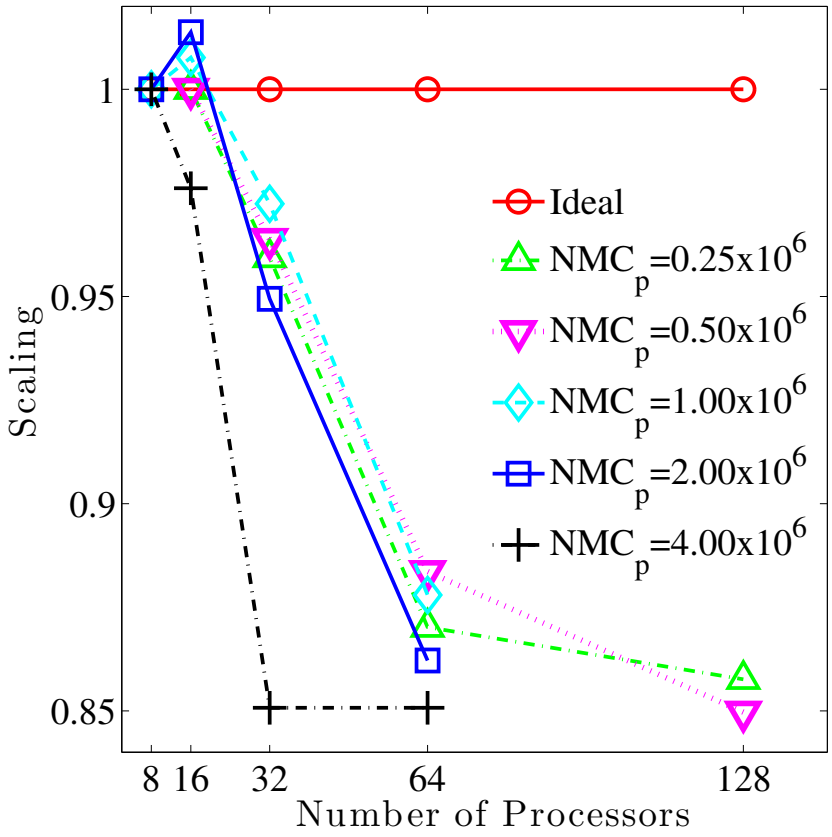

Figure A.3: Weak scaling for Flow-Diffusion method. NMC_p=Number of MC particles per processor.

number of MC particles per processor. The decrease in speedup for larger NMC_p can be explained due to the increase in communication costs.

The communication time increases significantly as the number of processors is increased, thus leading to decrease in scaling efficiency. A major factor in increasing the communication time is the need to communicate the updated particle information back to the originating processor, thus it essential that the load balancing algorithms minimize TotalMC.

A.4.3 Load Balancing for highly unbalanced load

An interesting application of the load balancing algorithms is in the case of an acutely unbalanced load. An illustrative example of this situation is Figure A.4 which shows the load distribution for an n-heptane spray. The spray is injected into a high pressure cubical closed

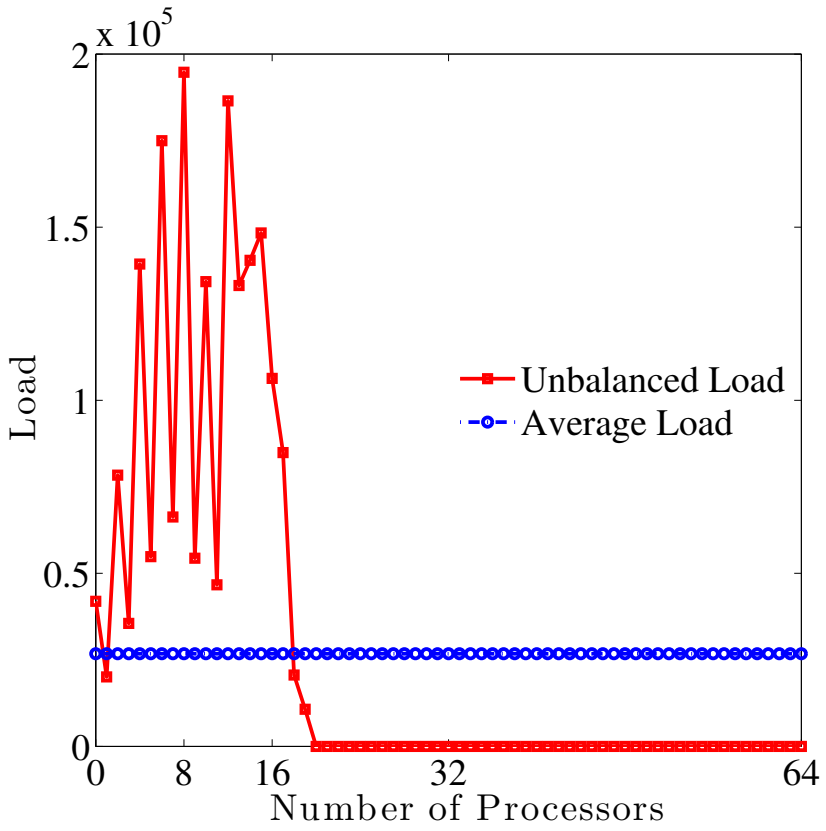

Figure A.4: Load distribution for n-heptane spray.

chamber with a quiescent atmosphere at high injection pressures. The jet breakups and evaporates with small liquid and vapor penetration lengths compared to the length of the physical domain in the spray direction. This implies that most of the physical domain has no evaporated fuel with most of the chemical reactions taking place in a small region relatively near to the nozzle along the axis of the spray, leading to highly overloaded processors in this region. Thus, 18 out of 64 processors are overloaded while the rest have either low or zero loads. This case presents a challenge for the load balance algorithms discussed above. The cut-paste algorithm results in a single overloaded processor communicating with a large number of zero or low load processors, leading to a higher MaxEdge. The flow-diffusion method results in long diffusion paths from heavily loaded processors to zero or low load through processors already having enough MC particles, leading to a high MaxMC.

The methods need to be modified in order to be applicable for highly unbalanced load distributions.

A.4.3.1 Modified Cut-Paste Repartitioning

The modification in the cut-paste repartitioning method is to limit the MaxEdge, that is, the maximum number of processors that a processor communicates with. The modified algorithm is as follows:

1. Overloaded processors are allowed to communicate particles to underloaded processors to fulfill their deficit until the maximum allowed number of communication partners (MaxEdge) is reached.

2. The overloaded processors are balanced by sending all extra particles to their last communication partner.

3. The process is repeated until load balance is achieved.

A.4.3.2 Multilevel Flow/Diffusion Method

The flow-diffusion method is modified to make it multilevel. In this method, an attempt is made to achieve load balancing by dividing the domain into smaller groups. The proposed algorithm is as follows:

1. The processors are sorted in descending order according to their weights.

2. The processors are then divided into fixed number of subdivisions or groups with balanced weights, to a specified tolerance, according to a predetermined sequence.

3. The processors within each group are then balanced according to the Flow/Diffusion method.

The algorithm is presented graphically in Figure A.5.

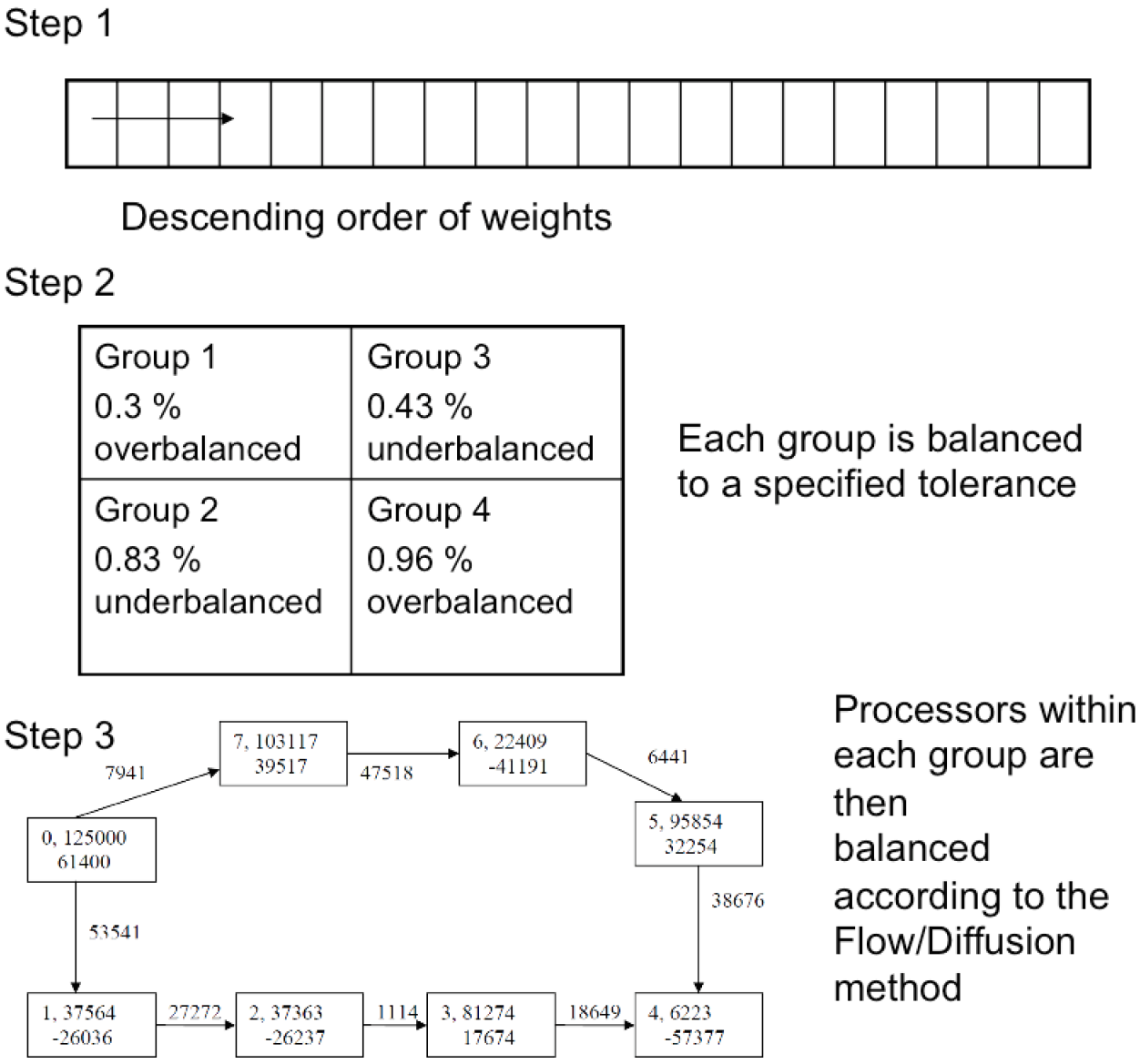

Figure A.5: Multilevel Flow/Diffusion Method.

Load Balancing Method	Edge-cut	MaxMC	TotalMC
Modified Cut-Paste Repartitioning with MaxEdge 3	125	203039	1822160
Modified Cut-Paste Repartitioning with MaxEdge 4	125	165514	1512665
Multilevel Flow/Diffusion Method with MaxEdge 3	176	165417	1974072
Multilevel Flow/Diffusion Method with MaxEdge 4	184	170797	1851947

Table A.7: Load Balancing algorithm parameters for modified cut-paste repartitioning and multilevel flow/diffusion algorithms applied to the load distribution in Figure A.4.

Table A.7 shows the parameters Edge-cut, MaxMC and TotalMC for the modified cut-paste repartitioning and multilevel flow/diffusion methods when they are applied to the highly unbalanced load distribution in Figure A.4. The parameter MaxEdge is an input variable in the modified cut-paste repartitioning method and can be adjusted in the multilevel flow/diffusion method by rearranging the processor graph for each group. A MaxEdge value of 3 leads to higher TotalMC in both the methods, while the multilevel method has a significantly higher edge-cut compared to the cut-paste repartitioning method.

Work is in progress to test the speedup and scaling associated with the modified cut-paste repartitioning and multilevel flow/diffusion algorithms for application in cases of highly unbalanced loads. Currently, the chemical reaction calculations are being carried out using explicit methods for detailed chemical mechanisms. Future work will focus on evaluating the processor loads for chemical reaction calculations based on ODE solvers and achieving balanced loads for these calculations.

BIBLIOGRAPHY

BIBLIOGRAPHY

[1] Amsden, A. A. , O'Rourke, P. J., Bulter, T. D., KIVA-ll: A Computer Program for Chemically Reactive Flows with Sprays, Los Alamos National Laboratory Report No LA-11560-MS UC-96, 1989.

[2] Miller, R.S., Bellan, J., Direct numerical simulation of a confined three-dimensional gas mixing layer with one evaporating hydrocarbon-droplet-laden stream, Journal of Fluid Mechanics 384 (1999) 293-338.

[3] Miller, R.S., Harstad, K., Bellan, J., Evaluation of equilibrium and non-equilibrium evaporation models for many-droplet gas-liquid flow simulations, International Journal of Multiphase Flow 24 (1998) 1025-1055.

[4] Almeida, T., Jaberi, F.A., Large Eddy Simulation of a Dispersed Particle-Laden Turbulent Round Jet, International Journal of Heat and Mass Transfer 51 (2008) 683-695.

[5] Almeida, T., Jaberi, F.A., Direct Numerical Simulations of a Planar Jet Laden with Evaporating Droplets, International Journal of Heat and Mass Transfer 49 (2006) 2113-2123.

[6] Jaberi, F.A., Mashayek, F., Temperature Decay in Two-Phase Turbulent Flows, International Journal of Heat and Mass Transfer 43 (2000) 993-1005.

[7] Mashayek, F., Jaberi, F.A., Particle Dispersion in Forced Isotropic Low Mach Number Turbulence, International Journal of Heat and Mass Transfer 42 (1999) 2823-2836.

[8] Jaberi, F.A., Temperature Fluctuations in Particle-Laden Homogeneous Turbulent Flows, International Journal of Heat and Mass Transfer 41 (1998) 4081-4093.

[9] Sirignano, W..A., Fluid Dynamics and Transport of Droplets and Sprays, New York: Cambridge University Press, 1999.

[10] Sazhin, S.S., Advanced models of fuel droplet heating and evaporation, Progress in Energy and Combustion Science 32 (2) (2006) 162-214.

[11] Tamim, J., Hallett, W., A continuous thermodynamics model for multicomponent droplet vaporization, Chem. Eng. Sci. 18 (1995) 2933-2942.

[12] Hallet, W., A simple model for the vaporization of droplets with large numbers of components, Combustion and Flame 121 (2000) 334-344.

[13] Lippert, A, Reitz, R., Modeling of multicomponent fuels using continuous distributions with application to droplet evaporation and sprays, SAE Technical Paper 972882, 1997.

[14] Zhang, L., Kong, S., Modeling of multicomponent fuel vaporization and combustion for gasoline and diesel spray, Chem. Eng. Sci. 64 (2009) 3688-3696.

[15] Zhang, L., Kong, S-C., Vaporization modeling of petroleum-biofuel drops using a hybrid multicomponent approach, Combustion and Flame 157 (2010) 2165-2174.

[16] Landis, R.B., Mills, A.F., Effect of internal diffusion resistance on the evaporation of binary droplets 5th Int. Heat Transfer Cont (Tokyo) Paper B7-9, 1974.

[17] Sirignano, W.A., Law, C.K., Transient heating and liquid phase mass diffusion in droplet vaporization Evaporation-Combustion of Fuels (Advances in Chemistry Series vol 166) ad J T Zung (Washington, DC: American Chemical Society) pp 1-26, 1978.

[18] Lara-Urbaneja, P., Sirignano, W.A., Theory of transient multicomponent droplet vaporization in a convective field gasification, 18th Symp. (Int.) Combustion (Pittsburgh, PA: The Combustion Institute) (1981) 1365-74.

[19] Aggarwal, S.K., Modeling of a dilute vaporizing multicomponent fuel spray, International Journal of Heat and Mass Transfer 30 (1987) 291-302.

[20] Chen, G., Aggarwal, S.K., Jackson, T.A., Switzer, G.L., Experimental study of pure and multicomponent fuel droplet evaporation in a heated air flow, Atomization and Sprays 7 (1997) 317-337.

[21] Renksizbulut, M., Bussmann, M., Multicomponent droplet evaporation at intermediate Reynolds numbers, International Journal of Heat and Mass Transfer 3 (1993) 2827-35.

[22] Zeng, Y., Lee, C.F., A multicomponent-fuel film-vaporization model for multidimensional computations, Propulsion and Power 16 (2000) 964-73.

[23] Zeng, Y., Lee, C.F., Modeling of spray vaporization and air-fuel mixing in gasoline direct-injection engine SAE Paper, 2000-OI-0537, 2000.

[24] Ra, Y., Reitz, R.D., A vaporization model for discrete multicomponent fuel sprays, International Journal of Multiphase Flow 35 (2009) 101-117.

[25] Torres, D., O'Rourke, P.J., A discrete multicomponent fuels model for GDl engine simulations, ILASS Americas 14th Annual Conference on Liquid Atomization and Spray Systems (Dearborn, MI), 2001.

[26] Torres, D.J., O'Rourke, P.J., Amsden, A.A., Efficient multicomponent fuel algorithm, Combustion Theory and Modelling 7 (2003) 67-86.

[27] Torres, D.J., O'Rourke, P.J., Amsden, A.A., A discrete multicomponent fuel model, Atomization and Sprays 13 (2-3) (2003) 131-172.

[28] Abramzon, B., Sirignano, W.A., Droplet vaporization model for spray combustion calculations, International Journal of Heat and Mass Transfer 32 (1989) 1605-1617.

[29] Gmehling, J., Rasmussen, P., Aa. Fredenslund, Vapor-liquid equilibria by UNIFAC group contribution. Revision and extension 2, Ind.Eng. Chem. Process Des. Dev. 21 (1982) 118-127.

[30] Smith, J.M., Van Ness, C., Introduction to Chemical Engineering Thermodynamics, McGraw-Hill Book Company, 1987.

[31] Dennis, J.E., Schnabel, R.B., Numerical methods for unconstrained optimization and nonlinear equations, Englewood Cliffs,N.J.; Prentice Hall, pp 169-189, 1983.

[32] Poling, B.E., Prausnitz, J.M., O'Connell, J.P., The properties of gases and liquids, 5th Edition, New York: McGraw-Hill, c2001.

[33] Afshari, A., Jaberi, F.A., Shih, T. I.-P. , Large-Eddy Simulation of Turbulent Flow in an Axisymmetric Dump Combustor, AIAA Journal 46(7) (2008) 1576-1592.

[34] Banaeizadeh, A., Afshari, A, Schock, H, Jaberi, F., Large-eddy simulations of turbulent flows in internal combustion engines, International Journal of Heat and Mass Transfer 60 (2013) 781-796.

[35] Smagorinsky, J., General Circulation Experiments with the Primitive Equations. 1. The Basic Experiment, Monthly Weather Review, 91(3) (1963) 99-164.

[36] Yoshizawa, A., Statistical theory for compressible turbulent shear flows, with the application to subgrid modeling, Physics of Fluids 29 (1986) 2152-2164.

[37] Germano, M., Piomelli, U., Moin, P., Cabot, W.H., A dynamic subgrid-scale eddy viscosity model, Physics of Fluids A 3 (1991) 1760-1765.

[38] Moin, P., Squires, K., Cabot, W., Lee, S., A dynamic subgrid-scale model for compressible turbulence and scalar transport, Physics of Fluids A 3 (1991) 2746-2757.

[39] Lilly, D.K., A proposed modification of the Germano subgrid-scale closure method, Physics of Fluids A 4 (1992) 633-635.

[40] Kim, W.-W. , Menon, S., LES of turbulent fuel/air mixing in a swirling combustor, AIAA Paper No. AIAA-1999-200 (1999).

[41] Stone, C., Menon, S., Simulation of fuel-air mixing and combustion in a trapped-vortex combustor, AIAA Paper No. AIAA-2000-478 (2000).

[42] Siebers, D.L., Liquid-Phase Fuel Penetration in Diesel Sprays, SAE Technical Paper 980809, 1998.

[43] Hentschel, W., Schindler, K.-P, Haahtela, O., European Diesel Research IDEA- Experimental Results from DI diesel Engine Investigations, SAE Technical Paper 941954, 1994.

[44] Mathieu, O., Djebaili-Chaumeix, N., Paillard, C-E., Douce, F., Experimental study of soot formation from a diesel fuel surrogate in a shock tube, Combustion and Flame 156 (2009) 1576-1586.

[45] Farrell, J.T., Cernansky, N.P., Dryer, F.L., Friend, D.G., Hergart, C.A., Law, C.K., McDavid, R.M., Mueller, C.J., Patel, A.K., Pitsch, H., Development of an Experimental Database and Kinetic Models for Surrogate Diesel Fuels, SAE Technical Paper 2007-01-0201, 2007.

[46] Mueller, C.J., Cannella, W.J., Bruno, T.J., Bunting, B., Dettman, H.D., Franz, J.A., Huber, M.L., Natarajan, M., Pitz, W.J., Ratcliff, M.A., Wright, K., Methodology for Formulating Diesel Surrogate Fuels with Accurate Compositional, Ignition-Quality, and Volatility Characteristics, Energy and Fuels 26 (2012) 3284-3303.

[47] Naber, J.D., Siebers, D.L., Effects of Gas Density and Vaporization on Penetration and Dispersion of Diesel Sprays, Transactions of the SAE, Vol. 105, Sect. 3, pp. 82-111, 1996.

[48] Baumgarten, C., Mixture Formation in Internal Combustion Engines, Springer-Verlag 2006.

[49] Beale, J.C., Reitz, R.D., Modeling Spray Atomization with the Kelvin-Helmholtz/Rayleigh-Taylor Hybrid Model, Atomization and Sprays 9(6) (1999) 623-650.

[50] Ricart, L.M., Reitz, R.D., Dec, J.E., Comparisons of Diesel Spray Liquid Penetration and Vapor Fuel Distributions with In-Cylinder Optical Measurements, Journal of Engineering for Gas Turbines and Power 122 (2000) 588-595.

[51] Som, S., Development and Validation of Spray Models for Investigating Diesel Engine Combustion and Emissions, PhD Thesis, University of Illinois at Chicago, 2009.

[52] Westbrook, C.K., Pitz, W.J., Westmoreland, P.R., Dryer, F.L., Chaos, M., Osswald, P., Kohse-Hoinghaus, K., Cool, T.A, Wang, J., Yang, B., Hansen, N., Casper, T, Proc. Combust. Inst. 2009, 32(1), 221-228.

[53] Demirbas, A., Biofuels sources, biofuel policy, biofuel economy and global biofuel projections, Energy Convers. Manage. 49(8) (2008) 2106-2116.

[54] Demirbas, A., Progress and recent trends in biofuels, Prog. Energy. Combust. Sci. 33(1) (2007) 1-18.

[55] Toulson, E., Allen, C., Miller, D.J., Lee, T., Modeling the Auto-Ignition of Oxygenated Fuels using a Multistep Model, Energy Fuels 24 (2010) 888-896.

[56] Toulson, E., Allen, C., Miller, D.J., Schock, H.J., Lee, T., Optimization of a Multistep Model for the Auto-ignition of Dimethyl Ether in a Rapid Compression Machine, Energy Fuels 24 (2010) 3510-3516.

[57] Toulson, E., Allen, C., Miller, D.J., McFarlane, J., Schock, H.J., Lee, T., Modeling the Autoignition of Fuel Blends with a Multistep Mdel, Energy Fuels 25 (2011) 632-639.

[58] Allen, C., Toulson, E., Hung, D.L.S., Schock, H., Miller, D., Lee, T., Ignition Characteristics of Diesel and Canola Biodiesel Sprays in the Low-Temperature Combustion Regime. Energy Fuels 25 (2011) 2896-2908.

[59] Squibb, C.W., Schock, H., Allen, C., Lee, T., Poort, M., Crayne, K., Optical Diagnostic Combustion Comparisons of Pump Diesel with Bio-Derived Diesel Blends in an Optical DI Diesel Engine, SAE Technical Paper 2012-01-0868, 2012.

[60] Allen, C., Toulson, E., Tepe, D., Schock, H., Miller, D., Lee, T., Characterization of the effect of fatty ester composition on the ignition behavior of biodiesel fuel sprays, Fuel 111 (2013) 659-669.

[61] Dombrovsky L., Sazhin, S., Absorption of thermal radiation in a semi-transparent spherical droplet: a simplified model, International Journal of Heat and Fluid Flow 24 (2003) 919-927.

[62] Irannejad, A., Jaberi, Farhad, Large eddy simulation of turbulent spray breakup and evaporation, International Journal of Multiphase Flow 61 (2014) 108-128.

[63] Irannejad, A., Jaberi, Farhad, Numerical study of high speed evaporating sprays, International Journal of Multiphase Flow 70 (2015) 58-76.

[64] Gorokhovski, M.A., Saveliev, V.L., Analyses of Kolmogorov's model of breakup and its application into Lagrangian computation of liquid sprays under air-blast atomization, Physics of Fluids 15, 184 (2003) .

[65] Silverman, I., Sirignano, W.A., Multi-droplet interaction effects in dense sprays, Int. J. Multiphase Flow 20 (1994) 99-116 .

[66] Naitoh, K., Itoh, T., Takagi, Y., Kuwahara, K., Large-eddy simulation of premixed flame in engine based on the multi-level formulation and the renormalization group theory, SAE Paper No. 920590, 1992.

[67] Haworth, D.C., Large-eddy simulation of in-cylinder flows, Oil Gas Sci. Technol. 54 (2) (1999) 175-185.

[68] Morse, A.P., Whitelaw, J.H., Yianneskia, M., Turbulent flow measurement by laser Doppler anemometry in a motored reciprocating engine, Imperial College Dept. Mech. Eng. Report FS/78/24, 1978.

[69] Verzicco, R., Mohd-Yusof, J., Orlandi, P., Haworth, D.C., Large-eddy simulation in complex geometric configuration using boundary body forces, AIAA J. 38 (3) (2000) 427-433.

[70] Mohd-Yusof, Interaction of massive particles with turbulence, Ph.D. thesis, Cornell University, 1996.

[71] Thobois, G. Rymer, T. Souleres, T. Poinsot, Large-eddy simulation for the prediction of aerodynamics in IC engines, Int. J. Veh. Des. 39 (4) (2005) 368-382.

[72] Amsden, A.A., KIVA-3: A KIVA program with block structured mesh for complex geometries, Los Alamos National Laboratory Report LA-12503-MS, 1993.

[73] Sone, K., Menon, S., Effect of subgrid modeling on the in-cylinder unsteady mixing process in a direct injection engine, J. Eng. Gas Turb. Power 125 (2) (2003) 435-443.

[74] Lee, D., Pomraning, E., Rutland, C.J., LES modeling of diesel engines, SAE Technical Paper 2002-01-2779, 2002.

[75] Lee, D., Rutland, C.J., Probability density function combustion modeling of diesel engines, Combust. Sci. Technol. 174 (10) (2002) 19-54.

[76] Jhavar, R., Rutland, C.J., Using large-eddy simulations to study mixing effects in early injection diesel engines combustion, SAE Technical Paper 2006-01-0871, 2006.

[77] Menon, S., Yeung, P.K., Kim, W., Effect of subgrid models on the computed interscale energy transfer of isotropic turbulence, Comput. Fluids 25 (2) (1996) 165-180.

[78] PROSTAR Version 3.103.521, Copyright 1988-2002, Computational Dynamics, Ltd.

[79] Dugue, V., Gauchet, N., Veynante, D., Applicability of large-eddy simulation to the fluid mechanics in a real engine configuration by means of an industrial code, SAE Technical Paper 2006-01-1194, 2006.

[80] Enaux, V. Granet, O. Vermorel, C. Lacour, C. Pera, C. Angelberger, T. Poinsot, LES study of cycle-to-cycle variations in a spark ignition engine, Proceedings of the Combustion Institute 33 (2011) 3115-3122.

[81] Bodin, O., Wang, Y., Mihaescu, M., Fuchs, L., LES of the Exhaust Flow in a Heavy-Duty Engine, Oil and Gas Science and Technology Rev. IFP Energies nouvelles 69(1) (2014) 177-188.

[82] Kuo, T-W, Yang, X., Gopalakrishnan, V., Chen, Z., Large Eddy Simulation (LES) for IC Engine Flows, Oil and Gas Science and Technology Rev. IFP Energies nouvelles, 69(1) (2014) 61-81.

[83] Misdariis, A. Robert, A., Vermorel, O, Richard, S., Poinsot, T., Numerical Methods and Turbulence Modeling for LES of Piston Engines: Impact on Flow Motion and Combustion, Oil and Gas Science and Technology Rev. IFP Energies nouvelles, 69(1) (2014) 83-105.

[84] Mittal, V., Kang, S., Doran, E., Cook, D., Pitsch, H., LES of Gas Exchange in IC Engines, Oil and Gas Science and Technology Rev. IFP Energies nouvelles, 69(1) (2014) 29-40.

[85] Piscaglia, F., Montorfano, A., Onorati, A., Brusiani, F., Boundary Conditions and SGS Models for LES of Wall-Bounded Separated Flows:An Application to Engine-Like Geometries, Oil and Gas Science and Technology Rev. IFP Energies nouvelles, 69(1) (2014) 11-27.

[86] Sakowitz, A., Reifarth, S., Mihaescu, M., Fuchs, L., Modeling of EGR Mixing in an Engine Intake Manifold Using LES, Oil and Gas Science and Technology Rev. IFP Energies nouvelles, 69(1) (2014), 167-176.

[87] Tillou, J., Michel, J.-B., Angelberger, C., Bekdemir, C., Veynante, D., Large-Eddy Simulation of Diesel Spray Combustion with Exhaust Gas Recirculation, Oil and Gas Science and Technology Rev. IFP Energies nouvelles, 69(1) (2014) 155-165.

[88] Fontanesi, S., Paltrinieri, S., D'Adamo, A., Duranti, S., Investigation of Boundary Condition and Field Distribution Effects on the Cycle-to-Cycle Variability of a Turbocharged GDI Engine Using LES, Oil and Gas Science and Technology Rev. IFP Energies nouvelles, 69(1) (2014), 107-128.

[89] Richard, S., Colin, O., Vermorel, O., Benkenida, A., Angelberger, C., Veynante, S., Towards large eddy simulation of combustion in spark ignition engines, Proceedings of the Combustion Institute 31 (2007) 3059-3066.

[90] Vermorel, O., Richard, S., Colin, O., Angelberger, C., Benkenida, A., Veynante, D., Multi-Cycle LES Simulations of Flow and Combustion in a PFI SI 4-Valve Production Engine, SAE Technical Paper 2007-01-0151, 2007.

[91] Zhou, L., Luo, K., Shuai, S., Jia, M., Numerical methods of improving computation efficiency on diesel spray and combustion using large eddy simulation in KIVA3V code, SAE Technical Paper 2014-01-1149, 2014.

[92] Zhou, L., Xie, M., Luo, K., Jia, M., Mixing Effects of Early Injection in Diesel Spray Using LES Model with Different Subgrid Scale Models, SAE Technical Paper 2013-01-1111, 2013.

[93] Devesa, A., Moreau, J., Poinsot, T., Helie, J., Large Eddy Simulations of Jet - Tumble Interaction in a GDI Model Engine Flow, SAE Technical Paper 2004-01-1997, 2004.

[94] Befrui, B., Corbinelli, G., Spiekermann, P., Shost, M., Large Eddy Simulation of GDI Single-Hole Flow and Near-Field Spray, SAE Int. J. Fuels Lubr. 5(2) (2012) 620-636.

[95] Keskinen, J., Vuorinen, V., Kaario, O., Larmi, M., Large Eddy Simulation of the Intake Flow in a Realistic Single Cylinder Configuration, SAE Technical Paper 2012-01-0137, 2012.

[96] Ranasinghe, C., Malalasekera, W., Clarke, A., Large Eddy Simulation of Premixed Combustion in Spark Ignited Engines Using a Dynamic Flame Surface Density Model, SAE Int. J. Engines 6(2) (2013) 898-910.

[97] Keskinen, J., Vuorinen, V., Larmi, M., Large Eddy Simulation of Flow over a Valve in a Simplified Cylinder Geometry, SAE Technical Paper 2011-01-0843, 2011.

[98] Piscaglia, F., Montorfano, A., Onorati, A., Towards the LES Simulation of IC Engines with Parallel Topologically Changing Meshes, SAE Int. J. Engines 6(2) (2013) 926-940.

[99] Pera, C., Angelberger, C., Large Eddy Simulation of a Motored Single-Cylinder Engine Using System Simulation to Define Boundary Conditions: Methodology and Validation, SAE Int. J. Engines 4(1) (2011) 948-963.

[100] Mobasheri, R., Peng, Z., Using Large Eddy Simulation for Studying Mixture Formation and Combustion Process in a DI Diesel Engine, SAE Technical Paper 2012-01-1716, 2012.

[101] ICE Physics and Chemistry, AVL FIRE user Manual v.2009. 1, 2009.

[102] Zhou, L., Luo, K., Jia, M., Shuai, S., Large Eddy Simulation of Liquid Fuel Spray and Combustion with Gradually Varying Grid, SAE Technical Paper 2013-01-2634, 2013.

[103] Rutland, C.J., Large-eddy simulations for internal combustion engines - a review, International Journal of Engine Research October 2011 vol. 12 no. 5421-45.

[104] Barths, H., Antoni, C., Peters, N., Three-dimensional simulation of pollutant formation in a DI diesel engine using multiple interactive flamelets, SAE Technical Paper 982459, 1998.

[105] Hergart, C., Barths, H., Peters, N., Modeling the combustion in a small-bore diesel engine using a method based on representative interactive flamelets, SAE Technical paper 1999-01-3550, 1999.

[106] Hasse, C., Barths, H., Peters, N., Modelling the effect of split injections in diesel engines using representative interactive flamelets, SAE Technical Paper 1999-01-3547, 1999.

[107] Felsch, C., Luckhchoura, V., Weber, J., Peters, N., Hasse, C., Wiese, W., Pischinger, S., Kolbeck, A., and Adomeit, P., Applying representative interactive flamelets (rif) with special emphasis on pollutant formation to simulate a DI diesel engine with roof-shaped combustion chamber and tumble charge motion, SAE Technical Paper 2007-01-0167, 2007.

[108] Abraham, J., Bracco, F. V., Reitz, R. D., Comparison of computed and measured premixed charged engine combustion, Combust. Flame 60(3) (1985) 309-322.

[109] Kong, S.-C., Reitz, R.D., Multidimensional modeling of diesel ignition and combustion using a multistep kinetics model, J. Eng. Gas Turbines Power 115(4) (1993) 781-789.

[110] Thobois, L., Lauvergne, R., Poinsot, T., Using LES to investigate reacting flow physics in engine design process, SAE Technical Paper 2007-01-0166, 2007.

[111] Im, H.G., Lund, T.S., Ferziger, J.H., Large eddy simulation of turbulent front propagation with dynamic subgrid models, Phys. Fluids 9(12), (1997) 3826-3833.

[112] Subramanian, G. Vervisch, l., Ravet, F., New developments in turbulent combustion modeling for engine design: ECFM-CLEH combustion sub-model, SAE Technical Paper 2007-01-0154, 2007.

[113] Shi, X, Li, G., Zheng, Y., DI diesel engine combustion modeling based on ECFM-3Z model, SAE Technical Paper 2007-01-4138, 2007.

[114] CD-Adapco. STAR-CD, Version 4.20, 2013.

[115] Vermorel, O., Richard, S., Colin, O., Angelberger, S., Benkenida, A., Veynante, D., Towards the understanding of cyclic variability in a spark ignited engine using multi-cycle LES, Combust. Flame, 156(8) (2009) 1525-1541.

[116] Hu, B., Jhavar, R., Singh, S., Reitz, R.D., Rutland, C.J., Combustion modeling of diesel combustion with partially premixed conditions, SAE Technical paper 2007-01-0163, 2007.

[117] Hu, B., and Rutland, C.J., Flamelet modeling with LES for diesel engine simulations, SAE Technical Paper 2006-01-0058, 2006.

[118] Wright, Y., Depaola, G., Boulouchos, K., Mastorakos, E., Simulations of spray autoignition and flame establishment with two-dimensional CMC, Combust. Flame 143(4) (2005) 402-419.

[119] Kim, S.H., Hu, K.Y., Fraser, R.A., Numerical prediction of the autoignition delay in a diesel-like environment by the conditional moment closure model, SAE Technical Paper, 2000-01-0200, 2000.

[120] De Paola, G, Mastorakos, E., Wright, Y.M., Boulouchos, K., Diesel engine simulations with multi-dimensional conditional moment closure, Combust. Sci. Technol. 180(5) (2008) 883-899.

[121] Jaberi, F.A., Colucci, P.J., James, S., Givi, P., Pope, S.B., Filtered mass density function for large-eddy simulation of turbulent reacting flows, J. Fluid Mech. 401 (1999) 85-121.

[122] Colucci, P.J., Jaberi, F.A., Givi, P., Pope, S.B., Filtered density function for large eddy simulation of turbulent reacting flows, Phys. Fluids 10 (2) (1998) 499-515.

[123] Pope, S.B., Computations of turbulent combustion: Progress and challenges, Proc. Combust. Inst. 23 (1990) 591-612.

[124] Gao, F., O'Brien, E.E., A large-eddy scheme for turbulent reacting flows, Phys. Fluids A 5 (6) (1993) 1282-1284.

[125] Givi, P., Filtered density function for subgrid scale modeling of turbulent combustion, AIAA J. 44 (1) (2006) 16-23.

[126] Haworth, D.C., Progress in probability density function methods for turbulent reacting flows, Prog. Energy Combust. Sci. 36 (2) (2010) 168-259.

[127] Sheikhi, M.R.H., Givi, P., Pope, S.B., Velocity-scalar filtered mass density function for large eddy simulation of turbulent flows, Phys. Fluids 19 (9) (2007) 095-106.

[128] Nik, M.B., Yilmaz, S.L., Sheikhi, M.R.H., Givi, P., Pope, S.B., Simulation of Sandia flame D using velocity-scalar filtered density function, AIAA J. 48 (7) (2010) 1513-1522.

[129] Nik, M.B., Yilmaz, S.L., Sheikhi, M.R.H., Givi, P., Grid resolution effects on VSFMDF/LES, Flow Turbul. Combust. (2010).

[130] Sheikhi, M.R.H., Givi, P., Pope, S.B., Frequency-velocity-scalar filtered mass density function for large-eddy simulation of turbulent flows, Phys. Fluids 21 (7) (2009) 075-102.

[131] James, S., Jaberi, F.A., Large Scale simulations of two-dimensional nonpremixed methane jet flames, Combust. Flame 123 (4) (2000) 465-487.

[132] Sheikhi, M.R.H., Drozda, T.G., Givi, P., Jaberi, F.A., Pope, S.B., Large-eddy simulation of a turbulent nonpremixed piloted methane jet flame (Sandia flame D), Proc. Combust. Inst. 30 (1) (2005) 549-556.

[133] Raman, V., Pitsch, H., Fox, R.O., Hybrid large-eddy simulation/lagrangian filtered density function approach for simulating turbulent combustion, Combust. Flame 143 (1-2) (2005) 56-78.

[134] Afshari, A., Jaberi, F.A., Shih, T.I-P., Large-eddy simulations of turbulent flows in an axisymmetric dump combustor, AIAA J. 46 (7) (2008) 1576-1592.

[135] Yaldizli, M., Mehravaran, K., Jaberi, F.A., Large-eddy simulations of turbulent methane jet flames with filtered mass density function, Int. J. Heat Mass Transfer 53 (11-12) (2010) 2551-2562.

[136] Yilmaz, S.L., Nik, M.B., Givi, P., Strakey, P.A., Scalar filtered density function for large eddy simulation of a bunsen burner, J. Prop. Power 26 (1) (2010) 84-93.

[137] Yilmaz, S.L., Nik, M.B., Sheikhi, M.R.H., Strakey, P.A., Givi, P., An irregularly portioned Lagrangian Monte Carlo method for turbulent flow simulation, J. Sci. Comp. 47 (1) (2011) 109-125.

[138] Banaeizadeh, A., Li, Z., Jaberi, F.A., Compressible scalar FMDF model for high speed turbulent flows, AIAA J. 49 (10) (2011) 2130-2143.

[139] Li, Z., Banaeizadeh, A., Jaberi, F.A., Two-phase filtered mass density function for LES of turbulent reacting flows, J. Fluid Mech. 760 (2014) 243-277.

[140] Yaldizli, M., Li, Z., Jaberi, F.A., A new model for large-eddy simulations of multiphase turbulent combustion, AIAA Paper No. 2007-5752, 2007.

[141] Li, Z., Yaldizli, M., Jaberi, F.A., Filtered mass density function for numerical simulations of spray combustion, AIAA Paper No. 2008-511, 2008.

[142] Banaeizadeh, A., Afshari, A., Schock, H., Jaberi, F.A., Large-eddy simulations of turbulent flows in IC engines, ASME Paper No. DETC2008-49788, 2008.

[143] Irannejad, A., Banaeizadeh, A., Jaberi F.,. Large eddy simulation of turbulent spray combustion, Combustion and Flame 162 (2) (2015) 431-450.

[144] Moin, P., Squires, W., Cabot, W.H., Lee, S., A dynamic subgrid-scale model for compressible turbulence and scalar transport, Phys. Fluids A 3 (11) (1991) 2746-2757.

[145] O'Brien, E.E., The Probability Density Function (PDF) approach to reacting turbulent flows, in: P.A. Libby, F.A. Williams (Ed.), Turbulent Reacting Flows, Topics in Applied Phys., vol. 44, Springer, 1980, p.185-218 (Chapter 5).

[146] Dopazo, C., O'Brien, E.E., Statistical treatment of non-isothermal reactions in turbulence, Combust. Sci. Technol. 13 (1976) 99-112.

[147] Borghi, R. Turbulent combustion modeling, Prog. Energy Combust. Sci. 14 (1988) 245-292.

[148] Delarue, B.J., Pope, S.B, Application of PDF methods to compressible turbulent flows, Physics of Fluids, 9(9) (1997), 2704-2715.

[149] Pope, S.B. PDF methods for turbulent reactive flows, Prog. Energy Combust. Sci. 11 (1985) 119-192.

[150] Gardiner, W., Handbook of Stochastic Methods, Springer-Verlag, New York, 1990.

[151] Lele, S.K., Compact finite difference schemes with spectral like resolution, J. Comp. Phys. 103 (1) (1992) 12-42.

[152] Mittal, M., Sadr, R., Schock, H.J., Fedewa, A., Naqwi, A., In-cylinder engine flow measurement using stereoscopic molecular tagging velocimetry (SMTV), Exp. Fluids 46 (2) (2009) 277-284.

[153] Banaeizadeh, A., PhD Dissertation, Department of Mechanical Engineering, Michigan State University, 2010.

[154] Griffiths, J.F., Jiao, Q., Kordylewski, W., Schreiber, M., Meyer, J., Knoche, K.F., Experimental and numerical studies of Ditertiary Butyl Peroxide combustion at high pressures in a rapid compression machine, Combustion and Flame 93, (1993) 303-315.

[155] Lee, D., Hochgreb, S., Rapid compression machines: heat transfer and suppression of corner vortex, Combustion and Flame 114 (1998) 531-545.

[156] Wurmel, J., Simmie, J.M., CFD studies of a twin-piston rapid compression machine, Combustion and Flame 141(4) (2005) 417-430.

[157] Mittal, G., Sung, C.J., Aerodynamics inside a rapid compression machine Combustion and Flame 145(1-2) (1996) 160-180.

[158] Mittal, G., Raju, Mandhapati P., Sung, C-J, Computational fluid dynamics modeling of the hydrogen ignition in a rapid compression machine, Combustion and Flame 155 (2008) 417-428.

[159] Mittal, G., Raju, Mandhapati P., Sung, C-J, CFD modeling of two-stage ignition in a rapid compression machine: Assessment of zero-dimensional approach, Combustion and Flame, 157(7) (2010) 1316-1324.

[160] Casey, A., Mittal, G., Sung, C-J, Toulson, E., Lee, T., An aerosol rapid compression machine for studying energetic-nanoparticle-enhanced combustion of liquid fuels, Proceedings of the Combustion Institute 33(2) (2011) 3367-3374.

[161] Affleck, W.S., Thomas, A., An opposed piston rapid compression machine for preflame reaction studies, Proceedings of the Institution of Mechanical Engineers, 183, 1968. $PIME_PROC_1968_183_034_02$.

[162] Brett., L., PhD thesis, National University of Ireland, Galway, 1999.

[163] Srivastava, S., Schock, H., Jaberi, F., Numerical simulations of turbulent sprays with a multicomponent evaporation model, SAE Technical Paper 2013-01-1603, 2013.

[164] Foster D., Herold, R., Lemke, J., Regner, G., Wahl, M., Thermodynamic Benefits of Opposed-Piston Two-Stroke Engines, SAE Technical Paper 2011-01-2216, 2011.

[165] Zhu Y.-X., Savonen C., Johnson, N.L., Amsden, A.A., Three-Dimensional Computations of the Scavenging Process in an Opposed-Piston Engine, SAE Technical Paper 941899, 1994.

[166] Hofbauer, P., Opposed Piston Opposed Cylinder (opoc) Engine for Military Ground Vehicles, SAE Technical Paper 2005-01-1548, 2005.

[167] Franke, M., Huang H., Liu, J.P., Geistert A., Adomeit, P., Opposed Piston Opposed Cylinder (opocTM) 450 hp engine: Performance Development by CAE Simulations and Testing, SAE Technical Paper 2006-01-0277, 2006.

[168] Kalkstein, J., Rver, W., Campbell, B., Zhong, L., Huang, H., Liu, J.P., Tatur, M., Geistert, A., Tusinean, A., Opposed Piston Opposed Cylinder (opoc) 5/10 kW Heavy Fuel Engine for UAVs and APUs, SAE Technical Paper 2006-01-0278, 2006.

[169] Venugopal, R., Abani N., MacKenzie, R., Effects of Injection Pattern Design on Piston Thermal Management in an Opposed-Piston Two-Stroke Engine, SAE Technical Paper 2013-01-2423, 2013.

[170] Blair, G.P., Design and Simulation of Two-Stroke Engines, Society of Automotive Engineers, Inc., Warrendale, PA 15096-0001.

[171] Assanis, D.N., Filipi, Z.S., Fiveland, S.B., Syrimis, M., A Predictive Ignition Delay Correlation Under Steady-State and Transient Operation of a Direct Injection Diesel Engine, Transactions of the ASME, Vol. 125, April 2003.

[172] Homing D.C., Davidson D.F., Hanson, R.K, Study of the High-Temperature Autoignition of n-Alkane/O2/Air Mixtures, Journal of Propulsion and Power 18(2) (2002).

[173] Hu, Y.F., Blake, R.J., Emerson, D.R., An optimal migration algorithm for dynamic load balancing, Concurrency - Pract. Exper. 10(6) (1998) 467-483.